2D-confined carrier systems have given access to the exploration of manifold quantum effects in fundamental research and also led to numerous device concepts for commercial electronic applications. Additionally, the possibility to control the 2D carrier density via gate voltages through the electric field-effect offers a great advantage of external manipulation of the system. With the optimization of lithography on a nanometre scale, gated 2D systems in semiconductor heterostructures are currently intensively studied as platforms for few to single-carrier devices. In this context, a precise control of the heterostructure layout including the doping, as well as an understanding of charge reconfiguration effects within the device, are important challenges. This thesis, addresses the heterostructure optimization and focuses on a precise field-effect control of Schottky top-gated modulation doped Si/SiGe heterostructures. For the optimization of the heterostructure design, several parameters which affect the strain, the band offset and the doping degree in Si/SiGe two-dimensional electron systems are precisely studied. In parallel, the field-effect influence on Si/SiGe heterostructures is used to identify the origin of disorder and possible sources of charge noise. In this connection, finally a modified charge transfer model including a polarizability of neutral phosphorous atoms inside the doping layer is developed.

Universitätsverlag Regensburg

ISBN 978-3-86845-123-8

gefördert von:

Alumni der physikalischen Fakultät der Universität Regensburg e.V.

Universität Regensburg

Michael Schmalzbauer

Heterostructure design of Si/SiGe two-dimensional electron systems for field-effect devices

Dissertationsreihe Physik - Band 45

Universitätsverlag Regensburg

45 Dissertationsreihe Physik

Michael Schmalzbauer

Heterostructure design of Si/SiGe two-dimensional electron systems for field-effect devices

Heterostructure design of Si/SiGe two-dimensional electron systems for field-effect devices

Dissertation zur Erlangung des Doktorgrades der Naturwissenschaften (Dr. rer. nat.)
der Fakultät für Physik der Universität Regensburg
vorgelegt von

Michael Schmalzbauer

aus Freyung

im September 2014

Die Arbeit wurde von Prof. Dr. Dominique Bougeard angeleitet.
Das Promotionsgesuch wurde am 07.05.2014 eingereicht.
Das Promotionskolloquium fand am 30.01.2015 statt.

Prüfungsausschuss: Vorsitzender: Prof. Dr. Karsten Rincke
1. Gutachter: Prof. Dr. Dominique Bougeard
2. Gutachter: Prof. Dr. Dieter Weiss
weiterer Prüfer: Prof. Dr. Milena Grifoni

Dissertationsreihe der Fakultät für Physik der Universität Regensburg, Band 45

Herausgegeben vom Präsidium des Alumnivereins der Physikalischen Fakultät:
Klaus Richter, Andreas Schäfer, Werner Wegscheider, Dieter Weiss

Michael Schmalzbauer

Heterostructure design of Si/SiGe two-dimensional electron systems for field-effect devices

Universitätsverlag Regensburg

Bibliografische Informationen der Deutschen Bibliothek.
Die Deutsche Bibliothek verzeichnet diese Publikation
in der Deutschen Nationalbibliografie. Detailierte bibliografische Daten
sind im Internet über http://dnb.ddb.de abrufbar.

1. Auflage 2015

Leibnizstraße 13, 93055 Regensburg

Konzeption: Thomas Geiger
Umschlaggestaltung: Franz Stadler, Designcooperative Nittenau eG
Layout: Michael Schmalzbauer
Druck: Docupoint, Magdeburg
ISBN: 978-3-86845-123-8

Weitere Informationen zum Verlagsprogramm erhalten Sie unter:
www.univerlag-regensburg.de

Contents

1 Introduction

In recent decades, semiconductor devices have more and more changed our world. Computer processors and flash memories are only two examples for the rapid progress in microelectronics which affects today's life. The development started in 1947 with the discovery of the first transistor made of germanium (Ge) which formed the technological basis for the very first integrated circuits. Since that time especially the category of gated semiconductor devices received considerable attention. Only a few years after the realization of the first silicon (Si) based transistor in 1954, the Si metal-oxide-semiconductor field-effect transistor (MOSFET) was demonstrated at Bell labs. This type of device exploits the field-effect to confine the motion of electrons in a plane at the Si/SiO_2 interface which leads to the formation of a so-called two-dimensional electron system (2DES). In the late 70s the evolution of the molecular beam epitaxy (MBE) growth technique and the invention of the modulation doping concept by Störmer et al. [1] resulted in a new transistor type in which distinctly higher mobilities could be reached. The high electron mobility transistor (HEMT) makes use of an undoped channel, created by a heterojunction of two materials with different band gaps and a separated n-type donor supply layer which provides electrons for the 2DES.

Moreover, two-dimensional electron systems entailed extensive research on confinement effects and low-dimensional physics which in 1980 resulted in the discovery of the integer quantum Hall effect (IQHE) by Klaus von Klitzing [2]. In his measurements on a high quality 4-terminal Si-MOSFET, for which he received the Nobel Prize in 1985, von Klitzing discovered that at low temperatures and high magnetic fields the transversal resistance shows plateaus while the longitudinal resistance simultaneously exhibits minima. Interestingly the plateau value is completely independent from the sample properties and only depends on fundamental physical constants. As a result, the Hall resistance is given by $R_H = R_K/\nu = h/\nu e^2 = 25812,8\Omega/\nu$, with the filling factor ν and the von Klitzing constant R_K which since that time is also used as standard resistor.

While the quantum Hall effect is bound to a two-dimensional system, a further reduction of the degree of freedom of the electron motion to 1D channels resulted in a new research field. In this context especially electrostatically defined quantum dots (QDs), which can be created by applying a voltage bias to several split gates on top of the surface of a 2DES, attracted great attention. Very first reports of

periodic oscillations in the conductance of quantum dots came up from the experiments of Meirav et al. and Field et al. [3, 4]. The increasing experience finally made it possible to control and isolate single electrons in electrostatically defined QDs. In fact, such single-electron devices are envisioned in quantum information processing (QIP). In this regard, Loss and Di Vincenzo originally suggested to use the spin states of coupled single-electron quantum dots for quantum computation [5]. Indeed, a successful implementation of quantum computing requires a series of coherent manipulations of specific pairs of qubits. Consequently, electron spins seem to be ideal candidates for qubits since they interact only weakly with their environment and thus are very robust against decoherence.

In the past few years, especially the III-V material system of GaAs semiconductors saw a lot of progress regarding quantum dot devices. However, in III-V materials the hyperfine interaction distinctly limits the coherence times [6] which affirms the need to explore different material systems in order to circumvent this drawback. Using Si and Ge as host materials drastically reduces the hyperfine interaction because only about 4,7% of natural Si and approximately 7,8% of Ge carry a nuclear spin [7, 8]. Recently, double quantum dot (DQD) systems have been realized in a Si/SiGe heterostructure as illustrated in the work of Wild and Shaji et al. [9, 10]. Since there is also the possibility to use the nuclear spin-less isotopes ^{28}Si and ^{74}Ge, the hyperfine interaction can be almost completely suppressed. First experiments on an electrostatically defined DQD in a ^{28}Si/SiGe 2DES have already been performed [11]. Although less hyperfine interaction was achieved, a loss of information is still possible by unwanted charge noise [12, 6]. As a potential source for these detrimental effects, a charging and/or discharging of the phosphorous doping layer between the 2DES and the sample surface was supposed [13]. In fact, similar charge reconfiguration effects were also observed in gated AlGaAs/GaAs heterostructures and attributed to charging events in the doping layer or deep impurities [14, 15]. However, since the doping layer is compulsory to form a two-dimensional electron system, feasible solutions have to be developed.

In contrast to Si MOSFETs in which the field effect is well understood, a precise controllability of Schottky gated Si/SiGe heterostructures lags behind. Nevertheless the Si/SiGe material system offers the possibility to precisely tune the band structure and the material composition by a selected epitaxial growth of Si and Ge. Consequently, the heterointerface between Si and SiGe can be grown with atomic precision compared to e.g. Si MOSFETs so that higher mobilities can be achieved. The aim of this thesis is to develop a high mobility and low density Schottky top-gated Si/SiGe 2DES in order to realize a suitable platform for future high quality quantum dot devices. In the scope of our analysis, the field-effect influence between gate and 2DES is explicitly and systematically studied since this strategy allows us to identify eventual drawbacks in the current heterostructure design.

The thesis is organized as follows:

- Chapter 2 presents the fundamental background regarding the peculiarities of Si/SiGe material system, the formation of a 2DES in this host system, the challenge of gating Si/SiGe heterostructures and the current state of the art.
- Chapter 3 introduces the experimental methods and set-ups as well as the corresponding specific measurement strategies which build the basis for all conducted experiments in this work.
- Chapter 4 presents the efforts which were made to optimize the current heterostructure design, in order to realize a high quality 2DES. In the scope of this analysis, different XRD and magnetotransport based overview wafer maps were developed which allow us to extract important parameters, e.g. the effective Ge content or the degree of relaxation of each sample on the wafer.
- Chapter 5 precisely focuses on the field effect controllability of Schottky gated Si/SiGe heterostructures. The study yields a charge reconfiguration model which allows us to understand the observed hysteresis and disorder effects, as well as the strong connection of the phosphorous doping degree and the capacitive coupling between gate and 2DES. Additionally, we deduce a quantitative method which enables to make statements about the dielectric constants of MBE grown Si and Ge.
- Chapter 6 explores the origin of detrimental leakage currents in Schottky gated Si/SiGe heterostructures. In this connection, we moreover demonstrate the validity and applicability of several leakage current models which are based on a triangular barrier and finally extract important parameters e.g. the Schottky barrier height and/or the energy level of trap states.
- Chapter 7 finally summarizes all results and gives a brief outlook on future perspectives and feasible solutions.

2 Theoretical background

In this chapter, the main focus lies on the theoretical concepts behind the development of two-dimensional electron systems in a Si/SiGe host material system. First of all, important bulk properties of silicon (Si) and germanium (Ge) are dealt with before the formation of a 2DES in this material environment is explained. In a next step, the two main growth methods of so called virtual substrates, which are an essential building block for two-dimensional electron systems, are covered and compared. Then, the theoretical basics of magnetotansport measurements are discussed. Finally, the general way of gating as well as the theory behind the field-effect control in our heterostructures are introduced.

2.1 Material properties of Si and Ge

Si and Ge are both members of group IV elements in the periodic table and crystallize in the diamond lattice. The lattice constant of silicon is $a_{Si} = 0.54310$ nm, whereas Ge has a slightly larger lattice constant of $a_{Ge} = 0.56575$ nm. From this follows that the lattice mismatch between both materials, which can be calculated with

$$f = \frac{a_{Si} - a_{Ge}}{a_{Si}} \tag{2.1}$$

is about 4.2 % [16]. Figure 2.1 shows the band structures of Si and Ge respectively. The band gap minimum of Si at room temperature lies close to the Δ-point and amounts to 1.11 eV. For bulk Si, this conduction band minimum is six-fold degenerate and therefore called Δ_6 minimum. The Ge band gap minimum of 0.66 eV for comparison can be found at the four-fold degenerate L_4-point of the first Brillouin zone. At the Δ-point, Ge exhibits a band gap of 0.85 eV [17]. Both materials are indirect semiconductors and completely miscible. The resulting $Si_{1-x}Ge_x$ alloys can easily be varied in interesting parameters like lattice constant, band structure or effective g-factor by continuously changing the Ge content x. For $x < 85$ %, the conduction band minimum in relaxed $Si_{1-x}Ge_x$ is Δ-like as in Si. With a Ge content higher than 85 %, the minimum gets Ge-like. Concerning low Ge concentrations, it is possible to use a linear interpolation according to Vegard's law in order to estimate the $Si_{1-x}Ge_x$ lattice constant:

$$a_{Si_{1-x}Ge_x} = a_{Si} + (a_{Ge} - a_{Si}) \cdot x \tag{2.2}$$

Using a parabolic interpolation leads to a more accurate description [18].

$$a_{Si_{1-x}Ge_x}[\text{nm}] = a_{Si}[\text{nm}] + 0.01992 \cdot x[\text{nm}] + 0.002733 \cdot x^2[\text{nm}] \qquad (2.3)$$

Epitaxial growth of lattice mismatched $Si_{1-x}Ge_x$ layers with different Ge content on top of each other results in strain and therefore leads to modifications in the band structure.

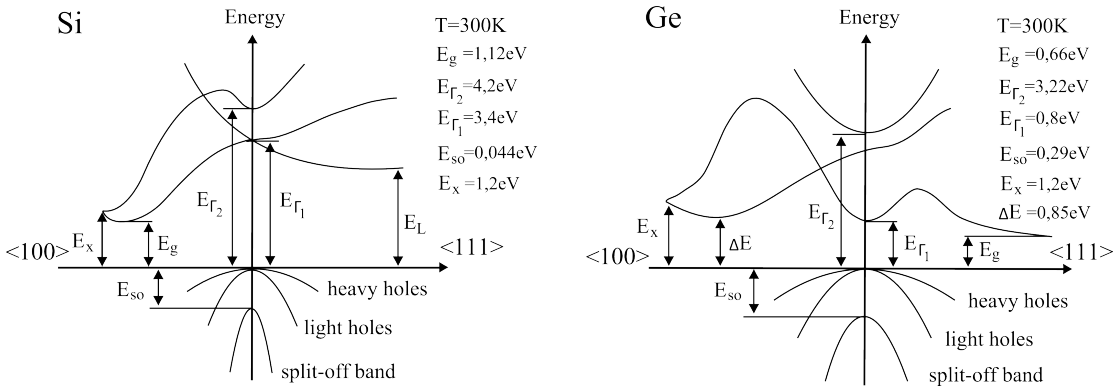

Figure 2.1: *Band structure diagrams of Si and Ge respectively. The conduction band minima for Si (Δ-point) and Ge (L_4-point) are shown. Additionally, the lowest energy gaps and several other energy minima are illustrated for room temperature conditions.*

2.2 2DES in a Si/SiGe material system

In 1985, Abstreiter and coworkers were the first to realize a 2DES at a Si/SiGe interface in a selectively doped $Si/Si_{0.5}Ge_{0.5}$ superlattice which was grown on a uniformly relaxed $Si/Si_{0.25}Ge_{0.75}$ buffer layer [18]. They explained their findings by strain induced modifications of the conduction band which cause electron confinement in the Si layer. Indeed, if Si is pseudomorphically grown onto a material with larger lattice constant like $Si_{1-x}Ge_x$, it is subject to tensile strain until a critical thickness is reached and plastic relaxation sets in. As a result of this tensile strain, the six-fold degenerate conduction band minimum of Si (Δ_6 minimum) is lifted due to the broken symmetry in the Brillouin zone [19]. Consequently, an energetically lower lying two-fold degenerate band minimum (Δ_2 valley) in growth direction and an energetically higher lying four-fold conduction band minimum (Δ_4 valley) perpendicular to the growth direction form (see figure 2.2a,b). Therefore, tensile strain in the Si layer causes a type-II band offset which depends mainly on the Ge content x of the $Si_{1-x}Ge_x$ layer. If we now sandwich a Si layer between two $Si_{1-x}Ge_x$ layers, a quantum well (QW) develops. Introducing a modulation doping layer on top of the $Si_{1-x}Ge_x$ spacer layer results in a confinement of electrons inside the QW [20]. The concept for modulation doping was first

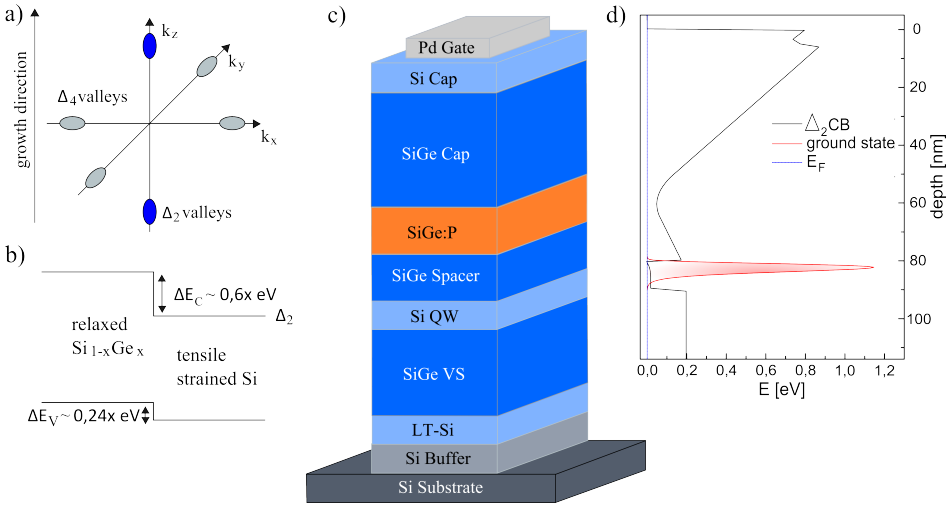

Figure 2.2: *a) Lifting of the six fold degenerate conduction band minimum into an energetically higher lying Δ_4 and an energetically lower lying Δ_2 band. Additionally, the surfaces of constant energy in the k-space are illustrated. b) Formation of a type-II band offset if Si is pseudomorphically grown on a relaxed SiGe layer. c) Schematic drawing of a Schottky gated modulation-doped Si/SiGe heterostructure. The active region from Si cap to Si QW is in scale in contrast to the virtual substrate (SiGe VS) which can be several µm thick. d) Picture of the according band structure profile (Δ_2 conduction band) simulated with nextnano++. The Fermi energy is set to zero in thermal equilibrium. Moreover, the occupation of the lowest state in the QW is indicated.*

introduced by Störmer et al. in 1978 for a GaAs/AlGaAs heterostructure [1]. Due to the spatial separation of charge carriers from the ionized dopants by inserting a spacer layer, scattering mechanisms like ionized impurity scattering are reduced. Additionally, as a result of the anisotropy of the effective mass in tensile strained Si, the transversal effective mass $m_t^* = 0.19 \cdot m_0$ gets smaller [19]. Because of these two reasons, higher mobilities according to $\mu = \frac{e \cdot \tau_t}{m_t^*}$ can be reached in modulation doped $Si/Si_{1-x}Ge_x$ heterostructures [21]. Here, τ_t displays the transport scattering time and e denotes the electron charge. In figure 2.2c, a typical MBE grown sample structure, which was used in this work as well as the corresponding band structure profile (see figure 2.2d), is shown. Starting from the bottom, the intrinsic Si wafer is overgrown with a so called virtual substrate (VS) to produce a fully relaxed $Si_{1-x}Ge_x$ buffer layer which provides the strain adjustment for the Si channel. The concept of VS will be explained in detail in the next section. Then, a 10 nm thick Si QW is sandwiched between the VS and a 15 nm SiGe spacer layer. This sequence is followed by a 15 nm SiGe:P modulation-doping layer [1].

[1] For the sake of completeness, it has to be mentioned that one sample which was investigated during this thesis had only a 2 nm thick modulation-doping layer which we call "quasi δ-doped". Indeed, the doping strength was adjusted in a way to achieve approximately the

Afterwards, the structure is capped with a 45 nm SiGe layer and a 5 to 10 nm Si layer to protect the sample against oxidation. Finally, after several lithographical steps (section 3.5), the Hall-bar patterned sample is covered with a Pd Schottky top gate.

2.3 Virtual Substrates

To achieve higher mobilities in $Si/Si_{1-x}Ge_x$ heterostructures, fully relaxed and defect-free buffer layers are compulsory. Monocrystalline $Si_{1-x}Ge_x$ wafers with a Ge content of 25-35 % are not commercially available, thus they have to be grown epitaxially on a Si substrate. These $Si_{1-x}Ge_x$ are called virtual substrates (VS). However, if we directly deposit $Si_{1-x}Ge_x$ with a Ge content of 25-35 % on a Si substrate, the SiGe is subject to compressible strain [22, 16]. After exceeding a critical thickness h_c, which depends on the Ge content, the strain will relax by forming crystal defects. In particular, threading dislocations will develop during this plastic relaxation process. They pierce the whole sample structure up to the surface and act detrimentally on the device performance. The density of threading dislocations in such single-step buffers is $1.0 \cdot 10^9 \mathrm{cm}^{-2}$ to $1.0 \cdot 10^{11} \mathrm{cm}^{-2}$ [19, 23, 24].

In order to produce a high quality 2DES, the best VS would be as flat and defect free as possible as well as completely free of any strain and thus fully relaxed. In a realistic crystal the complete absence of built-in crystal defects is not feasible but there are strategies to strongly reduce the amount of threading dislocations piercing through the whole structure. Hence, a flat and defect free surface of VS can be assured and higher mobilities in the two-dimensional electron systems are reached. In the following, the two main concepts for the growth of efficient VS will be presented. First of all, the graded buffer concept is introduced before the so called low-temperature LT-Si VS is discussed.

2.3.1 Graded buffer

Beginning with an intrinsic Si substrate, a 200 nm thick Si buffer layer is grown to guarantee an atomically flat surface. In a next step, a thick SiGe layer with gradually increasing Ge content is deposited on top of the Si buffer. The deposition itself starts with a Ge content of 5 % and is linearly increased until the wanted Ge content is achieved. For our samples, a continuous grading rate of 8 %/μm was used [25]. Due to this small linear increase in the Ge content and the high substrate temperatures of about T_s=600°C, the built-in strain relaxes faster due to very mobile threading dislocations, which bend to the side instead of moving to the

same doping degree as for the 15 nm thick doping layer.

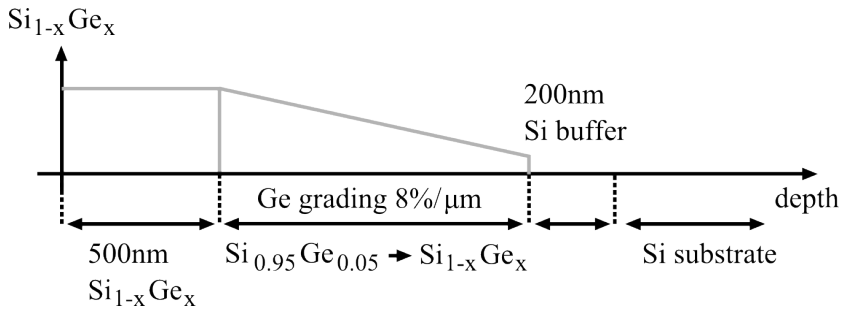

Figure 2.3: *Schematic drawing of a graded buffer VS growth process on a Si substrate. The SiGe growth is started with a Ge content of 5% and linearly increased with a grading rate of 8 %/µm until the desired Ge content is reached. Finally, the graded layer is overgrown with a 500 nm thick constant composition layer. Adapted from [25].*

top. A second important aspect is that for threading dislocations it is energetically more favourable to move in a layer with constant Ge content than crossing it [26, 27, 28]. Finally, the grading layer is overgrown with a 500 nm thick constant composition layer. A short scheme of the whole grading concept is sketched in figure 2.3. As a consequence of the aforementioned arguments, we deduce for the graded buffer concept that the slower the grading the lower the defect density on the VS surface. Additionally, the defect density is reduced by increasing the thickness of the constant composition layer. However, this optimization leads to a high material consumption which is needed for high quality buffers and enormous time costs that are necessary to grow more than 3μm thick buffer layers.

2.3.2 Low temperature Silicon

In contrast to the graded buffer concept, the low-temperature silicon (LT-Si) VS is far less time and material consuming. For this method again a 200 nm thick Si buffer layer is used to prepare a flat and defect free Si surface. Then, a 100 nm thick Si layer is deposited at low substrate temperatures and at high growth rates to introduce many point defects into this layer. The idea behind this concept is that the built-in point defects will pin threading dislocations in SiGe with both ends and twist them, preventing a piercing up to the surface [29, 30, 31]. On top of this defect rich layer, a 500 nm thick constant composition layer with the desired final Ge content is deposited. Figure 2.4 illustrates the whole growth procedure. In comparison to the graded buffer concept, the LT-Si VS seems to be better suited for larger sample series due to the above mentioned lower material consumption [32, 33, 34]. However, the large concentration of easily diffusing point defects may cause some disadvantages for future devices.

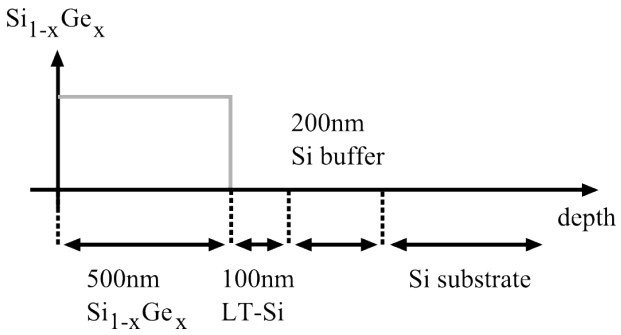

Figure 2.4: *Sketch of the low-temperature silicon VS layer layout. The process is started with a Si buffer layer followed by a 100nm thick Si layer which is grown at low substrate temperatures and high deposition rates to create point defects. Finally, this layer is overgrown with a 500 nm thick SiGe constant composition layer. Adapted from [25].*

It is experimentally not clear up to now to what extent these point defects create charge traps and therefore influence field-effect controlled devices.

2.4 Basic magnetotransport theory

The electrical characterization via magnetotransport experiments is done to obtain information about the carrier density and mobility which are important physical properties of our two-dimensional electron systems. The measurements were performed by sending a current I on the order of 10 to 50 nA through the Hall-bar and simultaneously recording the transversal and longitudinal resistance (see section 3.6.3). For cryogenic temperatures and low magnetic fields ($B \leq 0.5$T), the classical Hall effect occurs while for higher magnetic fields the integer quantum Hall effect (IQHE) is observed.

Starting at low magnetic fields, the perpendicular B field causes a Lorentz force which redirects electrons perpendicular to I and B and thus leads to a Hall voltage U_{xy} [16]. The resulting Hall resistance

$$\rho_{xy} = \frac{\mathrm{U}_{xy}}{I} = \frac{B}{|e|n} \tag{2.4}$$

is linear in B, and the longitudinal resistance of the 2DES

$$\rho_{xx} = \frac{\mathrm{U}_{xx} \cdot W}{I \cdot L} \tag{2.5}$$

is constant [16, 35, 36]. Here, W denotes the width of the Hall-bar whereas L is the distance between the Hall-bar terminals (see inset in figure 2.5). From the

slope

$$m = \left.\frac{\partial \rho_{xy}(B)}{\partial B}\right|_{B=0} \tag{2.6}$$

of the Hall resistance $\rho_{xy}(B)$, the carrier density

$$n = \frac{1}{|e|m} \tag{2.7}$$

with e being the elementary charge can be extracted. Furthermore, the mobility μ is determined by using the zero field resistance $\rho_{xx}(B = 0)$

$$\mu = \frac{1}{n|e|\rho_{xx}(B = 0)} \tag{2.8}$$

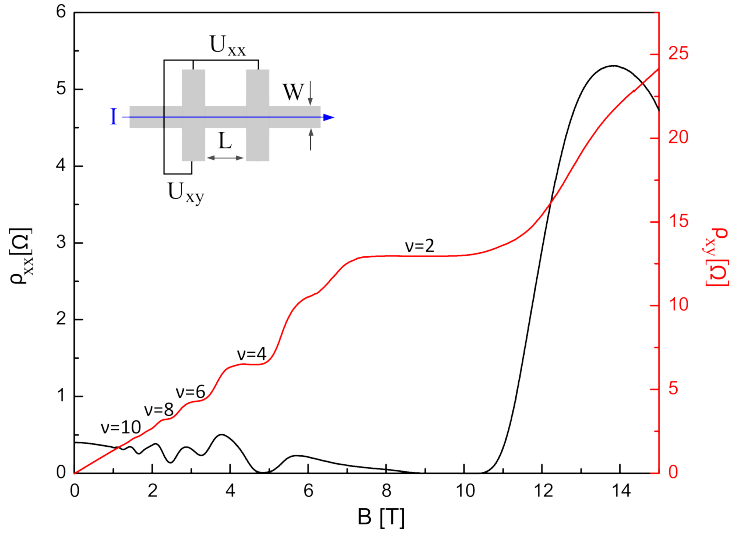

Figure 2.5: *Longitudinal ρ_{xx}(black curve) and Hall ρ_{xy}(red curve) resistivity as a function of magnetic field (B). The little inset shows the standard Hall-bar geometry with the width W and length L. ν displays the corresponding integer filling factors of each plateau in the Hall curve and the minima in the longitudinal resistance respectively.*

For higher magnetic fields where $\omega_c\tau_s > 1$, the Landau quantisation leads to a splitting of the continuous density of states into discrete energy levels, the so called Landau levels. Here, ω_c is the cyclotron resonance and τ_s is the single particle relaxation time which describes the lifetime of the quantum states [16, 35, 36]. Along with increasing magnetic fields, the degree of degeneration of the Landau levels, and thus the carrier density of each Landau level

$$n_L = \frac{eB}{h} \tag{2.9}$$

as well as the distance between them

$$\hbar\omega_c = \frac{\hbar eB}{m^\star} \tag{2.10}$$

rises but the total carrier density is constant [35]. Here, $m^\star$ denotes the effective mass and $\hbar$ is the reduced Planck constant. When the highest occupied Landau level gets completely depopulated, with rising B field, the Fermi energy jumps to the next occupied level. Consequently, oscillations in the longitudinal resistance, which are named Shubnikov-de Haas (SdH) oscillations, appear [35]. Figure 2.5 exemplarily shows a typical quantum Hall measurement from a sample which was investigated during this thesis. At high enough fields, each minimum in ρ_{xx} is simultaneously accompanied by quantized plateaus in the Hall resistance ρ_{xy}. The plateaus can be classified by the ratio

$$\nu = \frac{n}{n_L} \cdot \tag{2.11}$$

In this equation, ν is called filling factor. Therefore, in association with equation 2.4, the Hall resistivity assumes the following form [16, 35, 36]

$$\rho_{xy} = \frac{h}{e^2\nu} \tag{2.12}$$

Another important aspect is that by combining equation 2.9 and 2.11, the charge carrier density can be calculated directly out of the SdH minima [16, 35, 36].

$$n = B \cdot \nu \cdot \frac{e}{h} \tag{2.13}$$

2.5 Concept of gating

In 1936, Nevill Mott first developed a theory for the correct direction of rectification in metal semiconductor junctions [37, 38, 39]. Later on, Walter Schottky and Eberhard Spenke extended this theory which finally resulted in the formation of a Schottky barrier [40, 41]. Since that time, the deposition of metallic electrodes on semiconductors attracted more and more attention. As a matter of fact, these contacts led to a precise electrical control in several semiconductor devices. In the following, the formation of a Schottky top gate and the basic concept behind it are explained. Additionally, the direct application to the 2DES is introduced and the latest state of the art is discussed. Moreover, the advantages and drawbacks of this kind of gates are treated. Finally, the basic theory behind leakage current mechanisms and the applicability to our system is introduced.

2.5.1 Schottky contacts

In principle, one can distinguish between two types of metal semiconductor junctions. There are on the one hand Schottky contacts, which are used as gates, and on the other hand ohmic contacts. Schottky contacts are characterized by an energetic barrier between the metal and the semiconductor which results in a rectification of the electric current. Consequently, they are of great importance to the successful operation of semiconductor devices. In contrast, for ohmic contacts such a barrier does not exist. From this follows that a linear relation between current and voltage occurs [35]. To understand the formation of a Schottky barrier, we first consider a metallic electrode and a semiconductor separated from each other. For the metal, the work function is defined as the energy which is necessary to lift an electron from the metal Fermi energy E_{Fm} to the vacuum level E_{vac} [42, 43]:

$$\Phi_m = E_{vac} - E_{Fm} \tag{2.14}$$

Simultaneously, the semiconductor work function can be written as:

$$\Phi_s = E_{vac} - E_{Fs} \tag{2.15}$$

The electron affinity in the semiconductor is given by

$$\chi_s = E_{vac} - E_c = \Phi_s - (E_c - E_{Fs}) \tag{2.16}$$

The reference point in both systems is the vacuum level E_{vac}. In the following, we solely assume that $\Phi_m > \Phi_s$ and that we have an n-type semiconductor. This is comparable to the case of our gated Si/SiGe heterostructures. If now the semiconductor and the metal approach each other, the Fermi levels in the metal and in the semiconductor have to align in thermodynamic equilibrium (see figure 2.6). This is achieved by a charge transfer from the semiconductor to the metal. As a result, electrons accumulate at the metal surface and a depletion zone in the semiconductor develops. Consequently, the bands in the semiconductor bend up and an energetic barrier Φ_B between metal and semiconductor is formed according to:

$$\Phi_B = \Phi_m - \chi_s \tag{2.17}$$

If now a positive voltage is applied on the metal (forward bias), the depletion zone in the semiconductor is reduced and therefore the barrier is lowered. For a sufficient high voltage value, the barrier completely vanishes and a current can flow. In contrast to that, by application of a negative bias to the metal (reverse bias), the depletion zone in the semiconductor is enhanced and hence the barrier height is increased [42, 43]. In practice however, the barrier does not only depend on semiconductor and metal work functions but also on the properties of the interface which have been deliberately neglected until now. Indeed we have to take into account a small region between the metal and the semiconductor which is known as the interface specific region (ISR).

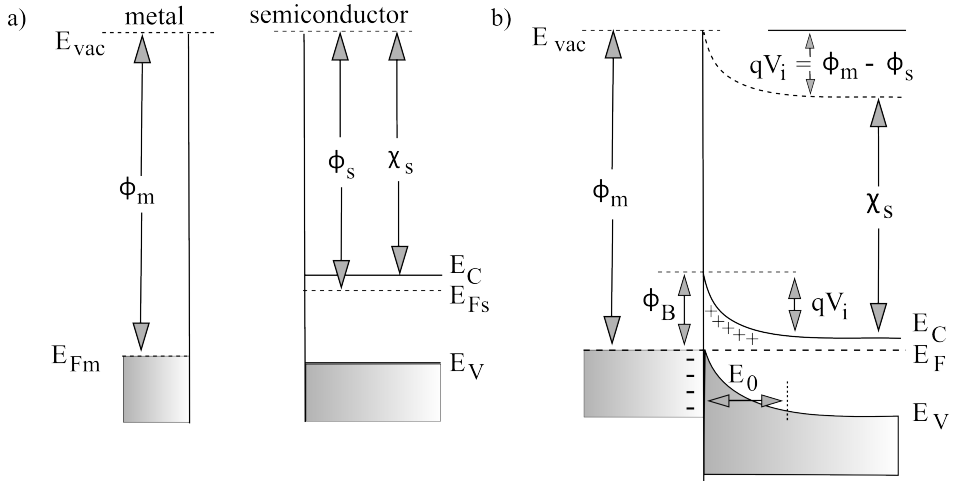

Figure 2.6: *a) Semiconductor and metal are separated. The vacuum energy E_{Vac} as well as the metal (E_{Fm}) and semiconductor (E_{Fs}) Fermi energies are indicated respectively. Moreover, both the metal work function Φ_m and the semiconductor electron affinity χ_s are illustrated. b) Shows the situation in which the metal and the n-type semiconductor are in contact. The Fermi levels approach each other and therefore electrons accumulate at the metal surface. As a consequence, the bands are bent up. The resulting Schottky barrier is displayed as Φ_B.*

This is the transitional region between the metal and the semiconductor where the magnitude of the Schottky barrier height (SBH) is determined. A term called Fermi level (FL) pinning has often been used in the past to describe the insensitivity of the experimental SBH to the metal and semiconductor work functions [44, 45]. It was shown that if the periodic structure of a crystal lattice is terminated at the surface, a lot of defects and dangling bonds are created [46, 47, 48]. Consequently, there are many states localized on the surface which lie energetically inside the band gap E_g. If the surface density of states is high, the Fermi level is pinned inside these states Φ_S. This effect is described with the Bardeen relation

$$\Phi_B^S = E_g - \Phi_S - \Delta\Phi \tag{2.18}$$

in which $\Phi_S = \frac{1}{3}E_g$ [44]. A second negative influence on the SBH is based on the image charge model, which is also known as Schottky effect, see figure 2.7 [49]. If an electron escapes from the metal, a positive image charge is created in the metal having the same distance x from the surface. The potential energy in this case is given by:

$$\mu(x) = \int_{-\infty}^{x} F dx = \int_{-\infty}^{x} \frac{-e^2}{4\pi\epsilon_0(2x)^2} dx = \frac{e^2}{16\pi\epsilon_0 x} \tag{2.19}$$

Here, ϵ_0 denotes the vacuum permittivity. Including the external electric field E, we attain:

$$\mu(x) = \frac{e^2}{16\pi\epsilon_0 x} + eEx \tag{2.20}$$

As a result, the barrier gets smaller and the maximum lies at

$$x_m = \frac{\sqrt{e}}{\sqrt{16\pi\epsilon_0\epsilon E}}. \tag{2.21}$$

By using this equation, the lowering of the barrier $\Delta\Phi$ is calculated

$$\Delta\Phi = 2eEx_m = \sqrt{\frac{e^3E}{4\pi\epsilon_0\epsilon}} \tag{2.22}$$

with the semiconductor dielectric constant ϵ.

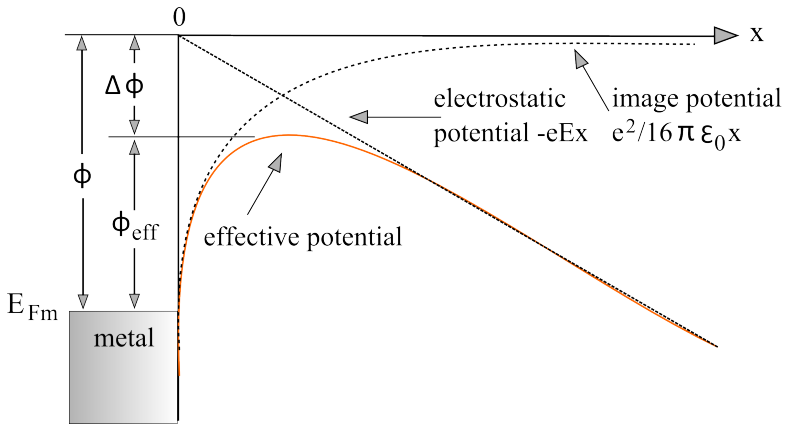

Figure 2.7: *Schematical picture of the image charge model (Schottky effect). The image potential energy and the energy due to the applied external electric field E (electrostatic potential) which cause the lowering of the barrier height $\Delta\Phi$ are shown. Moreover, the resulting effective barrier height Φ_{eff} is illustrated.*

2.5.2 Gating of 2DES

Over the past 20 years, metallic gates have become a powerful tool to electrostatically manipulate both doped and undoped two-dimensional electron systems. In particular, several groups reported high mobilities due to an effective Schottky gating in different material systems [50, 51, 52, 53, 54]. Recently, special attention was turned on gated modulation-doped heterostructures which form the basis for several few electron devices, e.g. electrostatically defined quantum dots (QD). The fact that changing the gate voltage not only influences the carrier density and the mobility but can also induces charge reconfigurations between the 2DES and deep traps or the doping layer has been scrutinized carefully [13, 15, 14] since these effects negatively affect the performance of QD devices. In this context, Rössler et al. studied hysteretic effects during a gate sweep regarding the carrier density in Schottky top-gated GaAs/AlGaAs heterostructures [14]. They explained their findings with charge redistributions in the δ-doping layer during the depletion of

the 2DES. Moreover, Burke et al. investigated the origin of gate hysteresis in p-type Si-doped AlGaAs/GaAs heterostructures and stated that the hysteresis becomes drastically worse if the gates are insulated. As a possible reason they suggested additional trap states which form in the dielectric under high voltage stress. Furthermore, Burke and coworkers demonstrated that the hysteresis in Schottky gated samples is mainly caused by shallow traps in contrast to n-type heterostructures which suffer from deep trapping DX centers [15]. Simultaneously, Wild et al. proposed a model for gate induced hysteresis effects in a Si/SiGe 2DES [13]. Similarly to Rössler et al., Wild and coworkers measured the 2DES density and mobility as a function of gate voltage via magnetotransport experiments. Additionally, they used self-consistent band structure simulations in a way that the simulated 2DES density can be fitted to the experimentally recorded hysteresis curve. As a result of this model, the corresponding occupation of the modulation doping layer n_p (if charge transfer is possible) as well as the 2DES density n_{2DES} could be extracted simultaneously. In the following, we will focus on this model since it introduces the fundamental principle for further gate dependent measurements in this thesis.

Figure 2.8a shows a typical n_{2DES} versus U_{HB} hysteresis curve. The curve is divided into four key regions as suggested by Wild et al. [13]. Section I is called linear regime due to the fact that with increasing gate voltage U_{HB}, the carrier density of the 2DES n_{2DES} is linearly enhanced. Additionally, it is possible to analytically calculate the capacitive coupling, in analogy to a simple capacitor model, from the slope in the n_{2DES} versus U_{HB} curve according to [35]

$$C_{th} = \frac{\partial n_{2DES}}{\partial U_{HB}} = \frac{\epsilon_0}{e}\left(\frac{d_{Si}}{\epsilon_{Si}} + \frac{d_{SiGe}}{\epsilon_{SiGe}} + \frac{\epsilon_0}{e^2}\frac{\partial E_F(n)}{\partial n}\frac{\epsilon_0}{e^2}\frac{\partial E_0(n)}{\partial n}\right)^{-1}. \tag{2.23}$$

Here, d_i are the thicknesses of the Si and the SiGe layers between the top gate and the 2DES. ϵ_i are the dielectric constants of Si and SiGe respectively. The third and the fourth term indicate the density of states in the 2DES and the quantum capacitance. However, since the contributions of the last two terms to C_{th} are small, (on the order of 2%) these quantities are neglected in the following. Furthermore, the pinch-off voltage U_{po} is estimated by extending the linear regime in negative gate voltage direction until the U_{HB} axis is intersected. Above a positive threshold voltage U_{th}, n(U) no longer behaves like a capacitor and a so called saturation regime II is reached (see figure 2.8a). Wild et. al. stated that when exceeding this threshold voltage, the energy level of the phosphorous atoms E_P gets equal to the Fermi energy E_F so that tunnelling from the 2DES to the doping layer is possible, see figure 2.8c [13]. As a result, the occupation of the doping layer density n_P increases as shown in figure 2.8b. When gradually further increasing the gate bias, the conduction band minimum E_{CB} in the doping layer reaches the Fermi level. Consequently, now charge reconfigurations are also possible into the conduction band minimum of the doping layer before they relax quickly into lower lying localized phosphorous states.

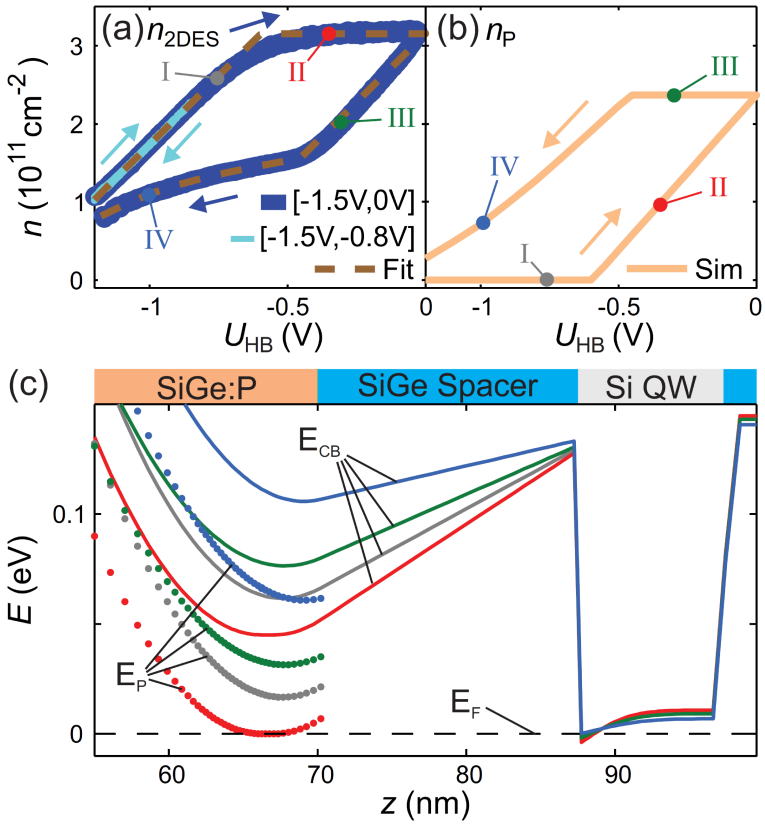

Figure 2.8: *a) 2DES density n_{2DES} during up- and down-sweep (indicated by dark blue arrows) in dependence of the applied Hall-bar gate voltage U_{HB}. The hysteresis loop is divided into four regions I-IV. The pinch-off voltage U_{po} is estimated by extending the linear regime to the point were n_{2DES} intersects the gate voltage (U_{HB}) axis. b) shows the simulated carrier density n_P in the doping layer. c) displays the according band structure profile for the configurations in sections I-IV. E_{CB} is the energy of the conduction band E_F denotes the Fermi energy and E_P labels the phosphorous energy level. Adapted from [13]*

Hence, the carrier density n_{2DES} saturates due to the fact that the delivered electrons from the ohmic contacts immediately are transferred into the doping layer. Moreover, the arising electrostatic potential in the doping layer entails a screening of the gate induced electric field. When sweeping the gate voltage back to the start value, n_{2DES} first decreases linearly due to an asymmetry in the charge transfer rates. This circumstance becomes clearer when the influence of the electric field is taken into consideration. As a matter of fact, the electric field which arises due to the positive applied gate voltage is still present in the same direction and is only lowered. This, in combination with the still occupied phosphorous states, results in a linear decreasing slope since a tunnelling process into the doping layer is furthermore possible (indicated in section III in figure 2.8a). This holds true

until a threshold voltage is reached under which the lowest phosphorous level is lifted above the Fermi level. Henceforth, the doping layer gets rapidly depleted since now tunnelling events from the 2DES into the doping layer are impossible (see region IV figure 2.8a,b). There are four important key characteristics in the $n(U)$ graph, namely the pinch-off voltage U_{po}, the capacitive coupling $C_m = \frac{\partial n}{\partial U}$, the saturation and the hysteretic behaviour due to charge reconfigurations from the 2DES into the doping layer. However, this characteristics depend on several parameters like the Schottky barrier height Φ_B, the dielectric constants of Si (ϵ_{Si}) and Ge (ϵ_{Ge}), layer thicknesses d_i of Si and SiGe as well as the doping concentration N. Consequently, Wild proposed three possible strategies to realize a convenient fit to the experimental data points in the hysteresis curve[13]. In strategy one, he assumed lower dielectric constants for Si and Ge than the literature values. Due to the reduced dielectric constants the pinch-off voltage shifts to more negative values which can only be compensated by reducing the Schottky barrier to $0.71eV$. Moreover, the nominal doping concentration N and the layer thicknesses d_i of Si and SiGe are kept constant. The corresponding dielectric constant of SiGe has always been calculated in a first approximation by

$$\epsilon_{SiGe} = (1 - x)\epsilon_{Si} + x\epsilon_{Ge} \tag{2.24}$$

in which x denotes the Ge content. For the second strategy, the thicknesses d_i were postulated to be larger than the nominal values, the Schottky barrier height was estimated to be $0.91eV$ and the doping concentration was considered to be lower than the nominal doping degree. Furthermore, literature values were used for the dielectric constants of Si and Ge. The third strategy leaves both the dielectric constants and the layer thicknesses unaffected and takes the nominal doping concentration as a fit parameter. Moreover, the Schottky barrier is said to have a value of about $0.85eV$. However, in this special case, a thin interfacial layer with a dielectric length of $d_i/\epsilon_i = 2.56nm$ has to be incorporated on top of the Si capping layer in order to receive good fitting results.

In the end, Wild came to the conclusion that each strategy by itself is rather unlikely since the deviations from literature values concerning the dielectric constants of Si and Ge, drastic deviations in the layer thicknesses and/or deviations in the doping concentration N are very unrealistic. Instead a combination of all strategies seems to be more likely which mitigates the necessity of some extremal fit parameters. Consequently, for simplicity of the modelling, Wild chose strategy three in which all uncertainties in the parameter selection were absorbed in the interfacial layer.

2.5.3 Basic leakage current mechanisms

The performance of various electronic devices especially field-effect transistors is restricted due to inherent leakage currents [55, 56]. Therefore in the past few years

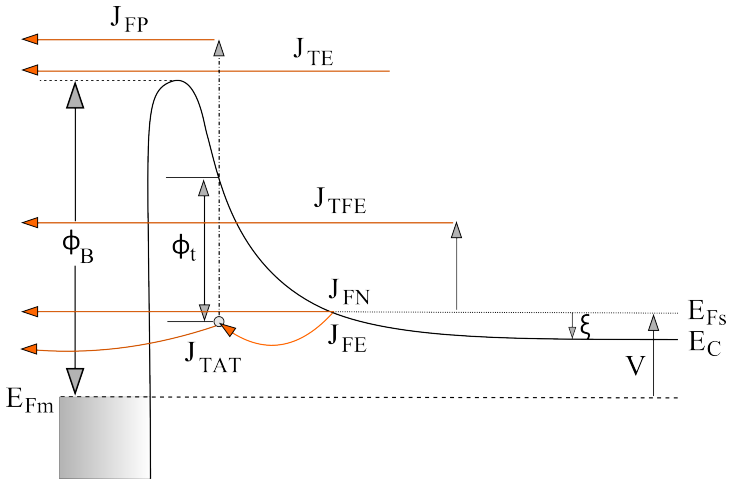

Figure 2.9: *Schematical drawing of several leakage current mechanisms in metal semiconductor junctions under forward bias: J_{FN} = Fowler-Nordheim tunnelling,J_{FE} = field emission, J_{TFE} = thermionic field emission, J_{TE} = thermionic emission, J_{TAT} = trap-assisted tunnelling, J_{PF} = Pool-Frenkel emission. Additionally, a trap state is indicated by a black open circle, V denotes the applied gate voltage, ξ is the difference between the Fermi level of the semiconductor E_{Fs} and the conduction band edge E_C.*

heroic efforts have been made to reduce the influence and to identify the origin of leakage [57, 58, 59]. Several attempts with high k-dielectrics like Al_2O_3 and HfO_2 were tested in metal insulator semiconductor field-effect transistors (MISFET) in order to decrease leakage currents [60, 61, 62, 63, 64]. As a first consequence, the leakage currents were reduced and high voltages could be applied to the gates. However, this progress was accompanied by the formation of many trap states and voltage stress effects in the dielectric which hamper the field effect control in most electrical devices [65, 66, 67, 68]. Indeed, one has to find a compromise in using gate dielectrics or direct deposited Schottky gates depending on the respective application. In the following, basic leakage current mechanisms which were developed for metal semiconductor junctions by assuming a triangular barrier and might be relevant in our Si/SiGe heterostructures are briefly presented, see figure 2.9.

Field emission

This model, which was developed by Padovani and Stratton, describes the tunnelling of charge carriers through Schottky barriers only due to the influence of the applied electric field. Corrections of the Schottky barrier height according to the Schottky effect (see section 2.5.1) are neglected in this approach and therefore a simple triangular barrier is taken into account [69, 70, 49]. Consequently, the

current density for the tunnelling process from the semiconductor to the metal is given by

$$J = \frac{2q}{h^3} \int_0^\infty [f_1(E) - f_2(E)]dE \int_0 P(E, p_y, p_z)dp_y dp_z \tag{2.25}$$

in which q is the elementary charge, E describes the electron energy, f_1(E) and f_2(E) are the Fermi-Dirac distributions in two conducting regions. Furthermore, p_y and p_z correspond to the components of the electron momentum perpendicular to the current flow and $P(E, p_y, p_z)$ the transition probability. According to the Wentzel-Kramers-Brillouin (WKB) approximation and in connection with a parabolic energy-momentum relation, the current density can be written as

$$J = \frac{4\pi m^\star q}{h^3} \int_0^\infty [f_1(E) - f_2(E)]dE \int_0^E P(E_x)dE_x \tag{2.26}$$

with

$$lnP(E_x) = -\frac{2\sqrt{2m^\star}}{h} \int_{x_1}^{x_2} (\Phi - E_x)^{\frac{1}{2}} dx \tag{2.27}$$

in which $\Phi(x)$ is the potential barrier energy, $E_x = \frac{p_x^2}{2m^\star}$ is the electron energy in x direction and $m^\star$ is the effective electron mass. Performing a Taylor expansion for equation 2.27 and neglecting higher order terms results in a new expression for the current density:

$$J = \frac{A^\star T^2 \exp(-b_1)}{(c_1 k_B T)^2} \frac{\pi c_1 k_B T}{\sin(\pi c_1 k_B T)} [1 - \exp(-c_1 qV)] \tag{2.28}$$

Here, V is the applied gate voltage, $A^\star = \frac{4\pi m^\star g k_B^2}{h^3}$ is the Richardson constant [71] and b_1 as well as c_1 are the first components of the Taylor expansion. If we assume tunnelling through a Schottky barrier, the exact formulas can be written as $b_1 = \frac{q(\Phi_B - V)}{E_{00}}$ and $c_1 = \frac{\log(4(\Phi_B - V)/\xi)}{2E_{00}}$. The factor $\xi = \frac{E_F - E_C}{q}$ displays the difference between the Fermi level energy and the conduction band energy. E_{00} represents an energy which is given by

$$E_{00} = \frac{q\hbar}{2} \sqrt{\frac{N}{m^\star \epsilon_S}} \tag{2.29}$$

in which N is the number of charge carriers and ϵ_S is the dielectric constant of the semiconductor. Additionally, there is a further condition for the WKB approximation, which limits the gate voltage V, so that ξ does not become equal to Φ_B and therefore

$$c_1 k_B T < 1 \tag{2.30}$$

has to be valid. In the range of large biases $c_1 V \gg 1$, the final leakage current density is described by [43]

$$J_{FE} = \frac{A^\star T \pi \exp[-q(\Phi_B - V)/E_{00}]}{c_1 k_B \sin(\pi c_1 k_B T)} [1 - \exp(-c_1 qV)] \tag{2.31}$$

Thermionic-field emission

In this model, electrons are assumed to tunnel from an energy level E_m which lies above the Fermi level but still lower than the barrier height [72, 70]. Consequently, the effective barrier is lower and therefore thermionic field emission occurs for fields below the field emission limit. Starting from V-I relationship, the current density can be expressed as [72, 73, 74]

$$J = \frac{A^\star}{2\pi k_B T} \exp\left(\frac{q\xi}{k_B T} - b_m - \frac{E_m}{k_B T}\right)\left(\frac{\pi}{f_m}\right)^{\frac{1}{2}} \times [1 + erf(E_m f_m^{1/2})] \tag{2.32}$$

in which b_m, c_m and f_m are components of a Taylor expansion for the exponent of transparency of the barrier around a particular energy E_m which satisfies equation

$$c_m k_B T = 1 \tag{2.33}$$

Moreover, $erf(E_m f_m^{1/2})$ is an error function which is set equal to 1. Furthermore, one has to take into account that these results are only valid in a certain temperature range.

$$c_1 k_B T > 1 \tag{2.34}$$

Additionally, the components of the Taylor expansion are calculated to:

$$b_m = \frac{1}{E_{00}}\left[(q\Phi_B - qV + q\xi)^{\frac{1}{2}}(q\Phi_B - qV + q\xi - E_m)^{\frac{1}{2}} - \frac{E_{00}E_m}{k_B T}\right] \tag{2.35}$$

$$c_m = \frac{1}{E_{00}}\left[\frac{(q\Phi_B - qV + q\xi)^{\frac{1}{2}} + (q\Phi_B - qV + q\xi - E_m)^{\frac{1}{2}}}{E_m^{1/2}}\right] \tag{2.36}$$

$$f_m = \frac{\cosh^2(E_{00}/k_B T)}{4E_{00}q(\Phi_B - V + \xi)} \tag{2.37}$$

The energy E_m can then be evaluated by combining equations 2.33 and 2.36.

$$E_m = \frac{q(\Phi_B - V + \xi)}{\cosh^2(E_{00}/k_B T)} \tag{2.38}$$

Employing b_m, c_m and f_m to equation 2.32, one can deduce that the current-voltage characteristic is mainly dominated by the exponential factor. As a result, we get

$$b_m + \left(\frac{E_m}{k_B}\right) = q\frac{\Phi_B - V + \xi}{E_0} \tag{2.39}$$

in which E_0 is given by

$$E_0 = E_{00}\coth(E_{00}/k_B T). \tag{2.40}$$

Analogous to the field emission model, the current density is expressed as a product of a saturation current and a voltage dependent term which results in the final thermionic field emission equation:

$$J_{TFE} = \frac{A^\star T[\pi E_{00}q(\Phi_B - V + \xi)]^{1/2}}{k_B \cosh(E_{00}/k_B T)} \exp\left[\frac{q\xi}{k_B T} - \frac{q(\Phi_B + \xi)}{E_0}\right] \exp\left(\frac{qV}{E_0}\right) \tag{2.41}$$

Thermionic Emission

The thermionic emission theory by Bethe [75] is derived from three assumptions: Firstly, k_BT is smaller than the barrier height Φ_B, secondly the thermal equilibrium is established at the plane that determines the emission, and thirdly the existence of a net current flow does not affect the equilibrium between the metal and the semiconductor [43]. Due to this hypotheses, the shape of the barrier profile depends solely on the barrier height. Therefore, the current density from the semiconductor to the metal is determined by the concentration of electrons with sufficient high energies to overcome the barrier in x-direction:

$$J_{s\to m} = \int_{E_{Fn}+q\Phi_B}^{\infty} qv_x dn \tag{2.42}$$

Here, $E_{Fn} + q\Phi_B$ is the minimum energy required for thermionic emission and v_x denotes the carrier velocity in transport direction. The electron density in an increasing energy range is given by [43]

$$dn = N(E)F(E)dE \approx \frac{4\pi(2m^\star)^{3/2}}{h^3}\sqrt{E-E_C}\exp\left(-\frac{E-E_C+q\xi}{k_BT}\right)dE \tag{2.43}$$

in which $N(E)$ and $F(E)$ are the density of states and the distribution function respectively. Assuming that the energy of the electrons in the conduction band is purely kinetic

$$E - E_C = \frac{1}{2}m^\star v^2 \tag{2.44}$$

leads to

$$dn \approx 2\left(\frac{m^\star}{h}\right)^3 \exp\left(\frac{q\xi}{k_BT}\right)\exp\left(-\frac{m^\star v^2}{2k_BT}\right)4\pi v^2 dv \tag{2.45}$$

If the splitting of the velocity in its components is taken into account, we obtain:

$$\begin{aligned} J = 2q\left(\frac{m^\star}{h}\right)^3 \exp\left(\frac{q\xi}{k_BT}\right)\int_{v_{0x}}^{\infty} v_x \exp\left(-\frac{m^\star v_x^2}{2k_BT}\right)dv_x \\ \int_{-\infty}^{\infty}\exp\left(-\frac{m^\star v_y^2}{2k_BT}\right)dv_y \int_{-\infty}^{\infty}\exp\left(-\frac{m^\star v_z^2}{2k_BT}\right)dv_z \\ = \frac{4\pi q m^\star k_B^2 T^2}{h^3}\exp\left(\frac{q\xi}{k_BT}\right)\exp\left(-\frac{m^\star v_{0x}^2}{2k_BT}\right) \end{aligned} \tag{2.46}$$

in which v_{0x} is the minimum velocity in x-direction to overcome the Schottky barrier given by

$$\frac{1}{2}m^\star v_{0x}^2 = q(\Psi_{bi} - V) \tag{2.47}$$

with $\Psi_{bi} = \Phi_B + \xi$ being the built in potential. Finally, after inserting equation 2.47 in 2.46, the current density for the thermionic emission model results in [43]:

$$J_{TE} = A^\star T^2 \exp\left(-\frac{q(\Phi_B - V)}{k_BT}\right) \tag{2.48}$$

Trap assisted tunnelling

Trap assisted tunnelling is a two step charge transport mechanism which is usually used in metal insulator semiconductor (MIS) structures [66, 76]. In this model, a tunnelling process from one trap state into another or into a trap followed by a direct tunnelling through the barrier is assumed. In fact, trap states can be formed from impurity atoms, crystal defects or interface roughness. The tunnelling rates during this two-step procedure are therefore expressed as [77, 78]:

$$R_1 = C_1 N_t (1 - f) P_1 \tag{2.49}$$

$$R_2 = C_2 N_t f P_2 \tag{2.50}$$

in which C_1 and C_2 are slowly varying functions of electron energy, N_t is the concentration of the involved traps, f is the occupation probability and P_1 as well as P_2 are the tunnelling probabilities calculated from the WKB approximation. Additionally, the tunnelling probabilities can be evaluated as follows:

$$P_1 = \exp\left(-2\int_0^{x_t} k(x)dx\right) \tag{2.51}$$

$$P_2 = \exp\left(-2\int_{x_t}^{x} k(x)dx\right) \tag{2.52}$$

with

$$k(x) = \sqrt{\frac{2m^\star(q\Phi(x) - E_x)}{\hbar^2}} \tag{2.53}$$

being the propagation constant. In the steady state case, the electron concentration in the traps is constant. As a result, the trap assisted tunnelling rate adopts the following form:

$$R_t = \frac{C_t N_t P_1 P_2}{P_1 + P_2} \tag{2.54}$$

Furthermore, the tunnelling current is given by [79]:

$$J = \int \frac{q C_t N_t P_1 P_2}{P_1 + P_2} dx \tag{2.55}$$

If the Schottky effect (see section 2.5.1) is neglected, the tunnelling probabilities are expressed as [78]:

$$P_1 = \exp\left(-\frac{4(2qm^\star)^{1/2}}{3\hbar F}(\Phi^{3/2}(x) - \Phi_t^{3/2})\right) \tag{2.56}$$

$$P_2 = \exp\left(-\frac{4(2qm^\star)^{1/2}}{3\hbar F}\Phi^{3/2}(x)\right) \tag{2.57}$$

Here, F displays the external electric field and Φ_t is the trap energy level. Finally, the current density is described by [79]

$$J_{TAT} = \frac{2qC_tN_t}{3A\sqrt{\Phi_t}} \exp\left(-\frac{4\sqrt{2m^\star\Phi_t}}{3\hbar qF}\right) \tag{2.58}$$

in which $C_t = (m_{Si}/m_x)^{5/2}(8E_i^{3/2})/3\hbar(q\Phi_{B,eff})^{1/2})$ [80], E_i is the total energy of an electron and $A = 4\sqrt{2m^\star}/3\hbar$. Here, the factor (m_{Si}/m_x) describes the ratio between the electron masses of different materials through which the tunnelling takes place. In case that no dielectric has been used between top gate and the heterostructure, this factor simplifies to 1.

Poole-Frenkel emission

Similarly to the trap-assisted tunnelling model, Pool-Frenkel emission depicts a carrier transport mechanism which exhibits two parts. Firstly, electrons are allowed to tunnel into trap states and secondly because of the high thermal energy hop into the conduction band and over the barrier. Additionally, it is possible that electrons reach energetically higher lying trap states followed by a tunnelling process through the barrier. This means that the effective barrier height is reduced in this case. The simplified formula for the current density is defined as [76, 81, 82]

$$J_{PF} \propto E_{Ox} \exp\left(-\frac{\Phi_B - \beta_{PF}E_{Ox}^{1/2}}{k_BT}\right) \tag{2.59}$$

in which $E_{Ox} = (V_G - V_{FB}/t_{Ox})$ is the electric field that accounts for the difference of the applied gate voltage V_G and the flat band voltage V_{FB}. Moreover, $\beta_{PF} = \sqrt{q/4\pi\epsilon_0 K}$ with K being the high frequency dielectric constant.

Fowler-Nordheim tunnelling

Fowler-Nordheim tunnelling describes a charge carrier tunnelling process through a triangular barrier in presence of a strong electric field usually in the order of $10^7\frac{V}{cm}$ [76, 83]. Since in our case we do not achieve electric fields in this order of magnitude, this leakage current model can be excluded. For the sake of completeness the simplified formula for the current density which was derived by Fowler and Nordheim is given by [83]:

$$J_{FN} = \frac{q^2}{8\pi h\Phi_B}F^2 \exp\left(-\frac{8\pi\sqrt{2m^\star q\Phi_B^3}}{3hF}\right) \tag{2.60}$$

Here, Φ_B stands for the barrier height and F is the external electric field.

3 Experimental methods

The fabrication as well as the analysis of high quality Si/SiGe heterostructures is very crucial since they build the basic platform for several devices. In the following, the machines and measurement methods used in this context are presented.

3.1 Molecular Beam Epitaxy

Molecular beam epitaxy (MBE) is a technique which is based on epitaxial growth of atomic layers by condensation of different molecular or atomic beams on the surface of heated Si substrates. Using MBE, it is possible to fabricate high quality interfaces so that most of the mobility limiting mechanisms like interface roughness scattering on defects or impurities can be minimized [84, 85].

All samples investigated during this thesis were grown unrotated in a Riber SIVA-32 MBE machine. Its design and cell geometry is shown schematically in figure 3.1. Additionally, the MBE is equipped with a power driven heating in order to adjust the substrate temperature during growth. Furthermore, a thermo couple is used as a measurement system to check the substrate temperature during the growth process [86]. The base pressure in the growth chamber is roughly $7,0 \cdot 10^{-11}$ mbar and can be further reduced by cooling the growth chamber walls with liquid nitrogen (lN_2). The MBE chamber was opened only once at the beginning of this thesis. From this follows that all samples have been grown under equal pressure conditions. The layers were deposited on (001) oriented, nominally intrinsic Si substrates (n-doping, $> 1500\Omega$cm) with a nominal thickness of $425 \pm 75\mu$m.

The most important sources are two electron beam evaporators for silicon (Si) and germanium (Ge) which are located directly beneath the wafer in the center of the main growth chamber [25]. Both sources are calibrated with reflection high energy electron diffraction (RHEED) during the growth of several mono layers (ML) for three different flux rates. The flux rate of the electron beams is always controlled and readjusted by Electron Impact Emission Spectroscopy (EIES) while the growth process takes place. Moreover, effusion cells for isotopically pure ^{70}Ge and ^{73}Ge as well as ^{28}Si are part of the system.

Additionally, there are three cells for doping: A boron (B) cell which is used for p-type doping, a GaP cell to realize the n-type doping with phosphorous (P) and

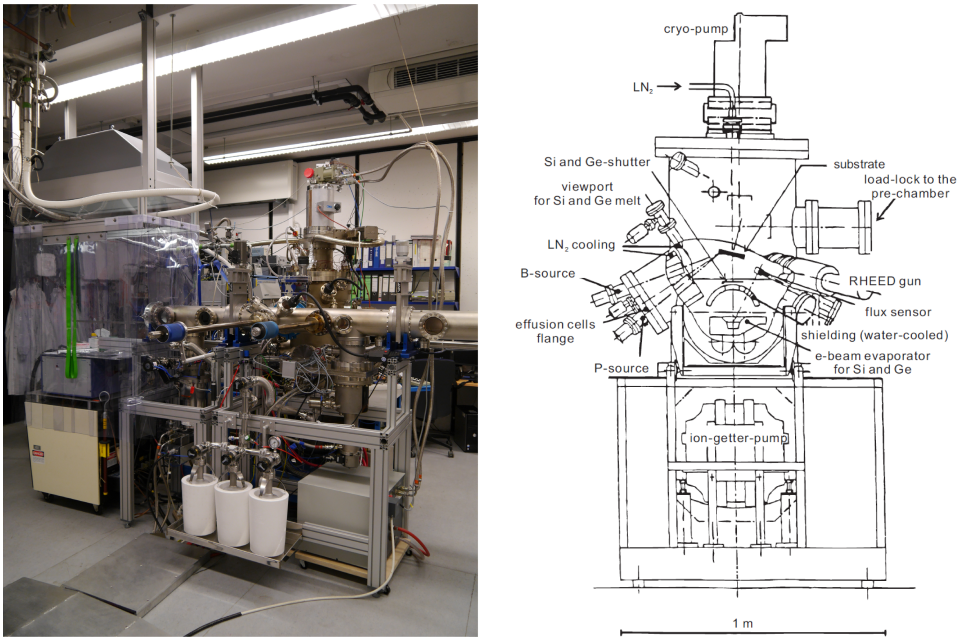

Figure 3.1: *Picture and sketch of the Riber Shiva-32 MBE and the according cell geometrie. Adapted from [86] [25]*

a manganese (Mn) source which could also be used for p-type doping as well as for magnetic doping or alloying [87, 88]. In this work the main focus lies on the fabrication of two-dimensional electron systems (2DES) so that we restrict ourselves to the temperature controlled GaP cell which is located approximately opposite to the RHEED gun. The calibration of the GaP cell is performed and regularly checked by Secondary Ion Mass Spectrometry (SIMS) (see section 3.2). Typical temperatures for n-type doping with the GaP cell lie around 650°C.

All wafer surfaces were well defined by a wet chemical oxide according to [86] in order to avoid contaminations prior to loading them into the MBE. Finally the oxide is thermally desorbed at $T \geq 750°C$ in the growth chamber directly before the first growth step. The surface quality is monitored in-situ by RHEED during the hole growth process.

3.2 Secondary Ion Mass Spectrometry

As already mentioned above, SIMS was used to quantify the effective Ge content, the layer thicknesses and the specific dopant concentration in Si/SiGe heterostructures. A simple sketch of the SIMS functionality is given in figure 3.2.

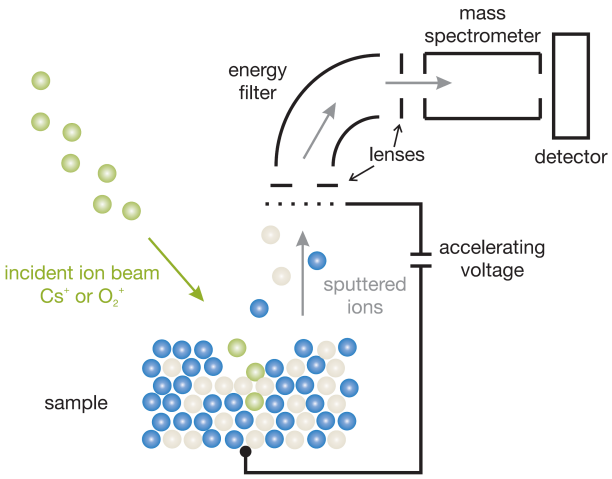

Figure 3.2: *Schematical drawing of the functional principle of the SIMS analysis method. Adapted from [89]*

The concept of SIMS is a destructive sputtering process of the sample by means of primary ions with energies between 1keV and 30keV and a simultaneous mass spectrometry of the sputtered sample particles (secondary ions). In order to achieve a high depth resolution, a progressive sputtering of the sample surface is necessary. An exact calibration of the depth profile is carried out with the help of a profilometer.

Depending on the desired analysis, Cs^+ or O^{2+} are used as primary beam and at the same time positive or negative ion detection are selected on the detector side. For the quantification of the Ge content x in our samples a low energy of about 3keV of the incoming Cs^+ ions is most adequate. However, this so-called MCs^+ technique suffers from a less precise quantification of the phosphorous (P) due to a low mass resolution. In order to get precise informations about the depth-resolved doping profiles, e.g. the P content, a high mass resolution SIMS measurement is necessary. The analysis conditions are then switched to a high impact energy (12keV) of primary Cs^+ ions. The thicknesses of the doping layers have to be at least 50 nm for this analysis because these conditions induce a low depth resolution.

In order to be able to quantify the mass spectrometry results, a standard is investigated in the same run under the same measuring conditions. Ideal results can be achieved by using different standards with a wide range of impurity concentrations as well as Ge contents from 19% to 35%. The investigated SIMS samples in this thesis were all cut out of the wafer center in order to calibrate our MBE sources. All measurements were conducted at PROBION (www.probion.fr, Bagneux, France).

3.3 X-ray Diffraction Analysis

High resolution X-ray measurements were performed on a three axis Philips X'Pert XRD. The samples were glued on a sample holder and attached to an Euler cradle prior to an irradiation with CuK_{α_1} radiation with a wavelength $\lambda = 1.54056\,\text{Å}$.

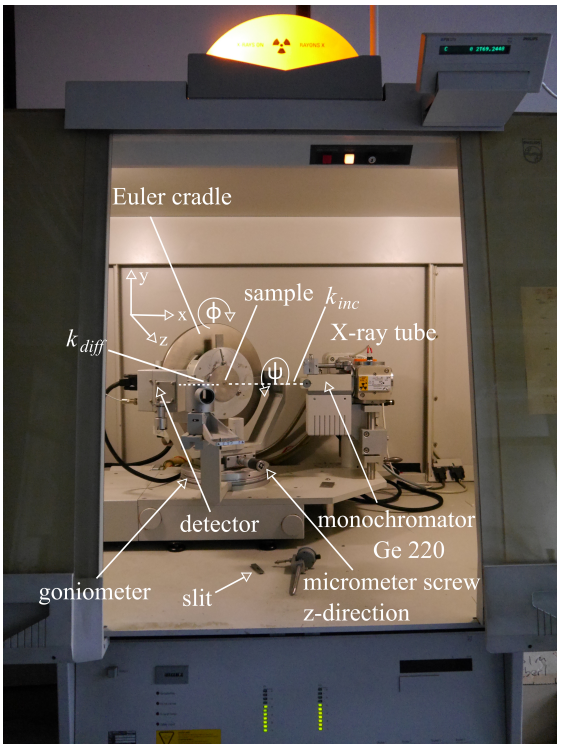

Figure 3.3: *Picture of the Philips X'Pert XRD and its working principle.*

The X-ray tube is fixed inside the machine and the Euler cradle as well as the detector are mounted on a goniometer, see figure 3.3. Both arms can be moved independently to control the angle ω, which is defined by the incident beam k_{inc} and the sample surface, as well as the angle 2Θ, which is defined by the diffracted beam k_{diff} and the incident beam k_{inc}, see figure 3.4a. A precise positioning of the sample is achieved by moving the x and y axes automatically via X'Pert Data Collector (measuring program) with an accuracy of 0.1 mm. The adjustment in z direction has to be conducted mechanically by hand with a micrometer screw. Moreover, it is possible to rotate the sample around the angle Φ with an accuracy of 0.1° and to tilt the x-y-plane by the angle Ψ with 0.01° precision. This high exactness is very important to precisely adjust the samples for the following measurements which were executed in the receiving slit mode [1].

[1] In the receiving slit mode a slit is used in front of the detector as attenuator and filter for the diffracted X-rays.

3.3.1 Reciprocal space mapping

X-ray diffraction experiments help us to get important information about the exact material compositions and the degree of relaxation of epitaxially grown layers. In this context, two different types of reflexes are investigated. From symmetric reflexes, where $\omega = \Theta$, the out-of-plane lattice constant $a_\perp$ (perpendicular to the sample surface) can be determined, whereas asymmetric reflexes, where $\omega \neq \Theta$, deliver information on both the out-of-plane $a_\perp$ and the in-plane lattice constant $a_\parallel$ (parallel to the sample surface). Figure 3.4a exemplarily shows the scattering geometry of a diffraction spectrum for an asymmetric reflex. The Bragg condition $h = k_{diff} - k_{inc} = G$ is fulfilled if the diffraction vector h is equal to a reciprocal lattice vector G. If multiple $\omega/2\Theta$ scans are performed consecutively for variable ω positions, a selected area in the reciprocal space is recorded which is also called reciprocal space map (RSM).

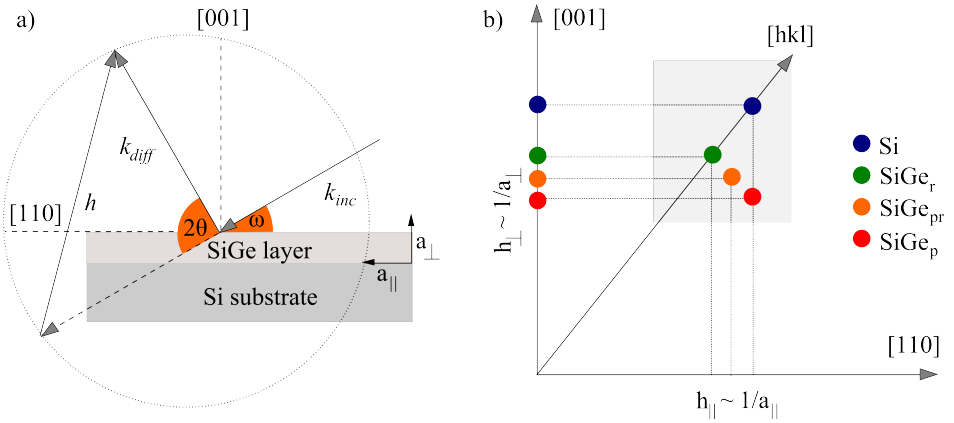

Figure 3.4: *a) Sketch of a coplanar scattering geometry in real space for an asymmetric reflex with $\omega \neq \Theta$. The SiGe layer and the Si substrate as well as the in-plane and out-of-plane lattice constants are indicated. b) Schematic representation of the correlation between distances in reciprocal space and the in-plane ($a_\parallel$) and out-of-plane ($a_\perp$) lattice constants for a pseudomorphic ($SiGe_p$, red circle), a partly relaxed ($SiGe_{pr}$, orange circle) and a fully relaxed ($SiGe_r$, green circle) SiGe layer grown on an undistorted Si substrate (blue circle). The light grey area represents an asymmetric RSM. It is clearly visible that the more the SiGe layer is relaxed the more it approaches the [hkl] axis connecting the origin and the Si substrate peak.*

Figure 3.4b shows a sketch of an asymmetric RSM (see grey highlighted area) of different SiGe layers which were grown pseudomorphically, partly relaxed or fully relaxed on an undistorted Si substrate. In fact, quantitative information on the degree of relaxation can be immediately achieved by looking at the position of SiGe layer peak relative to the position of the Si substrate peak. The more the SiGe layers are relaxed the more they approach the [hkl] axis which connects

the origin and the undistorted Si substrate peak. Simultaneously, it is possible to make statements about the Ge content x in the $Si_{1-x}Ge_x$ layer since from the position of the SiGe layer peak in reciprocal space we can directly draw inferences on the lattice constants from which x can be easily calculated.

However, for a correct evaluation of the degree of relaxation and material composition it is necessary to record an additional symmetric RSM because under certain circumstances it is possible that the lattice planes of the Si substrate and those of the epitaxial layers are tilted against each other. Indeed, such a tilt may arise e.g. due to a small miscut of the Si substrate. As a result, the SiGe layer peak lies not parallel to the Si substrate peak in the symmetric RSM. If this tilt is not taken into account and corrected this would lead to a defective evaluation of the degree of relaxation and the material composition. Therefore, in accordance with [90, 91], the (004) (symmetric) and (224) (asymmetric) reciprocal lattice points (RELPs), which exhibit the highest intensities in the Si/SiGe material system, were recorded, each consisting of 180 $\omega/2\Theta$ scans at different ω positions.

3.3.2 Evaluation of RSMs

The evaluation process has been developed by Koppensteiner and Bauer. It is shortly summarized below. For more details see [90, 91, 92].

At the beginning of every RSM, the angles ω and 2Θ at which Si and SiGe have their maximum intensity are determined for the (224) and (004) respectively in a procedure according to Sailer [92, 25]. Second, the theoretical angles of the Si substrate are evaluated by using geometrical considerations and the literature lattice constant of Si

$$\Theta_{Si,theo}[^\circ] = \arcsin\left(\frac{\lambda\sqrt{h^2k^2}l^2}{2a_{Si}}\right)\frac{360^\circ}{2\pi} \tag{3.1}$$

$$\alpha_{Si,theo}[^\circ] = \arccos\left(\frac{h+k}{\sqrt{2}\sqrt{h^2+k^2}+l^2}\right)\frac{360^\circ}{2\pi} \tag{3.2}$$

$$\omega_{Si,theo}[^\circ] = \alpha - 90^\circ + \Theta \tag{3.3}$$

with the Miller indices h,k,l, wavelength λ and the angle of inclination $\alpha_{Si,theo}$ [90, 91]. In a next step, the offset of Si between measured and theoretical values for both maps is calculated.

$$\Delta\omega = \omega_{Si,theo} - \omega_{Si,meas} \tag{3.4}$$

$$\Delta\Theta = \Theta_{Si,theo} - \frac{2\Theta_{Si,meas}}{2} \tag{3.5}$$

With the help of the specified offsets, the positions of both peaks, namely Si and SiGe, in every RSM are corrected as follows:

$$\omega_{Si,cor} = \omega_{Si,meas} + \Delta\omega \tag{3.6}$$

$$\Theta_{Si,cor} = \frac{2\Theta_{Si,meas}}{2} + \Delta\Theta \tag{3.7}$$

$$\omega_{SiGe,cor} = \omega_{SiGe,meas} + \Delta\omega \tag{3.8}$$

$$\Theta_{SiGe,cor} = \frac{2\Theta_{SiGe,meas}}{2} + \Delta\Theta \tag{3.9}$$

Consequently, the possible tilt between the Si and SiGe layer, which was already mentioned above, and can be seen in the (004) RSM, has to be annihilated.

$$\omega_{SiGe,tilt} = \omega_{SiGe,cor} - \Theta_{SiGe,cor} \tag{3.10}$$

All ω values for the SiGe layer have to be corrected in this way.

$$\omega_{SiGe,final} = \omega_{SiGe,cor} - \omega_{SiGe,tilt} \tag{3.11}$$

Finally, all corrected angles are transformed into reciprocal space coordinates.

$$h_{\parallel}[rlu] = \frac{1}{2}\left(\cos(\omega) - \cos(2\Theta - \omega)\right) \tag{3.12}$$

$$h_{\perp}[rlu] = \frac{1}{2}\left(\sin(\omega) + \sin(2\Theta - \omega)\right) \tag{3.13}$$

where the diffraction vector $h = h_{\parallel} + h_{\perp}$ is classified into components in growth direction along the [001] axis given by $h_{\perp}$ (out-of-plane) and perpendicular to the growth direction in [110] direction given by $h_{\parallel}$ (in-plane). Using equations 3.12 and 3.13, the in-plane and out-of-plane lattice constants are determined to

$$a_{\parallel} = \frac{1}{h_{\parallel}} \cdot \frac{\lambda}{2} \cdot \sqrt{h^2 + k^2} \tag{3.14}$$

$$a_{\perp} = \frac{1}{h_{\perp}} \cdot \frac{\lambda}{2} \cdot \sqrt{l^2} \tag{3.15}$$

Here, h, k and l are the Miller indices of the corresponding RELPs.

The determination of the degree of relaxation and the Ge content is then done iteratively. First of all, the in-plane lattice constant $a_{\parallel}$ is extracted from the (224) RSM and a Ge content of 50% is assumed. Then, a relaxed lattice constant a_{relax} and the elastic constants of SiGe are counted from this Ge content. From this values the out-of-plane lattice constant $a_{\perp}$ which would result if a_{relax} is forced to $a_{\parallel}$ is identified. After that, $a_{\perp}$ is compared to the average values of the measured (004) and (224) out-of-plane lattice constants. In fact, if the deviation is larger than 0.0001 Å a new Ge content has to be assumed and the evaluation process

has to be repeated. If the Ge content fits, the corresponding degree of relaxation is calculated by

$$R = \frac{f_{\parallel}}{f_{tot}} \tag{3.16}$$

in which $f_{\parallel} = \frac{h_{\parallel Si} - h_{\parallel SiGe}}{h_{\parallel SiGe}}$ is the experimentally determined in-plane strain of a SiGe layer and $f_{tot} = (f_{\perp} - f_{\parallel}) \cdot \frac{1-p_r}{1+p_r} + f_{\parallel}$ stands for the total lattice mismatch. Here, $p_r = p_{Si} - (p_{Si} - p_{Ge} \cdot x_{Ge})$ denotes the Poisson ratio and $f_{\perp}$ is the out-of-plane lattice mismatch [93].

3.4 Band structure simulation with nextnano++

Nextnano++ is a Schrödinger-Poisson-solver which allows us to perform self-consistent band structure simulations of semiconductor heterostructures in thermal equilibrium for 1D, 2D and 3D geometries [94, 95]. Based on the Fang-Howard variational approach for electrons in a 2DES the Schrödinger equation

$$-\frac{\hbar^2}{2}\left(\nabla\frac{1}{m^*(r)}\nabla + U(r)\right)\Psi_{\eta,k}(r) = E_{\eta}(k)\cdot\Psi_{\eta,k}(r) \tag{3.17}$$

is solved by following the effective mass approach. Here, $m^{\star}$ is the spatially varying electron mass and $U(r) = U_0(r) + U_{e,ion}(r) + U_{e,e}(r)$ denotes the single particle electrostatic potential. U_0 describes the conduction band energy of the unperturbed heterocrystal and $U_{e,ion}$ is the electrostatic potential energy of fixed charges in the heterostructure which can be calculated by the Poisson equation

$$-\nabla[\epsilon(r)\nabla U_{e,ion}] = \frac{\rho_{ion}(r)}{\epsilon_0} \tag{3.18}$$

where $\epsilon(r)$ is the spatially dependent dielectric function and ρ_{ion} is the distribution of fixed charges. In contrary, the term $U_{e,e}(r) = U_H(r) + U_{xc}(r)$ stands for all electron-electron many-particle interactions within the 2DES. Here U_{xc} displays the particle exchange energy. U_H is the Hartree potential which accounts for the Coulomb interaction of one electron with the electrons in the 2DES and is given by

$$-\nabla[\epsilon(r)\nabla U_H(r)] = \frac{en(r)}{\epsilon_0} \tag{3.19}$$

Figure 3.5 shows the program flow of a band structure simulation. The beginning of the simulation process is accompanied by a special input file. Within this file, the heterostructure geometry and the material compositions are defined. Important material properties of Si and Ge as well as special attributes of dielectrics and gate metals are specified in an additional database file [13].

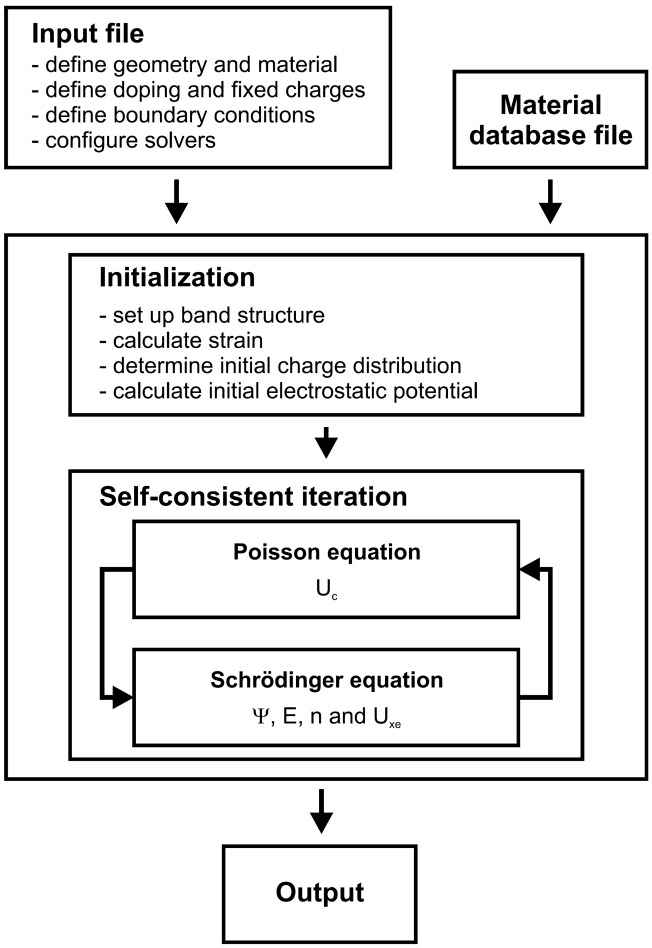

Figure 3.5: *nextnano++ working principle. Adapted from [13]*

Moreover, the input file defines the concentration of fixed charges or dopants in the simulated heterostructures. Furthermore, boundary conditions for the strain equations, the electrostatic potential, the wave functions, the Fermi energy at the contacts and the domain boundaries of the heterostructure have to be specified. In the initialisation routine, the input file and the database file are interrogated to set up the structure and to calculate the strain which affects the conduction as well as the valence band energies and influences the band offsets between Si and Ge. Finally, the initial charge distribution is evaluated and the initial electrostatic potential energy U_c is solved by combining fixed (see equation 3.18) and free charges (see equation 3.19) in a single solution of Poisson's equation [13]. Following the initialization, the Poisson and Schrödinger equations are solved alternately using several boundary conditions until a self-consistence is reached. This point is achieved when both the charge densities and the change of the Fermi energy fall below a user defined residuum. Then the Schrödinger equation 3.17 has to

be solved for the wave functions Ψ and the energy levels E from which the 2DES density is calculated according to equation 3.19. The resulting charge distribution $n(r)$ is then used to recalculate the Poisson equation. Finally, several characteristic properties e.g. strain, charge distribution or energy levels are output and are available for post-processing. However, the quantity of in this way obtained simulation results has to be scrutinized carefully for the physical meaning. Due to an insufficient knowledge of the local Fermi level E_F(r) in a heterostructure at cryogenic temperatures especially for externally applied electric fields, charge configurations can appear that are not in agreement with the thermal equilibrium requirement that is necessary for nextnano++ calculations [13].

3.5 Sample preparation methods

The MBE grown samples are patterned into Hall-bar shaped geometry so that an electrical characterization via magnetotransport experiments is possible. Figure 3.6 shows a brief overview of the most important steps in the lithographically process and therefore is shortly explained in the following. More detailed information on the lithography recipe can be found in appendix C.

First of all, the wafer has to be cut with a self-made cutter into $5 \times 4\ mm$ sample pieces for easier post-processing. Then, the samples pass through a series of different process steps in the clean room of Prof. Weiss. In a first step, the samples were cleaned in a standard procedure in aceton and isopropanol baths. In order to realize certain device geometries, the samples were coated with a positive resist before an illumination with UV light was executed through a specially defined resist mask [2] in a Karl Süss Micro Tec mask aligner. Now, the samples have to be developed and cleaned in deionized water. After that, a wet chemical etching step was carried out in an $HF : HNO_3$ solution. Finally, the resist was removed and the samples were ready for the next optical lithography process. In the scope of this optical lithography step, the samples were shortly dipped in a diluted HF solution in the end. Then, a subsequent metallization step with gold and antimony was performed in a Univex 450 deposition machine. Immediately after the deposition, the metal was removed on the unwanted regions by a lift-off process in aceton. Afterwards, the samples were placed in a rapid thermal annealer (RTA) and heated under forming gas atmosphere. As a result, the annealed layers form little droplets with small inverted pyramids underneath which connect the 2DES so that ohmic contacts arise. After that, the droplets were shorted in a second metallization step by a titanium gold layer in order to improve the stability of the ohmic contacts.

[2] wavelength between 200 and 450 nm

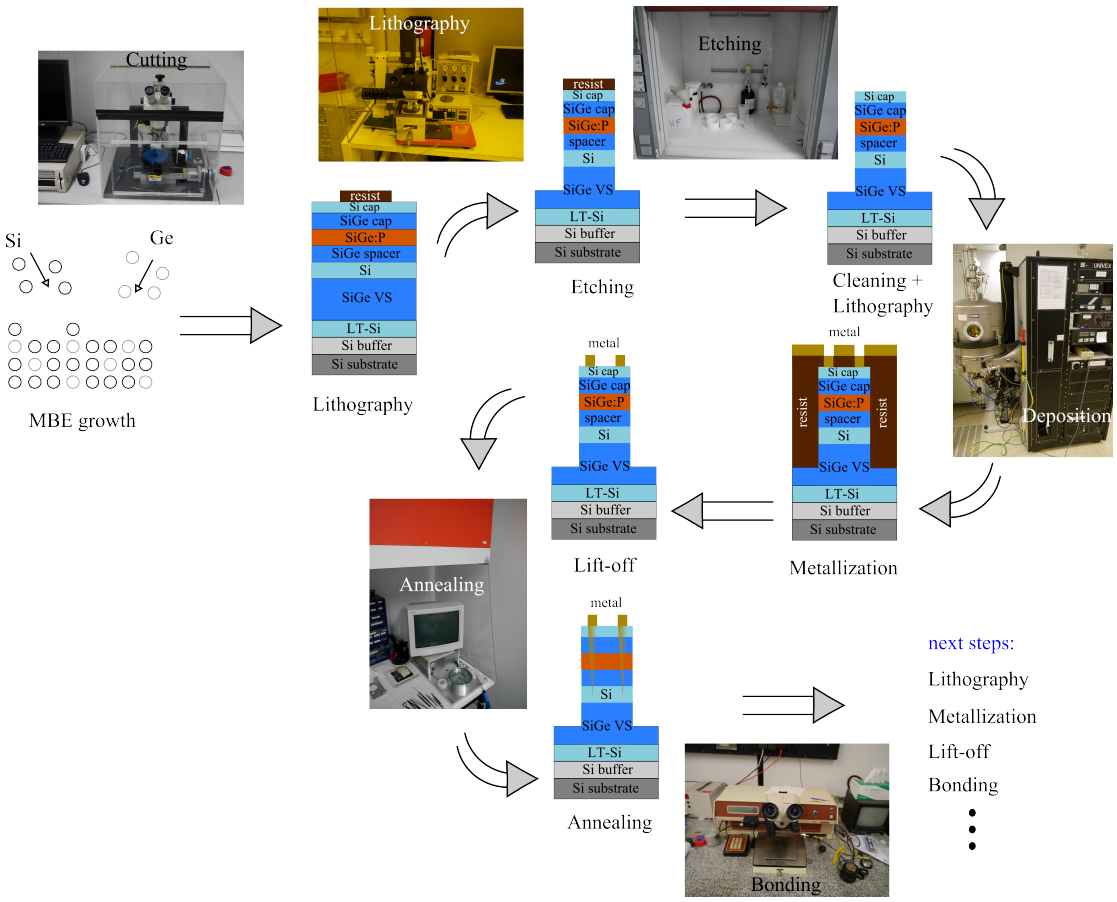

Figure 3.6: *Short sketch of the lithographic process circle and the utilized machines and items. Here, the steps towards ohmic contacts are shown. Further lithography and metallization steps are only indicated. Detailed information about the entire procedure is given in appendix C.*

Finally, a third metallization step was carried out in order to attain a Schottky top-gate on one third of the Hall-bar. Here, a HF dip prior to the palladium deposition is inevitable due to the fact that otherwise many surface states will be present on top of the sample which can hamper the field effect control [46, 47]. Last but not least, the samples were glued into a 8-pin ceramic chip carrier and bonded with aluminium and gold wires respectively.

3.6 Magnetotransport

The main characterization method used in this thesis are magnetotransport experiments in order to extract important fundamental properties like charge carrier density and mobility, which display a sign of quality in our samples. In the following, the different set-ups and measurement procedures are presented. First,

the standard rapid characterization set-up in the 65 litres helium dewar is described. Second, the Spectromag SM 4000 magnet cryostat is explained. Finally, the measurement techniques for gate controlled transport and leakage current measurements are introduced and illustrated.

3.6.1 Standard characterization set-up

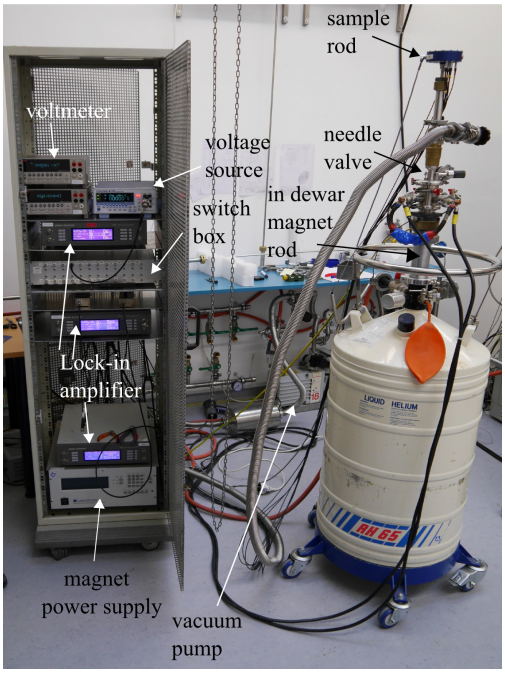

Figure 3.7: *Picture of the standard characterization set-up. The rack is equipped with three lock-in amplifiers to record both the longitudinal and the Hall resistance as well as the current along the Hall-bar. Additionally, the Lakeshore 625 magnet power supply, a Yokogawa GS-200 voltage source and two Keithley 2000 voltmeter are present. Furthermore, the He dewar, the in-dewar magnet rod and the sample rod are illustrated. With this set-up, temperatures of about* $1,4K$ *and high magnetic fields up to* $5T$ *can be reached.*

The set-up consists of an in-dewar magnet rod with a superconducting magnet coil, a sample rod, a vacuum pump, and an instrument rack which is equipped with a switch box, three lock-in amplifiers, two Femto DLPVA pre-voltage amplifiers, a Lakeshore 625 magnet power supply, a Yokogawa GS200 voltage source, a Femto current voltage converter, and a Keithley 2000 voltmeter. The whole set-up is shown in figure 3.7. By using this set-up we are able to investigate our samples at temperatures from $1.4K$ (by closing the needle valve at the magnet rod and pumping out the sample space) to $4.2K$ and magnetic fields up to $5T$. More information about the rapid characterization set-up can be found in [96] and [97].

3.6.2 Spectromag SM 4000

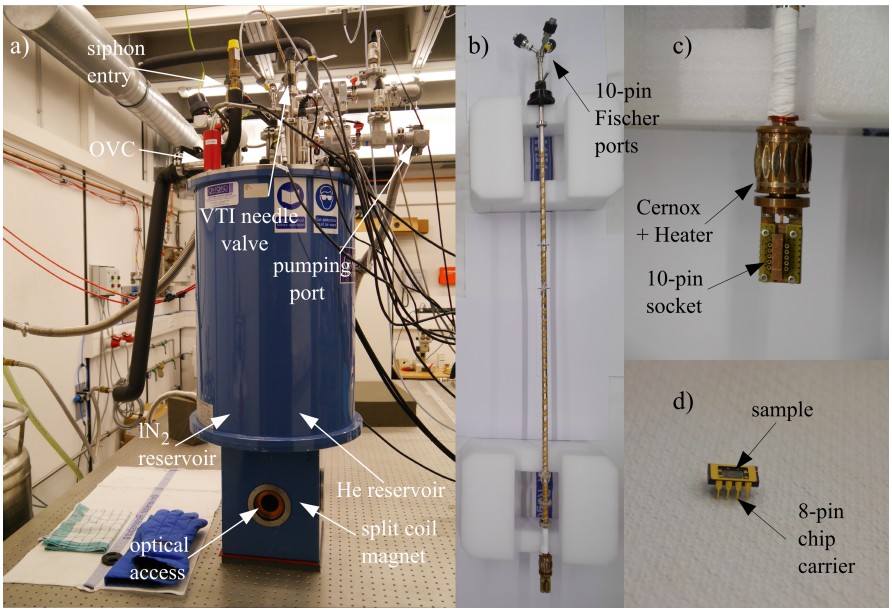

Figure 3.8: *a) Drawing of the Spectromag SM 4000 and its basic components. b) Image of the Spectromag sample rod. c) Detail image of the sample socket. The sample heater and the Cernox 1050 temperature sensor are included in the copper box. d) Picture of the 8-pin ceramic chip carrier with the bonded sample inside.*

The basic component, for the temperature dependent measurements, is a SM 4000 magnet cryostat which is a commercial system made by Oxford Instruments (see figure 3.8). The achievable temperature range lies around $1.2K$ and $300K$ with an accuracy of $\pm 0.1K$. With the help of an ITC temperature controller, the desired temperature is adjusted by generating a specific equilibrium between the flow of liquid He and the heater power at the sample rod and the variable temperature inset (VTI). Magnetic fields up to $\pm 7T$ at $4.2K$, and even $\pm 8T$ are reached if the temperature at the superconducting split coil magnets is reduced to $\leq 2.2K$. This system has an optical access to the sample space which was used in our case to orientate the sample perpendicular to the magnetic field. Temperatures below $4.2K$ can be attained by reducing the vapour pressure of liquid He in the sample space with a rotary pump. The flow of liquid He out of the main reservoir into the VTI on his part is controlled by a needle valve stepper motor. The cryostat dewar, which contains $20l$ of liquid He, is shielded with a $24l$ liquid nitrogen (lN_2) reservoir and an outer vacuum chamber (OVC) with a pressure of 10^{-6}mbar to reduce the evaporation of liquid He. The samples were fixed in a sample rod (see figure 3.8b,c) which contains a 10-pin sample socket, a Firerod $20V$ $40W$ sample heater and a Cernox 1050 temperature sensor. The instruments used for the electrical measurements are the same as in the standard characterization set-up.

3.6.3 Measurement methods

Several electrical measurement methods were applied in this thesis to extract information about the gated and ungated regions in Si/SiGe heterostructures. In the following, every measurement technique is explained in detail.

Standard magnetotransport

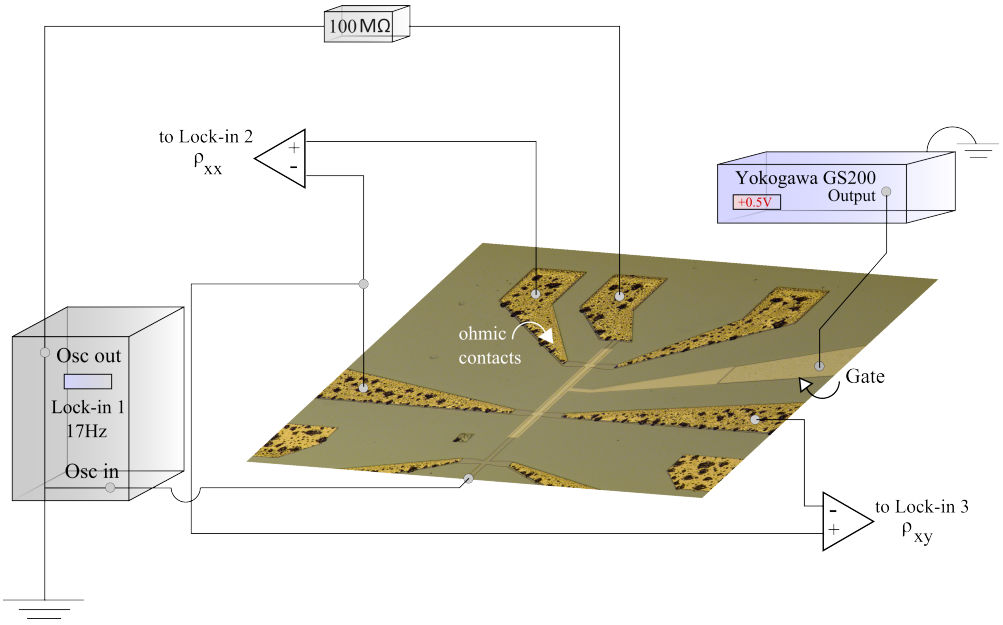

Figure 3.9: *Sketch of the general magnetotransport set-up in the gated region. A 50 nA current was created along the Hall-bar by sending a AC signal with an amplitude of 5V and a frequency of 17Hz over a 100 MΩ load resistor. The longitudinal as well as the transversal resistance were recorded by two Lock-in amplifiers after a pre-amplification by two Femto DLVPA pre-voltage amplifiers. The gate voltage was altered by a Yokogawa GS-200 voltage source.*

Basic magnetotransport measurements at low temperatures and high magnetic fields were performed to determine relevant properties of our 2DES. Figure 3.9 shows a short sketch of a gated Hall-bar sample together with the connected circuity. A Yokogawa GS200 DC-voltage source is connected to the Pd top-gate to tune the electron density of the 2DES capacitively. Moreover, Lock-in one outputs an AC signal with a frequency of 17Hz and a constant amplitude of 1-5V which is connected to the source contact of the sample in series with a 100MΩ load resistor. Consequently, a current in the order of 10-50 nA was sent through the Hall-bar and simultaneously measured by Lock-in one. To record both the longitudinal and the Hall voltage in a four point measurement configuration, we

used two additional Lock-in amplifiers (Lock-in 2 and 3). Most of the time two Femto DLPVA pre-voltage amplifiers with an input impedance of 1 $T\Omega$ were switched between the Hall-bar leads and the two Lock-in amplifiers in order to obtain a better signal to noise ratio and to avoid current losses over the Hall-bar terminals. To calculate the charge carrier density as well as the mobility, the acquired voltages were converted into resistivities ρ_{xx} and ρ_{xy} with the help of equations 2.5 and 2.4. Using equations 2.7 and 2.8, we finally extract the carrier density and mobility.

Leakage current measurements

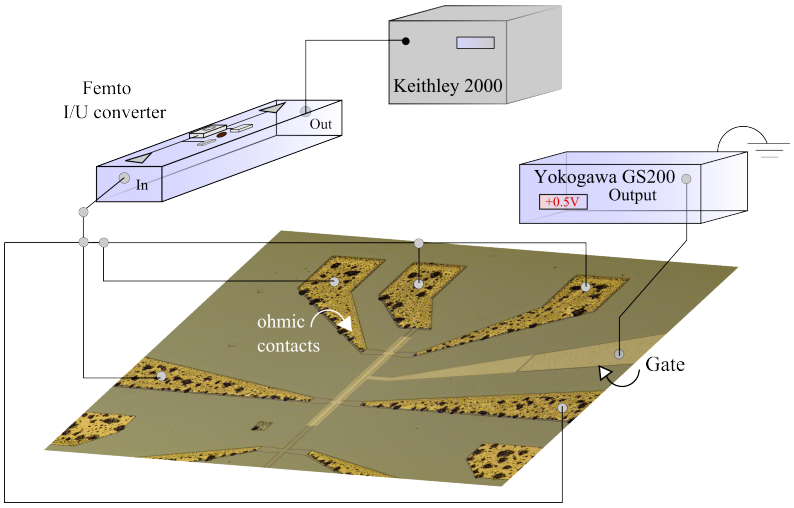

Figure 3.10: *Sketch of the leakage current measurement set-up. All ohmic contacts were short-circuited under the gated region. The leakage current was amplified by a I/U converter prior to the detection with a Keithley 2000 voltmeter. As a voltage source we employed a Yokogawa GS-200.*

In order to define the limits in which we can operate our Schottky top-gate, leakage current measurements were performed. Since leakage currents are detrimental for all transport experiments, the controllable gate region has to be exactly specified. Therefore, in a first step we short-circuited all ohmic contacts which lie under the top-gate and connected them to the input of a Femto DLPCA-200 current-voltage converter. The output of the I/U converter was then linked to a Keithley 2000 voltmeter. The top-gate is biased with a Yokogawa GS-200 DC voltage source which results in high electric fields between the Schottky top gate and the 2DES. We choose an amplification factor of 10^8 for the I/U converter so that $1V$ at the Keithley corresponds to $10nA$ leakage current. The complete measurement configuration is displayed in figure 3.10.

Gate sweep measurements

Gate sweep measurements were carried out in order to shed light on the interplay between the top-gate and the 2DES. However, first of all the pinch-off point of every sample has to be estimated to further specify the gate control range. The pinch-off point in this connection is defined as the point were the 2DES gets fully depleted [13, 98]. Thus, in combination with the leakage current measurements, we receive the whole area in which we can tune our 2DES. For this procedure, we utilized the general magnetotransport set-up (see figure 3.9). Starting from a point were the 2DES is occupied, the gate voltage was swept in negative voltage direction while the current along the Hall-bar was collected via Lock-in technique.

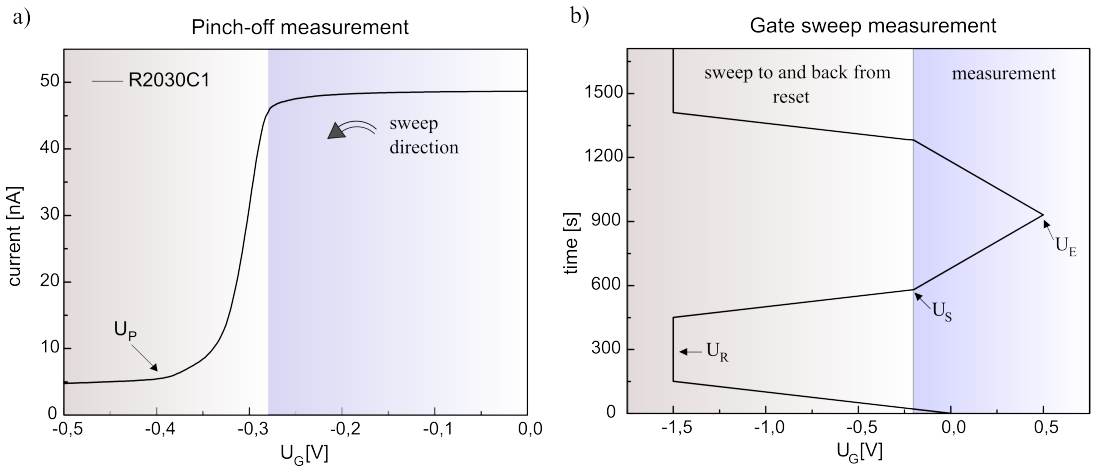

Figure 3.11: *a) Sketch of a typical pinch-off curve for sample R2030C1. The occupied 2DES region as well as the depletion region are highlighted with blue and grey colours respectively. The thick black arrow indicates the sweep direction and the other arrow denotes the pinch-off voltage which lies around $-0,4V$. b) This picture illustrates the entire sweep sequence. Both the reset and the measurement regions are also highlighted in grey and blue respectively. Moreover, the reset point U_R, the start value U_S for the sweep as well as the maximal voltage end value U_E are indicated. The time dependent course can also be extracted in detail.*

In figure 3.11a, a typical pinch-off curve is shown. Here, U_p stands for the pinch-off voltage. Ultimately, when the whole controllable top gate range is determined we are able to start with the actual sweep procedure. First, the gate voltage was swept with a rate of $5\frac{mV}{s}$ to a value far below the pinch-off point which is called reset point U_R from now on. This point is adjusted before every gate sweep or jump measurement in order to guarantee equal starting conditions. After a waiting duration of 5 minutes, the gate was swept slightly over the pinch-off value (U_S) were the 2DES has already formed and is stable [3]. Now the actual measurement

[3]It was shown in the theses of Wild and Sauther [13, 99], that a reset time of 5 minutes is

was performed by sweeping the gate voltage to the maximal possible gate value U_E before leakage sets in. Immediately after U_E was reached, the gate voltage was decreased to the initial voltage value. This sequence was executed with a sweep rate of 1-2$\frac{mV}{s}$. For the determination of both the carrier density and the mobility of the samples, it is mandatory to perform this sequence first in the absence of the magnetic field and second with a magnetic field of $B = 0,25T$. By using equations 2.7 and 2.8, the carrier density and the mobility can be calculated. In figure 3.11b the complete sweep process is shown schematically. For the temperature dependent sweep measurements, the change in temperature was always conducted during the reset phase.

Time resolved gate jump measurements

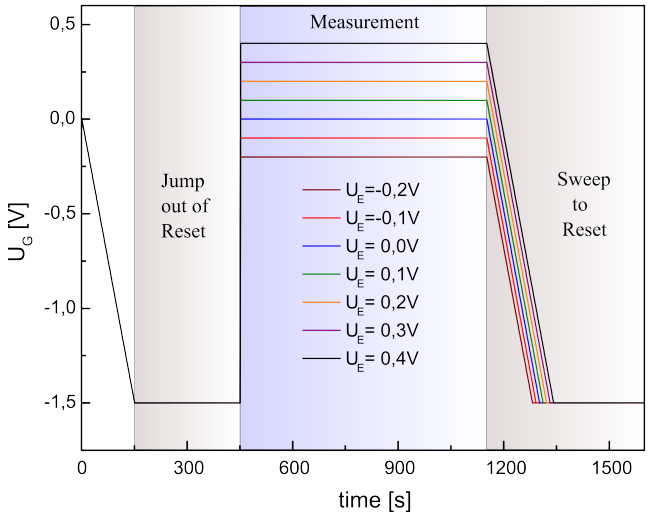

Figure 3.12: *Functional principle of the gate jump experiments exemplarily for several end voltage values U_E. Both the measurement and the reset areas are again underlayed in grey and blue. The current along the Hall-bar and the longitudinal as well as the Hall resistance were recorded during the relaxation process for several minutes.*

Continuous gate sweep measurements only provide precise information on changes in the 2DES during a non-equilibrium state. In order to attain detailed knowledge of time dependent and abruptly occurring mechanisms, time resolved gate jump measurements were executed. A sketch of the general procedure is indicated in figure 3.12. First of all, the heterostructure has to be reseted to ensure well defined starting conditions. After the mandatory waiting time of 5 minutes in the reset point, the gate voltage is suddenly altered with a jump rate of 10000$\frac{mV}{s}$

sufficient to guarantee equal starting conditions.

to the final voltage value U_E. The desired bias value is kept for several minutes during the whole measurement and both the longitudinal and the Hall resistance are determined. This process is called relaxation process from now on. The experiment has to be carried out again for different B-fields in order to obtain the carrier density and mobility according to 2.7 and 2.8. After the measurement is concluded, the voltage is swept back into the reset with a rate of $10\frac{mV}{s}$. Changes of temperature as well as the magnetic field are operated during the waiting time in the reset point.

4 Heterostructure optimisation

Strain, band offset and doping degree are very important parameters in the fabrication process of Si/SiGe heterostructures. In order to efficiently use these set screws for the optimisation of two-dimensional electron systems (2DES), all wafers were grown unrotated to exploit gradients which arise due to the cell geometry in the MBE main chamber. In fact, these gradients allow us to study several samples with different material compositions, relaxation degrees R and doping degrees on one single wafer. In a first step, we applied a reciprocal space mapping technique (RSM) to explore different gradients depending on the sample position on the wafer regarding the effective Ge content $x_{Ge_{eff}}$ and the degree of relaxation for two different virtual substrate concepts namely LT-Si and graded buffer VS (see section 2.3). Then, we systematically investigated the phosphorous (P) doping profile across the overall wafer since a precise controllability of the P doping degree in our heterostructures is absolutely necessary to achieve high mobilities. For this purpose, magnetotransport and SIMS measurements as well as nextnano band structure simulations were conducted. Finally, we applied our findings to a new growth series in order to fabricate high mobility Si/SiGe heterostructures.

4.1 RSM of different virtual substrates

To start our analysis, we exemplarily recorded RSMs of an LT-Si and a graded buffer based sample, each taken out from an arbitrary position on the wafer, to determine the exact $Si_{1-x}Ge_x$ material composition and the degree of relaxation with respect to the underlying buffer layers. Figures 4.1a and b show the symmetric (004) and asymmetric (224) RSMs of the LT-Si based sample R2004B8. The Si substrate and the SiGe layer peak are clearly visible in both RSMs. From the symmetric (004) RSM we see that the maxima of the Si substrate as well as of the SiGe layer peak are separated and lie on the same in-plane reciprocal lattice point (RELP) $h_{\parallel}$ which indicates that the lattice planes of both layers are parallel to each other. In the (224) RSM the separation of the Si substrate and the SiGe layer peak is not as good defined as in the (004) RSM. This circumstance results from a lower intensity in combination with a higher noise level in the asymmetric RSMs. In contrast to the LT-Si based sample, figures 4.1c and d display the RSMs of the graded buffer grown sample R1940A.

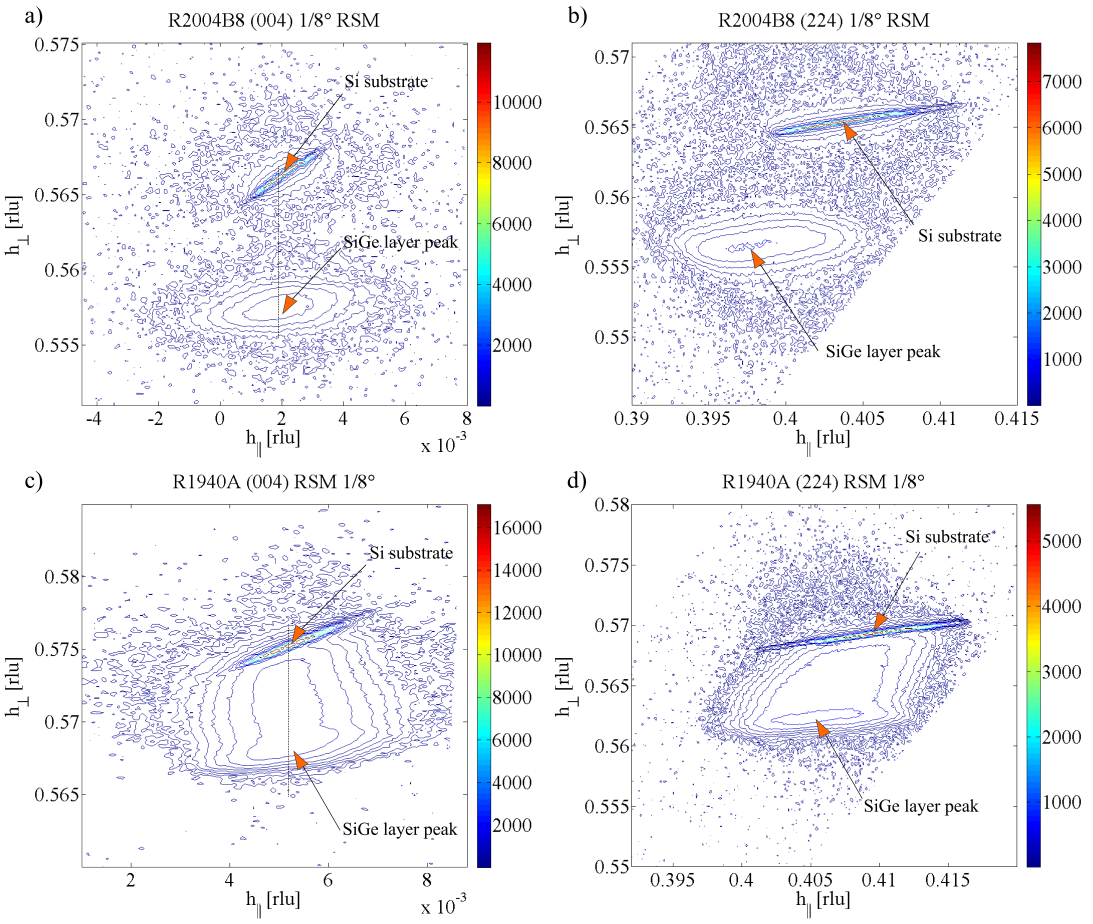

Figure 4.1: *a) RSM of the (004) reflex of sample R2004B8 which was grown on a LT-Si based VS. Both the Si layer peak and SiGe constant composition layer peak have the same $h_{\parallel}$ RELP, illustrated by the black dashed line. b) Picture of the according (224) RSM. c) and d) RSM of both the (004) and (224) reflex of sample R1940A. The Si layer peak and SiGe constant composition layer peak have again the same $h_{\parallel}$ RELP in the (004) RSM. Moreover, the linear grading from 5% towards 35% in the SiGe constant composition layer is visible in both maps.*

Here again, the Si substrate and the SiGe layer peak are very pronounced and lie on the same in-plane RELP $h_{\parallel}$ in the (004) RSM. Moreover, in this sample the linear grading in the SiGe buffer, which starts with a nominal Ge content of 5% and ends up with a final nominal Ge content of 35%, is visible in both RSMs. Finally, the RSMs of the LT-Si and the graded buffer based samples were evaluated as introduced in section 3.3.1. The degree of relaxation R as well as the effective Ge content $x_{Ge_{eff}}$ could be directly calculated from the positions of the SiGe layer peaks relative to the Si substrate peaks. As a result, we obtained a degree of relaxation of $R = 91,32\%$ and an effective Ge content of $x_{Ge_{eff}} = 38,47\%$ for the LT-Si based sample R2004B8, whereas the graded buffer based sample R1940A exhibited $R = 92,40\%$ and $x_{Ge_{eff}} = 30,85\%$. The determined results clearly point

to a good quality of the MBE grown buffer layers which form the basis for Si/SiGe heterostructures. In order to find out the optimal parameters for the fabrication of high mobility Si/SiGe 2DES and to compare LT-Si and graded buffer based samples, the gradients across the entire wafer have to be precisely mapped.

4.1.1 Comparison of LT-Si and graded buffer XRD maps

In this section, RSMs of LT-Si and graded buffer VS based wafers were systematically recorded for several $5 \times 5mm$ sample pieces which were cut out of different wafer regions. In this context, especially the effective Ge content, which can drastically influence the band offset in our Si/SiGe 2DES, the degree of relaxation in the buffer layers, which might affect the degree of strain in the Si QW as well as the deviations relative to the nominally wanted Ge content, in the wafer center were precisely studied. Figure 4.2 shows a sketch of the wafer, the positions of the extracted samples, the arrangement of the Si and Ge electron beam evaporators and the position of the GaP cell. In reality however, the Si and Ge electron beam evaporators are centrally arranged, directly below the wafer surface.

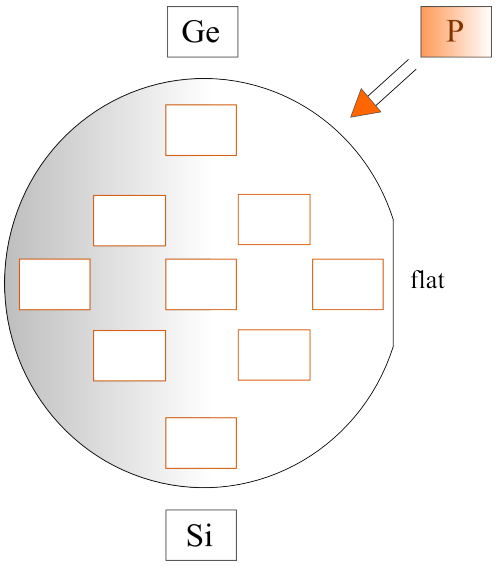

Figure 4.2: *Schematical drawing of the entire wafer and the sample positions at which the RSMs were systematically recorded (orange rectangles). Furthermore, the position of the Si and Ge electron beam evaporators as well as the P doping cell are indicated. In reality, the Si and Ge electron beam evaporators are centrally arranged, directly below the wafer surface.*

As a consequence of the systematic RSM investigation, new XRD overview maps were developed. Figure 4.3a shows an overview map averaged over three LT-Si based wafers R2001, R2004 and R2005. In comparison, figure 4.3b presents a corresponding overview map of the RSM results and the according gradients, obtained in the graded buffer based wafer R1940. In the following, the resulting $x_{Ge_{eff}}$, R and the deviations from $x_{Ge_{nom}}$ in both XRD overview maps are compared to each other and the differences/similarities are highlighted and discussed.

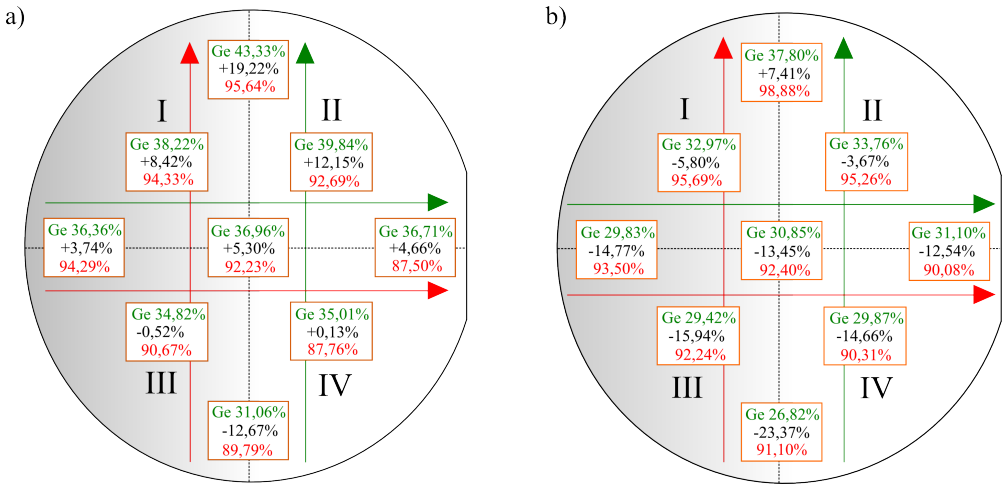

Figure 4.3: *a) XRD overview map of the averaged LT-Si wafer results (R2001, R2004, R2005) for a nominal Ge content of 35%. The effective Ge content ($x_{Ge_{eff}}$) values are marked in green. The degree of relaxation is written in red, whereas the deviation from the nominal Ge content in the wafer center is displayed in black numbers. Additionally, all four quality regions are illustrated in Roman letters. The degree of relaxation and the Ge content gradients are shown by red and green arrows respectively. b) Drawing of the results in wafer R1940 which is based on a graded buffer VS and exhibits nominally 35% Ge. The experimentally determined gradients are again illustrated with green (effective Ge content) and red (degree of relaxation) arrows respectively. The deviations from $x_{Ge_{eff}}$ and R are displayed in the same colour like the corresponding arrows, whereas the nominal Ge content $x_{Ge_{nom}}$ is indicated with black numbers.*

Effective Ge content $x_{Ge_{eff}}$: In the average LT-Si overview map, illustrated in figure 4.3a, we observed a strong increase in the effective Ge content $x_{Ge_{eff}}$ from the Si cell direction (bottom) to the Ge cell direction (top), whereas the Ge content increases only slightly from the left side to the right side of the wafer. Additionally, the effective Ge content of all three samples in the wafer median, where $x_{Ge_{eff}} \approx 37\%$, is approximately equal to the nominally wanted Ge content $x_{Ge_{nom}} = 35\%$. Indeed, this observation points to a correct Si and Ge flux calibration, which was adjusted via RHEED oscillations in the wafer center [1]. In order to confirm this fact we performed an additional high depth resolution SIMS measurement (see section 3.2) in a centred sample of wafer R2004 which is part of the average LT-Si XRD overview map. Figure 4.4 shows the SIMS results from which we can directly extract an effective Ge content of $x \approx 35\%$. Moreover, two dips are displayed in the SIMS measurement which indicate the position of the Si QW and the Si capping layer. However, an exact quantification of the material composition in these thin layers ($5 - 10nm$) is not possible due to a high sputter rate which is necessary to achieve a high depth resolution.

[1] Further information on this technique can be found in [20].

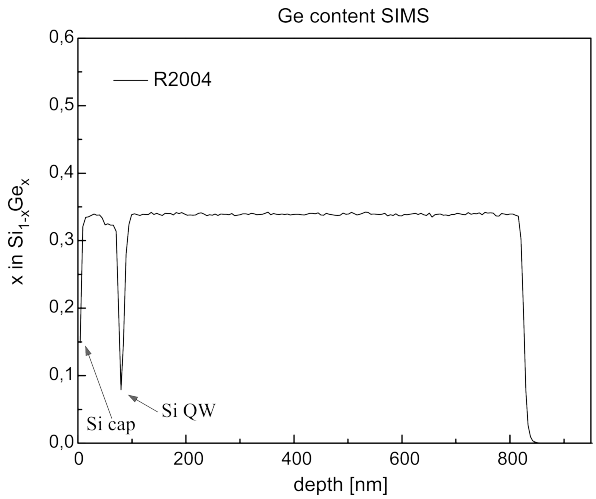

Figure 4.4: *A high depth resolution SIMS result of a centred sample of wafer R2004. At first glance, two dips occur which are attributed to the Si QW and the Si capping layer on top of the sample. Moreover, the experimentally extracted Ge content from the SIMS measurements $x \approx 35\%$ is almost equal to the one which was obtained from XRD RSMs $x_{Ge_{eff}} \approx 37\%$, see figure 4.3a.*

In contrast to the average LT-Si overview map, figure 4.3b presents the graded buffer overview map of wafer R1940 which was grown at the Walter Schottky Institute before the MBE System had been transferred to Regensburg. At first glance, we see that the Si and Ge flux calibration in wafer R1940 is distinctly shifted compared to the one in the average LT-Si overview map. This phenomenon can be explained by the fact that the growth position was readjusted in Regensburg which can have a distinct influence on the flux calibration since the RHEED spot can be shifted to another impinge position on the wafer surface. Nevertheless, the effective Ge content gradients in both the LT-Si and the graded buffer based wafers behave similarly. The effective Ge content increases approximately 12% from the bottom to the top and about 2% from the left to the right side of the wafer. Simultaneously, the deviations relative to the nominal Ge content $x_{Ge_{nom}}$ in the wafer center along these gradients amount maximally up to about 23%. Furthermore, these observations are in good agreement with XRD RSM measurements of Sailer who also studied the deviation of the nominally wanted Ge content in $Si_{0.95}Ge_{0.05}$ [25]. In his findings, he reported on an increasing effective Ge content gradient from the bottom to the top of the wafer with a maximal deviation of the effective Ge content relative to the nominal Ge content of approximately 23%.

Degree of relaxation R**:** The gradient concerning the degree of relaxation, in both virtual substrate concepts behaves roughly similarly to the effective Ge content $x_{Ge_{eff}}$ gradients. Comparing the LT-Si average XRD overview map in figure 4.3a with the graded buffer overview map in figure 4.3b, we found the

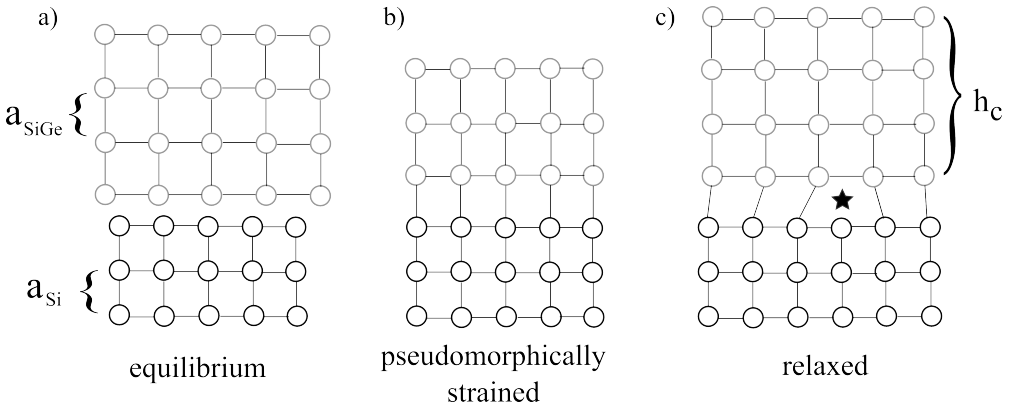

Figure 4.5: *a) Picture of a Si and SiGe layer in the equilibrium state. Moreover, the lattice constants of Si a_{Si} and $Si_{1-x}Ge_x$ a_{SiGe}, which explicitly depends on the Ge content according to equation 2.3, are illustrated. b) Image of a pseudomorphically strained SiGe layer. c) Drawing of the plastic relaxation process due to the formation of misfit dislocations (indicated by the $\star$). The onset of this relaxation process depends on the critical thickness h_c and therefore on the material composition of the $Si_{1-x}Ge_x$ layer or in other words the Ge content.*

continuous trend that starting from the Si cell and ending up at the Ge cell direction a higher degree of relaxation appeared with a simultaneously increasing effective Ge content. Regarding figures 4.5a-c, this observation gets plausible since a higher Ge content in the $Si_{1-x}Ge_x$ material composition leads to a bigger lattice constant which then results in a larger lattice mismatch $f = (a_{SiGe} - a_{Si})/a_{SiGe}$. Consequently, the critical thickness h_c is lowered according to $h_c \propto \frac{1}{f} \ln\left(\alpha \frac{h_c}{b}\right)$, where b stands for the burgers vector and α is the dislocation core parameter. As a result, the plastic relaxation process of the buffer layer sets in earlier due to a formation of misfit dislocations which reduce the strain and hence lead to a better degree of relaxation R. Additionally, we see that for equal effective Ge contents the graded buffer based wafer shows a higher degree of relaxation than the LT-Si based average overview wafer. This fact supports the assumption that the slow linear grading is responsible for a better distribution of misfit dislocations and therefore results in a lightly higher degree of relaxation. Beside this linear increasing R gradient from the bottom to the top of the wafer, we observed a second slightly decreasing degree of relaxation R from the left (Ge poor) to the right (Ge rich) side of the wafer. However, the origin of this phenomenon is not completely understood. It is possible that the deviations of R along this gradient lie within the reading accuracy of the measurements. In order to clarify this open question, further measurements are necessary.

Based on the experimentally obtained insights concerning the degree of relaxation, the deviations relative to the nominally wanted Ge content in the wafer center and the effective Ge content, the wafers could be finally divided into four quality regions, indicated by the black Roman numbers in figures 4.3a and b. In

this context, high quality means firstly a high degree of relaxation from which we deduce that there are less threading dislocations piercing through the active sample structure up to the surface. Secondly, a high band offset is advisable since the measurements on gated Si/SiGe heterostructures of Wild et al. [13], introduced in section 2.5.2, already showed that increasing the gate voltage leads to unwanted charge reconfigurations caused by tunnelling events from the 2DES into energetically lower lying energy states in the P doping layer. In order to suppress or avoid these tunnelling effects, which act detrimental on the gate controllability of the 2DES, one option is to increase the Ge content so that a higher band offset and therefore a higher energy barrier forms.

Starting with our quality classification, region I, which has the highest degree of relaxation and the highest effective Ge content $x_{Ge_{eff}}$, is located on the upper left quarter of the wafer. This area is followed by region II which lies on the upper right quarter of the wafer and exhibits a slightly poorer R but higher $x_{Ge_{eff}}$ in comparison to segment I. Region III, is ordered at the lower left side of the wafer and contains an even lower R and $x_{Ge_{eff}}$ than the other two regions. In the end, we define sector IV which includes the weakest quality concerning R.

4.1.2 Reproducibility

In a next step, we checked the reproducibility of our new findings regarding the $x_{Ge_{eff}}$ and R gradients in the XRD overview maps. Therefore, the gradients were studied in another LT-Si based wafer with a nominally lower Ge content of $x_{Ge_{nom}} = 30\%$. Moreover, the long term reproducibility of the gradients was reviewed, since we in note form recorded RSMs at random wafer positions of every grown wafer during the new growth period and compared the results with the ones of our XRD overview maps.

Variation of Ge content: In order to check the universal applicability of our experimentally determined gradients to wafers with a different nominal Ge content another LT-Si grown wafer R2052 with $x_{Ge_{nom}} = 30\%$ was produced and compared to the averaged LT-Si wafers with $x_{Ge_{nom}} = 35\%$. Figure 4.6a shows the exact results of wafer R2052 regarding the effective Ge content, the degree of relaxation and the deviations relative to the nominal Ge content in the wafer center. The effective Ge content increases approximately 11% from the bottom to the top and about 2% from the left to the right side of the wafer. Simultaneously, the deviation relative to the nominal Ge content $x_{Ge_{nom}}$ in the wafer center along these gradients amounts maximally up to about 21%. Moreover, the gradients with respect to the degree of relaxation behave equally to the ones in the average LT-Si overview wafer with $x_{Ge_{nom}} = 35\%$, whereby R is about 2% lower in the overall LT-Si based wafer with nominally 30% Ge content. This observation again points to the fact that the degree of relaxation R increases with increasing Ge concentration.

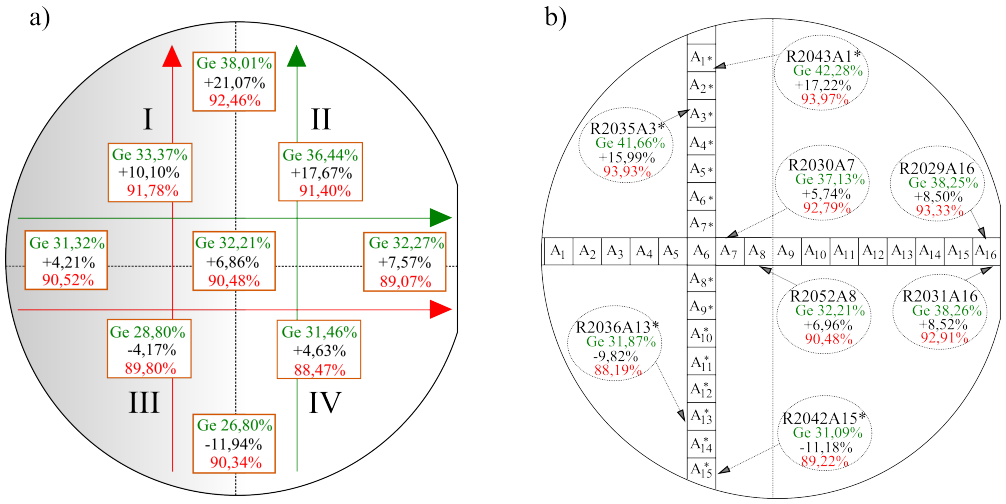

Figure 4.6: *a) RSM results of the LT-Si grown wafer R2052 with nominally 30% Ge content. The effective Ge content ($x_{Ge_{eff}}$) values are marked in green. The degree of relaxation is written in red and the deviation from the nominal Ge content is displayed in black numbers. All four quality regions are indicated in Roman letters, the degree of relaxation and the Ge content gradients are again shown by red and green arrows respectively. b) Schematic drawing of all in note form examined wafers from the new growth series, concerning the effective Ge content (green numbers), the deviation from the nominally wanted Ge content (black numbers) and the degree of relaxation (indicated in red). The results show a perfect agreement with the average LT-Si based XRD overview map which exhibits a nominally wanted Ge content of 35% see figure 4.3a.*

Comparing the average overview wafer ($x_{Ge_{nom}} = 35\%$) in figure 4.3a with the new LT-Si based one ($x_{Ge_{nom}} = 30\%$) in figure 4.6a, regarding the effective Ge content displays a difference of approximately 4% in each sample across the entire wafer (nominally 5% difference) which shows the high precision of the RSM technique. Interestingly, the wafer with nominally 30% Ge contained the same gradients like the ones within the average LT-Si based overview wafer with $x_{Ge_{nom}} = 35\%$ which leads us to the conclusion that precise predictions of the $x_{Ge_{eff}}$ and R gradients are possible independently of the $Si_{1-x}Ge_x$ material composition in the wafer.

Long term reproducibility: Figure 4.6b presents an overview of the results concerning the effective Ge content ($x_{Ge_{eff}}$), the degree of relaxation (R) and the deviation from $x_{Ge_{nom}}$ at different wafer positions for all investigated wafers (with $x_{Ge_{nom}} = 35\%$) during this thesis. The results nicely agree with the LT-Si based average XRD overview map which was recorded for wafers with $x_{Ge_{nom}} = 35\%$, see figure 4.3a and therefore strengthen our experimentally obtained gradients. All these facts give indeed a clear evidence for the quantitative stability and validity of the newly developed gradients over a long time although multiple new Si and Ge RHEED calibrations were executed.

Conclusion: Using a RSM technique, we for the first time systematically studied and precisely mapped geometrical gradients, concerning the degree of relaxation, the effective Ge content and the deviations relative to the nominally wanted Ge content in both LT-Si and graded buffer based wafers. As a result, we obtained similar gradients in LT-Si and graded buffer grown wafers, whereby the graded buffer based samples exhibited a slightly higher degree of relaxation ($\approx 3\%$) across the overall wafer. However, since the LT-Si virtual substrates also showed high degrees of relaxation up to approximately 96% and are far less time and material consuming, we conclude that LT-Si VS are better suited for the systematic optimisation of Si/SiGe heterostructures. In the following, we therefore mainly focused on LT-Si based wafers and checked the reproducibility of the experimentally obtained gradients in a further LT-Si based wafer with different material composition. Additionally, we reviewed the long-term reproducibility in note form in all LT-Si grown wafers during this thesis. The results clearly show that the discovered gradients are universally applicable, independent from the $Si_{1-x}Ge_x$ material composition and are stable over a long period of time. Based on our new findings concerning R and $x_{Ge_{eff}}$, we were finally able to divide the entire wafer into four quality regions. With respect to R and $x_{Ge_{eff}}$, we found a very good platform for high quality Si/SiGe heterostructures especially in the upper wafer half. In order to be able to fabricate a high mobility 2DES, the doping profile has to be precisely studied too. Therefore, we lay the main focus in the next section on an exact controllability of the P doping cell.

4.2 Precise controllability of P doping

Traditionally, the calibration of the phosphorous (P) dopant concentration is conducted in bulk Si calibration samples. In this chapter we tested whether the incorporation of phosphorous in SiGe differs from the incorporation in Si on a scale impacting the P dopant calibration.

4.2.1 Phosphorous cell calibration

Starting with the usually used P calibration in Si, a calibration wafer with four phosphorous doped Si boxes (Si:P) at relevant GaP cell temperatures and a typical growth rate of $r_{Si} = 0.16\,\text{Å/s}$ was fabricated [86, 20, 25]. Figure 4.7a shows the sample structure which consists of an intrinsic Si substrate followed by a thin Si buffer layer and an alternating layer sequence of four 100 nm thick P doped Si boxes, each doped at different cell temperatures ($657°C$,$653°C$,$649°C$,$645°C$) and four 250 nm thick Si buffer layers. However, in order to achieve the best suited calibration conditions comparable with the modulation doping process in our Si/SiGe heterostructures, a new calibration wafer was produced where the

P doping deposition is conducted in SiGe. Figure 4.7c displays an overview of a centred sample of the new calibration wafer. First of all, an LT-Si grown VS was fabricated in order to employ the desired $Si_{1-x}Ge_x$ material composition, see section 2.3.2.

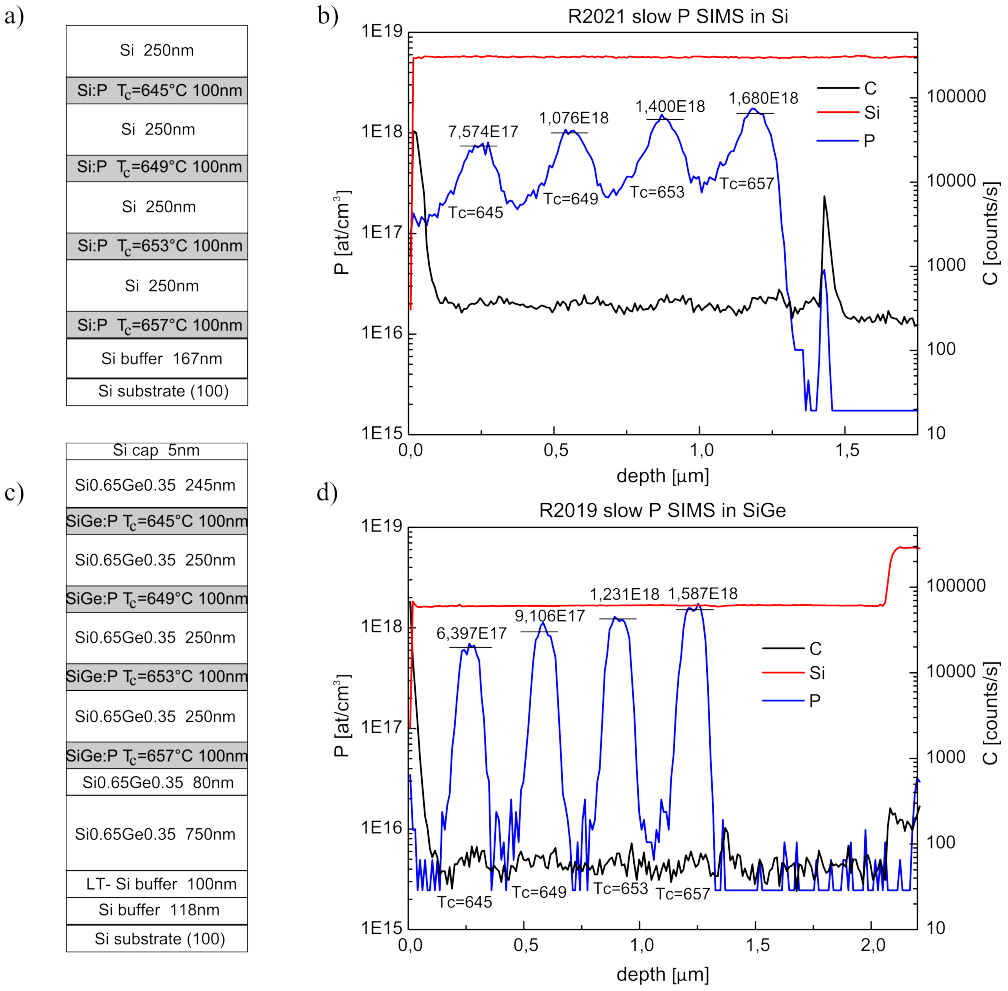

Figure 4.7: *a) Schematic drawing of the Si:P sample structure R2021. All four 100 nm thick P doped boxes are separated by 250 nm Si layers. b) High mass resolution SIMS measurement of the P doping profile in Si. The four boxes with different P doping profiles for 657°C, 653°C, 649°C and 645°C are clearly visible by the blue curve. The doping degree and the concerning P cell temperature are illustrated in black numbers. Additionally, the Si and C concentrations are given by the red and black curve respectively. c) Image of the SiGe:P sample R2019. The 100 nm thick SiGe:P boxes are separated by 250 nm thick SiGe layers. d) shows the according SIMS results of sample R2019 with P doping in SiGe. Again, all four SiGe:P boxes grown at different P cell temperatures are visible. Moreover, the doping degree, the P cell temperatures, as well as the Si and the C concentrations are given by the same colors like in the Si:P sample.*

Secondly, this time an alternating layer sequence of four 100 nm thick P doped SiGe boxes (SiGe:P) at the same four GaP cell temperatures (657°C,653°C,649°C, 645°C) and separated by three 250 nm thick SiGe layers was produced using a SiGe growth rate of $r_{SiGe} = 0.16\,\text{Å/s}$. Finally, the last SiGe:P box was capped by a 245 nm SiGe layer and a 5 nm Si layer to prevent the calibration wafer from oxidation.

Comparison Si:P and SiGe:P calibration: Figure 4.7b shows the high mass resolution SIMS results of a centred sample with varying P doping profiles in the Si:P calibration wafer. The carbon (C) and Si concentrations, which are given by the red and black curve, explicitly divide the calibration sample into three regions. The dip in the Si concentration indicates the sample surface, whereas the peaks in the C concentration clearly separate the doped layer sequence from the wafer substrate and the sample surface. In the doped layer sequence, we observed the four P doped box profiles (blue curve) for the corresponding GaP cell temperatures. In comparison, figure 4.7d displays the SIMS results of the SiGe:P (R2019) calibration sample. Here, again the C and Si concentration peaks/dips illustrate the separation of the sample surface, the doped layer sequence and the Si substrate. Comparing the exact doping levels in the Si:P and the SiGe:P sample, we see that the doping profile in the SiGe:P (R2019) sample was roughly about $1 \cdot 10^{17} cm^{-3}$ lower in each box than in the Si:P (R2021) calibration sample. Therefore, both samples seem to result within the limits of accuracy of the measurements in the same doping degree. However, it is obvious that the four P doped box profiles are better defined in the SiGe:P (R2019) calibration sample. Indeed, the P segregation seems to be markedly reduced in comparison to sample R2021, since the P levels fall down to the detection limit of approximately $1 \cdot 10^{15} cm^{-3}$ at the doping box edges. Consequently, it is distinctly easier to determine the exact layer thicknesses in the SiGe:P (R2019) calibration sample. In this context, we verified the nominally wanted layer thicknesses and width of the phosphorous doping boxes in the SiGe:P sample by directly extracting the thicknesses from the SIMS depth profile. Actually, the results are another hint for a correct Si and Ge RHEED flux calibration.

Conclusion: In summary, we showed that the incorporation of P in Si and SiGe calibration samples hardly differs. As a result, the determined P concentrations were almost equal in both samples. However, for a precise evaluation of the doping profile, a SiGe:P calibration sample is advisable since the Si:P calibration sample suffers from a strong phosphorous segregation. Moreover, these results are in good agreement with measurements of Nützel et al. and Christensen et. al [20, 100] who studied the segregation profiles in Si:P and SiGe:P respectively. In their investigations, they attained a phosphorous (P) diffusion length of 100 nm in Si, whereas for higher Ge content the P diffusion length decreased linearly. Hence, in a $Si_{0.8}Ge_{0.2}$ sample Nützel and coworkers estimated a phosphorous diffusion length of approximately 7 nm.

4.2.2 Systematic determination of P doping gradient

In this section, we for the first time experimentally determined and precisely mapped the geometrical phosphorous doping gradient by using standard magnetotransport measurements in the ungated Hall-bar regions of different samples all over the wafer. In the following, we exemplarily present the results of one single wafer R1931, illustrated in figure 4.8.

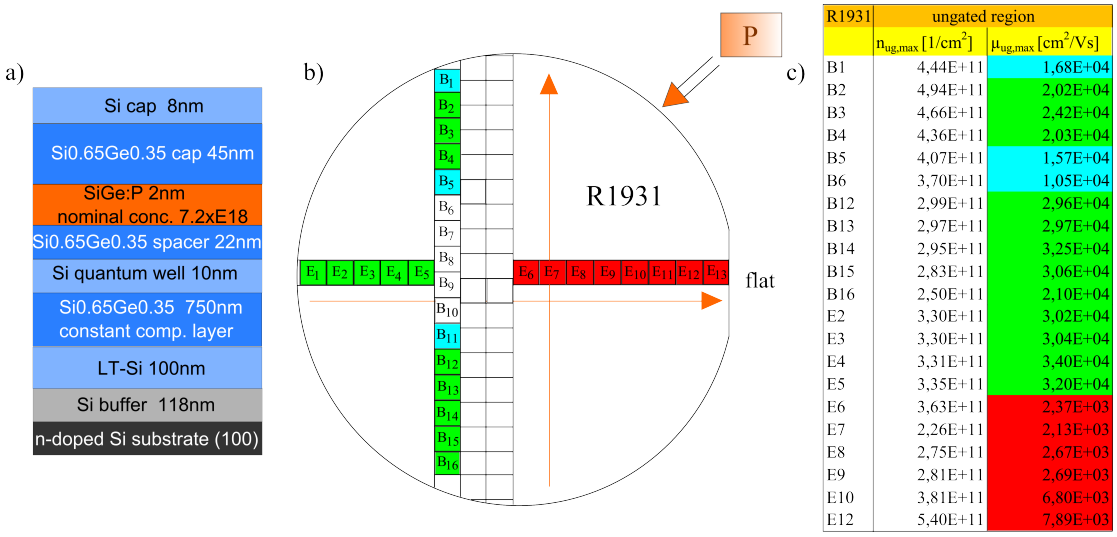

R1931	ungated region	
	$n_{ug,max}$ [1/cm^2]	$\mu_{ug,max}$ [cm^2/Vs]
B1	4,44E+11	1,68E+04
B2	4,94E+11	2,02E+04
B3	4,66E+11	2,42E+04
B4	4,36E+11	2,03E+04
B5	4,07E+11	1,57E+04
B6	3,70E+11	1,05E+04
B12	2,99E+11	2,96E+04
B13	2,97E+11	2,97E+04
B14	2,95E+11	3,25E+04
B15	2,83E+11	3,06E+04
B16	2,50E+11	2,10E+04
E2	3,30E+11	3,02E+04
E3	3,30E+11	3,04E+04
E4	3,31E+11	3,40E+04
E5	3,35E+11	3,20E+04
E6	3,63E+11	2,37E+03
E7	2,26E+11	2,13E+03
E8	2,75E+11	2,67E+03
E9	2,81E+11	2,69E+03
E10	3,81E+11	6,80E+03
E12	5,40E+11	7,89E+03

Figure 4.8: *a) Drawing of the basic sample layout for wafer R1931. The modulation doping layer is only 2 nm thick and therefore quasi "δ-doped". Additionally, the spacer layer was increased to 22nm. b) Overview of the results of different samples concerning both the carrier densities n and mobilities μ in vertical and horizontal wafer direction. The corresponding P doping gradients are indicated with orange arrows. Different colours highlight the mobility of the samples. c) Overview of the results of both the carrier density n and the mobility μ in the ungated regions in dependence of the wafer position, see figure 4.8b. The quality of the samples which is given by the maximum mobility is highlighted in different colours. Red indicates* $\mu = 1 \cdot 10^3 \frac{cm^2}{Vs}$ *up to* $1 \cdot 10^4 \frac{cm^2}{Vs}$*, mobilities in the range of* $1 \cdot 10^4 \frac{cm^2}{Vs}$ *to* $2 \cdot 10^4 \frac{cm^2}{Vs}$ *are shown in light blue, green stands for mobilities in the range of* $2 \cdot 10^4 \frac{cm^2}{Vs}$ *to* $4 \cdot 10^4 \frac{cm^2}{Vs}$*.*

In a first step, all samples were systematically investigated at a temperature of $1{,}4K$ regarding both the carrier density (n) and mobility (μ). Figure 4.8a illustrates the heterostructure layout whereas figure 4.8b and c give an overview of the sample positions on the wafer and indicate the mobility of every sample by different colours. Red denotes mobilities from $1 \cdot 10^3 \frac{cm^2}{Vs}$ up to $1 \cdot 10^4 \frac{cm^2}{Vs}$, light blue stands for mobilities in the range of $1 \cdot 10^4 \frac{cm^2}{Vs}$ to $2 \cdot 10^4 \frac{cm^2}{Vs}$, green indicates mobilities from $2 \cdot 10^4 \frac{cm^2}{Vs}$ to $4 \cdot 10^4 \frac{cm^2}{Vs}$. The maximally achievable values for both

the carrier density and the mobility in the ungated regions are presented for every measured sample at different wafer positions in figure 4.8c. Regarding figure 4.8b and c, we identified a linear gradient starting from the left side of the wafer (sample R1931E1) and ending up at the big flat on the right side (sample R1931E13). Surprisingly, all samples in the right half of the wafer showed very bad transport characteristics and did not work well even after illumination. In a first approach, we believed a high doping degree to be responsible for this circumstance since scattering effects on neutral and ionized impurities would increase with higher doping degree and therefore drastically reduce the mobility. Secondly, the probability that phosphorous is incorporated in the Si QW would also be enlarged. However, in order to completely resolve this open question more experiments are necessary.

Beside the linear gradient from the right to the left side of the wafer, a second gradient was discovered starting from sample R1931B16 and ending up at sample R1931B1. In figure 4.8b and c, we immediately see that the corresponding carrier density rises linearly from $2,50 \cdot 10^{11} cm^{-2}$ at the bottom to $4,94 \cdot 10^{11} cm^{-2}$ (sample R1931B2) at the top of the wafer. Unfortunately, samples R1931B10 up to R1931B6 were damaged during the lithography process and are therefore kept in white colours. Nevertheless, the climb gradient is still clearly visible. After careful consideration of this gradient, we are able to draw inferences on the best suited charge carrier densities in order to reach high mobilities in the ungated region. Therefore, at first glance densities in the range from $2,5 - 3,5 \cdot 10^{11} cm^{-2}$ seem to be most qualified since relatively high mobilities up to $\approx 3,4 \cdot 10^4 \frac{cm^2}{Vs}$ were reached, see figure 4.8c. Indeed, these results are quite good in comparison to earlier fabricated Si/SiGe heterostructures and define the optimal charge carrier density region for the growth of two-dimensional electron systems.

To further specify the P doping gradient, we studied the percental discrepancy of the measured charge carrier densities along the linear climb gradient, indicated in figures 4.8b and c, from the experimentally observed charge carrier density in the wafer center. Figure 4.9a displays the determined deviations across the carrier density gradient which amount up to 52% from the bottom to the top of the wafer. These results were then compared with a high mass resolution SIMS analysis of several samples at different wafer positions, in a Si:P calibration wafer carried out in the Phd thesis of Sailer [25]. Figure 4.9b illustrates the SIMS P climb gradient on the left side of the wafer which exhibits a deviation of 46% from the bottom to the top and therefore shows a good agreement with the percental deviations in the linear charge carrier density climb gradient of wafer R1931. Based on this result, the phosphorous gradient seems to be stable and independent of the doping strength. Furthermore, this observation points to the fact that from the percental deviations in the charge carrier density along the P climb gradient we can directly draw inferences about the deviations in the volume doping degree across this gradient.

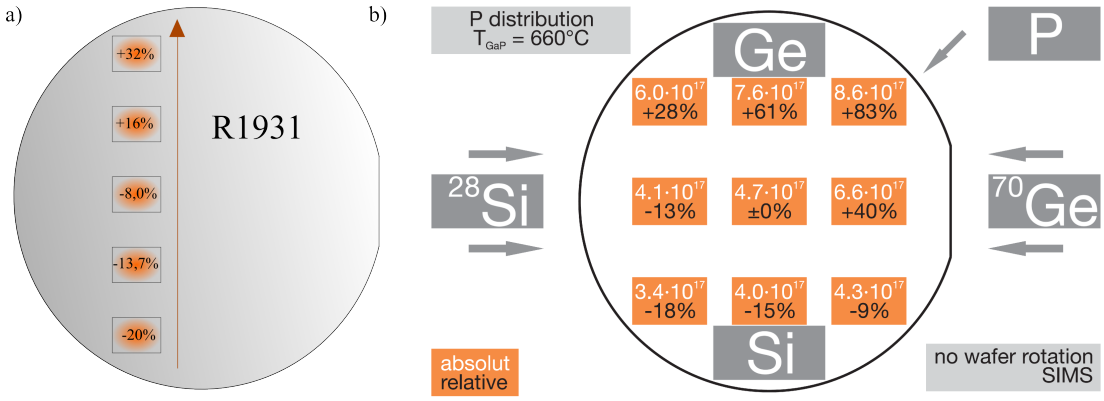

Figure 4.9: *a) Overview of the experimentally observed deviations along the charge carrier density climb gradient from the measured carrier density $n_{ug,meas}$ in the wafer center of R1931. In this context, inferences on the volume P doping degree can be drawn by measuring the carrier densities $n_{ug,meas}$ along this climb gradient which is illustrated by a brown arrow. b) Overview of the Si:P SIMS results of several samples at different wafer positions shown in the Phd thesis of Sailer [25]. The experimental P deviations (black numbers) from the wafer center match nicely to the deviations in the n climb gradient obtained in a).*

4.2.3 Determination of optimal parameters

In order to be able to fabricate a high quality 2DES, where charge reconfigurations are suppressed and simultaneously high mobilities are reached, we now have to take all experimentally obtained gradients into consideration. In the following, we efficiently exploit the P doping gradient as well as the R and the $x_{Ge_{eff}}$ gradients in nextnano band structure simulations to quantify the optimal parameters.

To start our analysis, the percental deviations along the P climb gradient, shown in figure 4.9a, and the effective Ge content $x_{Ge_{eff}}$ gradient, displayed in figure 4.3a, were utilized to get sample specific simulation input parameters for every sample of wafer R1931. Figure 4.10a shows the resulting band structure profiles of several samples lying on the P climb gradient which allow us to draw inferences about the best parameters regarding the $x_{Ge_{eff}}$ and the P doping degree. On closer inspection of the energy levels of the conduction band minima in the inset of figure 4.10a, we see that the increasing P doping concentration nearly compensates the increasing effective Ge content. However, since the conduction band minima slightly differ, we simultaneously observe a shift of the energetic position of the P states which are ordered $45meV$ below the conduction band edge. As a consequence of this interplay, the best sample region in order to achieve a relatively high mobility and a high energy barrier (band offset), so that detrimental charge reconfigurations can be longest suppressed, was discovered around the position of

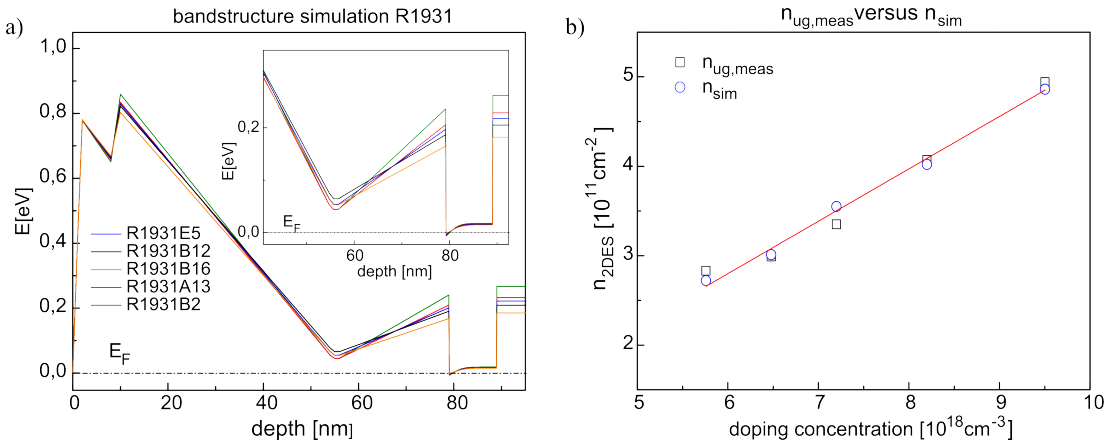

Figure 4.10: *a) Band structure simulations of several samples in the ungated region along the P climb gradient of wafer R1931. The simulations comprise the deviations of the nominal doping degree as well as of $x_{Ge_{eff}}$. The little inset offers a zoom into the band structure. As a consequence, we clearly see that the linear increase in the effective Ge content nearly compensates the increase in the doping degree. Thus, the best suited region to avoid charge reconfiguration lies around sample R1931B12. b) displays the simulated (blue open circles) and experimentally observed (black open cubes) carrier density values. The linear fit in red only serves as a guide to the eye and indicates the good agreement between both values.*

sample R1931B12, which contained an effective Ge content of approximately 35% and a carrier density of $\approx 3,0 \cdot 10^{11} cm^{-2}$. Based on these findings, we conclude that it is worthwhile to establish this charge carrier density as far as possible in the upper half of the wafer since the best degree of relaxation R was found in this area, see section 4.1.1.

Comparison of experiments and simulations: To reinforce the reliability of the conducted nextnano band structure simulations and to strengthen the usefulness of our effective Ge content ($x_{Ge_{eff}}$), degree of relaxation (R) and P doping gradients, we in the following compared the experimentally determined charge carrier density $n_{ug,meas}$ with the simulated carrier density n_{sim} along the $x_{Ge_{eff}}$ and P gradients in wafer R1931. In figure 4.10b, we clearly see that both $n_{ug,meas}$ and n_{sim} vary maximally by an order of $0,7 \cdot 10^{11} cm^{-2}$ in sample R1931E5. All other investigated samples differed only slightly in simulated and experimentally measured charge carrier densities. In fact, the astonishingly good agreement of simulated and experimentally measured charge carrier densities points to the fact that if the phosphorous cell calibration is correct and stable, the experimentally measured data can be predicted relatively well using nextnano band structure simulations which are based on the universally applicable effective Ge content ($x_{Ge_{eff}}$) and P doping gradients. Additionally, this result again shows that it is possible to draw inferences from the experimentally measured carrier density about the volume doping degree in the modulation doping layer.

4.3 Implementation of optimisation

In this section, we now tried to implement the optimisations, which were discovered in the previous sections 4.2.3, to our Si/SiGe heterostructures. First of all, we focussed on the readjustment of the desired density region. Therefore, we produced a first unrotated growth series consisting of three nearly identical wafers (R2029, R2030, R2031), see figure 4.11a, with a fixed nominal Ge content of 35% and varying nominal doping degrees in the wafer center.

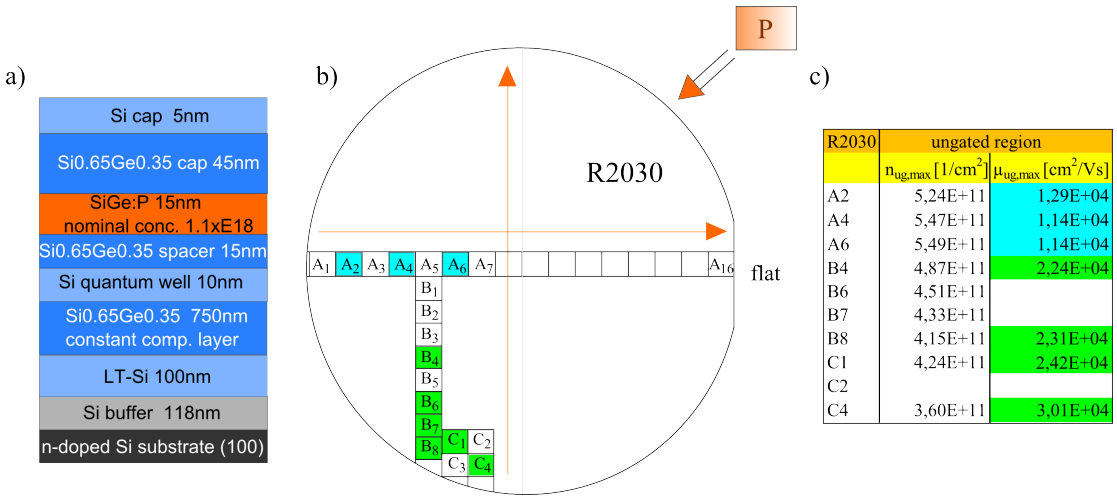

R2030	ungated region	
	$n_{ug,max}$ [1/cm^2]	$\mu_{ug,max}$ [cm^2/Vs]
A2	5,24E+11	1,29E+04
A4	5,47E+11	1,14E+04
A6	5,49E+11	1,14E+04
B4	4,87E+11	2,24E+04
B6	4,51E+11	
B7	4,33E+11	
B8	4,15E+11	2,31E+04
C1	4,24E+11	2,42E+04
C2		
C4	3,60E+11	3,01E+04

Figure 4.11: *a) Schematic drawing of the sample structure in wafer R2030. b) Overview of the exact positions of several samples distributed across the wafer R2030. The experimentally obtained P doping gradients are indicated with orange arrows. The experimentally calculated n_{meas} in the wafer center amounts approximately $5,5 \cdot 10^{11} cm^{-2}$. c) displays the results of both the carrier density n and the mobility μ in the ungated region in dependence of the wafer position. The quality of the samples which is given by the maximum mobility is again highlighted in different colours. Red indicates mobilities lower than $1 \cdot 10^4 \frac{cm^2}{Vs}$, mobilities in the range of $1 \cdot 10^4 \frac{cm^2}{Vs}$ to $2 \cdot 10^4 \frac{cm^2}{Vs}$ are shown in light blue, green stands for mobilities in the range of $2 \cdot 10^4 \frac{cm^2}{Vs}$ to $4 \cdot 10^4 \frac{cm^2}{Vs}$.*

At the beginning of our experiment, we once again checked the linear P climb gradient in wafer R2030 which contained a nominally wanted P doping degree of $1,1 \cdot 10^{18} cm^{-3}$ ($T_C = 652°C$). In this context, several samples were investigated regarding the charge carrier density and the mobility. Figure 4.11a shows the heterostructure layout of wafer R2030, whereas figures 4.11b and c display the sample positions on the wafer and indicate the mobility of every sample by different colours. Red still indicates mobilities below $1 \cdot 10^4 \frac{cm^2}{Vs}$, light blue denotes mobilities in the range of $1 \cdot 10^4 \frac{cm^2}{Vs}$ to $2 \cdot 10^4 \frac{cm^2}{Vs}$, whereas green illustrates mobilities in the range from $2 \cdot 10^4 \frac{cm^2}{Vs}$ to $4 \cdot 10^4 \frac{cm^2}{Vs}$. As a matter of fact, we could confirm

the linear P climb gradient from the Si cell up to the Ge cell direction and the slight increasing gradient from the left to the right side of the wafer. The maximal mobility $\mu_{ug,max} \approx 3,0 \cdot 10^4 \frac{cm^2}{Vs}$ was achieved in sample R2030C4 for a corresponding density of $n_{ug,max} \approx 3,6 \cdot 10^{11} cm^{-2}$, which strengthens our previous findings regarding the best density region of approximately $2,5 - 3,5 \cdot 10^{11} cm^{-2}$. However, on closer inspection of the measured P climb gradient we see that the desired density region was still part of the bottom side of the wafer which represents the region with the weakest degree of relaxation. Additionally, we compared the experimentally measured charge carrier density in the wafer center $n_{ug,meas} \approx 5,5 \cdot 10^{11} cm^{-2}$ with the simulated one which was obtained by nextnano band structure simulations to exclude a possible shift in the P cell calibration. As a result, figure 4.12 shows that both $n_{ug,meas}$ and n_{sim} differ only slightly from each other which indicates that the SiGe:P calibration is still valid and seems to be stable.

In order to get a better statistics about the P doping profile and the stability of the P cell calibration in SiGe over a longer period of time, we conducted further magnetotransport measurements on 2DES. In a first step, we therefore examined the other two wafers R2029 and R2031 [2]. Surprisingly, wafer R2029, which had the nominally lowest doping degree of $9,0 \cdot 10^{17} cm^{-3}$ ($T_C = 649°C$), exhibited the highest experimentally measured charge carrier density in the wafer center of $n_{ug,meas} \approx 6,43 \cdot 10^{11} cm^{-2}$. In contrary, wafer R2031, which contained the highest nominal P doping degree of $1,3 \cdot 10^{18} cm^{-3}$ ($T_C = 655°C$), showed a carrier density of approximately $5,59 \cdot 10^{11} cm^{-2}$ in the wafer center. Comparing again the results of simulated charge carrier densities with the measured ones in the wafer center leads to a very good agreement for wafer R2031, whereas the densities strongly disagreed in wafer R2029, see figure 4.12. Indeed, the reason for this deviation from the new developed SiGe:P SIMS calibration in wafer R2029 is not immediately obvious. However, in order to adjust the desired density regime in the upper half of the wafer we further reduced the GaP cell temperature. Furthermore, we compared the simulated density n_{sim} with the experimentally observed density value $n_{ug,meas}$ in the wafer center to check the stability of the P calibration.

Following this strategy, we prepared two completely equal LT-Si based wafers R2035 and R2036 [2] grown at a slightly lower GaP cell temperature ($T_C = 647°C$) with a nominal P doping concentration of $7,5 \cdot 10^{17} cm^{-3}$. Both wafers were fabricated within three days in order to test out the reproducibility of the GaP doping cell. As a result, the P doping profile could be markedly reduced in both wafers in comparison to the first growth series. Wafer R2035 contained a charge carrier density of approximately $4,7 \cdot 10^{11} cm^{-2}$, whereas test wafer R2036 showed a lightly lower density of $3,9 \cdot 10^{11} cm^{-2}$ in the vicinity of the wafer center. However, although the densities have been decreased, the desired nominal charge carrier density could not be shifted to the upper wafer half, see figure 4.12.

[2] The exact transport data maps of all investigated wafers during this thesis are illustrated in appendix A

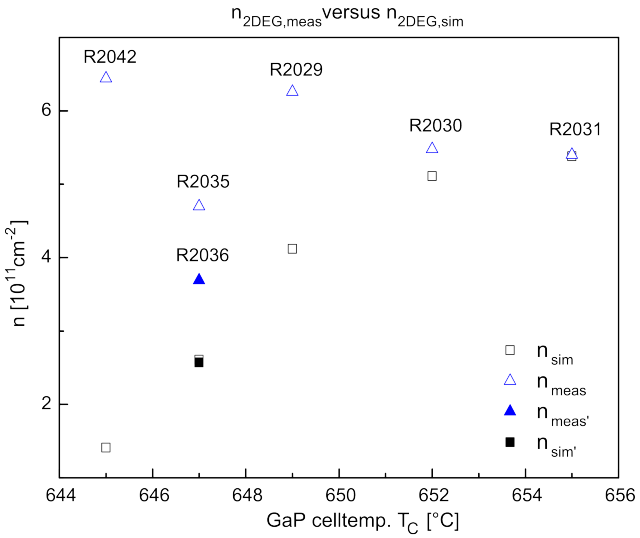

Figure 4.12: *Comparison of the experimentally obtained charge carrier densities n_{meas} with the simulated ones (n_{sim}) in dependence of the GaP cell temperature. Open triangles symbolize the measured data, whereas open cubes display the simulated data. Additionally, the experimental and simulated data of test wafer R2036 is indicated by filled triangles ($n_{meas'}$) and filled cubes ($n_{sim'}$) respectively. The whole picture displays the enormous deviations between simulated and measured data and therefore gives a distinct hint that the P cell behaves completely randomly.*

Therefore, we finally produced one last wafer R2042 [2] which was similarly grown to the previously studied ones but where the GaP cell temperature was further reduced to $T_C = 645°C$ which corresponds to a nominal phosphorous doping concentration of $7,0 \cdot 10^{17} cm^{-3}$ with respect to the first SiGe:P calibration in wafer R2019, see figure 4.7d. However, the results of the carrier density in the centred sample of wafer R2042 were puzzling. Contrary to our expectations, the charge carrier density was not markedly reduced but increased to values over $6 \cdot 10^{11} cm^{-2}$ in the center of wafer R2042, see figure 4.12.

Conclusion: In this section we started off with a first unrotated growth series of different wafers with varying P doping degrees in order to implement our optimisations so that a high quality 2DES can be realized. However, systematic magnetotransport investigations of several samples, taken from the center of the new wafers, showed a distinct discrepancy of simulated and measured charge carrier densities. In this context, especially the centred samples of wafer R2029 and wafer R2042, which contained the nominally lowest P doping degree (lowest P cell temperature), see figure 4.12, revealed dramatic deviations from the simulated charge carrier density. Indeed, the results clearly point to the fact that the temperature controlled GaP doping cell is not precisely controllable and stable over time. However, a possible shift of the SiGe:P calibration over a longer period of time could not be excluded so that the validity has to be checked.

4.4 Instabilities of the GaP cell

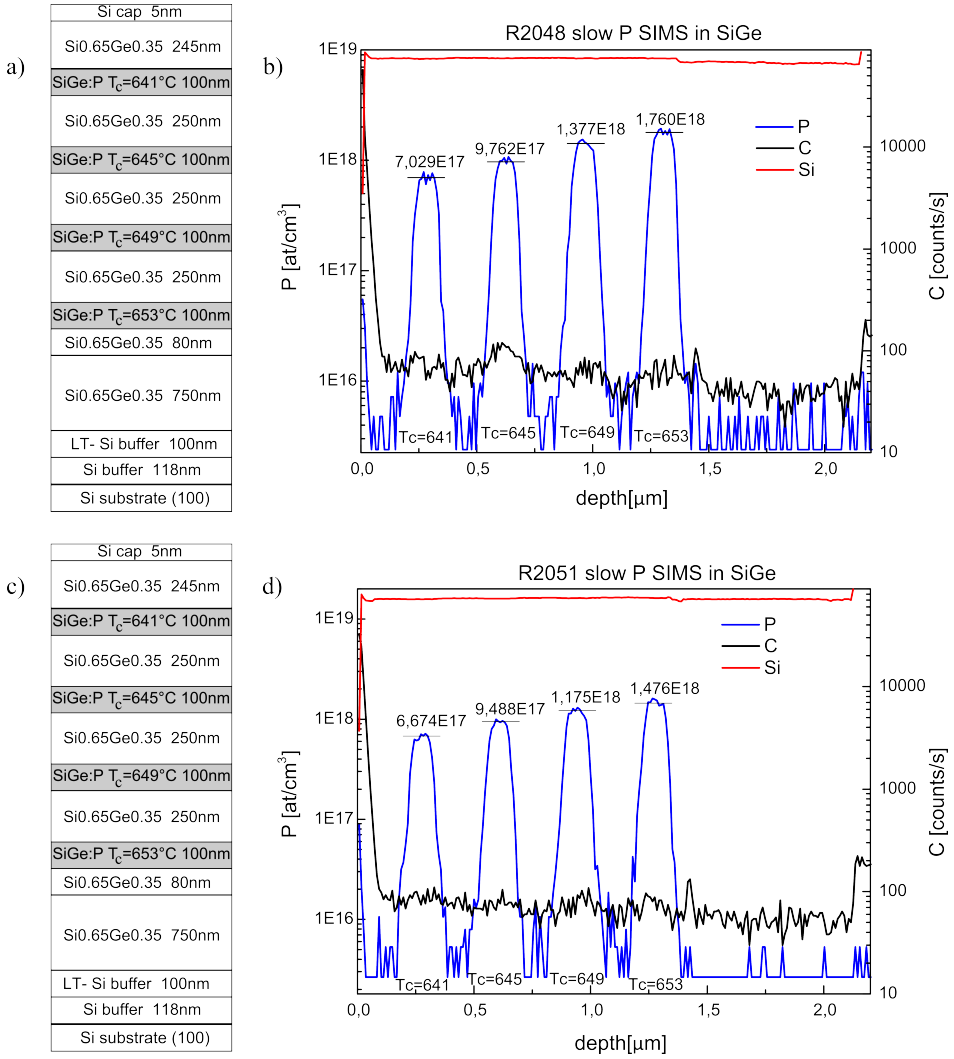

Figure 4.13: *a) Drawing of the SiGe:P sample structure R2048. All four 100 nm thick SiGe:P boxes are separated by 250 nm thick SiGe layers before the sample is capped with a 245 nm SiGe and a 5 nm Si layer. b) High mass resolution SIMS measurement of the phosphorous doping profile in wafer R2048. The boxes with different P doping profiles (for* $653°C, 649°C, 645°C, 641°C$*) are clearly visible and indicated by the blue curve. The doping degree and the corresponding GaP cell temperature are illustrated in black numbers. Additionally, the Si and C concentrations are given by red and black curves respectively. c) Image of the SiGe:P sample R2051. This calibration sample is completely identical to sample R2048. d) shows the according SIMS results. However, the doping profile in the phosphorous doped boxes is lower than in sample R2048 but higher than in the first SiGe:P wafer R2019, see figure 4.7d.*

In order to review now the validity of the current SiGe:P SIMS calibration (R2019), displayed in figure 4.7d, we fabricated a new SiGe:P SIMS calibration wafer (R2048) for comparison. However, this time we decreased the GaP cell temperatures in each doping box about $4°C$ due to the high P doping profiles which were observed in all wafers of the new growth series.

Figures 4.13a and b show the novel SiGe:P high mass resolution SIMS results of a centred sample of wafer R2048 and the according sample structure. The peaks/dips in the C and Si concentrations once again separate the active P doping sequence from the sample surface and the Si substrate respectively. After careful consideration of the doping profiles, we see that each of the four P doped boxes ($T_C = 641°C, 645°C, 649°C, 653°C$) exhibits a $\approx 5 \cdot 10^{17} cm^{-3}$ higher P doping concentration than in the first SiGe:P calibration wafer R2019. For this reason, we conclude that the P calibration in SiGe changed markedly. In order to confirm the new P calibration in wafer R2048 we then prepared another SiGe:P calibration wafer R2051, illustrated in figures 4.13c and d, which was completely identical to the previously studied one. Interestingly, the P doped boxes in wafer R2051 contained approximately $2 - 5 \cdot 10^{17} cm^{-3}$ less P doping than in wafer R2048 but about $3 \cdot 10^{17} cm^{-3}$ more phosphorous than in the first SiGe:P calibration wafer R2019, compare with figure 4.7d. As a result, figure 4.14 displays an overview of all three calibration curves which were extracted from the SIMS results in the three wafers R2019, R2048 and R2051. On closer inspection of the desired doping range of $0,7 - 1,0 \cdot 10^{18} cm^{-3}$ [3], we clearly see that the deviations in the P concentration at equal GaP cell temperatures are approximately $2 - 3 \cdot 10^{17} cm^{-3}$. Actually, these deviations make it almost impossible to precisely employ the wanted density region in the upper half of the wafer.

Conclusion: The SIMS results of the new SiGe:P calibration wafers demonstrate that the P calibration is not reproducible, not even within a few days. Indeed, we obtained deviations on a scale of $\approx 2 - 3 \cdot 10^{17} cm^{-3}$ between all three investigated calibration samples R2019, R2048 and R2051. Moreover, in this context we already identified that two-dimensional electron systems, which exhibit nominally the same parameters, behaved very different, see section 4.3. However, since we found out that the $x_{Ge_{eff}}$, R and P gradients are very stable over a long period of time, we suppose that this instability is caused by the GaP doping cell. Unfortunately, there were no systematic studies on the P doping in the past so that it is unclear whether the GaP cell got worse or if there is a conceptual problem. Furthermore, our analysis clearly shows that the SiGe:P calibration was not continuously shifted and provided evidence that the GaP cell behaved randomly. All in all, the results rather point to a conceptual problem with the temperature control in the GaP doping cell which makes it very difficult to employ the desired density region. As a result, we conclude that the performance limit of the GaP doping cell seems to be reached.

[3] The corresponding density range is approximately $2,5 - 3,5 \cdot 10^{11} cm^{-2}$.

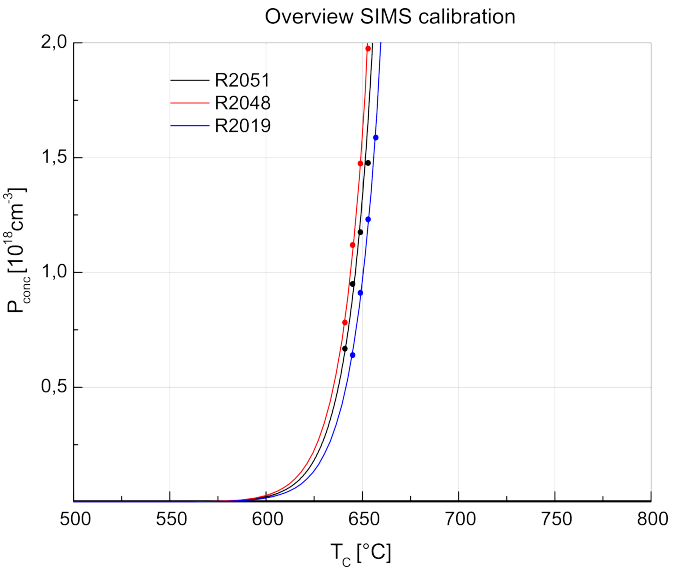

Figure 4.14: *Overview of all three P cell calibration curves which were extracted from the SIMS results of the centred samples. Close inspection leads to the insight that the calibration curves differ strongly from each other in the interesting P doping regime of* $0,7 \cdot 10^{18} cm^{-3}$ *to* $1,0 \cdot 10^{18} cm^{-3}$.

4.5 Mobility analysis

In the previous sections 4.3 and 4.4, we showed that the desired doping range of $2,5-3,5 \cdot 10^{11} cm^{-2}$ could not be adjusted in the upper part of the wafer since the GaP doping cell was not precisely controllable. Nevertheless, figures 4.15a and b exemplarily show that if we extract samples with a fairly convenient charge carrier density and a Ge content of approximately 35% from a wafer, which was fabricated during the new growth series, relatively high mobilities up to approximately $2,5-3,0 \cdot 10^4 \frac{cm^2}{Vs}$ could be observed in the ungated region. Based on these facts, we in the following reveal that the new Si/SiGe 2DES are nevertheless suitable to form a basic platform for high mobility field-effect devices. In a first step, we briefly show the field-effect influence on the mobility of the samples in wafer R2030. In the second part of our investigation, we performed a scattering time analysis to discover further mobility limiting processes in Si/SiGe heterostructures.

4.5.1 Record mobility

To start our analysis, several samples across the entire wafer R2030 were covered with Schottky top-gates and checked for the maximal achievable mobility. Figures 4.15a and b give an overview of the maximal charge carrier density and the mobility in dependence of an applied gate voltage in the overall gate controllable

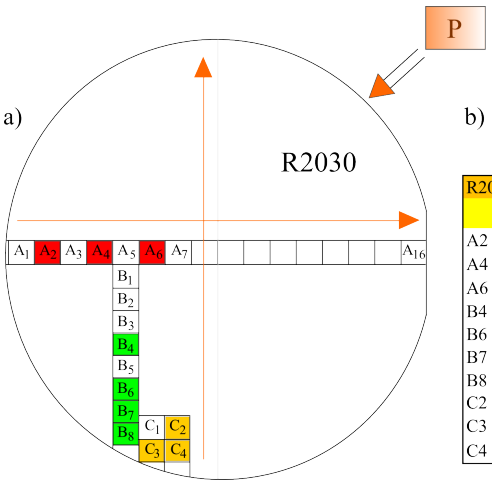

b)

R2030	ungated region		gated region		gate control. region	
	$n_{ug,max}$ [1/cm^2]	$\mu_{ug,max}$ [cm^2/Vs]	n_{max} [1/cm^2]	μ_{max} [cm^2/Vs]	interval[V]	U_{Gmax}[V]
A2	5,24E+11	1,29E+04	5,64E+11	8,85E+03	0,39	0,51
A4	5,47E+11	1,14E+04	4,90E+11	6,45E+03	0,32	0,47
A6	5,49E+11	1,14E+04				
B4	4,87E+11	2,24E+04	6,25E+11	2,57E+04	0,65	0,50
B6	4,51E+11		6,21E+11	2,39E+04	0,61	0,51
B7	4,33E+11		5,42E+11	3,34E+04	0,52	0,47
B8	4,15E+11	2,31E+04	5,10E+11	1,78E+04	0,50	0,38
C2			5,29E+11	5,08E+04	2,4	1,2
C3	3,74E+11		5,66E+11	4,78E+04	0,74	0,48
C4	3,60E+11	3,01E+04	5,43E+11	5,09E+04	2,7	1,2

Figure 4.15: *a) Overview of the exact positions of several samples distributed across the wafer R2030. The experimentally obtained P doping gradients are indicated with orange arrows. b) displays the results of both the carrier density n and the mobility μ in the ungated as well as the gated region in dependence of the wafer position. The maximum mobility, is highlighted in different colours. Red indicates mobilities lower than $1 \cdot 10^4 \frac{cm^2}{Vs}$, mobilities in the range of $1 \cdot 10^4 \frac{cm^2}{Vs}$ to $2 \cdot 10^4 \frac{cm^2}{Vs}$ are shown in light blue, green stands for mobilities in the range from $2 \cdot 10^4 \frac{cm^2}{Vs}$ to $4 \cdot 10^4 \frac{cm^2}{Vs}$, whereas yellow displays mobilities over $4 \cdot 10^4 \frac{cm^2}{Vs}$. Furthermore, the maximal gate controllable interval is illustrated. Samples R2030C2 and C4 were additionally covered with an Al_2O_3 gate insulator so that mobilities even up to $\approx 5 \cdot 10^4 \frac{cm^2}{Vs}$ could be reached.*

region [4]. The maximal mobility of all gated samples was highlighted in different colours. Red denotes mobilities worse than $1,0 \cdot 10^4 \frac{cm^2}{Vs}$, light blue stands for mobilities between $1,0 - 2,0 \cdot 10^4 \frac{cm^2}{Vs}$ and green indicates mobilities from $2,0 \cdot 10^4 \frac{cm^2}{Vs}$ to $4,0 \cdot 10^4 \frac{cm^2}{Vs}$, whereas yellow displays mobilities over $4,0 \cdot 10^4 \frac{cm^2}{Vs}$. As a result, we could determine a new record mobility of $4,78 \cdot 10^4 \frac{cm^2}{Vs}$ concerning our MBE system in the Schottky top-gated LT-Si based sample R2030C3 which exhibited a carrier density of $3,74 \cdot 10^{11} cm^{-2}$ in the ungated region. Figure 4.16 shows the corresponding magnetotransport measurement results for the maximal achievable gate voltage of $U_G = 0,48V$ as well as for two lower gate voltage values. The maximal mobility was calculated from the slope in the Hall resistance at low magnetic fields (B<1T) and from the minima in the Shubnikov-de Haas oscillations. In the scope of our analysis, we furthermore identified mobilities even up to $> 5,0 \cdot 10^4 \frac{cm^2}{Vs}$ in samples R2030C2 and R2030C4 which were additionally covered with an Al_2O_3 gate insulator material between the Schottky top-gate and the sample surface.

[4] An exact overview of all other investigated wafers concerning the maximal density and mobility in the gated as well as the ungated regions of each and every sample is given in A

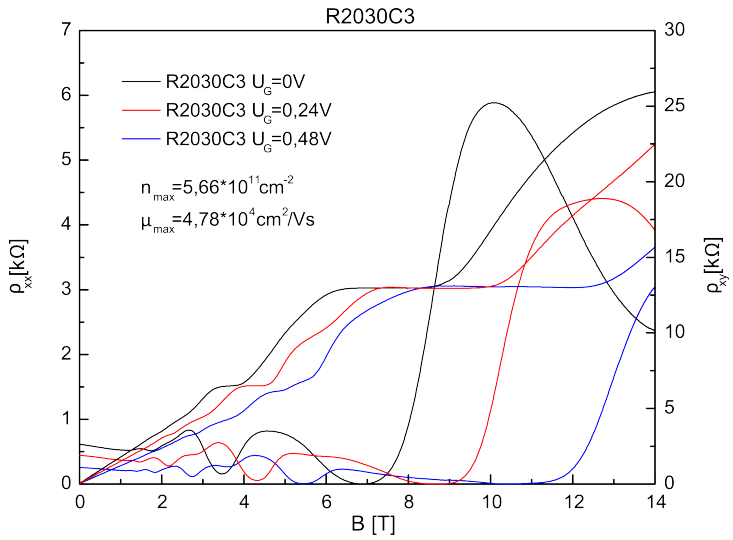

Figure 4.16: *Shows the Hall resistances of sample R2030C3 and the corresponding Shubnikov-de-Haas oscillations in dependence of the applied magnetic field B for three applied gate voltages. The maximal calculated mobility from the linear regime at low magnetic fields (B<1T) in the Hall resistance and from the minima in the SdHs yield about* $4,78 \cdot 10^4 \frac{cm^2}{Vs}$ *for a maximal gate voltage* $U_G = 0,48V$.

In conclusion, these results definitely show that although we were not able to establish stable low and reproducible charge carrier densities in the upper half of the wafer, where both a high degree of relaxation (R) and a high effective Ge content ($x_{Ge_{eff}}$) are achieved, a good basis for high quality field-effect devices could be developed.

4.5.2 Scattering time analysis

In order to find out more about the remaining mobility limiting processes in our Si/SiGe heterostructures, we in the following investigate scattering mechanisms and perform a scattering time analysis based on the evaluation of the low-field SdH oscillations. In a first step, we therefore give a brief overview about the theoretical background, discuss the physical meaning of the special scattering times before we then analyse the gate dependent experimental results.

Theoretical background: The scattering time analysis mainly considers the influence of different scattering mechanisms in two-dimensional electron systems and is based on the evaluation of the Dingle ratio

$$\alpha = \frac{\tau_t}{\tau_s} \tag{4.1}$$

in which τ_s is the single-particle relaxation time and

$$\tau_t = \frac{\mu m^\star}{e} \tag{4.2}$$

displays the transport lifetime with $m^\star$ being the effective electron mass and e the elementary charge. The single-particle relaxation time depends on the increase in the low field SdH amplitude and is correlated to the Landau level broadening, whereas the transport lifetime can be directly calculated from the measured mobility μ. In the transport theory the transport lifetime can also be derived from the Boltzmann equation to:

$$\frac{1}{\tau_t} = \int d\Theta P(k,k^{'})(1-\cos\Theta) \tag{4.3}$$

with $P(k,k^{'})$ being the quantum mechanical transition rate between states with momenta k and $k^{'}$, whereby Θ stands for the scattering angle. In this notation the single-particle relaxation time is described by

$$\frac{1}{\tau_s} = \int d\Theta P(k,k^{'}) \tag{4.4}$$

and can be determined by evaluating the low-field SdH oscillations in the low magnetic field regime of the longitudinal resistance. In this work we mainly used a model proposed by Ando et al. [101], which was later on modified by Bockelmann et al. [102] to extract the single-particle relaxation time. The central idea in this model is that the transport lifetime determines the classical part of

$$|\Delta\rho_{xx}(B)| = \frac{m^\star}{ne^2\tau_t}\frac{\xi}{\sinh\xi}X(\tau_t,\tau_s,B)e^{\pi/\omega_c\tau_s}, \tag{4.5}$$

whereas the single-particle relaxation defines the quantum mechanical corrections given by

$$X(\tau_t,\tau_s,B) = \frac{4[(\omega_c\tau_s)^2[(\omega_c\tau_t)^2-1+3\tau_t^2\tau_s^{-2}]+\tau_t^2\tau_s^{-2}]}{[1+(\omega_c\tau_s)^2][1+(\omega_c\tau_t)^2]} \tag{4.6}$$

with a temperature dependent function

$$\xi = \frac{2\pi^2 k_B T}{\hbar\omega_c}. \tag{4.7}$$

Here, $|\Delta\rho_{xx}(B)|$ is the low-field amplitude in dependence of the magnetic field B, n stands for the charge carrier density and $\omega_c = \frac{eB}{m^\star}$ is the cyclotron frequency.

Physical meaning of τ_s and τ_t: The single-particle relaxation time τ_s corresponds to the total scattering time of the system since all scattering angles are incorporated and weighted equally according to equation 4.4. Moreover, τ_s is a measure for the mean time a carrier remains in a particular momentum eigenstate before it is scattered. In contrary, the transport lifetime τ_t emphasises the

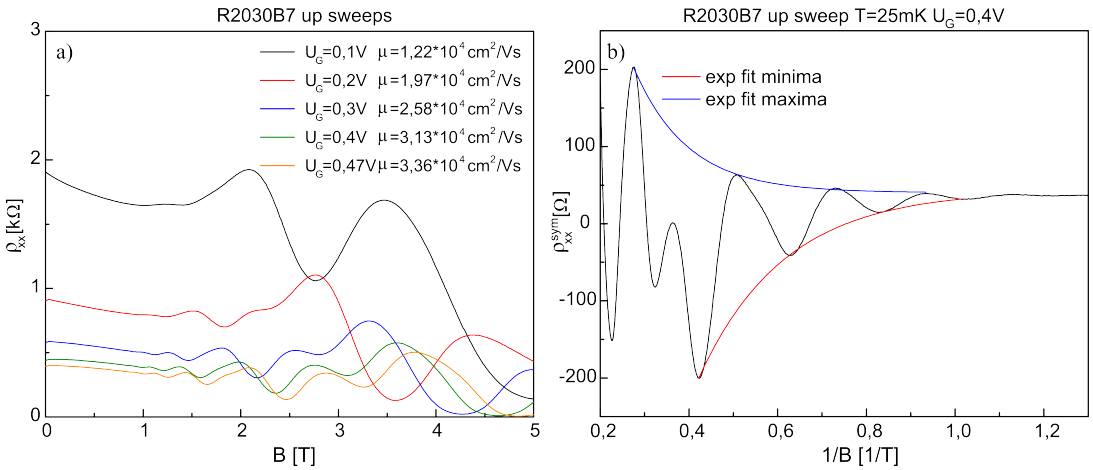

Figure 4.17: *a) Overview of the gate dependent SdH oscillations in the up sweeps of sample R2030B7. b) shows the exponential fits to the extrema of the symmetrised data for an applied gate voltage of $U_G = 0,4V$ in sample R2030B7. Based on this fits the single-particle relaxation times could be extracted from both the minima and maxima.*

importance of large angle over small angle scattering events. The ratio between transport lifetime and single-particle time, $\alpha = \tau_t/\tau_s$ can be derived from the magnetic field dependent amplitude of the SdH oscillations and provides information about the predominant large or small angle scattering mechanisms. A typical source for small angle scattering are long-range (Coulomb) potentials caused by remote or background impurities which were shown to significantly hamper the mobility in high quality Si/SiGe heterostructures [103, 104, 13, 105]. In this special case the dingle ratio $\alpha \gg 1$ [106, 51]. In contrast to that, interface and alloy scattering are usually associated with short range scattering events indicated by $\alpha \approx 1$ [20]. Additionally, it is important to know that the first mechanism varies regarding the channel thickness d with $1/d^6$ and therefore gets dominant for thin Si channels.

Experimental aspects and results: In our analysis, we focused on the low-field SdH oscillations where the spin degeneracy is not lifted [104]. Figure 4.17a presents the gate dependent SdH oscillations in sample R2030B7 as a function of the applied magnetic field B. The transport lifetime is calculated by using equation 4.2. In contrast, figure 4.17b shows the determination of the single-particle relaxation time for an applied gate voltage of $U_G = 0,4V$ by performing an exponential fit to the symmetrised SdH oscillations based on equation 4.5. More information on the fitting procedure can be found in the thesis of Lang [85]. The results of the fits to the SdH minima and maxima were almost identical so that we in the following concentrate on the fits to the SdH minima. However, it is important to mention that in the gated samples it was only possible to extract the single-particle relaxation times for gate voltages higher than $U_G = 0,1V$ because of too little oscillations for

R2030B7	U_G [V]	$\tau_{t,\uparrow}$ [ps]	$\tau_{t,\downarrow}$ [ps]	$\tau_{s,\uparrow}$ [ps]	$\tau_{s,\downarrow}$ [ps]	$\alpha_\uparrow$	$\alpha_\downarrow$
	0,1	1,32	1,08	NaN	NaN	NaN	NaN
	0,2	2,13	1,71	1,28	1,56	1,66	1,09
	0,3	2,79	2,22	0,80	1,02	3,50	2,17
	0,4	3,38	2,82	0,57	0,72	5,94	3,94
	0,47	3,63	3,41	0,49	0,48	7,47	7,05
R2030B6	U_G [V]	$\tau_{t,\uparrow}$ [ps]	$\tau_{t,\downarrow}$ [ps]	$\tau_{s,\uparrow}$ [ps]	$\tau_{s,\downarrow}$ [ps]	$\alpha_\uparrow$	$\alpha_\downarrow$
	0,1	0,90	0,79	NaN	NaN	NaN	NaN
	0,2	1,36	1,23	0,64	0,64	2,13	1,92
	0,3	1,82	1,63	0,59	0,63	3,07	2,58
	0,4	2,19	2,10	0,56	0,52	3,92	3,79
	0,46	2,31	2,33	0,53	0,54	4,38	4,33

Table 4.1: *Overview of the gate dependent Dingle results in sample R2030B7 and R2030B6. The data were obtained by an exponential fit to the SdH minima. The black little arrows ↑ and ↓ indicate the experimentally obtained values of the up and downsweep respectively. Interestingly, α increases with increasing gate voltage U_G which means that scattering on remote and/or background impurities rises. In comparison to sample R2030B7, sample R2030B6 showed lightly lower values of α with increasing gate voltage. This circumstance can be possibly attributed to a slightly higher modulation doping profile which lies only 15nm above the quantum well (QW). Consequently, short range scattering mechanisms might become more dominant.*

low bias voltages. The final gate dependent Dingle results conducted in sample R2030B6, R2030B7 as well as the ungated test sample R2030B8 are illustrated in figure 4.18 and table 4.1 for the B field up and the down sweeps. Regarding the results of the Dingle analysis in the samples R2030B7 and R2030B6, we see that the transport lifetime increases with increasing gate voltage (increasing carrier density n) independently of the B field up and down sweep. In contrast to that, the single-particle relaxation time decreased in sample R2030B7 for an enhanced gate voltage, whereas it nearly stayed constant in sample R2030B6. A possible reason for this observation could be the lightly higher modulation doping degree in sample R2030B6, which is about $N_P = 1,45 \cdot 10^{18} cm^{-3}$, whereas we have approximately $N_P = 1,25 \cdot 10^{18} cm^{-3}$ in sample R2030B7. If we consider that the doping layer lies only $15nm$ above the QW, we can imagine that short range scattering events could become more prominent in this case. In addition to that, test sample R2030B8 without a palladium (Pd) top-gate showed a Dingle ratio of $\alpha \approx 2$ which also indicates dominant long range scattering. Moreover, this result is in perfect agreement with former investigations of Lang and Ibrahim [85, 107] who also demonstrated that long range scattering events are the main mobility limiting mechanisms. In summary, we mainly observed dingle values were $\alpha > 1$ so that long range remote and/or background impurity scattering are identified

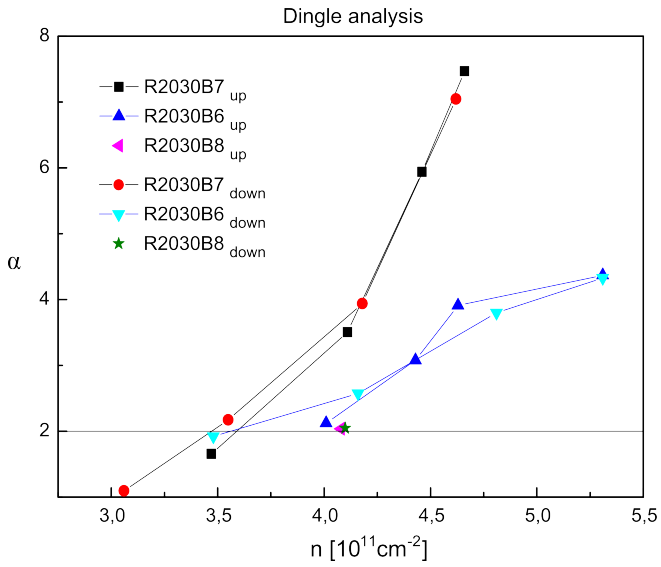

Figure 4.18: *Overview of the gate dependent Dingle rate analysis in samples R2030B6, R2030B7 and R2030B8 (ungated sample) as a function of the charge carrier density n for both the magnetic field up and down sweeps. The horizontal line at $\alpha = 2$ is just a guide to the eye and represents the Dingle ratio in the ungated case and for an applied gate voltage $U_G = 0V$ respectively.*

to be the dominant scattering mechanisms. However, it is not possible with this analysis alone to discriminate between remote or background impurity scattering. Therefore, another approach which will be discussed in the following is necessary to solve this open question.

Remote and/or background impurity scattering: In order to discriminate between the different scattering mechanisms, we now focus on a second model which is based on the evaluation of the behaviour of the electron mobility μ on the charge carrier density n. Therefore, in the following we first present the link between density and mobility in the different scattering mechanisms before we finally make statements about the dominant scattering event and give an estimation of a possible background doping.

Remote impurity scattering on doping atoms in the barrier: This scattering mechanism is especially dominant for low temperatures. In contrast to all other parts in our heterostructures, which can be improved by a better material quality, doping atoms are almost irreplaceable since they provide charge carriers for the QW so that a distinct measure of scattering events on this impurities is inevitable. In a first approach, the correlation between n and μ is given by [108]:

$$\mu_{remote} = \frac{16(\pi g_\nu g_s)^{1/2} e n^{3/2} d_s^3}{\hbar N_A} \tag{4.8}$$

Here, g_ν, g_s are the valley and spin degeneracy factor, d_s denotes the effective

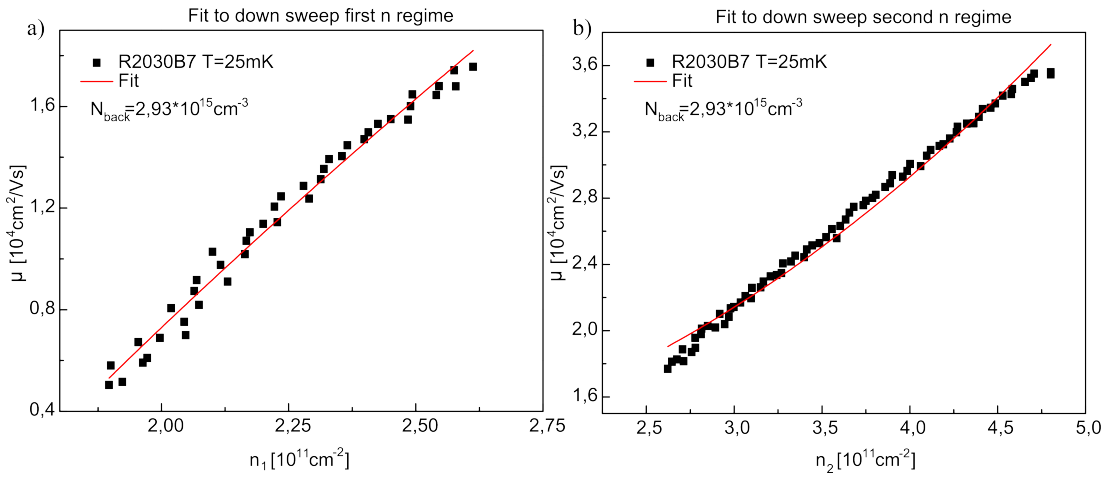

Figure 4.19: *a) Fit to the first density regime during the B down sweep in sample R2030B7. We extracted a parameter* $b = 0,52$ *and* $N_{back} = 2,93 \cdot 10^{15} cm^{-2}$. *b) shows the according fit to the second density regime where we obtained* $b \approx 2$.

distance between the QW and the impurity atoms also called spacer layer, whereby N_A is the area concentration of the impurities.

Background impurity scattering: In 1984, Walukiewicz et al. already modelled the influence of the impurities on the $\mu(n)$ correlation for GaAs/AlGaAs heterostructures [109, 110]. Their results show that the relative importance of background impurity over remote impurity decreases with increasing sheet carrier density. For a 2DES in Si, Gold similarly found several equations which allow to distinguish between the main scattering mechanisms [106]. For background impurity scattering he found

$$\mu_{back} = \alpha + \frac{2e}{\sqrt{\pi}\hbar N_{back}} \cdot n^{1/2} \tag{4.9}$$

with N_{back} being the density of background impurity scatterers and α representing contributions from other scattering sources. Moreover, he predicts that for $n > 10^{12} cm^{-2}$ and a spacer thickness of $d_s > 4nm$ remote doping limits the mobility in Si QWs, whereas homogeneous background impurity scattering becomes dominantly for $n < 10^{12} cm^{-2}$

Fitting $\mu(n)$ curves: Equations 4.8 and 4.9 obviously show the connection between n and μ. Applying now a fit of the form

$$\mu = a \cdot n^b + c \tag{4.10}$$

to the experimentally obtained down sweep data of sample R2030B7 allows us to distinguish between remote and background impurity scattering. As a result, we obtained two density dependent scattering regimes. In the first density section with $n \approx 1,9 - 2,6 \cdot 10^{11} cm^{-2}$, we achieved a good fitting result with a goodness

of fit $R^2 = 0,981$ and extracted a fitting parameter $b = 0,52$ which confirms that the dominant scattering mechanism in this density range is background impurity scattering, see figure 4.19a. On top of that, we could evaluate the density of the background impurities $N_{back} \approx 2,93 \cdot 10^{15} cm^{-3}$ which is in very good agreement with former investigations of Sailer and Wild [25, 13]. In contrary to these observations, we extracted, in the second density regime where $n \approx 2,6 - 4,95 \cdot 10^{11} cm^{-2}$, a parameter $b \approx 2$ for a fitting accuracy of $R^2 = 0,986$. Indeed, this is a strong hint that inside this density section scattering on remote impurities is the main mobility limiting mechanism, see figure 4.19b. Additionally, we also checked the up sweeps in sample R2030B7 and performed the same examination in sample R2030B6. We obtained similar results which are summarized in table 4.2.

sample	n_1 $[10^{11} cm^{-2}]$	b_1	N_{back} $[10^{15} cm^{-3}]$	n_2 $[10^{11} cm^{-2}]$	b_2
$R2030B6_{\downarrow}$	2,0-3,4	0,49	2,10	3,4-5,5	2,00
$R2030B6_{\uparrow}$	2,7-4,5	0,50	4,18	4,5-5,5	2,02
$R2030B7_{\downarrow}$	1,9-2,6	0,52	2,93	2,6-5,0	2,03
$R2030B7_{\uparrow}$	2,2-3,9	0,51	3,42	3,9-5,0	2,03
R1812 Sailer	1,2-2,7	0,50	6,62	-	-
R1870E Wild	1,2-2,2	0,50	1,86	-	-

Table 4.2: *Overview of the fitting results of the $\mu(n)$ curves. As a result, we obtained two density regimes were we found background or remote impurity scattering to be the dominant scattering mechanisms. Moreover, we present for comparison the results of Sailer and Wild [25, 13] who also performed a scattering time analysis in Si/SiGe heterostructures.*

4.6 Conclusion

In this chapter, we studied LT-Si and graded buffer based Si/SiGe heterostructures by XRD RSMs, standard magnetotransport and SIMS measurements as well as nextnano band structure simulations. In the scope of our analysis, we systematically investigated and for the first time precisely mapped the effective Ge content ($x_{Ge_{eff}}$), the degree of relaxation (R) and P doping gradients which arise on a wafer in an unrotated growth process due to the MBE cell geometry. Based on our experimental findings, we unveil a strong reproducibility in time and usefulness of the recorded gradients for the optimisation of the current heterostructure design.

First, we determined the best charge carrier density region to lie in the range of $2,5 - 3,5 \cdot 10^{11} cm^{-2}$ and showed relatively high mobilities in the ungated region in comparison to earlier fabricated two-dimensional electron systems. Secondly, we applied nextnano band structure simulations for several samples lying on these

gradients using experimental input parameters which were extracted from the observed $x_{Ge_{eff}}$ and P gradients. In this way, we were able to study the interplay of the increasing P doping and the simultaneously rising $x_{Ge_{eff}}$ gradient which finally allowed us to determine the optimal parameter region on a wafer to produce a high quality 2DES in which charge reconfigurations are minimized while simultaneously high mobilities can be reached. As a result, we found the best parameter region around a sample which contained an effective Ge content of $x_{Ge_{eff}} \approx 35\%$ and a carrier density of approximately $n_{2DES} \approx 3,0 \cdot 10^{11} cm^{-2}$. Since we observed the highest degree of relaxation in the upper half of the wafer, it is advisable to set this density range as far as possible in this region.

In order to precisely adjust the desired doping profile, an accurate P calibration is necessary. Starting with an old P calibration in Si, which was traditionally used in the past few years, we developed an optimized P calibration in SiGe, where the P doping deposition is conducted very similarly to the modulation doping process in Si/SiGe heterostructures. However, all attempts to establish stable and reproducible modulation doping profiles in our two-dimensional electron systems failed which leads us to the conclusion that the performance limit in terms of controllability of the GaP doping cell is already reached.

Nevertheless, if we extract samples from a wafer fabricated during the new growth series, which exhibit a fairly convenient charge carrier density in the ungated region and a Ge content of approximately 35%, we showed that covering these samples with gates results in the highest reported mobilities of LT-Si based two-dimensional electron systems. These results show that a good basis for high mobility field-effect devices can be formed.

We also performed a scattering time analysis to determine other mobility limiting processes concerning Si/SiGe heterostructures. As a result, we discovered that long range scattering events are the dominant scattering mechanisms in our Si/SiGe heterostructures which is in good agreement with former investigations of Lang and Ibrahim [85, 107]. Furthermore, we found two density regimes in our samples, where we could discriminate between background impurity and remote impurity scattering as the dominant scattering mechanism. Finally, we estimated the background impurity concentration to be on a scale of $N_{back} \approx 2-4 \cdot 10^{15} cm^{-3}$ which is also in good agreement with previous results of Sailer and Wild [25, 13].

5 Field-effect control of 2DES in Si/SiGe

A precise electrostatic control of two-dimensional electron systems is essential to realize high quality gate defined few electron QDs. However, the manipulation of a 2DES is often restricted by unwanted charge fluctuations which were observed by several groups [13, 14, 15]. The origin of these phenomenons could not be completely clarified up to now. In order to get a better understanding of the underlying effects, we systematically investigate Hall-bar shaped Schottky-gated Si/SiGe two-dimensional electron systems from different wafers and at different wafer positions. Starting with the findings of Wild et al. [13], see section 2.5.2, we mainly used the charge carrier density as a sensing observable to detect charge transfer processes and compare our results with nextnano band structure simulations. In this context, the current charge reconfiguration model suggested by Wild and coworkers [13] is modified and extended.

5.1 Time resolved jump measurements

Figure 5.1a shows the typical behaviour of the 2DES density n as a function of the gate voltage U_G in a top-gated Si/SiGe heterostructure. We have already mentioned in section 2.5.2 that sweeping U_G beyond the linear regime labelled "I" to the saturation regime II induces a hysteretic behaviour of n. Therefore, we introduced a model by Wild et al. [13] based on charge transfer processes which are activated when reaching regime II. In this model in the linear regime I, no detectable charge reconfigurations occur. On the other hand regime II is determined by a massive charge carrier transfer process into the barrier since increasing the gate voltage leads to a situation where the P levels reach the Fermi level (E_F) or even fall below it so that tunnelling events from the 2DES into P states are facilitated. The hysteretic difference between regime II (up-sweep of U_G) and III (down-sweep of U_G) is explained by a strong asymmetry in the charge carrier transfer process involving P states. As soon as the last P states are lifted above the Fermi energy at a threshold value of U_G the depletion of the P states is accelerated resulting in a shallower n versus U_G slope which is characteristic of regime IV, see figure 5.1a. To extend this study based on continuously sweeped voltages and to test the model we have conducted experiments in which a gate

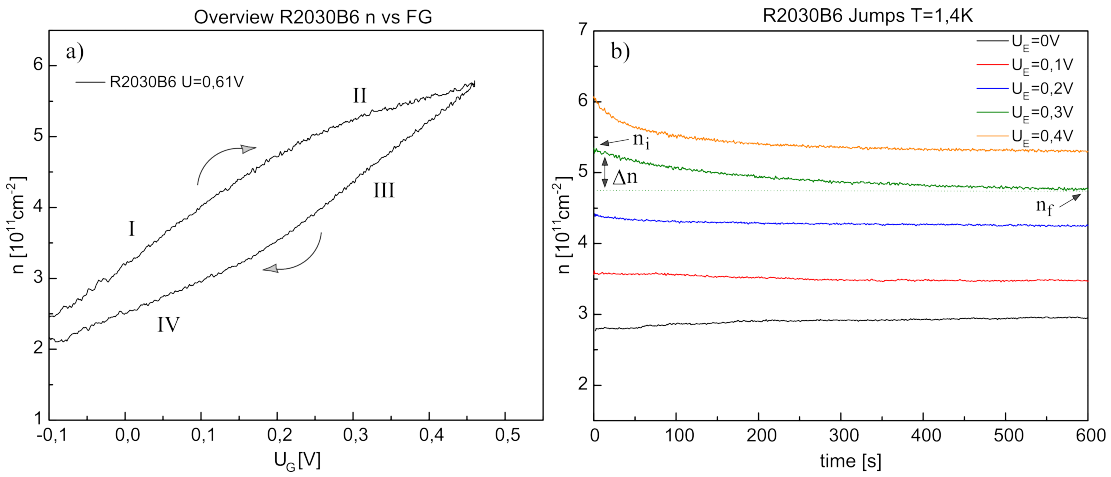

Figure 5.1: *a) shows the n versus U_G gate sweep curve of sample R2030B6. All four regions in the hysteresis curve, as suggested by Wild et al. [13], are indicated by black Roman numbers. Moreover the up and down sweeps are labelled by black arrows. b) Overview of the time resolved gate jump measurements in sample R2030B6 for several end voltage values U_E at $T = 1,4K$. The voltage end values of the jumps varied between $0V$ and $0,4V$ and the time dependent charge carrier density change was faster for higher end voltages. Additionally, the determination of the initial (n_i) and final (n_f) charge carrier density as well as the difference Δn between them are exemplarily displayed. Comparing the jump with the sweep measurements, we see that charge transfer processes should also be possible within the linear regime I.*

voltage lying within the hysteretic sweep curve is quasi instantaneously applied to a depleted 2DES. In the following, we denote these experiments as gate jump measurements.

Gate jump measurements: In a first step, we recorded time resolved gate jump experiments at $T = 1,4K$. Starting from the reset point U_R [1], which depletes the 2DES and removes all electrons from the barrier region above the QW, we pulsed the top-gate voltage with a rate of $1,0 \cdot 10^4 \frac{mV}{s}$ to different voltage end values (U_E) within the maximally gate controllable interval and then monitored the temporal evolution of the 2DES density n. During the pulse phase and stabilization, the experimental signal does not depict the real behaviour of the observable n due to the limited bandwidth of the measurement set-up. Figure 5.1b exemplarily shows the measured time resolved charge carrier density results of sample R2030B6 for several voltage values U_E. Interestingly, the density increases slightly for an applied gate voltage value of $U_E = 0V$ from $n \approx 2,8 \cdot 10^{11} cm^{-2}$ to $n \approx 3,0 \cdot 10^{11} cm^{-2}$, whereas for positive gate voltages with $U_E > 0,1V$ the density decreases markedly, e.g. for $U_E = 0,4V$ from $n \approx 6,1 \cdot 10^{11} cm^{-2}$ to $n \approx 5,25 \cdot 10^{11} cm^{-2}$.

[1] We always used $U_R = -1,5V$ with a reset duration of $\tau_r = 5min$

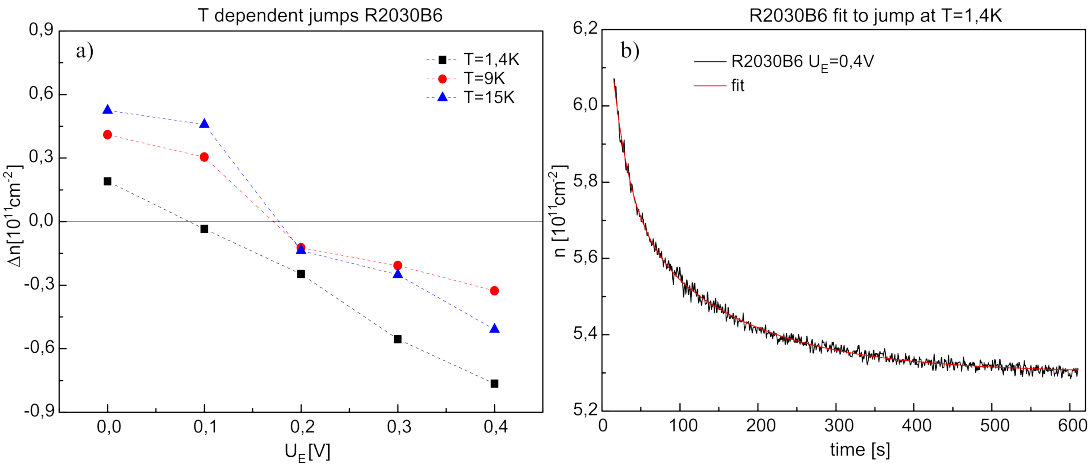

Figure 5.2: *a) Overview of the temperature dependent charge carrier density changes Δn after a pulse with a pulse duration of $\tau_p \approx 1s$ was conducted to different end voltages U_E. Interestingly, for voltages with $U_E < 0,1V$ we observed that the recorded density Δn is positive. Moreover, the quasi equilibrium state, where the time evolution of the density was constant, changed form $U_E \approx 0,08V$ at $T = 1,4K$ to $U_E \approx 0,17V$ for $T \geq 9,0K$. Additionally, the density changes are relatively similar for $T = 9,0K$ and $T = 15K$ and differ only weakly. b) Exemplary picture of a double exponential fit to one of the time resolved jump measurements for a gate voltage of $U_E = 0,4V$ at $T = 1,4K$.*

To quantify these dynamics of the charge carrier density concentrations, we in the following consider the difference between the initial n_i (first measurement point) and the final n_f (after long times, here $600s$) charge carrier density which is given by $\Delta n = n_f - n_i$, as labelled in figure 5.1b. The evolution of the carrier density change Δn as a function of different end voltage values is shown in figure 5.2a for sample R2030B6. The covered voltage region ranges from $0V$ to $0,4V$. For $U_E < 0,1V$, the density increases after the pulse ($\Delta n > 0$) whereas for higher pulse amplitudes with $U_E > 0,1V$, we discovered that the density decreases ($\Delta n < 0$) after the pulse. In this context, we observed the strongest density decrease of about $0,8 \cdot 10^{11} cm^{-2}$ for the maximal gate voltage of $U_E = 0,4V$. Additionally, we found a quasi equilibrium state ($\Delta n = 0$) for an applied gate voltage of $U_E \approx 0,08V$ which means that the carrier density holds constant throughout the entire measurement. While the density decrease ($\Delta n < 0$) and the equilibrium state ($\Delta n = 0$) can be understood within the charge transfer model proposed by Wild [13], the origin of the density increase ($\Delta n > 0$) is unclear up to now and has to be further investigated. Figure 5.2a also shows the equivalent experiments conducted at $9,0K$ and $15K$. At first glance, we clearly see a distinct difference of the charge carrier density change between $T = 1,4K$ and $T \geq 9,0K$ of $\Delta n \approx 0,3 - 0,5 \cdot 10^{11} cm^{-2}$ for each voltage value. In contrary, the charge carrier density change between $9,0K$ and $15K$ was very weak (maximal $\Delta n \approx 0,1 \cdot 10^{11} cm^{-2}$) and showed a similar behaviour. Additionally, we observed a T dependent shift

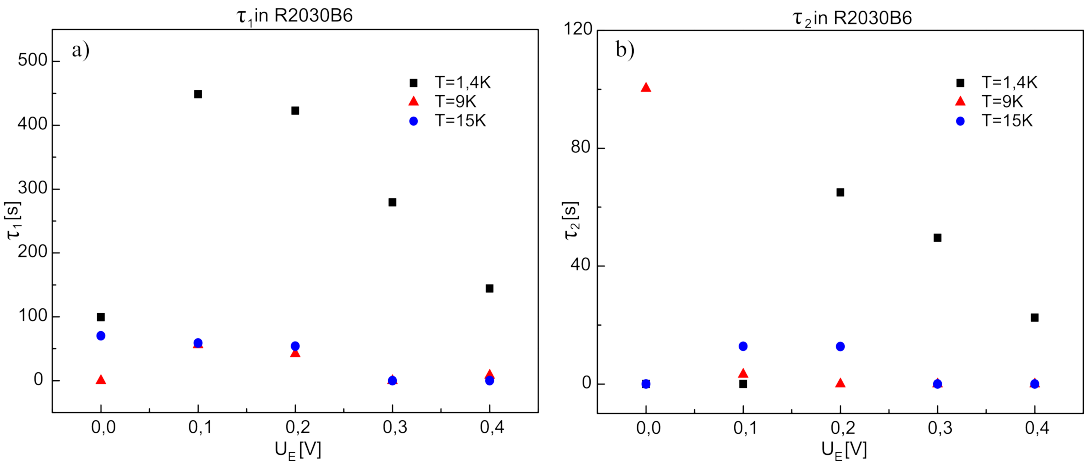

Figure 5.3: *a)and b) Overview of the extracted charge transfer times until an equilibrium ensures. The extracted longer decay times τ_1 were about several $100s$, whereas the second decay time τ_2 was in the range of several $10s$. Interestingly, both times showed a gate voltage and temperature dependence.*

of the quasi equilibrium state to a voltage of $U_E \approx 0,17V$ for $T \geq 9,0K$. If the temperature was increased above $T = 15K$, we always obtained $\Delta n = 0$ indicating that charge transfer processes are then thermally assisted and are too quick to be detected.

Charge transfer time investigation and discussion: Figure 5.2b exemplarily shows a fitting result of a time resolved jump for a gate voltage of $U_E = 0,4V$ at $T = 1,4K$. The best fits, especially for higher voltage end values, were determined by using a double exponential decay function of the following form:

$$y = y_0 + A_1 e^{-x/\tau_1} + A_2 e^{-x/\tau_2} \tag{5.1}$$

We obtained a long (τ_1) and a short (τ_2) decay time, whereby both get faster with increasing gate voltage U_E and/or T, see figures 5.3a and b. The decay times were on a time scale of several 10 or $100s$. While the origin of the second fast decay time (τ_2) could not be clarified up to now, the meaning of the long decay time (τ_1) can be understood within a quantitative charge transfer model which will be discussed in the following taking the density of states in the 2DES as well as in the modulation doping layer into account. In general such charge transfer processes or tunnelling events from an initial i to a final state f can be described by Fermi's golden rule

$$\Gamma_{i\to f} = \int dE \frac{2\pi}{\hbar} \mid M_{i\to f}(E) \mid^2 \rho_i(E)\rho_f(E), \tag{5.2}$$

where $M_{i\to f}(E)$ is the tunnelling matrix element and $\rho_{i/f}(E)$ are the densities of the occupied initial and final states in an absolute energy scale E. This equation

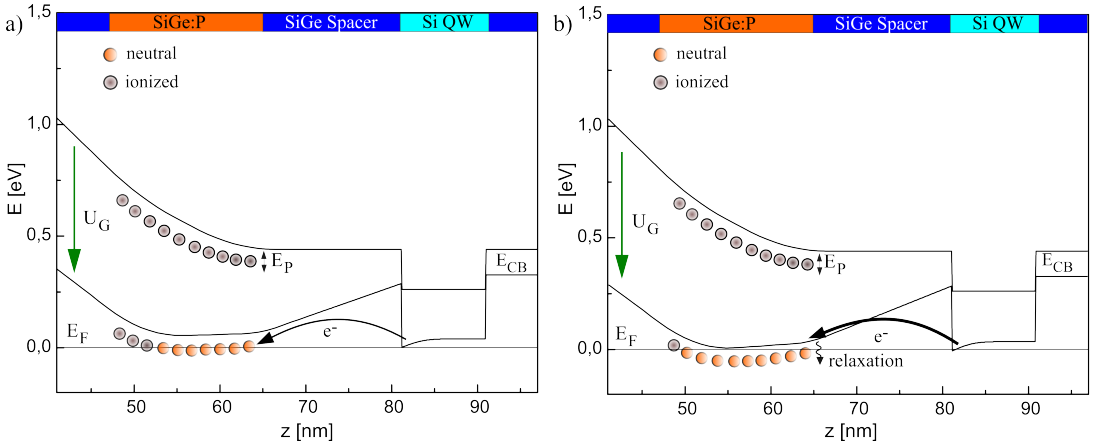

Figure 5.4: *a) Band structure profile of a jump (U_G) out of the reset to a positive gate voltage of $U_E = 0,1V$. The energetic position of the P states is illustrated by E_P, whereas E_F describes the position of the Fermi energy and E_{CB} displays the conduction band energy. In case when $E_P \approx E_F$, we clearly see a charge transfer process from the QW into the doping layer (indicated by the big black arrow) which results in a decrease of the carrier density in the 2DES. However, since the charge transfer rate from the 2DES into the barrier is lower than the gate sweep rate, the tunnelling events are not visible within the linear regime. b) Image of the according band structure profile for a gate voltage of $U_E = 0,4V$ when $E_{CB} = E_F$. Here, we observe a strong direct charge carrier transfer process into the conduction band minimum followed by a relaxation into the P states which enables a faster density decrease in the jump measurements. Indeed, the charge transfer rate gets faster than the sweep rate so that a saturation plateau appears.*

can be rewritten as

$$\Gamma_{i\to f} = \int dE \frac{2\pi}{\hbar} \mid M_{i\to f}(E) \mid^2 D_i(E) f(E - E_{F,i}) \cdot D_f(E)(1 - f(E - E_{F,f})), \quad (5.3)$$

with the densities of states $D_{i/f}$, the Fermi distribution f and the local Fermi energy $E_{F,i/f}$. In the low temperature regime, f is given by a step function and $D_i = g_s g_\nu m^\star/(2\pi\hbar^2)$ is the constant density of states of a 2DES, where $g_{s/\nu}$ stand for the spin and valley degeneracy factors. However, since we have almost no knowledge about the density of the final states D_f in the doping layer, we cannot further specify the matrix element.

Development of a quantitative charge transfer model: Based on our experimental findings from section 4.2, where we discovered a random behaviour of the temperature controlled GaP doping cell resulting in very high P doping concentrations in almost all wafers of the new growth series, we infer from sample specific band structure simulations that the conduction band (E_{CB}) minimum in the SiGe:P doping layer is energetically decreased due to a P "overdoping" which means that the P atoms reach the Fermi level ($E_F \approx E_P$) at the starting point of

our measurements. This circumstance was not considered in the picture of Wild et al. [13] and in the following is included in our considerations.

Figure 5.4a shows an image of the band structure profile of sample R2030B6 for a jump (U_G) out of the reset (upper band structure profile) to a positive voltage value of $U_E = 0,1V$ (lower band structure profile). Since the phosphorous atoms already reach the Fermi level, a charge transfer process from the QW into the doping layer sets in which leads to a decrease of the charge carrier density in the 2DES. Comparing this picture with figures 5.1a and b clearly points to the fact that charge reconfigurations are possible within the linear regime I since the gate voltage value of $0,1V$ is in the center of the linear regime in the n versus U_G gate sweep curve and we simultaneously obtain $\Delta n < 0$ in the gate jump measurements for $U_E = 0,1V$. This finding is in contrary to the suggestions of Wild et al. [13] and also implies that the charge transfer rate from the 2DES into the P states, which is equivalent to a tunnelling event from 2D into 0D, has to be distinctly slower than the gate sweep rate. Comparing the measured charge carrier transfer times in figure 5.3a, which are on the order of $\tau_1 \approx 400s$, with the sweep rate $(1 - 2mV/s)$, clearly provides evidence that this assumption is fulfilled because the sweep duration to a gate voltage of $U_G = 0,2V$ at the end of the linear regime would only last $150 - 300s$.

In a next step, we consider a gate jump U_G out of the reset point to a higher gate voltage value, e.g. $U_E = 0,4V$. Figure 5.4b displays the according band structure profile. In this case, the conduction band minimum already reaches the Fermi level ($E_{CB} = E_F$) so that a fast charge carrier transfer process from the 2DES into the conduction band (3D system) followed by a quick relaxation process into lower lying P states takes place. Based on this picture we can understand the development of a saturation plateau II as shown in figure 5.1a since the experimentally obtained charge carrier transfer times of $\tau_1 \approx 150 - 250s$, illustrated in figure 5.3a, are faster than the corresponding sweep duration to $U_E = 0,4V$ which amounts to $250 - 500s$. Indeed, this observation points to the fact that for higher gate voltage values the charge transfer rate becomes faster than the gate sweep rate which means that the density decrease gets visible in the n versus U_G gate sweep curve and finally results in a saturation.

5.2 Capacitive coupling between gate and 2DES

In this section, we explicitly focus on the capacitive coupling $C_m = \frac{\partial n}{\partial U_G}$ between the 2DES and the Schottky top-gate with respect to the underlying P doping gradient. This coupling, which can be directly extracted from the linear regime in the n versus U_G curve, is of pivotal importance to realize an accurate manipulation of electrons in a 2DES. For this purpose, gate sweep measurements were carried out with the help of the standard magnetotransport set-up, see section 3.6.3.

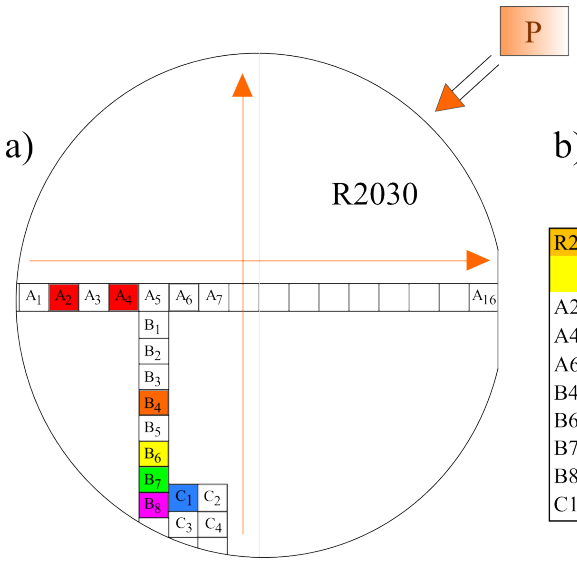

b)

R2030	ungated region	gate controllable region		
	$n_{ug,max}$ [1/cm^2]	interval[V]	U_{Gmax}[V]	dn/dU_G [V/cm^2]
A2	5,24E+11	0,39	0,51	9,19E+11
A4	5,47E+11	0,32	0,47	9,05E+11
A6	5,49E+11			
B4	4,87E+11	0,65	0,50	8,02E+11
B6	4,51E+11	0,61	0,51	7,70E+11
B7	4,33E+11	0,52	0,47	7,51E+11
B8	4,15E+11	0,50	0,38	6,50E+11
C1	4,24E+11	0,78	0,52	7,22E+11

Figure 5.5: *a) Overview of the exact positions of several samples distributed across the wafer R2030. The experimentally obtained P doping gradients are indicated with orange arrows. The calculated density n in the wafer center amounts approximately* $5,5 \cdot 10^{11} cm^{-2}$. *b) displays the results of the carrier density* $n_{ug,max}$ *in the ungated Hall bar region in dependence of sample position on the wafer. Furthermore, the maximal gate controllable interval and the capacitive coupling* C_m *calculated from the slope in the n versus* U_G *curve are illustrated. Interestingly,* C_m *increases with increasing P concentration (increasing* $n_{ug,max}$*). This observation is indicated by the rainbow colour gradient (from violet to red).*

Figures 5.5a and b exemplarily give an overview of the experimentally obtained capacitive couplings (C_m) in Schottky-gated samples of wafer R2030. Interestingly, C_m increases with increasing charge carrier density in the ungated region along the P doping gradient. This interplay is illustrated by a rainbow colour gradient starting at the bottom (violet colour) and ending up at the wafer median (red colour). The fact that the measured capacitive coupling C_m of our 2DES apparently depends on the P doping concentration in the modulation doping layer is surprising and counterintuitive. Moreover, this observation is not explicable with the theoretical predictions of the capacitive coupling (C_{th}) model developed by Ihn [35], see equation 2.23. According to this formula, which includes solely an effective Ge content but no P doping dependence, the theoretical capacitive coupling amounts to $8,9 - 9,2 \cdot 10^{11} V cm^{-2}$ regarding the coloured samples of wafer R2030. However, we only attain $C_m \approx C_{th}$ for charge carrier densities with $n > 5,2 \cdot 10^{11} cm^{-2}$, whereas for lower densities the measured and the theoretical capacitive couplings differed up to 28%, compare with sample R2030B8. Regarding this mismatch of the theoretical (C_{th}) and measured (C_m) capacitive couplings, raises the question of the validity of C_{th}. In the following, we investigate an additional possible influence of the P doping gradient on C_m and C_{th}.

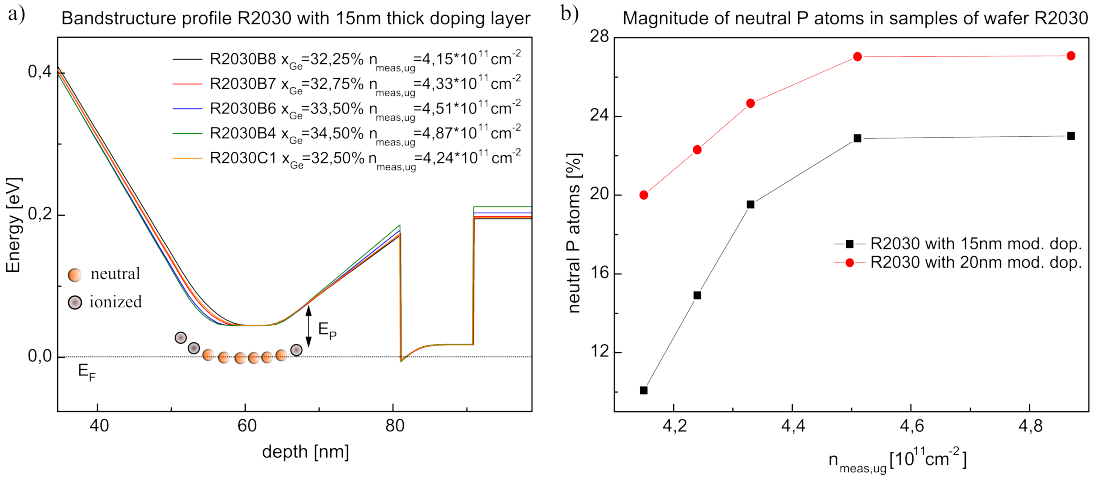

Figure 5.6: *a) Zoom into the band structure profiles of several samples along the P climb gradient in wafer R2030. The simulations were performed with sample specific input parameters which were extracted from the experimentally determined $x_{Ge_{eff}}$ and P gradients, see section 4. The Fermi energy is given by E_F, whereas the energy of the P atoms is given by E_P. Additionally, the experimentally measured charge carrier density $n_{meas,ug}$ and the effective Ge content, are indicated. b) shows the simulated percental magnitude of neutral P atoms for the measured charge carrier densities of different samples along the P gradient with a modulation doping layer of 15nm and 20nm (5nm P segregation) respectively.*

Based on former investigations of several groups who studied the polarizability of neutral impurities in doped semiconductors [111, 112, 113, 114, 115, 116] and demonstrated the distinct polarization influence on the dielectric constants as well as on the capacitive coupling, we assumed that in our case a polarization of phosphorous atoms in the modulation doping layer could also be possible. This assumption should be justified since we already identified markedly higher doping profiles due to the poor controllability of the GaP doping cell, see section 4.2.

We utilized nextnano band structure simulations to evaluate the P doping density for relevant samples. The effective Ge content $x_{Ge_{eff}}$ was extracted from the experimentally determined $x_{Ge_{eff}}$ gradient (see section 4.1.1) for each sample. Then, the P volume modulation doping concentration was adjusted as a fitting parameter in the nextnano simulation so that the simulated charge carrier densities exactly matched the experimentally measured ones in the ungated Hall-bar regions. We then analyse the fraction of P atoms with energies larger than E_F (ionized donors) and with energies lower than E_F (neutral donors) for each sample. Figure 5.6 a shows the corresponding band structure profiles. From this analysis, we conclude that for charge carrier densities in the ungated region with $n_{meas,ug} > 4,0 \cdot 10^{11} cm^{-2}$, which correspond to a P volume doping degree of $> 1,0 \cdot 10^{18} cm^{-3}$, not completely all of the P atoms are ionized. Figure 5.6b displays the amount of neutral P atoms (10-23%) in dependence of the charge

carrier density along the phosphorous gradient in wafer R2030 under the assumption that we have no P segregation. If we incorporate a slight P segregation of $5nm$ in our simulations, which is according to Nützel et al. very realistic for a $Si_{0.65}Ge_{0.35}$ material composition [20], the degree of neutral P atoms rises up to 20-30%, see figure 5.6b. Therefore in the following, we introduce a modified polarization model of neutral impurities proposed by Dhar et al. [114] in order to study and to explain the mismatch in the capacitive couplings of C_{th} and C_m as well as the influence on the dielectric constants and the associated linear increase of C_m along the P gradient. Consequently, this model, which is based on hydrogen like atoms, was adjusted to our Si/SiGe heterostructure system and the theoretical capacitive coupling formula (see equation 2.23) suggested by Ihn [35] was finally modified.

Expression for the dielectric constant: In a polarization model of Castellan and Seitz [111] developed for neutral dopants in bulk silicon, the local electric field E_L which differs in the vicinity of the impurity atoms from the macroscopic field E, is given by

$$E_L = E + \frac{N\alpha}{3\kappa_0} E_L \tag{5.4}$$

Here, N is the density of the impurity atoms (donors or acceptors), α is the polarizability of the impurity atom and κ_0 is the dielectric constant of the host material. Based on equation 5.4, the local electric field can be rewritten as

$$E_L = \frac{E}{1 - \frac{N\alpha}{3\kappa_0}} \tag{5.5}$$

However, according to Dhar et al. [114] the expression in 5.5 underestimates the actual situation because the polarization of the impurity atoms will change the polarization of the host atoms and vice versa. If the polarization of the host atoms is included, we obtain in analogy with equation 5.4

$$E_L = \frac{E}{1 - \frac{N_0\alpha_0}{3} - \frac{N\alpha}{3\kappa_0}} \tag{5.6}$$

with N_0 being the density of the host atoms and α_0 indicating the atomic polarizability of the host atoms. The total polarization P_T of the lattice in presence of the impurities is then defined as the sum of the polarizations arising from both the impurity atoms and the host atoms

$$P_T = (N_0\alpha_0 + N\alpha)\epsilon_0 E_L \tag{5.7}$$

Substituting the value of E_L from equation 5.6 into 5.7 yields

$$P_T = \frac{(N_0\alpha_0 + N\alpha)\epsilon_0}{1 - \frac{N_0\alpha_0}{3} - \frac{N\alpha}{3\kappa_0}} E \tag{5.8}$$

Because of $P_T = (\kappa - 1)\epsilon_0 E$, equation 5.8 results in

$$\kappa(N) = 1 + \frac{N_0\alpha_0 + N\alpha}{1 - \frac{N_0\alpha_0}{3} - \frac{N\alpha}{3\kappa_0}} \tag{5.9}$$

With the help of the Clausius-Mossotti relation, equation 5.9 can be rewritten as

$$\kappa(N) = \kappa_0 + \frac{N\alpha(\kappa_0 + 2)(4\kappa_0 - 1)}{9\kappa_0 - N\alpha(\kappa_0 + 2)} \tag{5.10}$$

This final equation for the dielectric constant takes into account both the effect of impurity polarization on the host atoms and the polarization of the host itself.

Model for polarizability: The polarizability of hydrogen-like atoms in semiconductors depends strongly on the bonding of the electron to the atom. One can treat a shallow impurity in a covalent bond as hydrogen-like atom [117]. Based on this idea, we are then able to derive a model for the polarizability. The electron of the impurity is assumed to be harmonically bound to the atom and the electron with charge e is bound by the action of the restoring force

$$F = -m\omega^2 r \tag{5.11}$$

in which m is the electron mass and $\omega = v/r$ is the angular velocity. If an external electric field E_a is applied to the system, the electron is displaced from its equilibrium position to a new position $r + \Delta r$. In this case the net force is:

$$F - eE_a = -m\omega^2(r + \Delta r) \tag{5.12}$$

A combination of equations 5.11 and 5.12 yields:

$$eE_a = m\omega^2 \Delta r \tag{5.13}$$

The induced dipole moment is $\mu = e\Delta r$ and since the polarizability is given by $\mu = \alpha\epsilon_0 E_a$ we find for the polarizability:

$$\alpha = \frac{e^2}{\epsilon_0 m\omega^2} \tag{5.14}$$

Furthermore, the ionization energy of a hydrogen-like impurity can be written as:

$$E_d = \frac{mr^2\omega^2}{2} \tag{5.15}$$

Additionally, Castellan and Seitz [111] have shown that the ionization energy depends on the impurity density according to

$$E_d = E_{d0} - kN^{1/3} \tag{5.16}$$

in which E_{d0} and k are constants. Combining equations 5.14-5.16 we get

$$\alpha = \frac{A}{1 - BN^{1/3}} \tag{5.17}$$

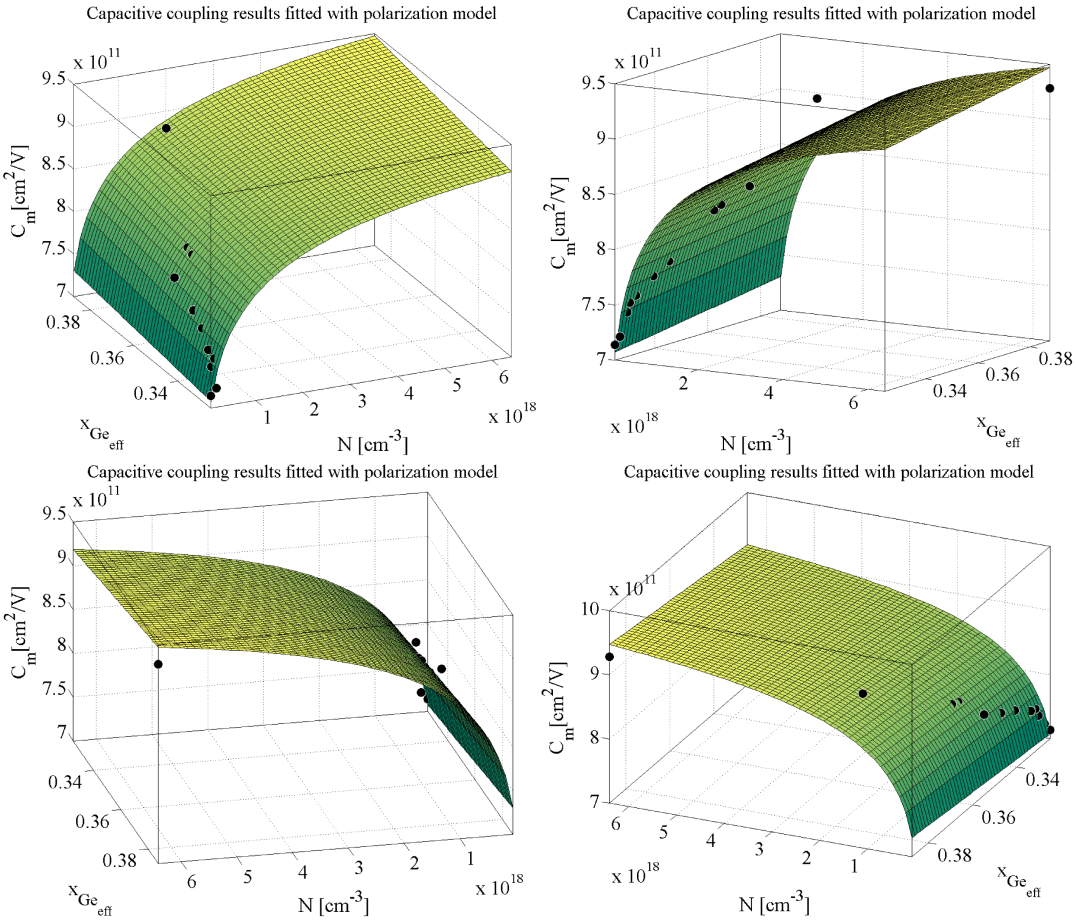

Figure 5.7: *Overview of a 2D fit to our experimentally measured capacitive couplings C_m in all Schottky-gated two-dimensional electron systems, which contained a relevant amount of neutral impurities, in dependence of the effective Ge content ($x_{Ge_{eff}}$) and the magnitude of neutral P doping atoms (N) at four different positions clockwise rotated. Indeed, the fit led to reliable results for fitting parameters $A = 2,03 \cdot 10^{-12} cm^3$ and $B = 5,24 \cdot 10^{-7} cm$ as well as the dielectric constants of $\epsilon_{Si} = 9,4$ and $\epsilon_{Ge} = 12,7$. Based on these realistic findings, we conclude that the polarization model is applicable to our Si/SiGe 2DES.*

where $A = r^2 e^2 / 2\epsilon_0 E_{d0}$ and $B = k/E_{d0}$ are constants which depend on the type of impurity and on the host material. Constant A moreover gives the polarizability for infinite dilution.

Application to our Si/SiGe heterostrucures: Considering the capacitive coupling (C_{th}) formula in equation 2.23, suggested by Ihn et al. [35], for our heterostructure layout, it gets obvious that this equation has to be modified since the SiGe:P modulation doping layer was not separately taken into account. However, based on a possible polarizability of neutral P atoms, this circumstance has to be included. In order to predict the capacitive coupling as a function of the degree

of neutral P atoms, formula 2.23 is modified to

$$C_{th} = \frac{\partial n_{2DES}}{\partial U_{HB}} = \frac{\epsilon_0}{e}\left(\frac{d_{Si}}{\epsilon_{Si}} + \frac{d_{SiGe}}{\epsilon_{SiGe}} + \frac{d_{SiGe:P}}{\epsilon_{SiGe:P}} + \frac{\epsilon_0}{e^2}\frac{\partial E_F(n)}{\partial n}\frac{\epsilon_0}{e^2}\frac{\partial E_0(n)}{\partial n}\right)^{-1} \quad (5.18)$$

where the d_i are the thicknesses of the Si, the SiGe and the SiGe:P layers between the top-gate and the 2DES. The ϵ_i are the dielectric constants of Si, SiGe and SiGe:P. Since the contributions of the fourth and fifth term, which indicate the density of states in the 2DES and the quantum capacitance, are very small ($\approx 2\%$) these quantities are neglected in the following so that equation 5.18 reduces to

$$C_{th} = \frac{\partial n_{2DES}}{\partial U_{HB}} = \frac{\epsilon_0}{e}\left(\frac{d_{Si}}{\epsilon_{Si}} + \frac{d_{SiGe}}{\epsilon_{SiGe}} + \frac{d_{SiGe:P}}{\epsilon_{SiGe:P}}\right)^{-1}. \quad (5.19)$$

If we now consider the dependence of the dielectric constant $\epsilon_{SiGe:P}$ on neutral impurities (P atoms) based on equation 5.10 we get:

$$\epsilon_{SiGe:P}(N) = \epsilon_{SiGe} + \frac{N\alpha(\epsilon_{SiGe}+2)(4\epsilon_{SiGe}-1)}{9\epsilon_{SiGe} - N\alpha(\epsilon_{SiGe}+2)} \quad (5.20)$$

Here, we replaced κ_0 by ϵ_{SiGe} and the P dependent dielectric constant $\kappa(N)$ by $\epsilon_{SiGe:P}(N)$. Moreover, for the polarizability we take equation 5.17 and for the Ge content dependent SiGe dielectric constant we use in a first approach

$$\epsilon_{SiGe} = (1-x)\epsilon_{Si} + x\epsilon_{Ge} \quad (5.21)$$

Fitting procedure: First of all, the fraction of P atoms with energies lower than E_F, i.e. the neutral donors, is extracted from the nextnano simulation-based fitting described in figure 5.6a. Then, combining equations 5.19, 5.20, 5.21 and 5.17 we can fit our experimentally obtained capacitive couplings C_m as a function of the density of neutral P atoms (N) and the effective Ge content ($x_{Ge_{eff}}$). The experimental results were plotted in 2D with the fit parameters A, B, ϵ_{Si} and ϵ_{Ge}. Figure 5.7 shows the fitting result for all Schottky-gated samples taken from different wafers fabricated during the new growth series which contain a relevant amount of neutral impurities. We obtain a goodness of fit of $R^2 = 0,94$ when considering a P segregation of up to $5nm$ which seems to be reasonable compared to experimental observations [20]. The fit yields the following fitting parameter values: $A = 2,03 \cdot 10^{-12} cm^3$, $B = 5,24 \cdot 10^{-7} cm$, $\epsilon_{Si} = 9,4$ and $\epsilon_{Ge} = 12,7$. These dielectric constants are about 20% lower than the literature values ($\epsilon_{Si} = 11,7$ and $\epsilon_{Ge} = 16,2$) according to [118, 119]. Fitting parameter A differs from the fitting parameter obtained by Dhar et. al [114], who investigated P donors in heavily doped Si, while we studied $Si_{0.65}Ge_{0.35}$. In contrast to that, fitting parameter B matches nicely to the value obtained by Dhar and coworkers.

Conclusion: Based on our experimental findings, we cannot completely exclude that the dielectric constants in MBE grown materials ($\epsilon_{Si} = 9,4$, $\epsilon_{Ge} = 12,7$) are

lower than the theoretical predictions or the ones for slowly pulled pure crystals. Although parameter A and B are strongly material dependent, we infer that using experimental input parameters our polarization model illustrates a plausible mechanism for the experimentally observed P doping dependence of the capacitive coupling $C_m = \frac{\partial n}{\partial U_G}$. However, we have to mention that four fitting parameters are quite a lot parameters and that the fit is not perfect. In order to regard this model as definitely the applicability has to be furthermore checked. In this context, especially independent measurements of MBE grown Si, Ge and SiGe might be helpful to gather separate informations on ϵ_{Si}, ϵ_{Ge} and ϵ_{SiGe}. Nevertheless, the experimental observation of the strong influence of the P volume doping concentration on the capacitive coupling is fact. An alternative model has to be capable of explaining this influence. However, we could not identify an alternative model. Therefore, we conclude that if our polarization model is valid, it points to the enormous influence of P doping selection not only for the 2DES density but also for the capacitive coupling in field-effect devices.

5.3 Variety in n versus U_G curves at $T = 1,4K$

In parallel to the systematic investigation of the capacitive coupling C_m between Schottky top-gate and 2DES, we identified a variety in the experimentally recorded n versus U_G curves. Interestingly, the maximal end gate voltage was restricted to a value of $U_G \approx 0,55V$, whereas the pinch-off voltage varied markedly. Figure 5.8 exemplarily presents an overview of the n versus U_G curves for several samples along the phosphorous climb gradient in wafer R2030. This overview shows three special cases which depend on the maximally controllable gate interval and the phosphorous (P) doping degree.

Linear regime: In the first case for a low gate controllable interval of $U < 0,5V$, we only observed the linear regime without any hysteresis, see sample R2030A4 in figure 5.8. In fact, the slope of the linear regime is determined by the P doping degree. The higher the P concentration the steeper is the linear regime. In order to check out the influence of the low gate interval on the $n(U_G)$ curve, an additional test sample was covered with an Al_2O_3 gate insulator prior to the deposition of the Pd Schottky top-gate. Indeed, in this sample the gate controllable interval was distinctly enlarged and therefore a full hysteresis loop could be detected.

Complete hysteresis loop: The second case was already identified by Wild et al. [13] who suggested charge reconfigurations to be responsible for this hysteresis type, see section 2.5.2. The shape of the characteristic hysteresis curve, especially the saturation regime, depends very strongly on the maximal gate controllable interval which reaches from $0,5V - 0,75V$. Possible examples for this hysteresis type are given in the curves of sample R2030B4 and B6 shown in figure 5.8. Despite these observations, we for the first time obtained an indication for a transition to

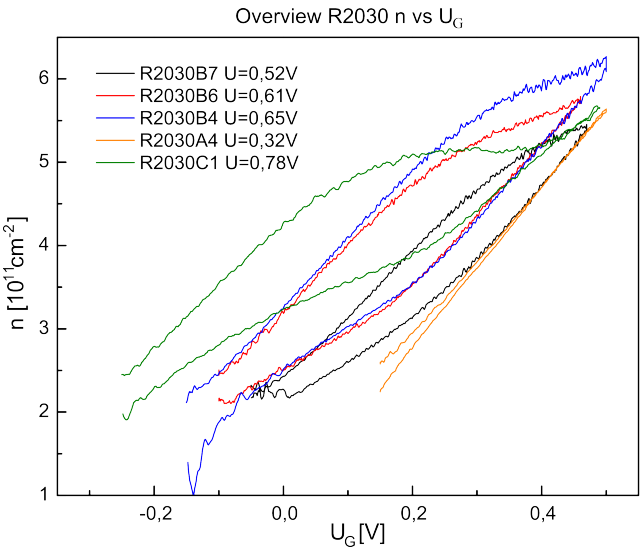

Figure 5.8: *Overview of the $n(U_G)$ gate sweep results of several samples arranged along the P gradient of wafer R2030 at $T = 1,4K$. For low gate intervals $U < 0,5V$, we only get a linear hysteresis-free regime. In an intermediate gate interval, we obtained a full hysteresis curve which was already identified in the special case considered by Wild [13], whereas for high gate intervals $U > 0,75V$ we found a second hysteresis-free linear regime.*

a flatter slope for large negative gate voltages in some samples, see low voltage region of sample R2030B4 in figure 5.8 which is maybe a sign for an increasing ionization of P atoms or a lower polarizability. However, this change of slope is certainly very difficult to detect since the current along the Hall-bar is very low in this voltage regime and we are just before pinch-off.

Complete hysteresis loop with second linear regime: For very large gate controllable intervals with $U > 0,75V$, we observed for the first time a second hysteresis free linear regime which started after a short decrease in the saturation regime, see sample R2030C1 in figure 5.8. Interestingly, this second linear increase was also observed in modulation doped Ge/SiGe hole gases (2DHGs) and GaAs/AlGaAs 2DEGs [96, 120]. Based on these findings, we suppose that this phenomenon is caused by the modulation doping layer and is independent of the underlying material system. In this context, Donner et al. tested an inverted doped layer in their heterostructures in order to check a possible influence of the modulation doping layer on the hysteresis effects. Inverted doped means that the doping layer is ordered below the QW and not between the Schottky top-gate and the 2DES. Consequently, the doping layer is no longer influenced by the gate induced electric field. As a result, this attempt finally led to an overall linear regime without any hysteresis and polarisation effects [96]. Indeed, this observation is another hint for the distinct influence of the modulation doping on the field effect controllability of two-dimensional electron systems.

Conclusion: In this section, we discovered three different types of n versus U_G curves which strongly depend on the maximally gate controllable region and the P volume doping in the modulation doping layer. In this context, the maximal tunable gate voltage was determined to $U_G \approx 0,55V$, whereas the pinch-off point distinctly varied. This phenomenon is probably caused by the lithography process and is therefore not precisely controllable. We suppose a possible influence of surface states which might be responsible for this inhomogeneity and the observed shift of the n versus U_G curves along the U_G axis. In the scope of our analysis, we moreover found a first indication for a transition to a flatter slope for large negative gate voltages at the end of the linear regime. This change of slope points to a possible influence of a polarisation of the P states. Additionally, we for the first time detected a second hysteresis free linear regime for large gate controllable regions which appeared after a slight decrease in the saturation plateau. This observation as well as the appearance of a complete hysteresis loop were also obtained in other modulation doped material systems and were shown to disappear when employing an inverted doped layer instead [96]. However the adjustment of an inverted doped layer in the SiGe material system is difficult because of a strong dopant segregation, as already shown in section 4.2, which leads to an incorporation of dopants in the QW and thus drastically reduces the mobilities.

5.4 Expansion of the charge transfer model

In the past sections, we already revealed a number of insights regarding the field effect influence on two-dimensional electron systems which could not be explained within the charge transfer model proposed by Wild et al. [13]. The fact that charge reconfigurations are also possible within the linear regime, the observation of the long charge transfer times, the correlation of the P doping degree and the capacitive coupling C_m between Schottky top-gate and the 2DES as well as the appearance of a second linear regime after the saturation plateau in large gate controllable samples ($U > 0,75V$) lead us to the conclusion that the current model is insufficient and has to be extended. In the following, we therefore modify the charge transfer model. We illustrate the model by representatively considering the experimental behaviour of sample R2030C1. This sample showed a comparatively high P doping degree and in turn a comparatively large fraction of neutral P atoms as well as a long gate controllable interval. The corresponding 2DES density (n) versus gate voltage (U_G) curve is shown in figure 5.9a.

Figures 5.10a-f illustrate the appropriate band structure simulations for the special configurations of $n(U_G)$ which are labelled by Arabic numerals in figure 5.9a and figures 5.10a-f. The band structure profile in figure 5.10a displays the starting point of our measurements, compare with section ① in figure 5.9a. As a consequence of the high P doping concentration ("P overdoping"), the conduction

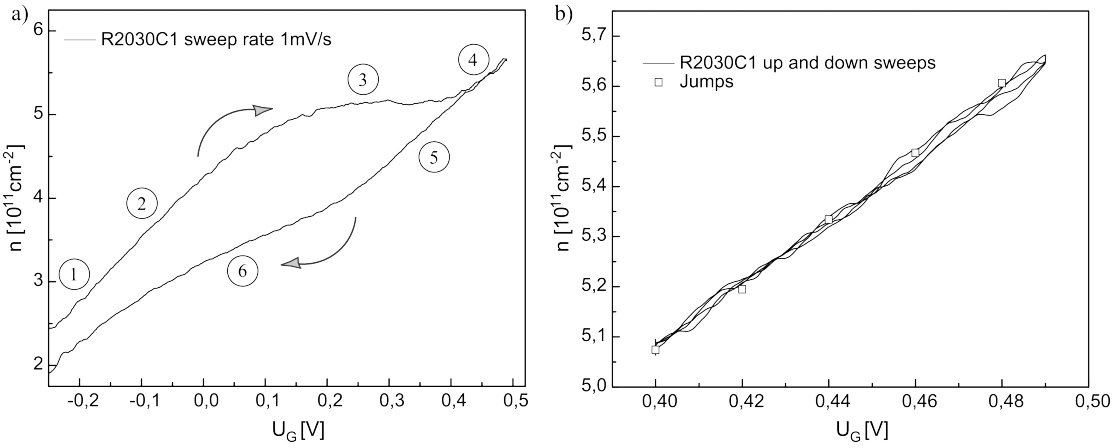

Figure 5.9: *a) $n(U_G)$ curve of sample R2030C1 for a sweep rate of 1mV/s. The black arrows indicate the sweep direction and the numbers mark different configurations of U and n for which the corresponding band structure is shown in figure 5.10a-f. b) Zoom into the second linear regime. Several sweeps back and force were performed in order to check the linearity. Moreover, gate jump measurements were conducted to exclude any hysteresis.*

band minimum E_{CB} is markedly lowered so that a situation is reached where the P states get equal to the Fermi energy ($E_F = E_P$) even without an applied gate voltage. As a result, a part of the phosphorous atoms stays neutral. This observation is reinforced by the gate jump measurement results in section 5.1 from which we can infer that the sweep duration from the reset point to the start voltage value is long enough to achieve a sufficiently high degree of neutral P atoms. Figure 5.10b illustrates the situation if we then apply a gate voltage. Consequently, the conduction band minimum is energetically lowered so that a charge transfer process from the 2DES into the P modulation doping layer sets in. However, the charge transfer rate is low because most of the energetically favourable P energy levels are already occupied. Comparing the band structure simulations in 5.10b with section ② in the n versus U_G sweep curve in figure 5.9a provides evidence that charge reconfigurations take place within the linear regime. Moreover, we see that applying a gate voltage not only leads to a neutralization of the P atoms but also entails a steep linear increase of the charge carrier density since the measured capacitive coupling C_m rises due to a simultaneously growing dielectric constant $\epsilon_{SiGe:P}$ according to equation 5.19. In this context, we showed in section 5.1 that in the linear regime the charge transfer rate is distinctly slower than the gate sweep rate so that the n versus U_G curve behaves still linearly although charge transfer processes are possible. Further increasing the gate voltage leads to an increasing and faster charge transfer process into the P doping layer. Consequently, the slope starts to get shallower and diverges from the linear regime. Finally, the band structure is lowered to a point, as shown in figure 5.10c, where the conduction band minimum in the doping layer approaches the Fermi level ($E_F = E_{CB}$).

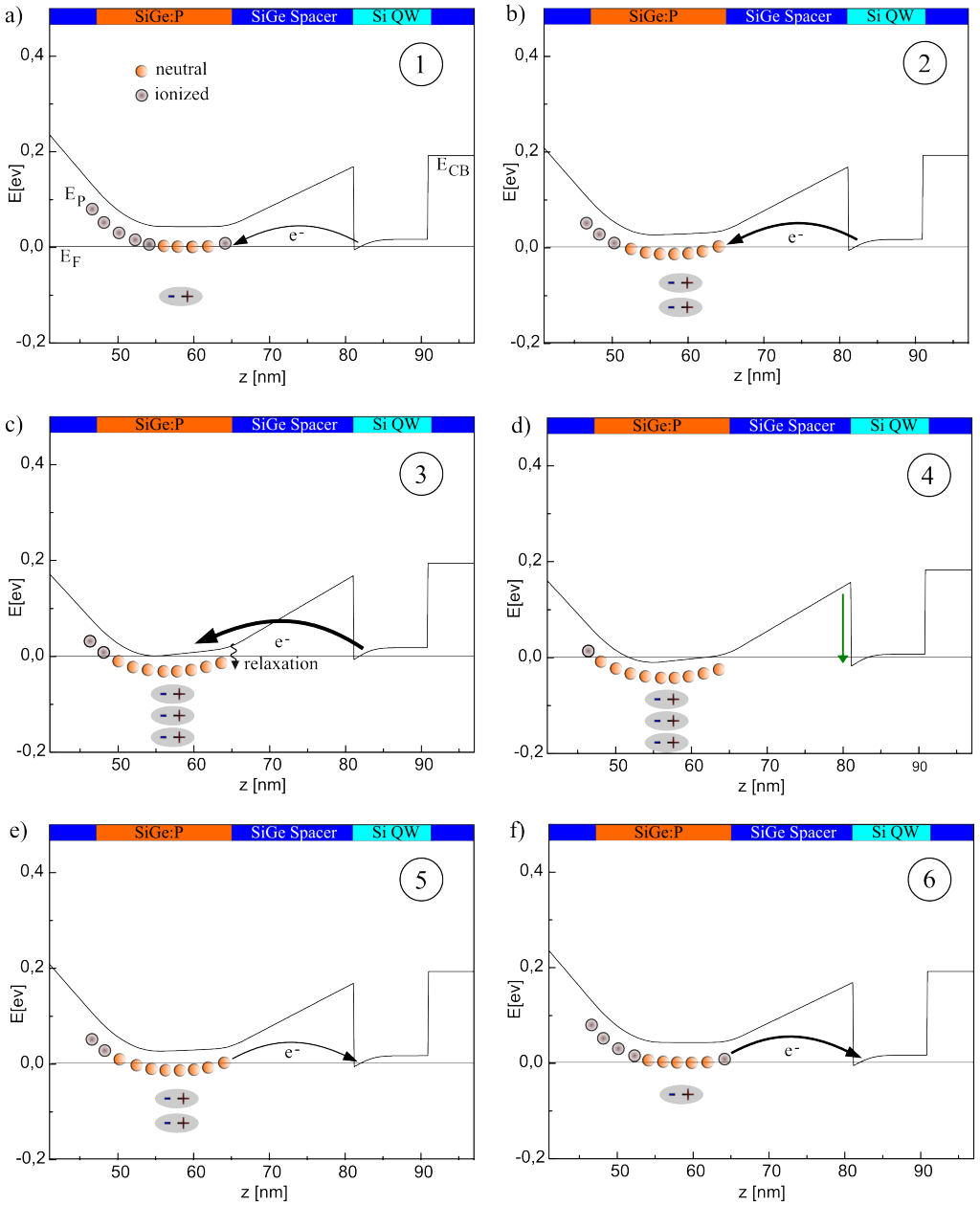

Figure 5.10: *a-f) The image illustrates the conduction band E_{CB} and the phosphorous donor energy $E_P = E_{CB} - 45meV$ in the spatial domain of the doping layer to the QW. The numbers in the upper right associate the diagrams with the configuration $n(U)$ in figure 5.9a. Moreover, E_F denotes the Fermi energy, whereas the strength of the polarization is indicated by a grey plus-minus symbol. Additionally, the neutral P atoms are indicated by circles filled in orange, whereas the ionized P atoms are illustrated by circles filled in brown. Furthermore, the charge transfer processes as well as the relaxation from the conduction band into P states are displayed by black arrows.*

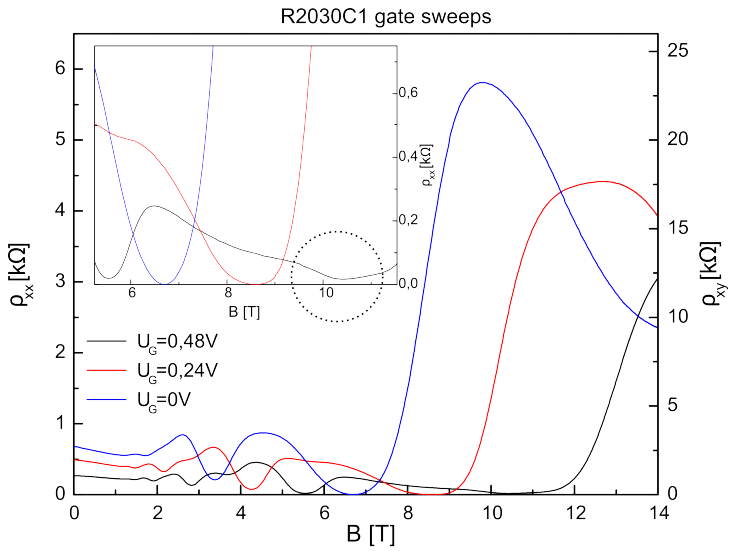

Figure 5.11: *Image of the Hall resistances in sample R2030C1 and the corresponding Shubnikov-de-Haas (SdH) oscillations in dependence of the applied magnetic field B for 3 applied gate voltages. The inset shows a zoom into the minima of the SdH's for filling factor $\nu = 2$ which at first glance seem to go to zero. However, by close inspection we see that for a gate voltage of $U_G = 0,48V$, which corresponds to a voltage value in the second linear regime, the minimum does not exactly reach 0Ω. Consequently, we cannot exclude a parallel conducting channel.*

Consequently, charge reconfigurations are also possible into the conduction band minimum in the doping layer before a fast relaxation process into lower lying localized phosphorous states takes place. This charge transfer process is now as strong as the subsequently delivered electrons from the ohmic contacts so that the density in the 2DES stays constant and a plateau develops, see section ③ of figure 5.9a. This circumstance can be again verified by the gate jump measurement results in section 5.1 which showed that, for higher end gate voltages, the charge transfer rate gets faster than the gate sweep rate resulting in a shallower slope in the n versus U_G curve. If the gate voltage is then swept beyond a second threshold voltage, almost every P atom is neutralized and the conduction band minimum is slightly pulled under the Fermi level which results in a parallel conducting channel, as displayed in the band structure profile in figure 5.10d. Comparing the band structure simulation with section ④ in the n versus U_G gate sweep curve of figure 5.9a, we observe a second linear regime. The linearity of the second linear regime was then checked by sweeping the gate voltage back and force in this interval for several times. Additionally, we once again performed time resolved jump measurements, as introduced in section 5.1, to review a possible hysteresis. As a result, the jump charge carrier density values, which were reached 10 minutes after the jumps were conducted, exactly lie on the back and force sweeped n versus U_G curve. The results are shown in figure 5.9b and

clearly give evidence for a linear and hysteresis-free increase in the charge carrier density. In order to verify a parallel conducting channel we then performed magnetotransport measurements for three gate voltages at different positions within the hysteresis curve. As a result, we obtained well developed Hall plateaus in the transversal and pronounced Shubnikov-de-Haas oscillations in the longitudinal resistances respectively, see figure 5.11. The SdH oscillations at filling factor $\nu = 2$ for gate voltages of $0V$ and $0,24V$ nicely reached zero Ohm. However, in contrary the SdHs at filling factor $\nu = 2$ and an applied gate voltage of $0,48V$, which corresponds to a voltage value inside the second linear regime, do not exactly go to zero, see inset in figure 5.11. This observation points to a parallel conducting channel which we also expect from the corresponding band structure simulations conducted with experimentally determined parameters[121, 122, 123].

If we finally sweep the gate voltage back to the initial value, n first decreases linearly, see section ⑤ in figure 5.9a. The observation of a hysteresis is interpreted to be caused by an asymmetry in the charge transfer rate, as suggested by Wild et al. [13] since a depletion of the still occupied P atoms is energetically unlikely until the neutral P atoms are lifted above the Fermi energy, as indicated in figure 5.10e. From this follows that if a lower threshold voltage is achieved the doping layer gets faster depopulated and thus the slope of the decreasing curve becomes shallower as shown in section ⑥ of figure 5.9a because now more and more P atoms are ionized and the polarizability is markedly reduced, see figure 5.10f.

5.5 Temperature influence on n versus U_G curves

We have also studied the temperature influence on charge reconfiguration and polarization effects. The n versus U_G curves were recorded in the maximal gate voltage interval which was previously determined in the leakage current and pinch-off measurements for different temperatures, presented in section 3.6.3. Figure 5.12 exemplarily shows the temperature dependent gate sweeps in sample R1870E. Starting with a gate sweep at $T = 1,4K$, we observe a "normal" full hysteresis loop where the saturation plateau is reached for the maximal gate voltage. For a temperature of $T = 6,0K$ the saturation plateau falls down for higher gate voltages, whereas for $T = 12,0K$ the maximum in n appeared earlier and is followed by a distinct charge carrier density drop above a threshold voltage before the density finally starts to increase again with further increased gate voltage. Interestingly, we figured out that with increasing T this density drop shifted to lower threshold voltage values. Additionally, the hysteresis became smaller and the up and down sweep coincided after the drop. If the temperature was increased to $T = 55K$, we observed an overall identical trace for the up and down sweep. this special behaviour was found in almost all investigated samples during this thesis.

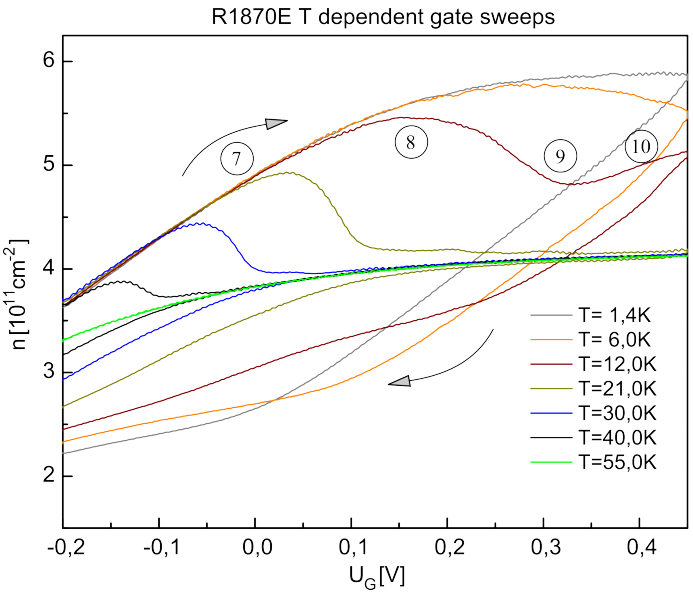

Figure 5.12: *Overview of the $n(U)$ curves in the temperature range from $1,4K$ up to $55K$ for sample R1870E. The up and down sweep direction is indicated by two black arrows. Indeed, the saturation regime is faster reached with increasing temperature. Interestingly, for higher T the charge carrier density drops when the gate voltage is swept above a temperature dependent threshold value. Beyond this special voltage, up and down sweep lie on top of each other. An exact explanation of this special behaviour during the temperature dependent n versus U_G sweep is given in figure 5.13.*

However, the threshold voltages, the onset of the density drop, the maximal gate controllable interval and the measurable temperature range markedly differed.

Figure 5.13a-d illustrates the role of the temperature in the framework of the charge transfer model described in the previous section and summarized in figure 5.10a-f. Figure 5.13a shows the band structure profile if we apply a gate voltage to the Schottky top-gate. Due to the "P overdoping" the conduction band minimum (E_{CB}) is already lowered to a point, where the Fermi energy is equal to the energy level of the P states ($E_F = E_P$). As a result, charge transfer processes from the 2DES into the P modulation doping layer set in. However, the charge transfer rate into the P states rises quickly with increasing T according to the noticeable influence of the thermal energy $E_{th} = k_B T$. This influence additionally allows the occupation of energetically higher lying states which finally leads to an earlier divergence from the linear regime and therefore to a shallower slope in the n versus U_G curve, see section (7) in figure 5.12. If the gate voltage is increased, the conduction band minimum more and more approaches the Fermi level, see figure 5.13b. Although, $E_F = E_{CB}$ is not reached yet, the thermal influence facilitates tunnelling events into the conduction band minimum followed by a fast relaxation process into lower lying P states. Consequently, the maximal saturation plateau

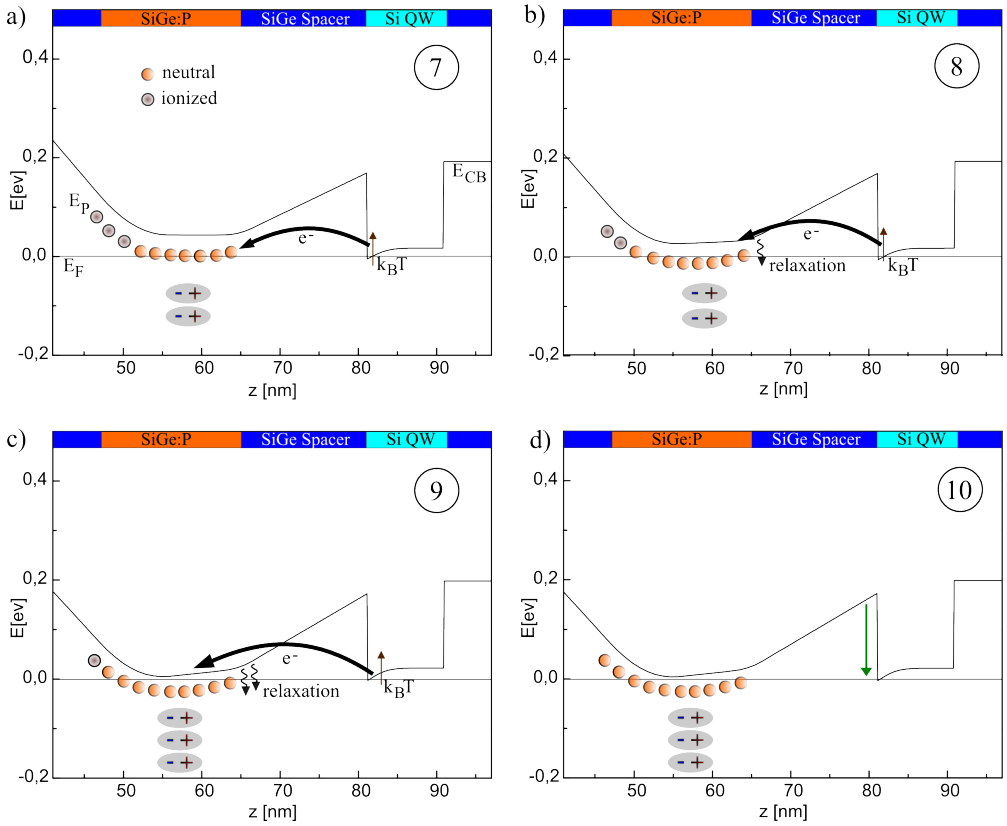

Figure 5.13: *a-d) Band structure overview including the thermionic influence k_BT at several positions during an $n(U)$ gate sweep curve. The conduction band energy is given by E_{CB}, whereas the phosphorous donor energy is E_P. The Arabic numerals in the upper right associate the diagrams with the configuration $n(U)$ in figure 5.12. Additionally, the charge transfer processes as well as the relaxation events are displayed by black arrows, whereas the brown arrow illustrates the thermionic influence. The neutral P atoms are indicated by circles filled in orange and the ionized P atoms are represented by circles filled in brown.*

in the $n(U)$ curve moves to lower gate voltages with increasing T, compare with section ⑧ in figure 5.12. Further increasing the gate voltage leads to a situation sketched in figure 5.13c, where the T assisted charge transfer rate into the P states seems to get temporary higher than the quantity of the delivered electrons from the ohmic contacts so that the charge carrier density drops crucially during this dynamical process, see section ⑨ in figure 5.12. In the end, nearly all P atoms are neutralized so that beyond a sufficient high gate voltage the carrier density in the 2DES is slightly increased. This circumstance can be understood by comparing figure 5.13d with section ⑩ in figure 5.12. If the gate voltage is finally lowered again, the asymmetry in the tunnelling events becomes obvious since charge transfer processes would still be possible but are rather unlikely regarding the persistently occupied P states, see figure 5.13d. As a result, the up and down

sweep more and more approach each other for increasing T, as shown in figure 5.12. Indeed, in case of high enough T the charge transfer processes are too fast and cannot be recorded within this set-up. Consequently, up and down sweep lie on the same trace during the whole gate sweep sequence, e.g. for $T = 55K$ in figure 5.12.

5.6 Conclusion

In this chapter, we explicitly studied the field effect control of 2DES in the Si/SiGe material system. For this purpose, we performed magnetotransport measurements in gated Hall-bar devices at cryogenic temperatures, where we mainly used the charge carrier density n as a sensing observable to investigate the electronic environment in our heterostructures.

In our analysis, we discovered for the first time a strong connection of the P doping concentration and the measured capacitive coupling C_m between Schottky top-gate and 2DES along the P doping gradient which was determined in section 4.2.2. However, this experimental observation could not be explained, neither with the charge reconfiguration model proposed by Wild et al. [13], nor with the theoretical predicted capacitive coupling formula of Ihn [35]. In order to solve this open question we extended the charge transfer model. First of all, we revealed that the high P doping leads to a lowering of the conduction band minimum so that charge reconfigurations are already possible within the linear regime of the 2DES density n as a function of the gate voltage U_G. In this context, time resolved gate jump experiments were performed which provided evidence that within the linear regime of n versus U_G, the charge transfer rate is slower than the gate sweep rate so that the slope in the n versus U_G curve still behaves linearly. In a next step, we introduced a polarizability of neutral P atoms in the modulation doping layer which explains the experimentally obtained increasing C_m for an increasing P doping degree since the dielectric constant in the modulation doping layer $\epsilon_{SiGe:P}$ directly increases with a rising degree of neutral P atoms (N). Finally, we checked the validity of this modified model in our Si/SiGe heterostructures with numerical band structure simulations which were based on experimental input parameters.

Based on these insights, we then developed a quantitative method to fit the measured capacitive couplings (C_m) as a function of the effective Ge content $x_{Ge_{eff}}$ and the degree of neutral impurities N in the modulation doping layer. The resulting fit parameters were reliable and allowed us to evaluate the dielectric constants of MBE grown Si and Ge. Actually, the extracted dielectric constants ($\epsilon_{Si} = 9,4$ and $\epsilon_{Ge} = 12,7$) were about 20% smaller than the literature values which is a realistic result with respect to the simplifications of the model. In addition to that, our modified charge transfer model was still suitable to describe the observed hysteresis and disorder effects even for increased temperatures. In fact, the temperature

assisted behaviour of charge reconfigurations manifested itself by an earlier onset of the saturation plateau followed by a density drop and a subsequent hysteresis-free increase of the density. However, in order to regard this model as definitely the applicability has to be checked further.

To summarize, the field-effect study of 2DES in Schottky-gated Si/SiGe heterostructures allowed us to develop an extended method with which the behaviour in the electronic environment of the 2DES can be better understood. Additionally, we were able to explain the coherence between the capacitive coupling and the P doping degree and finally make statements about the dielectric constants of MBE grown Si and Ge. Moreover, several efforts have been undertaken to clarify the temperature dependence and time dynamics of the gate induced effects as well as to identify and address device limiting parameters. In order to review further restrictions in our current gated Si/SiGe heterostructures, the next chapter explicitly dwells on leakage currents which especially influence Schottky-gated devices. In this connection, we also focus on the mechanisms behind leakage currents since they provide a facility to learn more about the entire heterostructure.

6 Leakage current analysis

This chapter deals exclusively with the occurrence and the mechanisms behind leakage currents in Si/SiGe 2DES. Historically, Schottky-gated devices have been drastically restricted by the onset of enormous gate leakage currents for even small gate voltages [124, 125, 51]. A possible reason for these early gating problems was ascribed to an "over-doping" of the modulation doping layer [125]. Consequently, these high doping profiles could furthermore lead to a segregation of the P doping in growth direction [20, 126] and therefore lower the effective Schottky barrier above the QW which facilitates leakage currents.

Based on a precise temperature dependent investigation of leakage currents in our Si/SiGe 2DES, we try to find out something about the location and the magnitude of trap states, as well as the effective Schottky barrier height. These parameters would give further insights into the exact sample structure and therefore yield vital information to realize future gated high quality 2DES. In a first step we consider and compare temperature dependent leakage currents for different sample structures. Then we show the applicability of different leakage current models based on a triangular barrier, which were already introduced in section 2.5.3, to our gated 2DES. In the following, we perform an exact analysis within two temperature ranges: Firstly from $1,4K$ to $40K$ and secondly from $40K$ to $100K$. Finally, we sum up all findings and give a short outlook.

6.1 Temperature dependent leakage currents

In this section, we present the first leakage current results for four different samples in a variable temperature range. An overview of the complete layer structure and their thicknesses, the nominal volume doping degree as well as the underlying virtual substrates (VSs) of each sample is given in table 6.1. The measurements were performed with the standard set-up which was introduced in section 3.6.3. Starting with a temperature of $T = 1,4K$ and an applied gate voltage of $0V$ after the cool down, the gate was firstly swept in negative voltage direction (reverse bias) to gather the lower limit of the leakage free region. Secondly, the gate voltage was increased until the breakthrough in positive voltage direction (forward bias) appeared. This sweep delivers the upper boundary in which we are able to manipulate our heterostructures without any leakage currents. In a next step,

sample	spacer	modulation doping	capping	t_{tot}	VS
R2030B6	$15nm$	$15nm\ N_{nom} = 1,1 \cdot 10^{18} cm^{-3}$	$50nm$	$80nm$	LT-Si
R1870E	$15nm$	$15nm\ N_{nom} = 0,9 \cdot 10^{18} cm^{-3}$	$55nm$	$85nm$	gr. buf.
R1931A16	$22nm$	$2nm\ N_{nom} = 7,2 \cdot 10^{18} cm^{-3}$	$58nm$	$79nm$	LT-Si
R2043A16	$25nm$	$15nm\ N_{nom} = 0,9 \cdot 10^{18} cm^{-3}$	$50nm$	$90nm$	LT-Si

Table 6.1: *Overview of the underlying virtual substrate (VS) and the different layer thicknesses as well as the total layer thickness t_{tot} between the Schottky top-gate and the QW in four investigated leakage current samples. Additionally, the nominally wanted volume modulation doping N_{nom} is illustrated.*

the gate voltage was decreased to the reset point U_R (we choose $U_R \approx -1,5V$ in every sample, further information on that is given in section 3.6.3) before the temperature was increased to a higher value. Then the down and up sweeps were repeated again in order to find out the borders in the new temperature regime. This measurement cycle was performed across the maximal possible temperature range in which we can reliably tune our samples. The underlying sweep velocities were varied in a range between $2 - 10\frac{mV}{s}$. Due to the reason that similar leakage current measurements conducted with different sweep rates showed a completely equal behaviour, we mainly chose a sweep rate of $10\frac{mV}{s}$ since this was markedly time saving.

Figures 6.1a and b show an overview of the temperature (T) dependent leakage currents in the samples R2030B6 and R1870E respectively. Both samples, which were completely identical except for the VS the P doping concentration and the capping layer clearly, show almost equal breakthrough voltages at $T = 1,4K$ of about $0,52V$. Increasing the temperature leads to an earlier onset of leakage currents for distinctly lower gate voltages. However, sample R2030B6 showed a stronger temperature dependence than sample R1870E and was therefore only measurable up to $40K$. The reason for that is revealed by a closer look at the breakthrough voltage in reverse bias direction. It is clearly visible that a sensible reset (see section 3.6.3), which is necessary for all gate sweep experiments in order to realize equal starting conditions, is not possible any more for higher temperatures. Interestingly, we observed dips or peaks (indicated by the black open circle in figures 6.1a and b) in the leakage current curves independent of sweep direction, sweep rate and time [98]. Consequently, we suppose that these effects are not caused by noise fluctuations or arise due to measurement artefacts. The position of these unexpected fluctuations moves only slightly to higher voltage values with increasing temperature. Indeed, we were able to bring this effect in line with temperature dependent pinch-off curves (see section 3.6.3) which exhibit the pinch-off point nearly at the same voltage values as the dips/peaks in the leakage current measurements, see figures 6.1c and d. We expect that this correlation can be ascribed to the depopulation/population of the two-dimensional electron system.

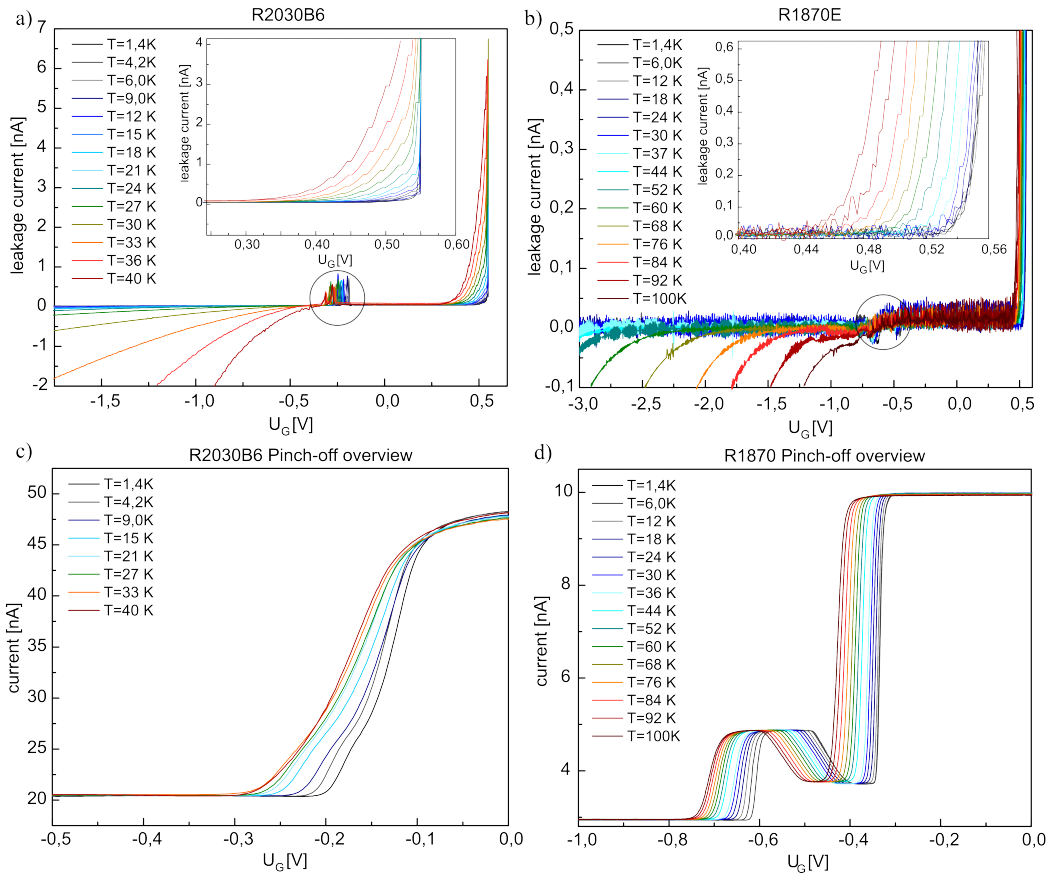

Figure 6.1: *a) Temperature (T) dependent leakage current measurements in the LT-Si based sample R2030B6. The leakage free region is clearly visible and becomes narrower with increasing T. b) Image of the according T dependent leakage currents in the graded buffer based sample R1870E. In comparison to R2030B6 this sample is less sensible to the temperature and therefore measurable until* $100K$*. The peak and dip positions in both samples are indicated by a black open circle. The two insets in figure a) and b) display a zoom into the leakage current curves. c) Results of the T dependent pinch-off measurements in sample R2030B6. It is obvious that the pinch-off point lies around* $-0,25V$ *and thus is consistent with the peaks in sample R2030B6. d) shows the pinch-off results of sample R1870E. We clearly see two minima in sample R1870E around* $-0,4V$ *and* $-0,7V$*, which match nicely to the two dips observed in the leakage current curves. The reason why the pinch-off curves contained two minima and no direct pinch-off point is still an open question.*

Moreover, by close inspection of the experimentally obtained leakage currents, we are able to construct a 3D map concerning the leakage current density [1] in dependence of temperature and the applied gate voltage in forward bias direction.

[1] In order to gather the leakage current density, we took the experimentally obtained leakage current per top-gate area.

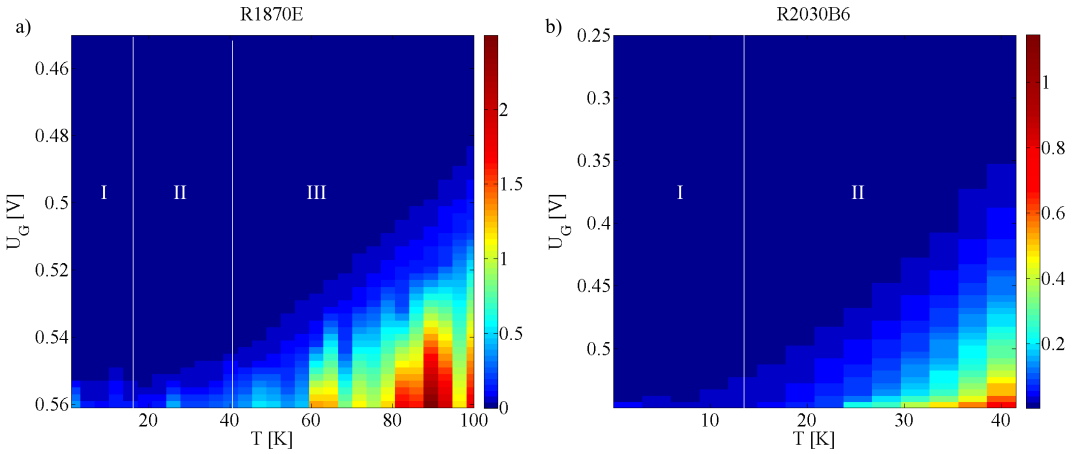

Figure 6.2: *a) 3D leakage current density map of sample R1870E in dependence of T and U_G. The white lines separate different temperature regions indicated by white Roman numbers. b) 3D leakage current density map of sample R2030B6. The strong temperature dependence is clearly visible and the different T dependent regions are again illustrated.*

Due to the fact that the leakage currents were recorded at random voltage values during each gate sweep, we interpolated the experimentally obtained data to a regular voltage scale. Based on these interpolated data, figure 6.2a and b illustrate the 3D maps of samples R2030B6 and R1870E. At first glance, we see that the 3D maps consist of different temperature dependent regions which are indicated by white Roman numbers. Region I, which starts from $1,4K$ and ends up at $15K$, shows only a very slight temperature dependence in both samples. However, region II (reaches from $18K$ to $40K$) exhibits a moderate increasing T dependence in sample R1870E, whereas we observed a stronger T dependence in sample R2030B6. Finally, region III, which was achieved only in sample R1870E and ranges from $40K$ to $100K$, displays also a very strong T dependence. In order to further investigate the influence of the underlying virtual substrates (VS), the total sample thicknesses and the P doping profile, two more samples based on a LT-Si VS (R1931A13 and R2043A16) were measured and compared. Sample R1931A13, which is quasi "$\delta - doped$", exhibits the lowest distance between Schottky top-gate and QW, whereas R2043A16 has the largest thickness due to a bigger spacer layer, see table 6.1. Both samples were examined according to the aforementioned procedure. The results of the temperature dependent leakage currents are shown in figures 6.3a and b. The breakthrough voltage at $T = 1,4K$ in sample R2043A16 occurred around $0,55V$ which is slightly higher than in sample R2030B6 and R1870E. In contrast, sample R1931A13 exhibits the breakthrough point around $0,49V$ at $T = 1,4K$. These circumstances allow the assumption that the position of the breakthrough point is somehow associated with the distance between the Schottky top-gate and the QW as well as the P volume doping degree which can have an influence on the P segregation [20].

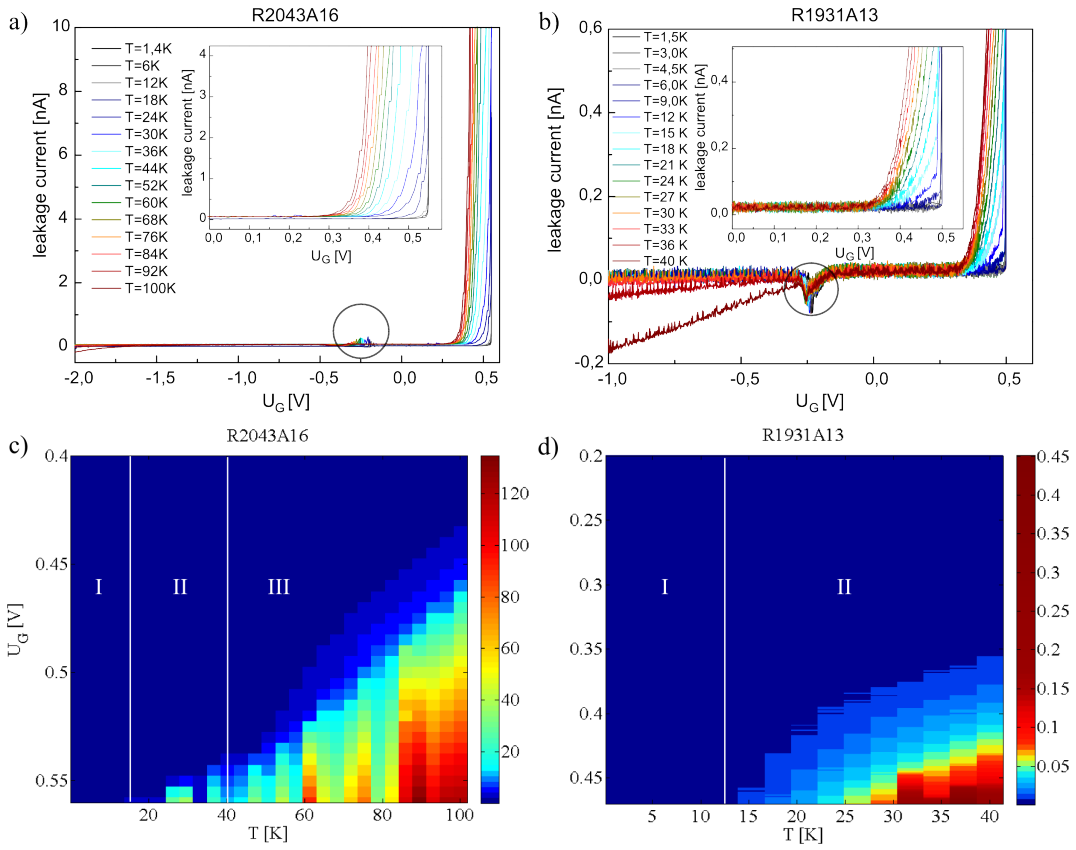

Figure 6.3: *a) Image of the T dependent leakage currents in the thickest sample R2043A16 (spacer layer 25nm). We clearly see the low temperature dependence equally to sample R1870E and therefore observe again three T dependent regions (indicated in white Roman numbers). b) T dependent leakage current results of sample R1931A13. Under close inspection, we attain the same behaviour like in sample R2030B6 which is measurable up to 40K. In fact the leakage free region is again clearly visible and becomes smaller with increasing T. The peak and dip positions in both samples are indicated similarly by black open circles. Furthermore, the two insets in figure a) and b) display a zoom into the leakage current curves. c) 3D leakage current density map of sample R2043A16. d) shows the 3D current density map of sample R1931A13. The T dependence is exactly the same as in sample R2030B6 and is therefore divided into two regions indicated by white Roman numbers. Interestingly, all borders of the T dependent regions have nearly the same temperature value.*

Additionally, we observed the mandatory behaviour that with increasing T the breakthrough point migrates to lower gate voltages in both samples. The strange phenomenon of suddenly appearing peaks and dips in the temperature dependent leakage current curves at a special gate voltage was again detected in each sample. The voltage values where we identified this effect were once more identical to the pinch-off points recorded in the pinch-off measurements. Furthermore, the 3D

leakage current density maps for the new samples are shown in figures 6.3c and d. In fact we were able to determine again temperature dependent regions in figures 6.3c and d which feature exactly the same borders and behaviours like the ones in sample R2030B6 and R1870E (for comparison see figure 6.2). However, sample R1931A13 showed a strong temperature dependence equally to sample R2030B6 and was therefore only measurable up to $40K$. In contrast, sample R2043A16 behaved similarly to sample R1870E, which has a large total distance. Hence, we believe that this is another hint for the influence of the total distance between top-gate and QW on the leakage currents.

6.2 Application of suitable models to our Si/SiGe heterostructures

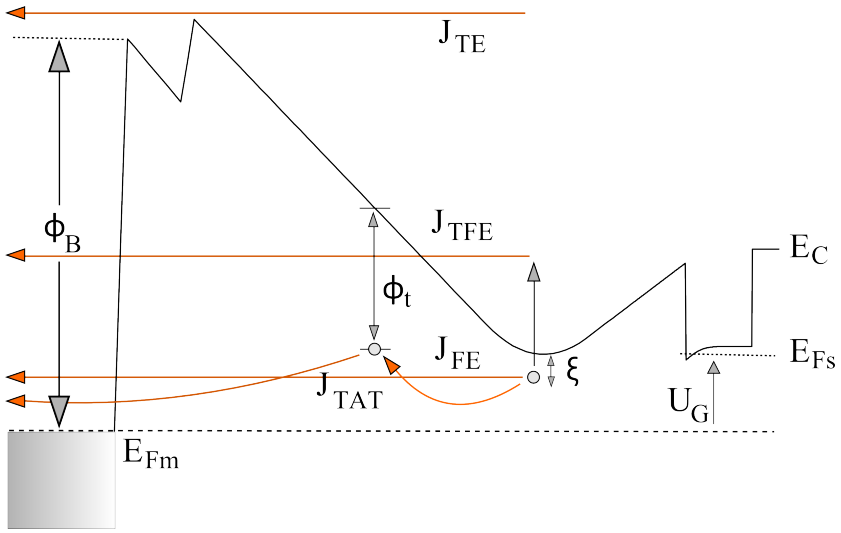

Figure 6.4: *Simulated band structure profile with different incorporated leakage current mechanisms which are applicable to our Si/SiGe heterostructures:* J_{FE} = *field emission,* J_{TFE} = *thermionic field emission,* J_{TE} = *thermionic emission,* J_{TAT} = *trap assisted tunnelling. The phosphorous doping energy level is given by* ξ, U_G *symbolizes the applied gate voltage and* E_C *stands for the conduction band energy. Moreover, another possible trap state with trap energy* Φ_t *is indicated by a second grey dot. If we consider* J_{TAT} *in the phosphorous states, we assume* $\Phi_t = \xi$.

Now we try to bring light into the darkness regarding the mechanisms behind the experimentally obtained leakage currents in Si/SiGe heterostructures. Based on our findings in chapter 5, we learned that above a special threshold top-gate voltage a strong charge carrier transfer process into the P modulation doping layer sets in which persistently occupies the phosphorous states. Therefore, the assumption

that the largest leakage current contribution stems from an electron transfer of the still occupied P states in the modulation doping layer to the top-gate is justified. Beginning with this simplification we are able to apply different leakage current models, which are based on a triangle-shaped barrier (introduced in section 2.5.3), to describe the observed leakage currents in different temperature regimes. Figure 6.4 illustrates a schematical drawing of the band structure profile in our 2DES as well as the according leakage current mechanisms which are applicable to our Si/SiGe heterostructures. In a next step, we will show the applicability of these models to Si/SiGe two dimensional electron systems. In the following, we mainly focus on the results of sample R1870E since all other samples showed a similar behaviour in each of the temperature dependent regimes which were found out in section 6.1.

6.2.1 Temperature ranges from 1.4K to 15K and 18K to 40K

Starting with low temperatures, field emission (FE) and Fowler-Nordheim tunnelling seem to be the ideal candidates to describe leakage currents [69, 70, 76, 83]. However, Fowler-Nordheim tunnelling is only valid in an electric field regime of $F > 10^7 \frac{V}{cm}$ [76, 83]. Since we maximally reached fields up to $\approx 6,5 \cdot 10^5 \frac{V}{cm}$, this mechanism can be excluded. In contrast, field emission is applicable to our experimentally obtained data as long as equation 2.30 is fulfilled. Therefore we get an upper temperature boundary of $\approx 40K$ for this model.

Based on a first approach, the leakage current density in the temperature range from $1,4K$ to $40K$ was fitted in sample R1870E by using formula 2.31 and the Schottky barrier height as the only fitting parameter. Moreover, for the doping concentration the nominally P volume doping degree was assumed, whereas for the trap depth of the P atoms a standard literature value of $\xi = 45meV$ was used [127, 128, 129]. The entire experiments were carried out in the Master thesis of Schafberger [98] and resulted in an average Schottky barrier height of $0,673eV$ and an averaged goodness of fit (R^2) of 0,9337. A precise overview of these results can be found in [98].

However, a closer look at region II ($18K - 40K$) in the 3D leakage current density maps studied in the previous section (see figures 6.2a, b and 6.3c, d) shows a moderate temperature dependence starting at $T \approx 18K$. Although the trap assisted tunnelling (TAT, see equation 2.58) should be temperature independent, it is still possible that a small thermal activation energy is sufficient to reach higher lying P states [2].

[2] due to the band bending, some P states lie energetically higher than others see the band structure profile in figure 6.4

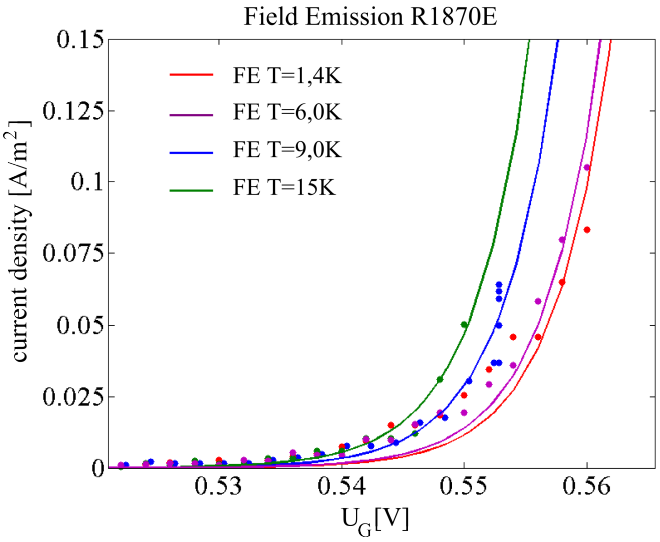

Figure 6.5: *Zoom into a few field emission fitting results of sample R1870E in the temperature range of 1,4K up to 15K. These results showed an average goodness of fit $R^2 = 0,927$. Detailed results for every temperatures are shown in table 6.2.*

T $[K]$	Φ_t $[eV]$	Φ_B $[eV]$	N_P $[cm^{-3}]$	R^2
1,4	0,045	0,690	$9,0 \cdot 10^{17}$	0,892
3,0	0,045	0,693	$9,0 \cdot 10^{17}$	0,913
6,0	0,045	0,697	$9,0 \cdot 10^{17}$	0,892
9,0	0,045	0,694	$9,0 \cdot 10^{17}$	0,909
12	0,045	0,696	$9,0 \cdot 10^{17}$	0,989
15	0,045	0,697	$9,0 \cdot 10^{17}$	0,947
average	0,045	0,695	$9,0 \cdot 10^{17}$	0,927

Table 6.2: *Overview of the temperature dependent field emission results. The trap depth Φ_t and the P doping concentration N_P were fixed whereas the Schottky barrier height Φ_B was used as the only fitting parameter. The goodness of fit R^2 is also illustrated. Moreover, the average results are indicated in green.*

Therefore, we applied a combination of FE which shows a light T dependence and TAT to this region $(18K - 40K)$. In doing so we used the Schottky barrier height Φ_B, the trap depth Φ_t and the trap concentration N_t as fitting parameters, whereas the P doping concentration N_P was fixed and $\Phi_t = \xi$ was assumed.

Beginning with region I, which starts from $1,4K$ and ends up at $15K$, the leakage current density was solely fitted by the field emission model as already presented in the thesis of Schafberger [98].

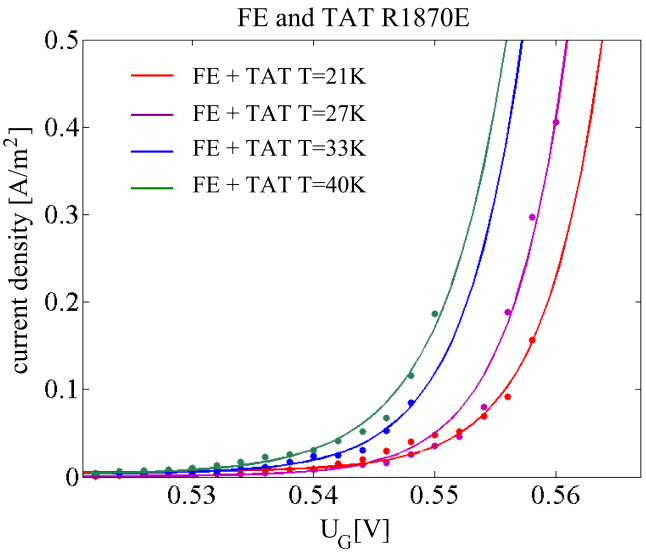

Figure 6.6: *This image shows a zoom into some fits of sample R1870E in the temperature regime from 18K to 40K. The combination between field emission (FE) and trap assisted tunnelling (TAT) yielded the best fitting results.*

T $[K]$	Φ_t $[eV]$	Φ_B $[eV]$	N_P $[cm^{-3}]$	N_t $[m^{-3}]$	R^2
18	0,04061	0,6974	$9,0 \cdot 10^{17}$	$4,73 \cdot 10^{13}$	0,9464
21	0,048	0,6924	$9,0 \cdot 10^{17}$	$4,88 \cdot 10^{13}$	0,9839
24	0,04138	0,6959	$9,0 \cdot 10^{17}$	$5,48 \cdot 10^{13}$	0,9817
27	0,04077	0,6967	$9,0 \cdot 10^{17}$	$5,21 \cdot 10^{13}$	0,9815
30	0,04015	0,6963	$9,0 \cdot 10^{17}$	$4,73 \cdot 10^{13}$	0,9615
33	0,04017	0,6939	$9,0 \cdot 10^{17}$	$4,88 \cdot 10^{13}$	0,9687
36	0,0396	0,6963	$9,0 \cdot 10^{17}$	$4,88 \cdot 10^{13}$	0,9788
40	0,04625	0,696	$9,0 \cdot 10^{17}$	$5,21 \cdot 10^{13}$	0,989
average	0,0421	0,696	$9,0 \cdot 10^{17}$	$5,0 \cdot 10^{13}$	0,974

Table 6.3: *Overview of the results obtained with a combination of field emission and trap assisted tunnelling in the moderate temperature dependent region II from 18K to 40K. The trap depth Φ_t, the Schottky barrier height Φ_B and the trap concentration N_t were used as fitting parameters. The goodness of fit R^2 is also illustrated as well as the unchanged P doping concentration N_P. Moreover, the average results are indicated in green.*

Figure 6.5a shows an overview of the field emission (FE) model applied to the measured leakage current densities in sample R1870E for the slightly temperature dependent region I (see figure 6.2a). The FE model delivered good fitting results and yielded an average value for the Schottky barrier height of $\Phi_B = 0,695eV$ as well as a goodness of fit of $R^2 = 0,927$. A complete overview of all fitting results is given in table 6.2. On top of that, the combined fitting model of field emission

and trap assisted tunnelling matched very nicely to the experimentally observed leakage current densities in the temperature range from $18K$ up to $40K$ (see figure 6.6). Interestingly, we observed an averaged trap depth of $42,1meV$ which is indeed in good agreement with literature values for the phosphorous energy level in Si ($\xi = 45meV$) [127, 128, 129]. Moreover, an average trap concentration of $5,0 \cdot 10^{13} m^{-3}$ was found for this sample which seems to be quite a reliable result since this value is far below the maximal value of background impurities obtained in section 4. Additionally, a Schottky barrier height of $\Phi_B = 0,696eV$ was detected which is regarding the simplifications also in good accordance with literature values of $\Phi_B \approx 0,72eV$ [130, 131, 132]. An overview of the results is shown in figure 6.6 and table 6.3 for different temperatures.

sample	T	fit model	Φ_t $[eV]$	Φ_B $[eV]$	N_t $[m^{-3}]$	R^2
R1870E	1,4K-15K	FE	-	0,695	-	0,927
R2030B6	1,4K-15K	FE	-	0,682	-	0,959
R2043A16	1,4K-15K	FE	-	0,684	-	0,933
R1931A13	1,4K-15K	FE	-	0,626	-	0,912
R1870E	18K-40K	FE+TAT	0,0421	0,696	$5,0 \cdot 10^{13}$	0,974
R2030B6	18K-40K	FE+TAT	0,0437	0,684	$1,25 \cdot 10^{15}$	0,977
R2043A16	18K-40K	FE+TAT	0,0461	0,675	$2,41 \cdot 10^{17}$	0,976
R1931A16	18K-40K	FE+TAT	0,0441	0,618	$1,25 \cdot 10^{15}$	0,969

Table 6.4: *Overview of the average results of all investigated samples for the temperature dependent regions I and II respectively. In the temperature range from $1,4K$ to $15K$, we solely used field emission, whereas in the range from $18K$ to $40K$ we applied a combination of field emission and trap assisted tunnelling. It is clearly visible that all samples behave almost equal and that the results are definitely reliable.*

In comparison to the fitting results of sample R1870E, sample R2030B6 showed very similar results (see appendix B). Here, we extracted a Schottky barrier height of $0,682eV$ and $R^2 = 0,959$ in region I, whereas we found $\Phi_B = 0,684eV$, $\Phi_t = 0,0437eV$ and $R^2 = 0,977$ in region II ($18K$ to $40K$). However, we obtained $N_t = 1,25 \cdot 10^{15} m^{-3}$ which is markedly higher than the result in sample R1870E. If we now have a closer look at the magnetotransport measurements in both samples, we clearly see that sample R2030B6 ($n = 4,48 \cdot 10^{11} cm^{-2}$) compared to the transport data of R1870E [3] exhibited a distinctly higher charge carrier density in the ungated region than expected from the nominally wanted P volume doping degree. Consequently, a stronger P segregation process seems to be possible and therefore a higher N_t is realistic. The analysis of sample R2043A16 resulted in $\Phi_B = 0,684eV$ and $R^2 = 0,933$ for region I which perfectly confirms the averaged results obtained in R2030B6 and R1870E. In region II we extracted

[3] $n = 3,8 \cdot 10^{11} cm^{-2}$ obtained in the PhD thesis of Sailer [25]

$\Phi_B = 0,675eV$, $N_t = 2,41 \cdot 10^{17}m^{-3}$, $R^2 = 0,976$ and $\Phi_t = 0,0461eV$ (see appendix B). Unfortunately, the high N_t value in this sample is not understood until now. In contrary, the large Schottky barrier height can eventually be ascribed to the largest spacer layer which attenuates the charge carrier tunnelling process from the QW into the modulation doping layer. Finally, sample R1931A13 was checked. In region I we determined $R^2 = 0,912$ and $\Phi_B = 0,626$ which is the lowest Schottky barrier height up to now. A possible explanation for this phenomenon could be the quasi "$\delta - doping$" layer which contains nominally $7,2 \cdot 10^{18}cm^{-3}$ P doping and therefore maybe faces a stronger P segregation which can drastically lower the Schottky barrier height as proposed by Wild et al. [125]. Additionally, we observed $\Phi_B = 0,618eV$, $\Phi_t = 0,0441eV$, $R^2 = 0.969$ and $N_t = 1,25 \cdot 10^{15}m^{-3}$ in region II. In table 6.4 all obtained average fitting results for region I and II are summarized. A precise overview of every single result calculated from each temperature is given in appendix B.

6.2.2 Temperature range from 40 to 100K

For temperatures higher than $40K$, the FE model is no longer suitable to fit the measured leakage current densities (see equation 2.30). However, according to equation 2.34, thermionic field emission (TFE) should be an accurate fitting model to describe the experimentally obtained data.

Consequently, in a first step the TFE model was applied to sample R1870E for the strongly temperature dependent leakage current densities in a range from $40K$ up to $100K$ in region III (see figure 6.2a). This was also done in the master thesis of Schafberger [98] and resulted in an averaged Schottky barrier height of $\Phi_B = 0,705eV$ with an average $R^2 = 0.9645$. These results revealed a good agreement of the TFE fitting model with the experimental data in this temperature regime. Moreover, we reviewed the applicability of thermionic emission (TE), which is also a possible mechanism for this temperature region. The corresponding fits however resulted in distinctly smaller Schottky barrier heights and a markedly poorer averaged R^2, see [98]. As a consequence, the temperatures seem to be too low for a completely thermal activated leakage current mechanism. Hence, we conclude that the electric field still contributes to the leakage currents.

Despite all these attempts, we furthermore checked a combination of TFE and TAT since TAT is also a possible leakage current mechanism and was shown to significantly contribute to the leakage current densities in the temperature range from $18K$ to $40K$. In the scope of this analysis, we again used the Schottky barrier height Φ_B, the trap depth Φ_t and the trap concentration N_t as fitting parameters, whereas the P doping concentration N_P was kept constant.

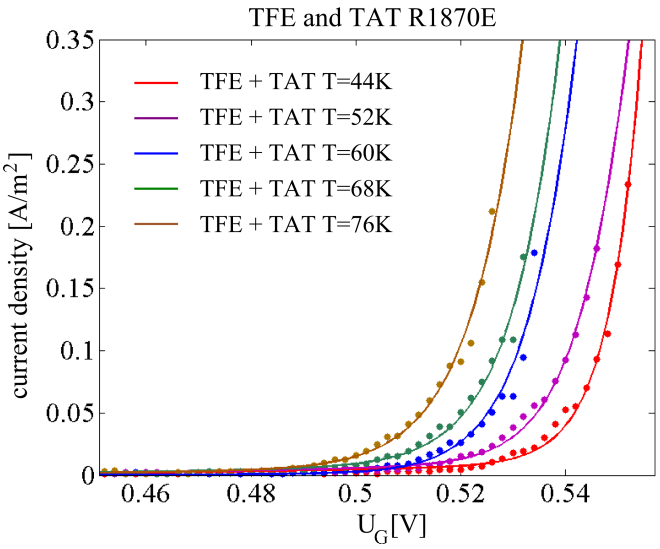

Figure 6.7: *This image shows a zoom into some fits of sample R1870E in the temperature regime from 40K to 80K. The combination of thermionic field emission (TFE) and trap assisted tunnelling (TAT) yielded the best fitting results.*

T $[K]$	Φ_t $[eV]$	Φ_B $[eV]$	N_P $[cm^{-3}]$	N_t $[m^{-3}]$	R^2
44	0,04014	0,6606	$9,0 \cdot 10^{17}$	$5,10 \cdot 10^{13}$	0,9899
48	0,03773	0,6085	$9,0 \cdot 10^{17}$	$4,88 \cdot 10^{13}$	0,976
52	0,03957	0,6069	$9,0 \cdot 10^{17}$	$5,21 \cdot 10^{13}$	0,9938
56	0,04292	0,6071	$9,0 \cdot 10^{17}$	$4,55 \cdot 10^{13}$	0,9604
60	0,045	0,6213	$9,0 \cdot 10^{17}$	$4,88 \cdot 10^{13}$	0,9824
64	0,040	0,6049	$9,0 \cdot 10^{17}$	$5,21 \cdot 10^{13}$	0,9805
68	0,03982	0,6081	$9,0 \cdot 10^{17}$	$4,54 \cdot 10^{13}$	0,983
72	0,03972	0,6097	$9,0 \cdot 10^{17}$	$5,06 \cdot 10^{13}$	0,9949
76	0,03777	0,7071	$9,0 \cdot 10^{17}$	$4,46 \cdot 10^{13}$	0,9849
80	0,03597	0,6258	$9,0 \cdot 10^{17}$	$5,54 \cdot 10^{13}$	0,9837
average	0,0403	0,626	$9,0 \cdot 10^{17}$	$4,88 \cdot 10^{13}$	0,983

Table 6.5: *Overview of the results obtained with a combination of thermionic field emission and trap assisted tunnelling in the strong temperature dependent region III from 40K to 80K in sample R1870E. The trap depth Φ_t, the Schottky barrier height Φ_B and the trap concentration N_t were used as fitting parameters. The goodness of fit R^2 is also illustrated as well as the fixed P doping concentration N_P. Moreover, the average results are indicated in green.*

Thus, we observed good fitting results up to a temperature of $80K$. Here we determined an averaged $\Phi_B = 0.626eV$, $\Phi_t = 0,0403eV$ and a trap depth of $N_t = 4,878 \cdot 10^{13} m^{-3}$ for a $R^2 = 0.983$. Higher T however led to unrealistic trap

depths and Schottky barriers. This circumstance brings us to the conclusion that above $80K$, TFE is the dominant leakage current mechanism. Figure 6.7 and table 6.5 display the fitting results in the temperature range from $40K$ to $80K$, where a combination of TFE and TAT yielded the best results.

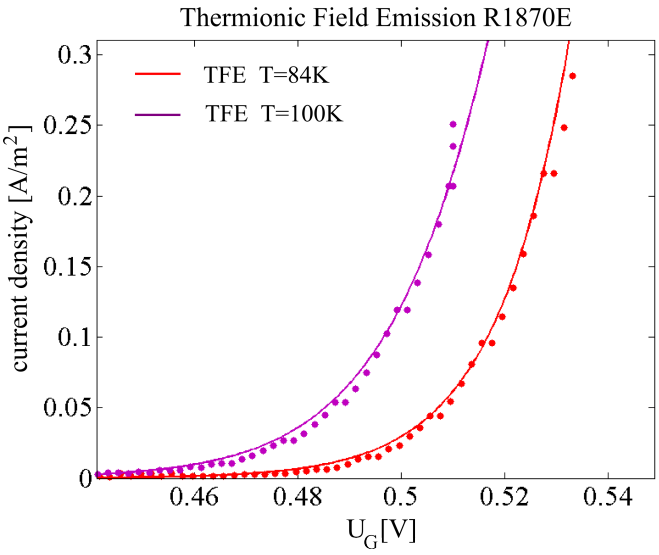

Figure 6.8: *This image shows an exemplary zoom into two thermionic field emission fitting results of sample R1870E for $T = 84K$ and $T = 100K$ respectively.*

$T\ [K]$	$\Phi_t\ [eV]$	$\Phi_B\ [eV]$	$N_P\ [cm^{-3}]$	R^2
84	0,045	0,7322	$9,0 \cdot 10^{17}$	0,9786
88	0,045	0,7397	$9,0 \cdot 10^{17}$	0,9723
92	0,045	0,7461	$9,0 \cdot 10^{17}$	0,9901
96	0,045	0,7483	$9,0 \cdot 10^{17}$	0,9356
100	0,045	0,7555	$9,0 \cdot 10^{17}$	0,9569
average	0,045	0,744	$9,0 \cdot 10^{17}$	0,9667

Table 6.6: *Overview of the thermionic field emission temperature dependent results in sample R1870E. The P doping concentration N_P and the trap depth Φ_t were fixed whereas the Schottky barrier height Φ_B was used as the only fitting parameter. The goodness of fit R^2 is also shown. The average results are still indicated in green.*

Furthermore, figure 6.8 and table 6.6 present the results for the TFE model applied to temperatures from $80K$ to $100K$, where we observed $\Phi_B = 0.744eV$ and $R^2 = 0.9667$ for fixed $\Phi_t = 0,045eV$ and $N_P = 9,0 \cdot 10^{17} cm^{-3}$. In comparison to the results achieved in sample R1870E, sample R2043A16, which was also measurable up to $100K$, showed a similar behaviour. Indeed we figured out an averaged

Schottky barrier height of $\Phi_B = 0,604eV$ an average trap depth of $\Phi_t = 0,046eV$ and a trap concentration $N_t = 2,20 \cdot 10^{17} m^{-3}$ with a goodness of fit $R^2 = 0,988$ in region III from $40K$ to $80K$ (TFE+TAT), whereas in the temperature range from $80K$ to $100K$ we observed $\Phi_B = 0,704eV$ for $R^2 = 0,943$ by using solely the TFE model.

6.3 Conclusion

In the first part of this chapter we studied temperature dependent leakage currents of four different samples. After an interpolation of the measured data to a regular voltage scale, 3D leakage current density maps were determined. By close inspection of the 3D maps obtained in this way, two or three different T dependent regions could be identified. Interestingly, all samples contained exactly the same T dependent borders in each region. Region I, which ranges from $1,4K$ to $15K$, showed a very slight T dependence, whereas section II, starting from $18K$ and ending up at $40K$, displayed a greater leakage current density increase. In contrast, region III, which was only observed in two of the investigated samples, exhibited the strongest temperature dependence from $40K$ to $100K$. Furthermore, we observed a strange phenomenon of suddenly appearing dips/peaks at certain gate voltage values during each leakage current measurement which was shown to be independent of sweep rate, direction and time [98, 13]. Indeed, this effect could be ascribed to the population/depopulation of the 2DES since we were able to bring the temperature dependent peak/dip voltage values in the leakage currents in line with temperature dependent pinch-off voltages.

In the second part, the main focus was laid on the mechanisms behind leakage currents in our Si/SiGe heterostructures. Based on our previous findings in chapter 5, we already knew that above a threshold top-gate voltage a strong charge carrier transfer process into the modulation doping layer sets in which persistently occupies the P atoms. Therefore it is justified to assume that the largest contribution to the leakage currents comes from an electron transfer of still occupied phosphorous states in the doping layer to the top-gate at the sample surface. As a matter of fact, this simplification allowed us to apply different leakage current models to our two-dimensional electron systems, which are based on a triangular barrier.

Consequently, we were able to gather very good fits to our data in all samples. In region I ($1,4K$ to $15K$), we used the field emission model which resulted in an averaged Schottky barrier height of $\Phi_B \approx 0,687eV$ with a goodness of fit $R^2 > 0,912$. In the temperature range from $18K$ to $40K$ (region II), where a combination of field emission (FE) and trap assisted tunnelling (TAT) seemed to be best suited, we attained an averaged $\Phi_B \approx 0,684eV$, a trap depth $\Phi_t \approx 0,0442eV$ and trap concentrations $N_t < 2,41 \cdot 10^{17} m^{-3}$ which are reasonable results. However, sample

R1931A13 showed slightly lower Schottky barriers in both regions I and II respectively. A possible explanation for this circumstance is the quasi "$\delta - doping$" layer (nominally $N_P = 7,2 \cdot 10^{18} cm^{-3}$) which might cause a stronger P segregation and therefore decreases the Schottky barrier [125]. In region III, which starts from $40K$ and ends up at $100K$, we utilized a combination of thermionic field emission (TFE) and trap assisted tunnelling (TAT). Close inspection revealed good fitting results of $\Phi_B \approx 0,626eV$ and $\Phi_t \approx 0,0403eV$ as well as trap concentrations $N_t < 2,7 \cdot 10^{17} m^{-3}$ up to a temperature of $80K$. Interestingly, the observed trap concentrations coincided well with the ones obtained in the temperature dependent region II. Above $80K$, TFE alone yielded the best fits thus we extracted an averaged Schottky barrier of $\Phi_B = 0,724eV$. Nevertheless, it is possible that TFE is the only appropriate fitting model in the entire region III since Schafberger et al. achieved also very good results ($\Phi_B = 0,705eV$ for $R^2 = 0,965$) using solely TFE [98].

In summary, the fitting results of the observed trap depths can be clearly linked to the energy level of phosphorous atoms ($45meV$) in Si [127, 128, 129] and therefore seem to be very realistic. Moreover, this result is a strong hint that a trap assisted tunnelling mechanism in the modulation doping layer is possible and that the observed charge reconfiguration and disorder effects (see section 5) can be reliably attributed to the P states. Additionally, the obtained Schottky barrier heights were in good agreement with literature values of Pd/Si junctions $\Phi_B \approx 0,72eV$ [130, 131, 132] and therefore confirm the correctness and validity of the applied models to our Si/SiGe two dimensional electron systems.

7 Summary and outlook

The goal and the associated challenge of this thesis was to investigate and improve the heterostructure design in order to adjust a precise field-effect control of Schottky top-gated Si/SiGe two-dimensional electron systems (2DES).

In the first part of this work, we focussed on the optimization of the heterostructure design. We utilized an unrotated epitaxy process to efficiently exploit different gradients which arise due to the MBE cell geometry. Using XRD RSM and magnetotransport measurements, we investigated and precisely mapped both LT-Si and graded buffer based Si/SiGe heterostructures with respect to the effective Ge content $x_{Ge_{eff}}$, the degree of relaxation R, as well as the P doping gradients along the wafer. Using these parameters as input parameters in numerical band structure simulations, we can identify the most suited samples in order to reach high mobilities and large gate voltage intervals without disturbing charge reconfigurations. The latter are caused by tunnelling events from the QW to the P modulation doping layer when the energy level of the P states crosses the Fermi energy. In this context, we discovered the highest mobilities in the ungated region of our Schottky top-gated 2DES in those samples with an effective Ge content of approximately 35% and a charge carrier density in the range of $2,5 - 3,5 \cdot 10^{11} cm^{-2}$.

These results underline the importance of a precisely controlled doping profile for the realization of a high quality 2DES. After introducing an optimized calibration for phosphorous (P) doping in SiGe, we thus investigated the precision in doping concentration of the GaP cell. Unfortunately, it was not possible to precisely control the GaP cell so that the desired carrier density range of $n < 3,5 \cdot 10^{11} cm^{-2}$ could not be stably adjusted in the upper part of the wafer where we observed the highest degree of relaxation. Nevertheless, we always achieved carrier densities with $n \geq 3,5 \cdot 10^{11} cm^{-2}$ at different positions in the investigated wafers due to the arising P doping gradients. If we then extract samples from a wafer fabricated during a new growth series, which exhibit a fairly convenient charge carrier density in the ungated region and a Ge content of approximately 35%, we showed that covering these samples with Schottky top-gates results in record mobilities of $\mu = 4,78 \cdot 10^4 \frac{cm^2}{Vs}$ for an LT-Si based 2DES. During our mobility analysis, we additionally addressed other mobility limiting mechanisms in Si/SiGe heterostructures. Conducting a so-called scattering time analysis, we identified long-range scattering events to be the main mobility limiting mechanisms. This result was in very good agreement with former investigations of Lang and Ibrahim [85, 107].

Interestingly, we found two carrier density regimes, in which we could discriminate between background and remote impurity scattering as the dominant scattering mechanism. In the first density section where $n \approx 1,9 - 2,6 \cdot 10^{11} cm^{-2}$, we achieved a good fitting result with a fit of the form $\mu = a \cdot n^b + c$ and extracted a fitting parameter $b = 0,52$ (goodness of fit $R^2 = 0,981$) which confirms that the dominant scattering mechanism in this density range is background impurity scattering. In contrary to these observations, the second density regime appeared for $n \approx 2,6 - 4,95 \cdot 10^{11} cm^{-2}$. Here, we extracted a parameter $b \approx 2,0$ with a goodness of fit of $R^2 = 0,986$. This is a strong hint that inside this density section scattering on remote impurities is the main mobility limiting mechanism. Based on these findings, we moreover estimated the background impurity concentration to $N_{back} \approx 2 - 4 \cdot 10^{15} cm^{-3}$ which is also in good agreement with previous results of Sailer and Wild [25, 13].

In a next step, we studied the field-effect control of Si/SiGe heterostructures. We for the first time discovered a strong correlation of the P doping concentration and the measured capacitive coupling C_m between the Schottky top-gate and the 2DES along the P doping gradient. This observation could not be explained, neither with the charge reconfiguration model suggested by Wild et al. [13], nor with the predicted capacitive coupling formula of Ihn [35]. In order to solve this experimental observation we extended the charge reconfiguration model. First of all, we showed that a higher P doping leads to a lowering of the conduction band minimum in the modulation doping layer so that the Fermi energy is already equal to the P energy states even without an applied gate voltage. As a result, a fraction of the P states stay neutral. Applying a gate voltage then results in charge transfer between 2DES and the doping layer and therefore a further neutralization of the P atoms. However, time resolved gate jump experiments showed that within the linear regime of the n versus U_G gate sweep curve, the charge transfer rate is low and distinctly slower than the gate sweep rate so that the slope in the n versus U_G curve still behaves linearly. Based on these facts, we invoked a polarizability of neutral P atoms in the modulation doping layer. This polarizability explains the experimentally observed increasing C_m for an increasing P concentration since the dielectric constant in the doping layer $\epsilon_{SiGe:P}$ directly increases with an increasing degree of neutral P atoms. Then, we developed a quantitative method to fit the measured capacitive couplings as a function of the effective Ge content $x_{Ge_{eff}}$ and the degree of neutral impurities N in the modulation doping layer. The resulting fit parameters were reliable and allowed us to evaluate the dielectric constants of MBE grown Si and Ge. The extracted dielectric constants ($\epsilon_{Si} = 9,4$ and $\epsilon_{Ge} = 12,7$) were approximately 20% smaller than the literature values which is a realistic result regarding the simplifications in this quantitative method. The extended charge transfer model was not only suitable to explain the observed correlation between the P doping concentration and the capacitive coupling C_m, but could also be included in the model explaining the experimental n versus U_G hysteresis of our gated two-dimensional electron systems.

In a final part, we reviewed the influence of leakage currents on the controllability of our Schottky gated two-dimensional electron systems. In a first step, the temperature dependence of leakage currents was examined. As a result, we discovered two or three different temperature dependent regions which contained exactly the same temperature borders in all investigated samples. Interpolating the experimental data to a constant voltage scale, allowed us to determine 3D leakage current density maps. Under close inspection of these 3D maps, it is obvious that region I, which ranges from $1,4K$ to $15K$, showed a slight T dependence, whereas section II, ranging from $18K$ up to $40K$, displayed a moderate leakage current density increase. Finally region III, which was only observed in two of the investigated samples, exhibited a strong T dependence up to $100K$.

In order to detect possible sources which are responsible for an early onset of leakage, we then applied several leakage current models to get further informations about Schottky-gated Si/SiGe heterostructures. Based on our extended charge transfer model, we already knew that above a threshold voltage a charge transfer process into the barrier region sets in. Therefore, it seems justified to assume that the largest amount to the leakage current stems from an electron transfer of the still occupied P states to the Schottky top-gate at the sample surface. This simplification allows us to use different leakage current models, which are based on a triangular barrier, to our heterostructures. In the leakage current analysis, we then performed fits to the experimentally measured and temperature dependent data which allowed us to extract important parameters like the Schottky barrier height Φ_B, the trap concentration N_t and the trap depth Φ_t. As a result, field emission (FE) was found to be the dominant mechanism in region I and a Schottky barrier height in the order of $\Phi_B \approx 0,687eV$ with a goodness of fit $R^2 > 0,912$ was evaluated. For comparison, in the temperature dependent region II, we obtained the best fits with a combination of field emission and trap assisted tunnelling (TAT). Here, we determined $\Phi_B \approx 0,684eV$, $\Phi_t \approx 0,0442eV$ as well as a trap concentration of $N_t < 2,41 \cdot 10^{17} m^{-3}$ which are realistic results. In region III, we found a combination of thermionic field emission (TFE) and trap assisted tunnelling to be best suited to fit our experimental leakage currents up to $T = 80K$. Indeed, we extracted $\Phi_B \approx 0,626eV$, $\Phi_t \approx 0,0403eV$ and $N_t < 2,7 \cdot 10^{17} m^{-3}$. Above $80K$ TFE alone yielded the best results, that is a Schottky barrier height of $\Phi_B \approx 0,724eV$.

Based on these insights, we could link the observed trap depths with the literature energy level of phosphorous atoms in Si ($45meV$) [127, 128, 129] which is a strong hint that the charge transfer processes into the barrier region and the discovered disorder effects can be reliably attributed to a charging of P states. Moreover, the extracted Schottky barrier heights showed a good agreement with literature values of Pd/Si junctions with $\Phi_B \approx 0,72eV$ [130, 131, 132] and therefore confirms the applicability and validity of the applied leakage current models to our Si/SiGe heterostructures. While Wild [13] was not able to find out a final

correct fitting strategy in order to exactly trace the n versus U_G gate sweep curve, our experimentally observed lower Schottky barrier heights as well as the 20% smaller dielectric constants of Si (9,4) and Ge (12,7) point to the applicability of his proposed fitting strategy one.

In future experiments, the charge transfer model which was extended by a polarizability of neutral P atoms in the doping layer to explain the experimentally observed increasing capacitive coupling C_m with increasing P doping concentration has to be checked further to fully confirm this model. Furthermore, the experimentally obtained dielectric constants of MBE grown Si and Ge should be further investigated to find out whether the values for MBE material differ from literature values. Here, separated studies on MBE grown Si, Ge, and SiGe layers might be helpful. Additionally, other material systems like Ge/SiGe hole or GaAs/AlGaAs two-dimensional electron systems are of great interest to test the model.

In summary, we showed that a precise controllability of the entire heterostructure and in particular the P doping is essential with respect to charge noise, which can be induced by random charge reconfigurations. This fact is one of the greatest challenges in few to single-electron devices. As a matter of fact, this circumstance can stretch the epitaxy cells to their controllability limits. Regarding modulation doped heterostructures, one way could be a field-effect based control of the ionization of the donors by a precise positioning of the band structure. First studies in double quantum dots (DQDs) in which an additional global top-gate covers the entire doping area showed good results [11]. Another way could be the omission of the doping layer and the implementation of a 2DES with a MOS-like Si/SiGe heterostructure [133]. In this context, also promising results regarding the coherent control of spin qubits were demonstrated [134]. However, regarding the accumulation mode devices, the boundary surface between semiconductor and oxide comes to the fore. Therefore, only few studies on single-electron devices which are based on this topic are available yet.

A Transport data map results

a)

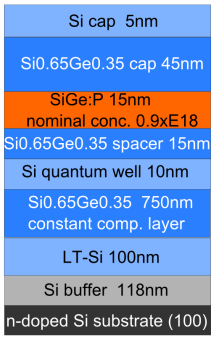

b)

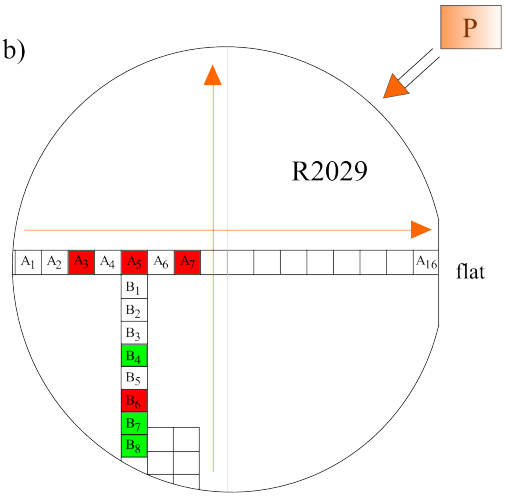

c)

R2029	ungated region		gated region		gate controllable region		
	$n_{ug,max}$ [1/cm^2]	$\mu_{ug,max}$ [cm^2/Vs]	n_{max} [1/cm^2]	μ_{max} [cm^2/Vs]	interval[V]	U_{Gmax}[V]	dn/dU_G [V/cm^2]
A3	5,60E+11	1,12E+04					
A5	6,26E+11	1,23E+04	6,18E+11	9,52E+03	0,43	0,51	9,28E+11
A7	6,43E+11	1,44E+04	6,64E+11	9,86E+03	0,49	0,51	9,76E+11
B4	5,50E+11	2,40E+04	6,46E+11	2,38E+04	0,73	0,45	8,41E+11
B7	5,10E+11	2,50E+04	5,85E+11	2,50E+04	0,69	0,44	8,24E+11
B8	4,52E+11	2,10E+04	5,61E+11	2,00E+04	0,57	0,45	6,79E+11

Figure A.1: *a) Drawing of the basic sample layout of wafer R2029. The modulation doping layer is 15 nm thick with a nominally phosphorous doping concentration of* $0,9 \cdot 10^{18} cm^{-3}$ *(*$T_{GaP} = 649°$*). b) Overview of the results of different samples concerning both the carrier densities (n) and mobilities (*μ*) in vertical and horizontal wafer direction. The corresponding phosphorous doping gradients are indicated with orange arrows. Different colours highlight the quality (mobility) of the samples. c) The appropriate results of both the carrier density and the mobility in the ungated as well as the gated regions are shown in dependence of the wafer position. The quality of each sample is indicated by different colours. Red displays* $\mu = 1 \cdot 10^3 \frac{cm^2}{Vs}$ *up to* $1 \cdot 10^4 \frac{cm^2}{Vs}$*, mobilities in the range of* $1 \cdot 10^4 \frac{cm^2}{Vs}$ *to* $2 \cdot 10^4 \frac{cm^2}{Vs}$ *are shown in light blue, green stands for mobilities in the range of* $2 \cdot 10^4 \frac{cm^2}{Vs}$ *to* $4 \cdot 10^4 \frac{cm^2}{Vs}$*. Additionally, the maximal gate controllable region and the capacitive coupling* $C = \frac{\partial n}{\partial U_G}$ *are illustrated.*

For the sake of completeness, we give a brief overview of all remaining samples of different wafers and the special positions which were systematically investigated via magnetotransport measurements in the gated as well as the ungated Hall-bar regions during this thesis. The experiments were performed by using the standard magnetotransport set-up which was precisely explained in section 3.6.3.

In a first step, the charge carrier densities and the mobilities, which served as a figure of merit in our Si/SiGe heterostructures, were studied in dependence of the different gradients as already presented in section 4. The mobility of each sample was therefore highlighted similarly by different colours. Red, denotes mobilities from $1 \cdot 10^3 \frac{cm^2}{Vs}$ up to $1 \cdot 10^4 \frac{cm^2}{Vs}$, light blue stands for mobilities in the range of $1 \cdot 10^4 \frac{cm^2}{Vs}$ to $2 \cdot 10^4 \frac{cm^2}{Vs}$, green illustrates mobilities from $2 \cdot 10^4 \frac{cm^2}{Vs}$ to $4 \cdot 10^4 \frac{cm^2}{Vs}$. Finally, the charge carrier density gradients were indicated in every wafer by orange arrows. Moreover, an exact overview of the maximally gate controllable regions and the capacitive coupling $C_m = \frac{\partial n}{\partial U_G}$, which was extracted from the linear slope in the n versus U_G curve in the gated Hall-bar region, is given for each sample. Interestingly, C_m was always found to increase with increasing modulation doping degree along the P doping gradient (see figure A.1-A.4). This phenomenon was explicitly studied in section 5.

To start our overview, we present wafer R2029 which had a nominally P modulation doping concentration of $0,9 \cdot 10^{18} cm^{-3}$ ($T_C = 649°C$). The entire sample structure is shown in figure A.1a, whereas figure A.1b displays the positions of different samples on the wafer. As a result, we observed a charge carrier density of $6,26 \cdot 10^{11} cm^{-2}$ in the wafer center. This is drastically higher than the desired density ($n_{ug,min}$) range between $2,5 \cdot 10^{11} cm^{-2}$ and $3,5 \cdot 10^{11} cm^{-2}$ in the upper half of the wafer which was suggested in section 4.2.2 to be the most promising density range in order to reach high mobilities and simultaneously suppress charge reconfiguration and disorder effects.

Furthermore, the sample structure as well as the transport results of wafer R2031, which was fabricated in the same growth series like wafer R2029 and R2030 (see section 4), are presented in A.2a-c. The overall sample structure was grown completely identical to wafer R2029 except for the nominal P modulation doping degree which had a higher doping degree of $1,3 \cdot 10^{18} cm^{-3}$ ($T_C = 655°C$) instead. However, in comparison to wafer R2029, wafer R2031 showed a lower charge carrier density $n_{ug,min} = 5,59 \cdot 10^{11} cm^{-2}$ in the wafer center, which was very surprising, since the nominally P doping degree in the modulation doping layer was higher. This circumstance was possibly caused by the worse controllability of the temperature controlled GaP doping cell which had been investigated in section 4.3.

In order to prevent a renewed phosphorous overdoping, two completely identical wafers R2035 and R2036 with a reduced GaP cell temperature $T_C = 647°C$ were fabricated, see figures A.3a-f. Additionally, the Si capping layer was slightly increased up to $7nm$.

a)

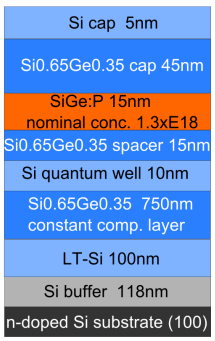

b)

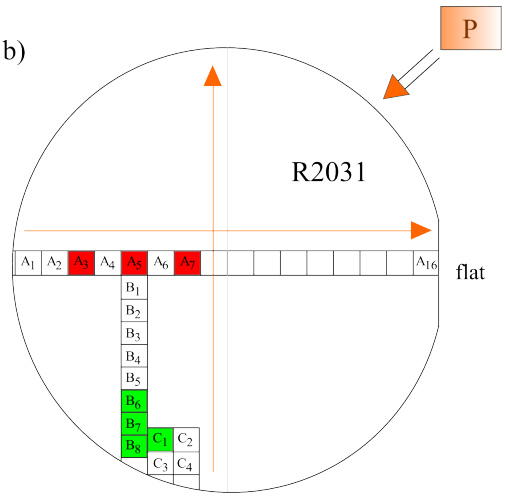

c)

R2031	ungated region		gated region		gate controllable region		
	$n_{ug,max}$ [1/cm^2]	$\mu_{ug,max}$ [cm^2/Vs]	n_{max} [1/cm^2]	μ_{max} [cm^2/Vs]	interval[V]	U_{Gmax} [V]	dn/dU_G [V/cm^2]
A3	5,36E+11	1,09E+04	6,10E+11	6,40E+03	0,46	0,48	1,00E+12
A5	5,40E+11	9,85E+03					
A7	5,59E+11	1,40E+04	6,46E+11	9,42E+03	0,50	0,49	1,02E+12
B6	4,21E+11	2,49E+04	5,52E+11	2,58E+04	0,65	0,40	7,42E+11
B7	4,14E+11	2,05E+04	5,55E+11	2,05E+04	0,62	0,37	6,50E+11
B8	3,95E+11	2,69E+04	5,10E+11	2,05E+04	0,55	0,40	5,79E+11
C1	4,05E+11	2,59E+04	4,91E+11	3,26E+04	0,85	0,30	7,14E+11

Figure A.2: *a) Image of the basic sample layout for wafer R2031. This wafer is completely identical to wafer R2029 except for the nominally P doping concentration which is* $1,3 \cdot 10^{18} cm^{-3}$ *(*$T_{GaP} = 655°$*) instead. b) Overview of the results of different samples concerning both the carrier densities* n *and mobilities* μ *in vertical and horizontal wafer direction. The corresponding P doping gradients are indicated with orange arrows. Different colours display the quality (mobility) of the samples. c) Overview of the results of both* n *and* μ *in the ungated as well as the gated regions in dependence of the wafer position. The quality of the samples, which is given by the maximum mobility, is highlighted in similar colours like in wafer R2029. Additionally, the maximal gate controllable region and* C *are shown.*

Moreover, we manufactured both wafers within three days to test the reproducibility of the GaP cell. Indeed, the charge carrier density $n_{ug,min}$ could be reduced to $4,7 \cdot 10^{11} cm^{-2}$ and $3,9 \cdot 10^{11} cm^{-2}$ in the vicinity of the wafer center in wafer R2035 and R2036 respectively, see figures A.3b,c,e,f. However, the desired density range $n_{ug,min} < 3,5 \cdot 10^{11} cm^{-2}$ in the upper half of the wafer could still not be employed. Nevertheless, the charge carrier density in the wafer center has been markedly reduced. Based on these insights, we produced a last wafer R2042, which was grown completely identical to wafer R2029 except for a further reduced the nominal phosphorous doping concentration of $0,7 \cdot 10^{18} cm^{-3}$ ($T_{GaP} = 645°C$), see figure A.4a. However, the results of the charge carrier density $n_{ug,min}$ in the wafer center were puzzling.

a)

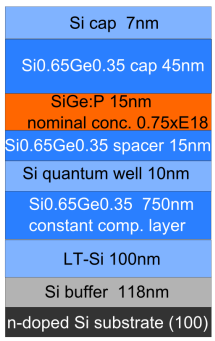

b)

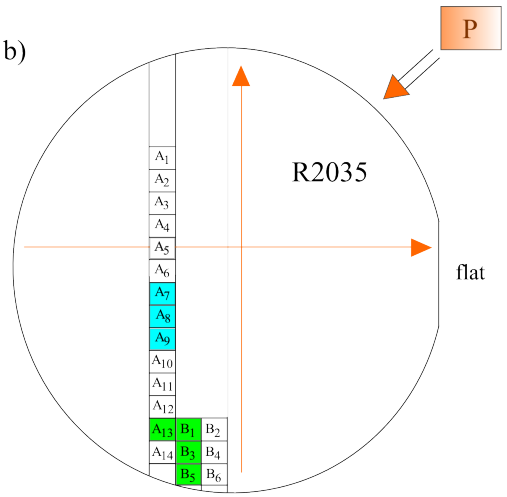

c)

R2035	ungated region		gated region		gate controllable region		
	$n_{ug,max}$ [1/cm^2]	$\mu_{ug,max}$ [cm^2/Vs]	n_{max} [1/cm^2]	μ_{max} [cm^2/Vs]	interval[V]	U_{Gmax}[V]	dn/dU_G [V/cm^2]
A7	4,69E+11						
A8	4,67E+11	1,56E+04					
A9	4,33E+11	1,68E+04					
A13	3,58E+11	2,45E+04	4,48E+11	2,92E+04	0,32	0,52	7,51E+11
B1			4,42E+11	2,51E+04	0,37	0,30	7,50E+11
B3			4,42E+11	3,09E+04	0,40	0,30	7,63E+11
B5			4,54E+11	3,38E+04	0,52	0,38	7,54E+11

d)

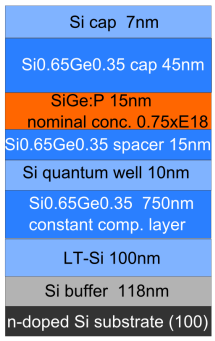

e)

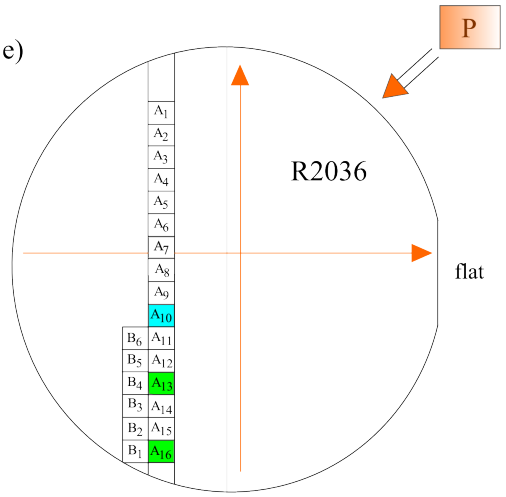

f)

R2036	ungated region		gated region		gate controllable region		
	$n_{ug,max}$ [1/cm^2]	$\mu_{ug,max}$ [cm^2/Vs]	n_{max} [1/cm^2]	μ_{max} [cm^2/Vs]	interval[V]	U_{Gmax}[V]	dn/dU_G [V/cm^2]
A10	3,69E+11	1,07E+04					
A13			4,35E+11	2,86E+04	0,37	0,52	7,60E+11
A16			4,00E+11	3,00E+04	0,35	0,50	7,22E+11

Figure A.3: *a) Drawing of the basic sample layout for wafer R2035. This wafer exhibited a nominally P doping concentration of* $0,75 \cdot 10^{18} cm^{-3}$ *(*$T_{GaP} = 647°$*) and a Si capping layer of 7nm. b) and c) Overview of the results of both the carrier density n and the mobility* μ *in the ungated as well as the gated regions. Moreover, the maximal gate controllable region and the capacitive coupling are shown. d)-f) Overview of the corresponding results in wafer R2036. This wafer was reproduction of wafer R2035.*

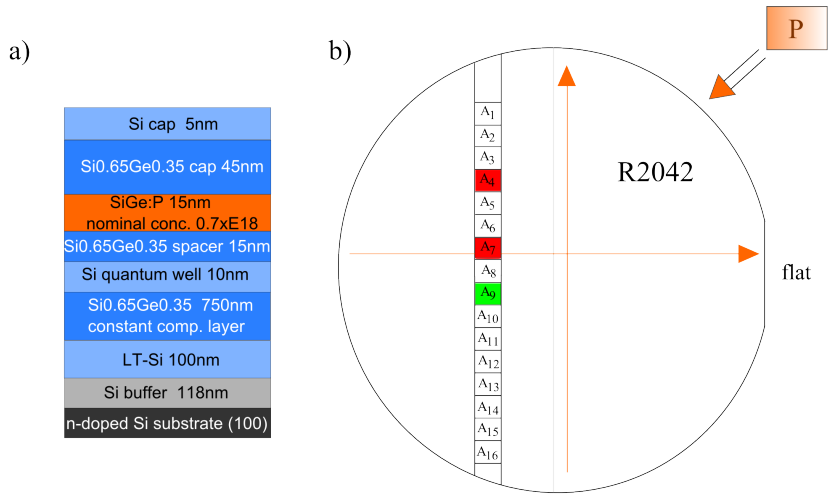

c)

R2042	ungated region		gated region		gate controllable region		
	$n_{ug,max}$ [1/cm^2]	$\mu_{ug,max}$ [cm^2/Vs]	n_{max} [1/cm^2]	μ_{max} [cm^2/Vs]	interval[V]	U_{Gmax} [V]	dn/dU_G [V/cm^2]
A4			7,36E+11	5,77E+03	0,50	0,40	1,01E+12
A7	6,44E+11	1,00E+04	6,33E+11	9,78E+03	0,45	0,40	9,16E+11
A9AlO			8,28E+11	2,31E+04	1,65	2,50	7,91E+11

Figure A.4: *a) Drawing of the basic sample layout for wafer R2042. This wafer was completely identical to wafer R2031 but exhibited a nominally P modulation doping of* $0,7 \cdot 10^{18} cm^{-3}$ *(*$T_{GaP} = 645°$*). b) and c) Overview of the results of both the carrier density* n *and the mobility* μ *in ungated as well as gated regions. Moreover, the maximal gate controllable region and* C *are still illustrated. Furthermore, sample R2042A9 was covered with a gate insulator in the gated Hall-bar region in order to check the hysteresis behaviour since we observed no saturation regimes in high modulation doped Schottky gated samples.*

Contrary to our expectations, the experimentally obtained charge carrier density $n_{ug,min}$ in the wafer center drastically increased to $6,44 \cdot 10^{11} cm^{-2}$, see figure A.4b,c. This circumstance gives a clearly points to the worse controllability of the GaP cell. Due to the fact that the charge carrier density was to high in wafer R2042, we solely observed a linear slope in the n versus U_G curve in the Schottky gated samples (for further information see section 5). In order to run the rule over this phenomenon, we covered sample R2042A9 with an Al_2O_3 gate insulator to be able to apply higher gate voltages. As a result, a complete hysteresis loop could be performed.

B Leakage current density fitting results

In the following, we present all experimental leakage current fitting results of the remaining investigated samples (R2030B6, R2043A16, R1931A13). Starting with a temperature range from $1,4K$ to $15K$, we already know from section 6 that field emission (FE) is the dominant leakage current mechanism. After that, the temperature range from $18K$ to $40K$, where a combination of field emission and trap assisted tunnelling (TAT) yielded the best fitting results, is treated. Finally, the temperature range from 40K to 100K, which was only once more achieved in sample R2043A16 and was fitted up to $80K$ by a combination of thermionic field emission (TFE) and trap assisted tunnelling (TAT), is displayed. For the temperature range from 80K to 100K, TFE purveyed the best fits.

B.1 Temperature range from 1,4K to 15K

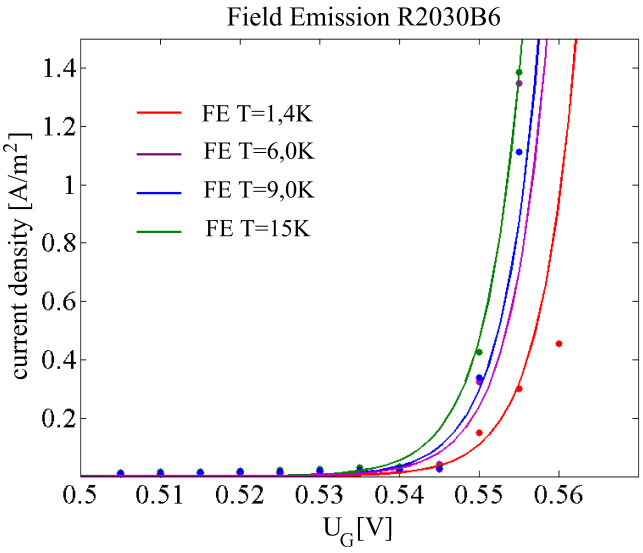

Figure B.1: *Zoom into a few field emission fitting results of sample R2030B6 in the temperature range of 1,4K up to 15K. These results showed an average goodness of fit $R^2 = 0,959$. Results for every temperature are shown in table B.1.*

$T\ [K]$	$\Phi_t\ [eV]$	$\Phi_B\ [eV]$	$N_P\ [cm^{-3}]$	R^2
1,4	0,045	0,682	$1,1 \cdot 10^{18}$	0,964
4,2	0,045	0,680	$1,1 \cdot 10^{18}$	0,968
6,0	0,045	0,680	$1,1 \cdot 10^{18}$	0,968
9,0	0,045	0,680	$1,1 \cdot 10^{18}$	0,955
12	0,045	0,682	$1,1 \cdot 10^{18}$	0,955
15	0,045	0,684	$1,1 \cdot 10^{18}$	0,934
average	0,045	0,682	$1,1 \cdot 10^{18}$	0,959

Table B.1: *Overview of the field emission results in sample R2030B6. The trap depth Φ_t and the P doping concentration N_P were fixed, whereas the Schottky barrier height Φ_B was used as the only fitting parameter. The goodness of fit R^2 is also illustrated. Moreover, the average results are indicated in green.*

Figure B.1 and table B.1 give an overview of the field emission results in sample R2030B6 in the temperature range from $1,4K$ to $15K$. We took the Schottky barrier height Φ_B as the only fitting parameter, whereas the trap depth ($\xi = 0,045eV$ see literature values for P energy levels in Si [127, 128, 129]) and the phosphorous doping concentration N_P were fixed. In this way, we were able to gather an average Schottky barrier height of $\Phi_B = 0,682eV$ with a goodness of fit $R^2 = 0,959$. In comparison, sample R2043A16 (see figure B.2 and table B.2) showed an averaged Schottky barrier height of $0,684eV$ with $R^2 = 0,934$. Both results are in good agreement and hence give a clear hint for the correct applicability of the FE leakage current model in this temperature range.

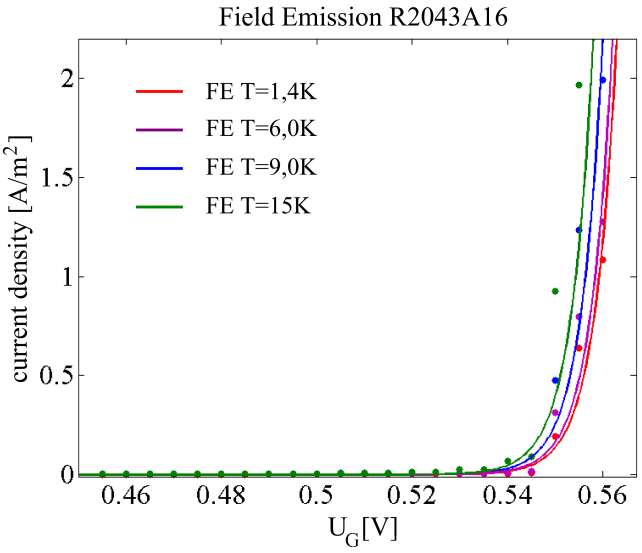

Figure B.2: *Zoom into a few field emission fitting results of sample R2043A16 in the temperature range of 1,4K up to 15K. The results showed an average goodness of fit $R^2 = 0,934$. Results for each temperature are shown in table B.2.*

$T\ [K]$	$\Phi_t\ [eV]$	$\Phi_B\ [eV]$	$N_P\ [cm^{-3}]$	R^2
1,4	0,045	0,683	$9,0 \cdot 10^{17}$	0,940
3,0	0,045	0,690	$9,0 \cdot 10^{17}$	0,892
6,0	0,045	0,686	$9,0 \cdot 10^{17}$	0,955
9,0	0,045	0,685	$9,0 \cdot 10^{17}$	0,939
12	0,045	0,682	$9,0 \cdot 10^{17}$	0,939
15	0,045	0,681	$9,0 \cdot 10^{17}$	0,920
average	0,045	0,684	$9,0 \cdot 10^{17}$	0,934

Table B.2: *Overview of the field emission results in sample R2043A16 in the range from 1,4K to 15K. The trap depth Φ_t and the P doping concentration N_P were fixed, whereas the Schottky barrier height Φ_B was again employed as the only fitting parameter. The goodness of fit R^2 is also illustrated. The average results are indicated in green.*

In contrast to the above mentioned samples R2030B6 and R2043A16, sample R1931A13 showed a distinctly lower Schottky barrier height in this temperature regime. We found an averaged $\Phi_B = 0,626eV$ with a goodness of fit $R^2 = 0,912$, see figure B.3 and table B.3. We suppose that this phenomenon stems from the high quasi "$\delta - doping$" [1] with $N_P = 7,2 \cdot 10^{18} cm^{-3}$ (see table 6.1 in section 6) which could markedly reduce the Schottky barrier height due to a possible stronger phosphorous segregation as proposed by Wild et al.[125].

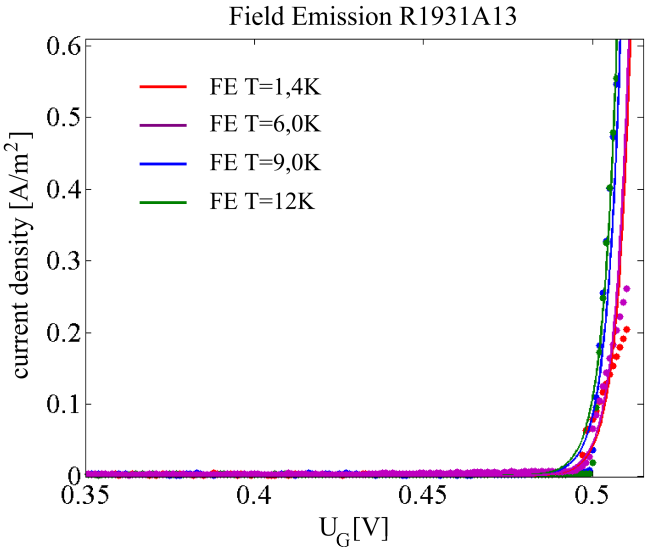

Figure B.3: *Zoom into some field emission fitting results of sample R1931A13 in the temperature range from 1,4K up to 12K. These results showed an average $R^2 = 0,912$. The data for each temperature are listed in table B.3.*

[1] in this sample the modulation doping layer is only $2nm$ thick

$T\ [K]$	$\Phi_t\ [eV]$	$\Phi_B\ [eV]$	$N_P\ [cm^{-3}]$	R^2
1,4	0,045	0,626	$7,2 \cdot 10^{18}$	0,886
3,0	0,045	0,623	$7,2 \cdot 10^{18}$	0,921
4,2	0,045	0,626	$7,2 \cdot 10^{18}$	0,919
6,0	0,045	0,622	$7,2 \cdot 10^{18}$	0,925
9,0	0,045	0,634	$7,2 \cdot 10^{18}$	0,920
12	0,045	0,625	$7,2 \cdot 10^{18}$	0,930
average	0,045	0,626	$7,2 \cdot 10^{18}$	0,912

Table B.3: *Overview of the field emission results for several temperatures in the range from 1,4K to 12K in sample R1931A13. Additionally, the goodness of fit R^2 is illustrated. The average results are still indicated in green. Interestingly, the Schottky barrier height was slightly lower than in the other samples.*

B.2 Temperature range from 18K to 40K

If we now increase the temperatures over $18K$, a combination of field emission and trap assisted tunnelling led to the best fitting results, see section 6. In sample R2030B6 we therefore achieved an averaged trap depth of $\Phi_t = 0,0437eV$, a Schottky barrier height of $\Phi_B = 0,684eV$ and a trap density $N_t = 1,25 \cdot 10^{15}m^{-3}$ with an averaged goodness of fit $R^2 = 0,977$. A precise overview of some important fitting results is given in figure B.4 and table B.4.

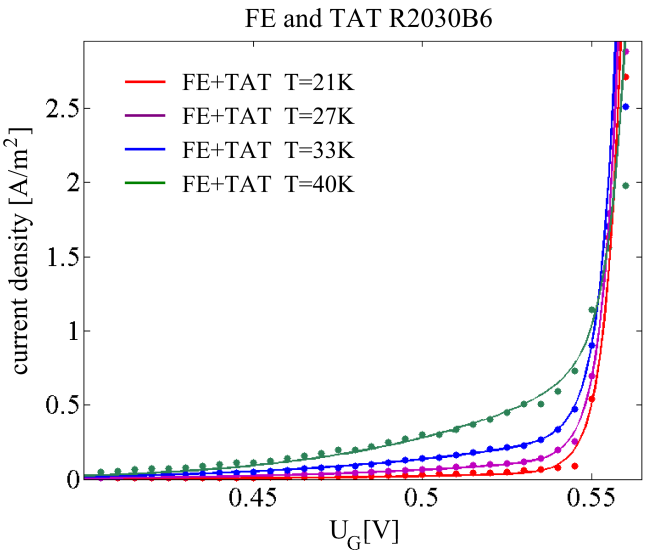

Figure B.4: *Zoom into fitting results of sample R2030B6 where a combination of field emission and trap assisted tunnelling was used. The results exhibit an average $R^2 = 0,977$. Exact data for every temperature are listed in table B.4.*

T $[K]$	Φ_t $[eV]$	Φ_B $[eV]$	N_P $[cm^{-3}]$	N_t $[m^{-3}]$	R^2
18	0,0488	0,682	$1,1 \cdot 10^{18}$	$1,25 \cdot 10^{15}$	0,923
21	0,0467	0,682	$1,1 \cdot 10^{18}$	$1,25 \cdot 10^{15}$	0,935
24	0,0483	0,682	$1,1 \cdot 10^{18}$	$1,25 \cdot 10^{15}$	0,991
27	0,0428	0,683	$1,1 \cdot 10^{18}$	$1,25 \cdot 10^{15}$	0,988
30	0,0413	0,684	$1,1 \cdot 10^{18}$	$1,25 \cdot 10^{15}$	0,997
33	0,0400	0,685	$1,1 \cdot 10^{18}$	$1,25 \cdot 10^{15}$	0,998
36	0,0387	0,687	$1,1 \cdot 10^{18}$	$1,25 \cdot 10^{15}$	0,992
40	0,0431	0,692	$1,1 \cdot 10^{18}$	$1,25 \cdot 10^{15}$	0,989
average	0,0437	0,684	$1,1 \cdot 10^{18}$	$1,25 \cdot 10^{15}$	0,977

Table B.4: *Overview of the results obtained with a combination of field emission and trap assisted tunneling in the moderate temperature dependent region II from 18K to 40K. The trap depth Φ_t, the Schottky barrier height Φ_B and the trap concentration N_t were used as fitting parameters. The goodness of fit R^2 is also illustrated as well as the unchanged P doping concentration N_P. Moreover, the average results are indicated in green.*

Interestingly, sample R2043A16 showed very similar results. We were able to extract an averaged trap depth $\Phi_t = 0,0469eV$, a Schottky barrier of $\Phi_B = 0,675eV$ and a trap concentration $N_t = 2,76 \cdot 10^{17} m^{-3}$ with an averaged goodness of fit $R^2 = 0,976$. The reason why we obtained a markedly higher trap concentration is not clear until now. Figure B.5 and table B.5 display an overview of some fitting results.

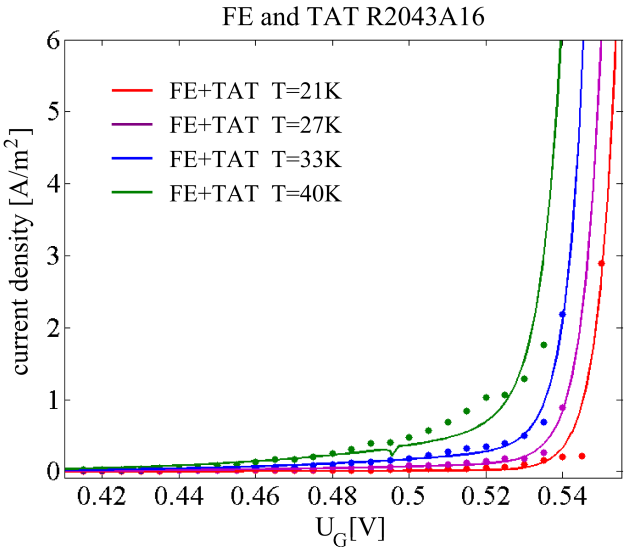

Figure B.5: *Zoom into fitting results of sample R2043A16 where a combination of field emission and trap assisted tunnelling was used. The results exhibit an average $R^2 = 0,976$. The data for each temperature are shown in table B.5.*

T $[K]$	Φ_t $[eV]$	Φ_B $[eV]$	N_P $[cm^{-3}]$	N_t $[m^{-3}]$	R^2
18	0,0406	0,697	$9,0 \cdot 10^{17}$	$4,73 \cdot 10^{13}$	0,947
21	0,0490	0,683	$9,0 \cdot 10^{17}$	$5,58 \cdot 10^{16}$	0,984
24	0,0450	0,679	$9,0 \cdot 10^{17}$	$2,98 \cdot 10^{16}$	0,979
27	0,0490	0,673	$9,0 \cdot 10^{17}$	$4,62 \cdot 10^{17}$	0,977
30	0,0490	0,675	$9,0 \cdot 10^{17}$	$4,53 \cdot 10^{17}$	0,966
33	0,0490	0,649	$9,0 \cdot 10^{17}$	$4,91 \cdot 10^{17}$	0,992
36	0,0401	0,670	$9,0 \cdot 10^{17}$	$2,14 \cdot 10^{17}$	0,977
40	0,0473	0,670	$9,0 \cdot 10^{17}$	$2,24 \cdot 10^{17}$	0,989
average	0,0461	0,675	$9,0 \cdot 10^{17}$	$2,41 \cdot 10^{17}$	0,976

Table B.5: *Overview of the results obtained in the moderate temperature dependent region II from 18K to 40K in sample R2043A16. The trap depth Φ_t, the Schottky barrier height Φ_B and the trap concentration N_t were used as fitting parameters. The goodness of fit R^2 is also illustrated as well as the unchanged P doping concentration N_P. Moreover, the average results are indicated in green.*

In contrast to the samples R2030B6 and R2043A16, sample R1931A13 exhibited again a markedly lower average Schottky barrier height $\Phi_B = 0,620eV$, a trap depth $\Phi_t = 0,0441eV$ and a trap concentration of $1,25 \cdot 10^{15} m^{-3}$ with a fitting accuracy of $R^2 = 0,969$. Figure B.6 and table B.6 illustrate an overview of some fitting results. Indeed, the calculated trap concentration N_t showed the same value as in sample R2030B6. However, this circumstance is not understood up to now.

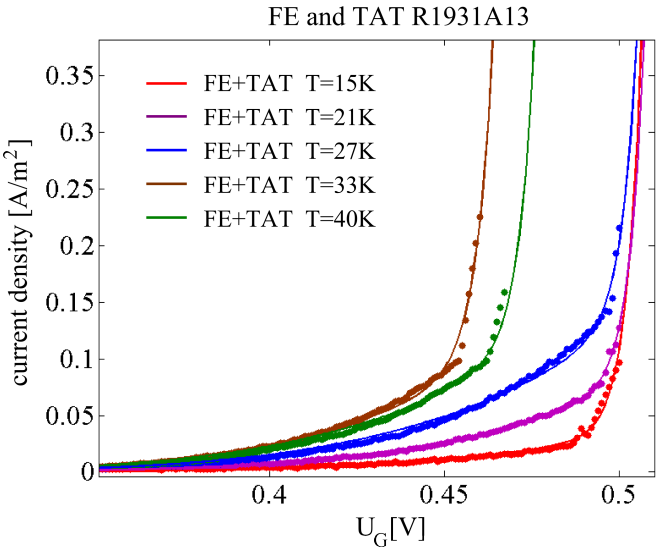

Figure B.6: *Zoom into a few fitting results of sample R1931A13 where a combination of field emission and trap assisted tunnelling was used. The results exhibit an average $R^2 = 0,969$. The data for every temperature are shown in table B.6.*

T $[K]$	Φ_t $[eV]$	Φ_B $[eV]$	N_P $[cm^{-3}]$	N_t $[m^{-3}]$	R^2
15	0,0481	0,625	$7,2 \cdot 10^{18}$	$1,25 \cdot 10^{15}$	0,953
18	0,0466	0,627	$7,2 \cdot 10^{18}$	$1,25 \cdot 10^{15}$	0,951
21	0,0453	0,627	$7,2 \cdot 10^{18}$	$1,25 \cdot 10^{15}$	0,987
24	0,0440	0,630	$7,2 \cdot 10^{18}$	$1,25 \cdot 10^{15}$	0,988
27	0,0431	0,627	$7,2 \cdot 10^{18}$	$1,25 \cdot 10^{15}$	0,992
30	0,0403	0,598	$7,2 \cdot 10^{18}$	$1,25 \cdot 10^{15}$	0,977
33	0,0420	0,610	$7,2 \cdot 10^{18}$	$1,25 \cdot 10^{15}$	0,986
36	0,0418	0,597	$7,2 \cdot 10^{18}$	$1,25 \cdot 10^{15}$	0,989
40	0,0404	0,621	$7,2 \cdot 10^{18}$	$1,25 \cdot 10^{15}$	0,976
average	0,0441	0,620	$7,2 \cdot 10^{18}$	$1,25 \cdot 10^{15}$	0,969

Table B.6: *Overview of the results obtained with a combination of field emission and trap assisted tunnelling in the moderate temperature dependent region II from 18K to 40K. The trap depth Φ_t, the Schottky barrier height Φ_B and the trap concentration N_t were used as fitting parameters. The goodness of fit R^2 is also illustrated as well as the unchanged P doping concentration N_P. Moreover, the average results are indicated in green. The averaged Schottky barrier height was again slightly lower than in the other examined samples.*

B.3 Temperature range from 40K to 100K

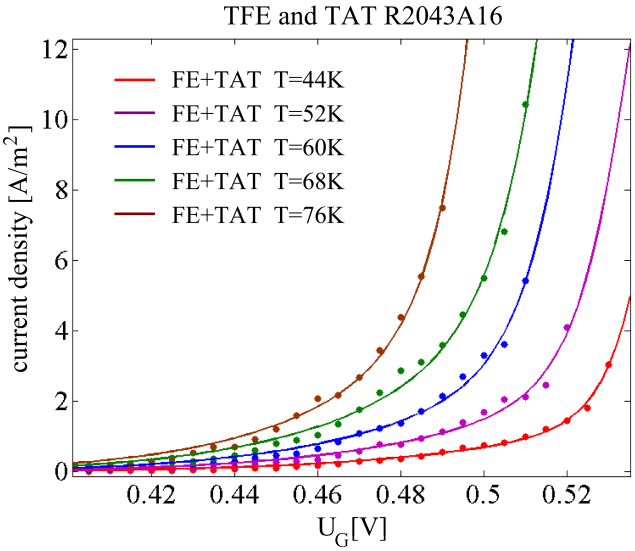

Figure B.7: *Zoom into a few fitting results of sample R2043A16 where a combination of thermionic field emission and trap assisted tunnelling was used. The results exhibit an average $R^2 = 0,988$. The data for each temperature are listed in table B.7.*

T $[K]$	Φ_t $[eV]$	Φ_B $[eV]$	N_P $[cm^{-3}]$	N_t $[m^{-3}]$	R^2
44	0,0429	0,621	$1,1 \cdot 10^{18}$	$2,44 \cdot 10^{17}$	0,990
48	0,0467	0,579	$1,1 \cdot 10^{18}$	$2,44 \cdot 10^{17}$	0,992
52	0,0450	0,546	$1,1 \cdot 10^{18}$	$2,00 \cdot 10^{17}$	0,986
56	0,0497	0,567	$1,1 \cdot 10^{18}$	$2,44 \cdot 10^{17}$	0,990
60	0,0450	0,564	$1,1 \cdot 10^{18}$	$8,80 \cdot 10^{16}$	0,986
64	0,0454	0,547	$1,1 \cdot 10^{18}$	$2,00 \cdot 10^{17}$	0,985
68	0,0467	0,570	$1,1 \cdot 10^{18}$	$2,44 \cdot 10^{17}$	0,986
72	0,0465	0,590	$1,1 \cdot 10^{18}$	$2,44 \cdot 10^{17}$	0,984
76	0,0458	0,598	$1,1 \cdot 10^{18}$	$2,44 \cdot 10^{17}$	0,991
80	0,0459	0,600	$1,1 \cdot 10^{18}$	$2,44 \cdot 10^{17}$	0,995
average	0,0460	0,624	$1,1 \cdot 10^{18}$	$2,20 \cdot 10^{17}$	0,988

Table B.7: *Overview of the results obtained with a combination of thermionic field emission and trap assisted tunnelling in the temperature dependent region III from 40K to 80K. The trap depth Φ_t, the Schottky barrier height Φ_B and the trap concentration N_t were used as fitting parameters. The goodness of fit R^2 is also illustrated as well as the unchanged P doping concentration N_P. Moreover, the average results are indicated in green.*

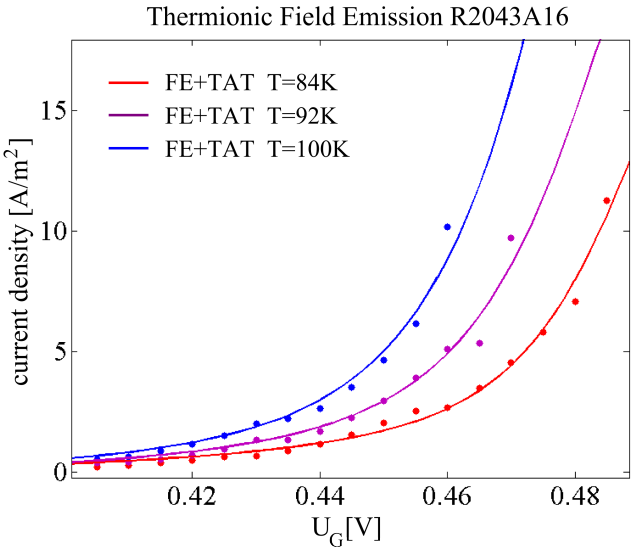

Figure B.8: *Zoom into a few thermionic field emission fitting results of sample R2043A16. The results exhibit an average $R^2 = 0,982$. The data for each temperature are listed in table B.8.*

Finally, we investigated the temperature regime from $40K$ to $100K$ which was only found in sample R2043A16 and R1870E (see section 6). In the range from $40K$ to $80K$, we found that a combination of thermionic field emission (TFE) and

trap assisted tunnelling was best suited to get very good fitting results. In doing so, we still used the Schottky barrier height, the trap depth and the trap concentration as fitting parameters whereas the P doping concentration was fixed. As a consequence, we obtained $\Phi_B = 0,624eV$, $\Phi_t = 0,0460eV$, $N_t = 2,20 \cdot 10^{17} m^{-3}$ with an averaged goodness of fit $R^2 = 0,988$. All relevant fitting results are given in a brief overview in figure B.7 and table B.7. However, it was shown in section 6 that in the temperature range from 80K to 100K solely thermionic field emission (TFE) yielded the best fitting results. As a matter of fact, we extracted an averaged Schottky barrier $\Phi_B = 0,702eV$. An overview of these results is presented in figure B.8 and table B.8.

$T\ [K]$	$\Phi_t\ [eV]$	$\Phi_B\ [eV]$	$N_P\ [cm^{-3}]$	R^2
84	0,045	0,720	$9,0 \cdot 10^{17}$	0,982
88	0,045	0,683	$9,0 \cdot 10^{17}$	0,977
92	0,045	0,704	$9,0 \cdot 10^{17}$	0,979
96	0,045	0,702	$9,0 \cdot 10^{17}$	0,980
100	0,045	0,701	$9,0 \cdot 10^{17}$	0,984
average	0,045	0,702	$9,0 \cdot 10^{17}$	0,982

Table B.8: *Overview of the thermionic field emission results of sample R2043A16. Moreover, the goodness of fit R^2 is illustrated. The average results are still indicated in green.*

C Process technology

In this chapter, detailed information on the complete process technology which is necessary to fabricate gated Hall-bar devices on Si/SiGe heterostrutures is given. In the following, we will also give some background information on how and why special steps were executed.

Sample cutting: All samples were usually cut out of different wafer regions into $5 \times 4mm^2$ pieces with a self made cutter, using a computer controlled diamond scriber which can be precisely adjusted in $x - y$ direction. Moreover, we ballasted the diamond scriber arm with a weight of $50g$ to achieve a fine groove. In order to avoid a covering of the sample surface with dirt e.g. very small cutting fragments or dust, which can't be blown away by a nitrogen purge, the entire process is conducted in a flow box. Finally, the samples were broken out of the wafer and put into a sample box.

Standard cleaning: The first step before the photo-lithography is a standard cleaning process. Therefore, we cleaned the samples in two acetone baths and a concluding isopropanol bath to remove all remaining acetone. Every time after leaving the acetone baths, the samples were additionally flushed with acetone to ensure a completely clean surface. Last but not least the samples were purged dry with nitrogen. However, in the worst-case scenario where we still identify dirt on the sample surface, we put the samples 20 seconds in an ultrasonic acetone bath before the mandatory isopropanol bath and the nitrogen purging conclude the cleaning process.

Photo-lithography: In every lithography step the same Shipley S1813 positive resist and a $NaOH$ developer (Allresist AR-326) is used which only differ in the post lithography handling.

- standard cleaning
- put sample on spinner: cover the surface with S1813 resist
- spinner parameters: acceleration 0, duration $35s$, speed 4500 rpm
- soft-bake on hotplate: $4min$ at $90°C$
- exposure mask aligner: $75s$ at $275W$, hard contact

- development: $40s$ in $NaOH : H_2O = 1 : 3$
- stopping in DI water, purging with N_2
- for mesa etching: hard-bake $3min35s$ on hotplate at $120°C$

Mesa etching:

- final etchant: $HF(0,5\%) : HNO_3(96\%) = 20 : 90$
- etch time $\approx 1min\ 45s$
- etch rate $\approx 1\frac{nm}{s}$

Mesa etching is the first step in the process chain. For our Si/SiGe material system, it was shown that a mixture of diluted HF (0,5%) and a concentrated HNO_3 (96%) in a ratio of 20:90 is suitable to wet chemically etch Hall-bar structures [25, 135]. In this case, the HNO_3 oxidates the Si and SiGe whereas HF removes the material. The diluted $HF(0,5\%)$ was derived from a 40% HF solution. Therefore, we took $158ml$ DI water and mixed it quite good with $2ml$ HF (40%). As a matter of fact, it is absolutely necessary to mingle the obtained diluted HF. Otherwise a HF gradient would develop and lead to irregular etching results or would even never etch.

Since the utilized etching process is diffusion limited [135] or in other words the rate is determined by the speed at which the reactant can be supplied to the sample surface, it is worthwhile to stir each sample continuously in the etch solution. Moreover, one has to keep in mind that HNO_3 is very sensible to light and decomposes after a while. Consequently, we maximally etch 3 samples before we mix a new final etch solution. Finally, all etched samples were neutralized in two DI water baths before they were purged with nitrogen. Last but not least all the resist has to be removed from the sample surface. This is done by placing the samples back to front in a warm acetone bath.

Ohmic contacts: Ohmic contacts are made by the deposition of a AuSbAu tri-layer and a subsequent annealing step in a forming gas atmosphere. Sb has shown to be the best candidate to form ohmic contacts in Si/SiGe two-dimensional electron systems since it is the only n-type dopant which can be easily evaporated and does not need high temperature annealing steps. The most important step towards ohmic contacts are given in note form.

- standard cleaning
- standard photo-lithography, no hard bake!
- mounting of the samples on a glass slide with double side adhesive tape
- HF-Dip: $30s$ in 5% HF to remove the natural oxide

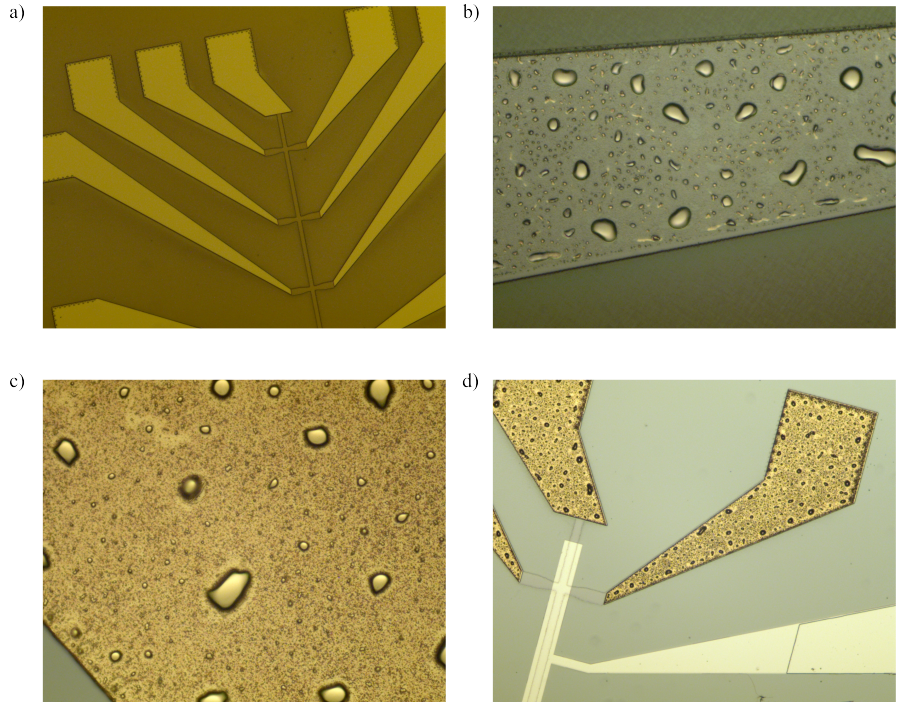

Figure C.1: *a) shows the sample structure after the AuSbAu evaportation. b) Contact lead image after an annealing step at $T = 375°C$ under forming gas atmosphere. c) Picture of a contact lead after the TiAu contact reinforcement. d) displays the sample after the Pd top-gate deposition.*

- thermal evaporation of AuSbAu
- sticking layer: $2nm$ Au, deposited at $r_{Au} \leq 0,3\,\text{Å}s^{-1}$
- contact layers: $30nm$ Sb, $120nm$ Au, $r_{Sb} \leq 0,5\,\text{Å}s^{-1}$
- annealing: forming gas atmosphere, $t = 300s$ at $T = 375°C$ $ramp = 250s$

The deposition of the AuSbAu was conducted in the Univex A deposition machine in the clean room of Prof. Weiss . The native oxide from the Si capping layer was removed prior to the deposition process in a $30s$ $HF(5\%)$ dip. Then the samples were placed as fast as possible into the deposition machine since the HF dip only lasts maximally $30min$. The deposition on his part was carried out after 1 hour of pumping under a pressure of approximately $1 \cdot 10^{-6}mbar$. First of all, a very thin Au layer which serves as a sticking layer was deposited [1]. Next, the deposition of the Sb and Au layers was carried out before a subsequent lift-off process was performed in order to remove the metal from the unwanted positions. After that, we performed an annealing step of the AuSbAu tri-layer in order to realise low-resistive ohmic contacts. Therefore, we put 2 samples on a wafer piece in the

[1] A direct deposition of Sb onto the Hall-bar leads was not possible since the adhesion of Sb on the Si surface is very bad.

center of the annealing oven and heated them for $300s$ at a temperature of $375°C$ under a forming gas atmosphere. At these temperatures we see a characteristic change of the metallic surface morphology from flat and shiny gold to dark and grainy looking as depicted in figure C.1a and b. It was shown in the Phd thesis of Sailer [25] that droplets form at the surface which build small inverted pyramids and pierce through the entire layer structure to the strained Si channel so that an ohmic contact is created.

Contact reinforcements:

- standard cleaning
- put sample on spinner: cover the surface with S1813 resist
- spinner parameters: acceleration 0, duration $35s$, speed 6000 rpm
- soft-bake on hotplate: $4min$ at $90°C$
- exposure mask aligner: $90s$ at $275W$, hard contact
- development: $40s$ in $NaOH : H_2O = 1 : 3$
- stopping in DI water, purging with N_2
- no hard-bake!
- mounting of the samples on a glass slide with double side adhesive tape
- no HF-Dip necessary!
- evaporation of TiAu
- sticking layer: $20nm$ Ti, using an electron beam evaporator (ebeam)
- bonding layer: $180nm$ Au, thermally evaporated

Since the ohmic contacts are created only through these little inverted pyramids, the stability of these contacts has to be improved with a TiAu reinforcement layer. In this way, all inverted pyramids are shortened so that unwanted phenomenons e.g. a contact breakdown [85] can be excluded. However, the dark and grainy looking surface of the leads causes problems during the standard lithography process since there were always resist remains around the droplets which could not be developed. In order to circumvent this problem, we enhanced the spinner speed to 6000 rpm and increased the exposure time in the mask aligner to $90s$. In this way we obtained nice lithography results, see figure C.1c.

Finally, we checked the quality of our ohmic contacts with the help of transmission line structures like in the thesis of Lang [85]. Using this technique, we observed very good contact resistances of approximately $R_C = 80 - 130\Omega$ as well as sheet resistances of $R_{sheet} = 2,8 - 3,2k\Omega$, see figure C.2.

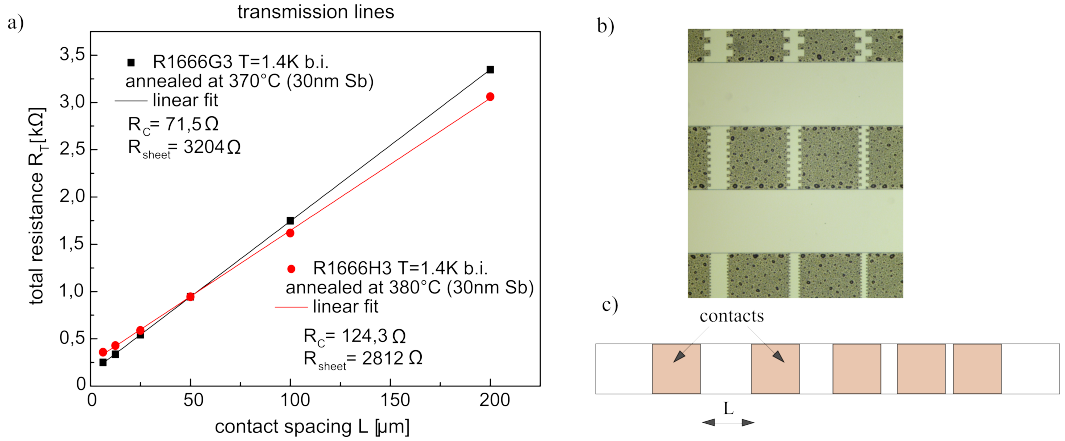

Figure C.2: *a) Overview of two investigated transmission line samples R1666G3 and R1666H3 in order to check the quality of the ohmic contacts. We clearly see low resistive contact resistances which indicate well developed contacts. b) and c) present a typical transmission line with different contact spacings.*

Pd gates:

- standard cleaning
- standard photo-lithography, no hard bake!
- mounting of the samples on a standard sample holder
- HF-Dip: $30s$
- evaporation of $60nm$ Pd with ebeam, deposited at $r_{Pd} \leq 0,6\,\text{Å}s^{-1}$

The lithography was done in the same way as for the ohmic contacts. In contrast to the TiAu evaporation, a HF dip prior to the deposition is inevitable since otherwise based on the native oxide on the surface the samples would suffer extremely from hysteresis effects and therefore result in a worse controllability. In the scope of this deposition run, it is absolutely necessary to bring the dipped samples as fast as possible into vacuum and to start the deposition as soon as possible in order to avoid a renewed oxidation. The final sample structure is shown in figure C.1d.

Lift-off: The lift-off procedure was carried out in warm acetone, immediately after every metallisation step. After some seconds in warm acetone small bubbles will become visible in the metal film. Now the samples can be purged with acetone using a syringe. This eases the lift-off behaviour drastically. Sometimes, only if necessary, a very short treatment in an ultrasonic bath is conducted.

D List of abbreviations

0D	zero-dimensional
2D	two-dimensional
3D	three-dimensional
2DES	two-dimensional system
AC	alternating current
Al_2O_3	aluminium(III) oxide
ALD	atomic layer deposition
Au	Gold
B	boron
CB	conduction band
CHE	classical Hall-Effect
DC	direct current
DQD	double quantum dot
EIES	electron impact emission spectroscopy
E_{CB}	conduction band energy
E_F	Fermi energy
E_P	phosphorous energy
FE	field emission
FET	field effect transistor
FL	Fermi level
FN	Fowler-Nordheim tunneling
Ge	germanium
HEMT	high electron mobility transistor
HF	hydrofluoric acid

HfO_2	hafnium(IV) oxide
HNO_3	nitric acid
IQHE	integer quantum Hall-Effect
IRS	intface specific region
LHe	liquid helium
MBE	molecular beam epitaxy
MISFET	metal insulator semiconductor field effect transistor
ML	monolayer
Mn	manganese
MOSFET	metal oxid semiconductor field effect transistor
N_2	nitrogen
P	phosphorus
Pd	palladium
QC	quantum computer
QD	quantum dot
QHE	quantum Hall-Effect
qubit	quantum bit
QW	quantum well
RHEED	reflection high energy electron diffraction
RELP	reciprocal lattice point
RSM	reciprocal space map
Sb	antimony
SBH	Schottky barrier height
SdH	Shubnikov-de-Haas
SIMS	secondary ion mass spectrometry
Si	silicon
TAT	trap assisted tunneling
TE	thermionic emission
Ti	titanium

TFE	thermionic field emission
UV	ultraviolet
VB	valence band
VS	virtual substrate
VTI	variable temperature inset
WKB	Wentzel-Kramers-Brillouin
XRD	X-ray diffractometer/X-ray diffraction

Bibliography

[1] R. Dingle, H. L. Stoermer, A. C. Gossard, and W. Wiegmann: *Electron mobilities in modulation-doped semiconductor superlattices.* App. Phys. Lett., **33**:655, (1978). http://dx.doi.org/10.1063/1.90457.

[2] K. v. Klitzing, G. Dorda, and M. Pepper: *New Method for High-Accuracy Determination of the Fine-Structure Constant Based on Quantized Hall Resistance.* Phys. Rev. Lett., **45**:494, (1980). http://dx.doi.org/10.1103/PhysRevLett.45.494.

[3] Stuart B. Field, M. A. Kastner, U. Meirav, J. H. F. Scott-Thomas, D. A. Antoniadis, Henry I. Smith, and S. J. Wind: *Conductance oscillations periodic in the density of one-dimensional electron gases.* Phys. Rev. B, **42**:3523–3536, (1990). http://link.aps.org/doi/10.1103/PhysRevB.42.3523.

[4] U. Meirav, M. A. Kastner, and S. J. Wind: *Single-electron charging and periodic conductance resonances in GaAs nanostructures.* Phys. Rev. Lett., **65**:771–774, (1990). http://link.aps.org/doi/10.1103/PhysRevLett.65.771.

[5] D. Loss and D. P. Di Vincenzo: *Quantum computation with quantum dots.* Phys. Rev. A, **57**:120–126, (1998). http://dx.doi.org/10.1103/PhysRevA.57.120.

[6] F. A. Zwanenburg, A. S. Dzurak, A. Morello, M. Y. Simmons, L. C. L. Hollenberg, G. Klimeck, S. Rogge, S. N. Coppersmith, and M. A. Eriksson: *Silicon quantum electronics.* Reviews of Modern Physics, **85**:961–1019, (2013). http://dx.doi.org/10.1103/RevModPhys.85.961.

[7] E. Abe, A. M. Tyryshkin, S. Tojo, J. J. L. Morton, W. M. Witzel, A. Fujimoto, J. W. Ager, E. E. Haller, J. Isoya, S. A. Lyon, M. L. W. Thewalt, and K. M. Itho: *Electron spin coherence of phosphorous donors in silicon: Effect environmental nuclei.* Phys. Rev. B, **82**:121201, (2010). http://dx.doi.org/10.1103/PhysRevB.82.121201.

[8] W. Witzel, R. de Sousa, and S. Das Sarma: *Quantum theory of spectral-diffusion-induced electron spin decoherence.* Phys. Rev. B, **72**:161306, (2005). http://dx.doi.org/10.1103/PhysRevB.72.161306.

[9] A. Wild, J. Sailer, J. Nützel, G. Abstreiter, S. Ludwig, and D. Bougeard: *Electrostatically defined quantum dots in a Si/SiGe heterostructure.* New J. Phys., **12**:113019, (2010). doi:10.1088/1367-2630/12/11/113019.

[10] N. Shaji, C. B. Simmons, M. Thalakulam, L. J. Klein, H. Qin, H. Luo, D. E. Savage, M. G. Lagally, A. J. Rimberg, R. Joynt, M. Friesen, R. H. Blick, S. N. Coppersmith, and M. A. Eriksson: *Spin blockade and lifetime-enhanced transport in a few-electron Si/SiGe double quantum dot.* Nature Physics, **4**:540–544, (2008). doi:10.1038/nphys988.

[11] A. Wild, J. Kierig, J. Sailer, J. W. Anger, E. E. Haller, S. Ludwig, and D. Bougeard: *Few electron double quantum dot in an isotopically purified* ^{28}Si *quantum well.* Appl. Phys. Lett., **100**:143110, (2012). http://dx.doi.org/10.1063/1.3701588.

[12] T. Fujisawa and Y. Hirayama: *Charge noise analysis of an AlGaAs/GaAs quantum dot using transmission-type radio-frequency single-electron transistor technique.* Appl. Phys. Lett., **77**:543, (2000). http://dx.doi.org/10.1063/1.127038.

[13] A. Wild: *Development of a robust platform for spin qubits in SiGe heterostructures.* Phd thesis, Technische Universität München, (2013).

[14] C. Rössler, T. Feil, P. Mensch, T. Ihn, K. Ensslin, D. Schuh, and W. Wegscheider: *Gating of high-mobility two-dimensional electron gases in GaAs/AlGaAs heterostructures.* New Journal of Physics, **12**(4):043007, (2010). http://stacks.iop.org/1367-2630/12/i=4/a=043007.

[15] A. M. Burke, D. E. J. Waddington, D. J. Carrad, R. W. Lyttleton, H. H. Tan, P. J. Reece, O. Klochan, A. R. Hamilton, A. Rai, D. Reuter, A. D. Wieck, and A. P. Micolich: *Origin of gate hysteresis in p-type Si-doped AlGaAs/GaAs heterostructures.* Phys. Rev. B, **86**:165309, Oct (2012). http://link.aps.org/doi/10.1103/PhysRevB.86.165309.

[16] D. Weiss and W. Wegscheider: *Skript zur Halbleiterphysik.* Regensburg, (2008).

[17] P. Y. Yu and M. Cardona: *Fundamentials of Semiconductors. Physics and Materials Properties.* Springer Verlag, (2005).

[18] G. Abstreiter, H. Brugger, T. Wolf, H. Jorke, and H. J. Herzog: *Strain-induced two-dimensional electron gas in selectively doped superlattices.* Phys. Rev. Lett., **54**:2441–2444, (1985). http://link.aps.org/doi/10.1103/PhysRevLett.54.2441.

[19] F. Schäffler: *High-mobility Si and Ge structures.* Semiconductor Science and Technology, **12**:1515, (1997). doi:10.1088/0268-1242/12/12/001.

[20] J. Nützel: *Modulationsdotierte Silizium-Germanium-Heterostrukturen.* Phd thesis, Technische Universität München, (1995).

[21] K. Ismail, F. K. LeGoues, K. L. Saenger, M. Arafa, J. o. Chu, P. M. Mooney, and B. S. Meyerson: *Identification of a Mobility-Limiting Scattering Mechanism in Modulation-Doped Si/SiGe Heterostructures.* Phys. Rev. Lett, **73**(25):3447, (1994). `http://link.aps.org/doi/10.1103/PhysRevLett.73.3447`.

[22] J. Y. Tsao, B. W. Dodson, S. T. Picraux, and D. M. Cornelison: *Critical stresses for Si_xGe_{1-x} strained-layer plasticity.* Phys. Rev. Lett., **59**:2455, (1987). `http://link.aps.org/doi/10.1103/PhysRevLett.59.2455`.

[23] F. Schäffler: *High-electron mobility Si/SiGe heterostructures: Influence of the relaxed sige buffer layer.* Semiconductor Science and Technology, **7**:260, (1992).

[24] C. K. Maiti, L. K. Bera, and S. Chattopadhyay: *Strained Si heterostructure field effect transistors.* Semicond. Sci. Technol., **13**:1225, (1998). `doi:10.1088/0268-1242/13/11/002`.

[25] J. Sailer: *Materials and devices for quantum information processing in Si/SiGe.* Phd thesis, Technische Universität München, (2010).

[26] S. Y. Shiryaev, F. Jensen, and J. W. Petersen: *On the nature of cross-hatch patterns on compositionally graded $Si_{1-x}Ge_x$ layers.* Appl. Phys. Lett., **64**:3305, (1994). `http://dx.doi.org/10.1063/1.111287`.

[27] M. A. Lutz, R. M. Feenstra, F. K. LeGoues, P. M. Mooney, and J. O. Chu: *Influence of misfit dislocations on the surface morphology of $Si_{1-x}Ge_x$ films.* Appl. Phys. Lett., **66**:724, (1995). `http://dx.doi.org/10.1063/1.115287`.

[28] M. Albrecht, S. Christiansen, J. Michler, W. Dorsch, H. P. Strunk, P.O. Hansson, and E. Bauser: *Surface ripples, crosshatch pattern, and dislocation formation: Cooperating mechanisms in lattice mismatch relaxation.* Appl. Phys. Lett., **67**:1232, (1995). `http://dx.doi.org/10.1063/1.115017`.

[29] K. K. Lindner, F. C. Zhang, J. S Rieh, P. Bhattacharya, and D. Houghton: *Reduction of dislocation density in mismatched SiGe/Si using a low-temperature Si buffer layer.* Appl. Phys. Lett., **70**:3224, (1997). `http://dx.doi.org/10.1063/1.119132`.

[30] Y. H. Luo, J. Wan, J. L Forrest, J. L. Liu, G. Jin, M. S. Goorsky, and K. L. Wang: *Effective compliant substrate for low-dislocation relaxed SiGe growth.* Appl. Phys. Lett., **78**:454, (2001). `http://dx.doi.org/10.1063/1.1351520`.

[31] T. Ueno, T. Irisawa, Y. Shiraki, A. Uedono, and S. Tanigawa: *Low temperature buffer growth for modulation doped SiGe/Ge/SiGe heterostructures with high hole mobility.* Thin Solid Films, **369**:320, (2000). http://dx.doi.org/10.1016/S0040-6090(00)00872-5.

[32] F. Isa, A. Marzegalli, A. G. Taboada, C. V. Falub, G. Isella, F. Montalenti, H. von Känel, and L. Miglio: *Onset of vertical threading dislocations in $si_{1-x}ge_x/si$ (001) at a critical ge concentration.* APL Materials, **1**(5):052109, (2013). http://scitation.aip.org/content/aip/journal/aplmater/1/5/10.1063/1.4829976.

[33] C. S. Peng, Z. Y. Zhao, H. Chen, J. H. Li, Y. K. Li, L. W. Guo, D. Y. Dai, Q. Huang, J. M. Zhou, Y. H. Zhang, T. T. Sheng, and C. H. Tung: *Relaxed $Ge_{0.9}Si_{0.1}$ alloy layers with low threading dislocation densities frown on low-temperature Si buffers.* Appl. Phys. Lett, **72**(24):3160–3162, (1998). http://scitation.aip.org/content/aip/journal/apl/72/24/10.1063/1.121579.

[34] M. Bauer, K. Lyutovich, M. Oehme, E. Kaspar, H. J. Herzog, and F. Ernst: *Relaxed SiGe buffers with thicknesses below 0.1μm.* Thin solid Films, **369**:152–156, (2000). DOI:10.1016/S0040-6090(00)00796-3.

[35] T. Ihn: *Semiconductor Nanostructures: Quantum States and Electronic Transport.* Oxford Univ. Press., Oxford, (2011).

[36] C. Hamaguchi: *Basic Semiconductor Physics.* Springer, Berlin, (2001).

[37] N. F. Mott and H. Jones: *The theory of the properties of metals and alloys.* Clarendon Press, (1936).

[38] N. F. Mott: *Note on the contact between a metal and an insulator or semiconductor.* Mathematical Proceedings of the Cambridge Philosophical Society, **34**:568–572, October (1938), ISSN 1469-8064. http://journals.cambridge.org/article_S0305004100020570.

[39] N. F. Mott: *The theory of crystal rectifiers.* Proc. R. Soc. Lond. A, **171**:27–38, May (1939). doi:10.1098/rspa.1939.0051.

[40] W. Schottky and E. Spenke: *Wissenschaftliche Veröffentlichungen aus den Siemens-Werken.* Springer, (1939).

[41] W. Schottky: *Vereinfachte und erweiterte Theorie der Randschicht Gleichrichter.* Zeitschrift für Physik, **118**:539–592, February (1942). doi:10.1007/BF01329843.

[42] B. Sapoval and C. Hermann: *Physics of semiconductors.* Springer, (2003).

[43] S. M. Sze and K. Ng. Kwok: *Physics of Semiconductor Devices.* John Wiley & son, Inc., 3 edition, (2007).

[44] John Bardeen: *Surface states and rectification at a metal semi-conductor contact.* Phys. Rev., **71**:717–727, 1947. http://link.aps.org/doi/10.1103/PhysRev.71.717.

[45] N. Tomonori, K. Koji, and T. Akira: *Evidence for strong Fermi-level pinning due to metal-induced gap states at metal/germanium interface.* Appl. Phys. Lett., **91**:123123, (2007). http://dx.doi.org/10.1063/1.2789701.

[46] O. F. Sankey, R. E. Allen, and J. D. Dow: *Si/transition-metal Schottky barriers: Fermi-level pinning by Si dangling bonds at interfacial vacancies.* Solid State Communications, **49**:1–5, 1984. http://dx.doi.org/10.1016/0038-1098(84)90548-9.

[47] O. F. Sankey, R. E. Allen, S. F. Ren, and J. D. Dow: *Dangling bonds and schottky barriers.* J. Vac. Sci. Technol., **B3**:1162, 1985. http://dx.doi.org/10.1116/1.583032.

[48] W. Mönch: *Semiconductor Surfaces and Interfaces.* Springer, (1993).

[49] E. L. Murphy and R. H. Good: *Thermionic emission, field emission, and the transition region.* Phys. Rev., **102**:1464–1473, 1956. http://link.aps.org/doi/10.1103/PhysRev.102.1464.

[50] J. Y. Li, C. T. Huang, L. P. Rokhinson, and J. C. Sturm: *Extremely low electron density in a modulation-doped Si/SiGe electron gases by effective Schottky gating.* ECS Trans., **50**:145–149, (2013). http://www.princeton.edu/~sturmlab/pdfs/publications/CP.288.pdf.

[51] R. B. Dunford, N. Griffin, D. J. Paul, M. Pepper, D. J. Robbins, A. C. Churchill, and W. Y. Leong: *Schottky gating high mobility $Si/Si_{1-x}Ge_x$ 2D electron systems.* Thin Solid Films, **369**:316–319, (2000). http://dx.doi.org/10.1016/S0040-6090(00)00871-3.

[52] J. E. F. Frost, D. A. Ritchie, and G. A. C. Jones: *The growth of shallow high mobility two-dimensional electron gas structures.* Journal of Crystal Growth, **111**:305–308, (1991). http://www.sciencedirect.com/science/article/pii/002202489190990M.

[53] B. E. Kane, L. N. Pfeiffer, K. W. West, and C. K. Harnett: *Variable density high mobility two-dimensional electron and hole gases in a gated $GaAs/Al_xGa_{1-x}As$ heterostructure.* Appl. Phys. Lett., **63**:2132–2134, (1993). http://scitation.aip.org/content/aip/journal/apl/63/15/10.1063/1.110563.

[54] K. Ismail, M. Arafa, F. Stern, J. O. Chu, and B. S. Meyerson: *Gated Hall effect measurements in high-mobility n-type Si/SiGe modulation-doped structures.* Appl. Phys. Lett., **66**:842, (1995). http://dx.doi.org/10.1063/1.113440.

[55] H. Hasegawa, T. Inagaki, S. Ootomo, and T. Hashizume: *Mechanisms of current collapse and gate leakage currents in AlGaN/GaN heterostructure field effect transistors.* J. Vac. Sci. Technol. B, **21**:1844–1855, (2003). http://dx.doi.org/10.1116/1.1589520.

[56] S. Oyama, T. Hashizume, and H. Hasegawa: *Mechanisms of current leakage through metal/n-GaN interfaces.* J. Appl. Phys., **190**:322–325, (2002). http://dx.doi.org/10.1016/S0169-4332(01)00902-3.

[57] B. H. Lee, L. Kang, W. J. Qi, R. Nieh, Y. Jeon, K. Onishi, and J. C. Lee: *Ultrathin hafnium oxide with low leakage and excellent reliability for alternative gate dielectric application.* IEEE, **IEDM99**:133–136, (1999). doi:10.1109/IEDM.1999.823863.

[58] J. Dickmann, H. Daembkes, S. Schildberg, H. J. Fitting, P. Ellrod, and F. J. Tegude: *Analytical Model to Determine the Gate Leakage Current in $In_{0.52}Al_{0.48}/In_xGa_{1-x}As$ Pseudomorphic Modulation Doped Field-Effect Transistors Caused by Thermionic Field Emission.* Jpn. J. Appl. Phys., **33**:1735–1739, (1994).

[59] L. Albasha, C. M. Snowden, and R. D. Pollard: *A New HEMT Breakdown Model Incorporating Gate and Thermal Effects.* VLSI Design, **8**:349–353, (1998). http://dx.doi.org/10.1155/1998/37965.

[60] G. C. Jegert: *Modeling of Leakage Currents in High-κ Dielectrics.* Phd thesis, Technische Universität München, (2011).

[61] S. Hall, O. Buiu, I. Z. Mitrovic, Y. Lu, and W. M. Davey: *Review and perspective of high-κ dielectrics on silicon.* Journal of Telecomunication and Information Technology, **2**:33–43, (2007).

[62] A. Bouazra, S. Abdi-Ben Nasrallah, A. Poncet, and M. Said: *Current tunnelling through MOS devices.* Materials Science and Engineering: C , **28**:662–665, (2008). http://www.sciencedirect.com/science/article/pii/S0928493107001737.

[63] W. Luo, T. Yuan, Y. Kuo, J. Lu, J. Yan, and W. Kuo: *Charge trapping and dielectric relaxation in connection with breakdown of high-κ gate dielectrics.* Appl. Phys. Lett., **88**:202904, (2006). http://dx.doi.org/10.1063/1.2203942.

[64] A. Ludsteck: *Optimierung von Gate-Dielektrika für die MOS Technologie.* Phd thesis, Universität der Bundeswehr München, (2005).

[65] T. P. Ma and He W.: *Inelastic electron tunneling spectroscopy study of traps in ultrathin high-κ gate dielectrics.* App. Phys. Lett., **83**:5461, (2003). http://dx.doi.org/10.1063/1.1636519.

[66] D. J. DiMaria and E. Cartier: *Mechanisms for stress-induced leakage currents in thin silicon dioxide films.* J. Appl. Phys., **78**:3883–3894, (1995). http://scitation.aip.org/content/aip/journal/jap/78/6/10.1063/1.359905.

[67] Z. Xu, M. Houssa, R. Carter, M. Naili, S. De Gendt, and M. Heyns: *Constant voltage stress induced degradation in HfO_2/SiO_2 gate dielectric stacks.* J. Appl. Phys., **91**:10127, (2002). http://dx.doi.org/10.1063/1.1471920.

[68] P. Samanta, T. J. Man, Q. Zhang, C. Zhu, and M. Chan: *Direct tunneling stress-induced leakage current in ultrathin HfO_2/SiO_2 gate dielectric stacks.* J. Appl. Phys., **100**:094507, (2006). http://dx.doi.org/10.1063/1.2372313.

[69] R. Stratton: *Volt-current characteristics for tunnelling through insulating films.* J. Phys. Chem. Solids, **23**:1177–1190, (1962). http://dx.doi.org/10.1016/0022-3697(62)90165-8.

[70] F. A. Padovani and R. Stratton: *Field and thermionic-field emission in Schottky barriers.* Solid-State Electronics, **9**:695–707, (1966). http://dx.doi.org/10.1016/0038-1101(66)90097-9.

[71] C. R. Crowell: *The Richardson constant for thermionic emission in Schottky barrier diodes.* Solid-State Electronics, **8**:395–399, (1965). http://dx.doi.org/10.1016/0038-1101(65)90116-4.

[72] R. Stratton: *Theory of Field Emission from Semiconductors.* Phys. Rev., **125**:67–82, (1962). http://link.aps.org/doi/10.1103/PhysRev.125.67.

[73] Y. J. Lin: *Application of the thermionic field emission model in the study of a Schottky barrier of Ni on p-GaN from current-voltage measurements.* Appl. Phys. Lett., **86**:122109, (2005). http://dx.doi.org/10.1063/1.1890476.

[74] M. Juang and J. Lee: *Analysis of Schottky Barrier Height in Small Contacts Using a Thermionic-Field Emission Model.* ETRI Journal, **24**(6):455–461, (2002).

[75] H. A. Bethe: *Theory of the Boundary Layer of Crystal Rectifiers.* MIT Radiat. Lab. Rep., pages 12–43, (1942).

[76] R. Perera, A. Ikeda, R. Hattori, and Y. Kuroki: *Trap-assisted leakage current conduction in thin silicon oxynitride films grown by rapid thermal oxidation combined microwave excited plasma nitradation.* Microelectrnic Engineering, **65**:357–370, (2003). http://dx.doi.org/10.1016/S0167-9317(02)01025-0.

[77] E. Suzuki, D. K. Schroder, and Y. Hayashi: *Carrier conduction in ultrathin nitrided oxide films.* J. Appl. Phys., **60**:797, (1988). http://dx.doi.org/10.1063/1.337568.

[78] X. R. Cheng, Y. C. Cheng, and B. Y. Liu: *Nitridation-enhanced conductivity behaviour and current transport mechanism in thin thermally nitrided SiO_2.* J. Appl. Phys., **63**:3616, (1986). http://dx.doi.org/10.1063/1.340072.

[79] M. P. Houng, Y. H. Wang, and W. J. Chang: *Current transport mechanism in trapped oxides: Ageneralized trap-assisted tunneling model.* J. Appl. Phys., **86**:1488, (1999). http://dx.doi.org/10.1063/1.370918.

[80] B. L. Yang, H. Wong, and Y. C. Cheng: *Modelling of trap-assisted electronic conduction in thin thermally nitrided oxide films.* Solid State Electronics, **39**:385, (1996). http://dx.doi.org/10.1016/0038-1101(95)00134-4.

[81] R. G. Southwick, J. Reed, C. Buu, H. Bui, R. Butler, G. Bersuker, and W. B. Knowlton: *Temperature (5.6-300K) Dependence Comparison of Carrier Transport Mechanisms in HfO_2/SiO_2 and SiO_2 MOS Gate Stacks.* IEEE, pages 48–54, (2008). 10.1109/IRWS.2008.4796084.

[82] S. D. Ganichev, E. Ziemann, W. Prettl, I. N. Yassievich, A. A. Istratov, and E. R. Weber: *Distinction between Poole-Frenkel and tunneling models of electric-field-simulated carrier emission from deep levels in semiconductors.* Phys. Rev. B, **61**(15):10361–10365, (1999). http://dx.doi.org/10.1103/PhysRevB.61.10361.

[83] R. H. Fowler and L. Nordheim: *Electron Emission in Intense Electric Fields.* Proc. R. Soc. Lond. A, **119**:173–181, (1928). doi:10.1098/rspa.1928.0091.

[84] M. A. Herrman and H. Sitter: *Molecular Beam Epitaxy: Fundamentals and Current Status.* Springer Verlag, (1996).

[85] V. Lang: *Characterisation of two-dimensional Electron Systems in natural and isotopically pure Si/SiGe Heterostructures.* Diploma thesis, Technische Universität München, (2008).

[86] E. Friess: *Molekularstrahl-Epitaxie von dotierten Si/SiGe-Schichtsystemen: Grundlagen für neue Heterostrukturbauelemente.* Phd thesis, Technische Universität München, (1992).

[87] S. Ahlers: *Ferromagnetische Eigenschaften mangan-dotierter Germanium-Nanostrukturen.* Diploma thesis, Technische Universität München, (2004).

[88] S. Ahlers: *Magnetic and electric properties of epitaxial GeMn.* Phd thesis, Technische Universität München, (2008).

[89] N. Sircar: *Electrical Characterisation of Germanium and Germanium Manganese thin films.* Diploma thesis, Technische Universität München, (2006).

[90] G. Bauer, J. H. Li, and E. Koppensteiner: *X-ray reciprocal space mapping of $Si/Si_{1-x}Ge_x$ heterostructures.* J. Cryst. Growth, **157**:61–67, (1995). http://dx.doi.org/10.1016/0022-0248(95)00372-X.

[91] E. Koppensteiner, G. Bauer, H. Kibbel, and E. Kasper: *Investigation of strain-symmetrized and pseudomorphic Si_mGe_n superlattices by x-ray reciprocal space mapping.* J. Appl. Phys., **76**:3489–3501, (1994). http://dx.doi.org/10.1063/1.357478.

[92] J. Sailer: *Electron channels in strained silicon.* Diploma thesis, Technische Universität München, (2006).

[93] W. X. Ni, K. Lyutovich, J. Alami, C. Tengstedt, M. Bauer, and E. Kasper: *X-ray reciprocal space mapping studies of strain relaxation in thin SiGe layers($\leq$ 100nm) using a low temperature growth step.* J. Cryst. Growth, **227**:756–760, (2001). http://dx.doi.org/10.1016/S0022-0248(01)00821-1.

[94] T. Zibold: *Semiconductor based quantum information devices: Theory and simulations.* Phd thesis, Technische Universität München, (2007).

[95] T. Andlauer: *Optoelectronic and spin-related properties of semiconductor nanostructures in magnetic fields.* Phd thesis, Technische Universität München, (2009).

[96] A. Donner: *Gating of hybrid semiconductor nanostructures.* Master thesis, Universität Regensburg, (2012).

[97] M. Furthmeier: *Entwicklung Aufbau und Inbetriebnahme eines Messsystems zur Durchführung von Magnetotransportuntersuchungen an Halbleiterstrukturen bei tiefen Temperaturen.* Diplomarbeit, Hamburger Fern-Hochschule, (2010).

[98] M. Schafberger: *Electrostatic control of two-dimensional electron gases in Si/SiGe heterostructures.* Master thesis, Universität Regensburg, (2012).

[99] S. Sauther: *Characterization of high mobility two-dimensional electron systems in Si/SiGe heterostructures.* Bachelor thesis, Technische Universität München, (2011).

[100] J. S. Christensen: *Dopant diffusion in Si and SiGe.* Phd thesis, Royal Institute of Technology Stockholm, (2004).

[101] T. Ando, Y. Matsumoto, and Y. Uemura: *Theory of Hall Effect in a two-dimensional electron system.* J. Phys. Soc. Jpn., **39**:279, (1983). http://dx.doi.org/10.1143/JPSJ.39.279.

[102] U. Bockelmann, G. Abstreiter, G. Weimann, and W. Schlapp: *Single-particle and transport scattering times in narrow $GaAs/Al_xGa_{1-x}As$ quantum wells.* Phys. Rev. B, **41**:7864, (1990). http://dx.doi.org/10.1103/PhysRevB.41.7864.

[103] A. Gold: *Electronic transport properties of a two-dimensional electron gas in a silicon quantum well structure at low temperature.* Phys. Rev. B, **35**:723–733, (1987). http://dx.doi.org/10.1103/PhysRevB.35.723.

[104] D. Többen, F. Schäffler, A. Zrenner, and G. Abstreiter: *Magnetotransport studies of remote doped $Si/Si_{1-x}Ge_x$ heterostructures grown on relaxed SiGe buffer layers.* Thin Solid Films, **222**:15, (1992). http://dx.doi.org/10.1016/0040-6090(92)90028-A.

[105] D. Monroe, Y. H. Xie, E. A. Fitzgerald, P. J. Silverman, and G. P. Watson: *Comparison of mobility limiting mechanisms in high mobility $Si_{1-x}Ge_x$ heterostructures.* J. Vac. Sci. Technol. B, **11**:1731–1737, (1993). http://dx.doi.org/10.1116/1.586471.

[106] A. Gold: *Scattering time and single-particle relaxation time in a disordered two-dimesional electron gas.* Phys. Rev. B, **38**:10798, (1988). http://dx.doi.org/10.1103/PhysRevB.38.10798.

[107] A. Ibrahim: *Investigation of electrically active impurities in Si/SiGe heterostructures.* Bachelor thesis, Technische Universität München, (2011).

[108] G. Bastard: *Wave mechanics applied to semiconductor heterostructures.* les editions de physique, Paris, (1988).

[109] W. Walukiewicz, H. E. Ruda, J. Langowski, and H. C. Gatos: *Electron mobility in modulation-doped heterostructures.* Phys. Rev. B, **30**:4571, (1984). http://dx.doi.org/10.1103/PhysRevB.30.4571.

[110] D. Jena, A. C. Gossard, and U. K. Mishra: *Dislocation scattering in a two-dimensional electron gas.* Appl. Phys. Lett., **76**:1707, (2000). http://dx.doi.org/10.1063/1.126143.

[111] G. W. Castellan and F. Seitz: *Semiconducting Materials.* Buttersworth, London, (1951).

[112] J. Benthin, T. G. Castner, and N. K. Lee: *Polarizabilities of shallow donors in silicon.* Solid State Communications, **14**:1321–1324, (1974). http://dx.doi.org/10.1016/0038-1098(74)90657-7.

[113] T. S. Castner, N. K. Lee, G. S. Cielozyk, and G. L. Salinger: *Dielectric anomaly and the metal-insulator transition in n-type silicon.* Phys. Rev. Lett., **34**:1627–1630, (1975). http://dx.doi.org/10.1103/PhysRevLett.34.1627.

[114] S. Dhar and A. H. Marshak: *Static Dielectric Constant of heavily doped Semiconductors.* Solid State Electronics, **28**:763–766, (1985). http://dx.doi.org/10.1016/0038-1101(85)90061-9.

[115] S. Ristic, A. Prijic, and Z. Prijic: *Dependence of static dielectric constant of silicon on resistivity at room temperature.* Serbian J. Electr. Eng., **1**:237–247, (2004). doi:10.2298/SJEE0402237R.

[116] M. A. Alzamil: *Study of Static Dielectric Constant of n-type InAs.* Res. J. Appl. Sci. Eng. Technol., **28**:481–484, (2013).

[117] N. W. Ashcroft and N. D. Mermin: *Solid State Physics.* Saunders College, Philadelphia, (1976).

[118] Silicon Ioffe Institute, NSM Archive. http://www.ioffe.ru/SVA/NSM/Semicond/Si/basic.html.

[119] Germanium Ioffe Institute, NSM Archive. http://www.ioffe.ru/SVA/NSM/Semicond/Ge/basic.html.

[120] C. Neumann: *Fabrication and characterization of hole quantum dots in Ge/SiGe heterostructures.* Diploma thesis, Technische Universität München, (2013).

[121] M. van der Burgt, V. C. Karavolas, F. M. Peeters, J. Singleton, R. J. Nicholas, F. Herlach, J. J. Harris, M. Van Hove, and G. Borghs: *Magnetotransport in a pseudomorphic $GaAs/Ga_{0.8}In_{0.2}As/Ga_{0.25}Al_{0.75}As$ heterostructure with a Si δ-doping layer.* Phys. Rev. B, **52**:12218, (1995). http://dx.doi.org/10.1103/PhysRevB.52.12218.

[122] F. Fischer and M. Grayson: *Influence of voltmeter impedance on quantum Hall measurements.* J. Appl. Phys., **98**:013710, (2005). http://dx.doi.org/10.1063/1.1948530.

[123] S. Contreras, W. Knap, E. Frayssinet, M. L. Sadowski, M. Goiran, and M. Shur: *High magnetic field studies of two-dimensional electron gas in a GaN/GaAlN heterostructure: Mechanisms of parallel conduction.* J. Appl. Phys., **89**:1251, (2001). http://dx.doi.org/10.1063/1.1328788.

[124] G. D. Scott, M. Xiao, H. W. Jiang, E. T. Croke, and E. Yablonovitch: *Sputtered gold as an effective Schottky gate for strained Si/SiGe nanostructures.* App. Phys. Lett., **90**:032110, (2007). http://dx.doi.org/10.1063/1.2430935.

[125] A. Wild: *Materials for g-factor switching in Si/SiGe heterostructures.* Diploma thesis, Technische Universität München, (2009).

[126] N. R. Zangenberg, J. Fage-Pedersen, J. L. Hansen, and A. N. Larsen: *Boron and phosphorous diffusion in strained and relaxed Si and SiGe.* J. Appl. Phys., **94**:3883, (2003). http://dx.doi.org/10.1063/1.370918.

[127] G. L. Pearson and J. Bardeen: *Electrical properties of pure silicon and silicon alloys containing boron and phosphorous.* Phys. Rev., **75**:865, (1949). http://dx.doi.org/10.1103/PhysRev.75.865.

[128] J. W. Chen and A. G. Milnes: *Energy levels in silicon.* Ann. Rev. Mater Sci., **10**:157–228, (1980).

[129] W. Kohn and J. M. Luttinger: *Theory of donor states in silicon.* Phys. Rev., **98**:915, (1955). http://dx.doi.org/10.1103/PhysRev.98.915.

[130] M. Mamor, O. Nur, M. Karlsteen, M. Willander, and F. D. Auret: *Fermi level pinning and Schottky barrier heights on epitaxially grown fully strained and partially relaxed n-type $Si_{1-x}Ge_x$ layers.* J. Appl. Phys., **86**:6890, (1999). http://dx.doi.org/10.1063/1.371768.

[131] L. L. Tongson, B. E. Knox, T. E. Sullivan, and S. J. Fonash: *Comparative study of chemical and polarization characteristics of Pd/Si and $Pd/Si0_x/Si$ Schottky barrier type devices.* J. Appl. Phys., **50**:1535, (1979). http://dx.doi.org/10.1063/1.326106.

[132] R. Purtell, G. Hollinger, G. W. Rubloff, and P. S. Ho: *Schottky barrier formation at Pd, Pt and Ni/Si (111) interfaces.* J. Vac. Technol. A, **1**:566, (1983). http://dx.doi.org/10.1116/1.571958.

[133] S. Pfähler: *Investigation of undoped Si/Ge heterostructures for double quantum dots.* Diploma thesis, Technische Universität München, (2013).

[134] B. M. Maune, M. G. Borselli, B. Huang, T. D. Ladd, P. W. Deelman, K. S. Holabird, A. A. Kiselev, I. Alvarado-Rodriguez, R. S. Ross, A. E. Schmitz, M. Sokolich, C. A. Watson, M. F. Gyure, and A. T. Hunter: *Coherent singlet-triplet oscillations in a silicon-based double quantum dot.* Nature, **481**:344–347, (2012). http://dx.doi.org/10.1038/nature10707M3.

[135] J. L. Vossen and W. Kern: *Thin Film Processes II.* Academic Press Inc, (1991).

Danksagung

Am Ende dieser Arbeit möchte ich mich rückblickend bei allen Personen bedanken, die zum guten Gelingen dieser Arbeit beigetragen haben. Mein besonderer Dank gilt:

- Prof. Dr. Dominique Bougeard für die überragende Betreuung dieser Doktorarbeit. Für seine Gabe auch in schwierigen Situationen jederzeit das Maximum herauszuholen, aber auch für die Zeit und Geduld, die er mir gewährte, um mich in ein neues Aufgaben- und Themengebiet einzuarbeiten. Dominique, Danke!

- Prof. Dr. Dieter Weiss für sein Interesse an dieser Arbeit und die damit verbundene Zweitkorrektur. Des Weiteren möchte ich mich für die Nutzung des Reinraumes und den dort vorhandenen Geräten bedanken.

- Mario Bamesreiter und Josef Loher. Bessere Kollegen als euch kann man sich wahrlich nicht wünschen. Ich hoffe, dass unsere Freundschaft auch in Zukunft bestehen bleibt!

- Christian Neumann für das ausführliche Korrekturlesen, aber auch für die zahlreichen Diskussionen und guten Ideen sowie die unzähligen Anregungen bezüglich dieser Arbeit.

- Johannes Kierig für das Aufdampfen der vielen Pd Schottky top-gates an unserer Zweigstelle dem Walter Schottky Institut in Garching.

- Meinem ehemaligen Diplomanden Michael Schafberger sowie meinem Bachelor Studenten Korbinian Sterr für die gute und erfolgreiche Zusammenarbeit sowie ihren Einsatz unser gemeinsames Projekt voranzubringen.

- Meinen ehemaligen Arbeitskollegen Martin Utz, Jürgen Sailer und Andreas Wild, von denen ich vieles lernen konnte und die mir gerade in meiner Anfangsphase mit Rat und Tat zur Seite standen.

- Christian Fritsch für die letzten Messungen an meinen Proben die die Arbeit ergänzt haben.

- Dr. Dieter Schuh für die unzähligen Diskussionen sowie einige hilfreiche Tipps bezüglich elektrischer Messungen.

- Unserem Techniker Andreas Schützenmeier für die tatkräftige Unterstützung beim Aufbau der einzelnen Setups und beim Wachstum einiger Wafer.
- Imke Gronwald und Peter Müller für die allezeit kollegiale und nette Zusammenarbeit.
- Allen Mitgliedern unserer Arbeitsgruppe für die gute und freundliche Arbeitsatmosphäre inklusive unserer Sekretärin Ulla Franzke, ohne die ich wohl heute noch mit tausenden von Formularen kämpfen würde.
- Meinem Kumpel Simon Böhm für das Korrekturlesen und das Einfügen unzähliger Kommata.
- Meiner Mutter Angelika zum einen für die finanzielle Unterstützung während des Studiums aber auch dafür, dass du immer für mich da bist.
- Meiner gesamten Familie, die mich stets aufbaute wenn es mal nicht so lief und immer voll hinter mir steht.
- Und zu guter Letzt meiner Freundin Lena für deine ganze Unterstützung, dass du immer an mich glaubst und ich mich voll auf dich verlassen kann!